Study of magnetic fields in massive stars and intermediate-mass stars

Aurore Blazère

THÈSE DE DOCTORAT

de l'Université de recherche Paris Sciences et Lettres
PSL Research University

Préparée à l'Observatoire de Paris

Weak magnetic fields in massive and intermediate-mass stars

Ecole doctorale n°127

Astronomie et Astrophysique d'Île-de-France

Spécialité ASTROPHYSIQUE

COMPOSITION DU JURY :

Mme STEHLE Chantal
LERMA, Présidente du jury

M. MATHYS Gautier
ESO, Rapporteur

M. RICHARD Olivier
LUPM, Rapporteur

Mme. NEINER Coralie
LESIA, Directrice de thèse

M. PETIT Pascal
IRAP, Directeur de thèse

M. ALECIAN Georges
LUTH, Examinateur

M. LANDSTREET John
University of Western Ontario
Examinateur

M. HENRICHS Huib
Anton Pannekoek Institute for Astronomy, Examinateur

M. LIGNIERES François
IRAP, Invité

Soutenue par Aurore **BLAZÈRE**
le 07 10 2016

Dirigée par Coralie **NEINER (LESIA)**
Pascal **PETIT (IRAP)**

Remerciements

Après trois années de thèse, voici venu le temps des remerciements. Je tiens tout d'abord à remercier les membres de mon jury, Chantal Stehle, John Landstreet, Georges Alecian et François Lignières, et en particulier mes rapporteurs Olivier Richard et Gautier Mathys, d'avoir consacré de leur temps à la lecture de ce manuscrit. Une thèse ne repose pas uniquement sur les épaules du doctorant et je souhaite dire ici un grand merci à mes directeurs de thèse, Coralie Neiner et Pascal Petit, de m'avoir si bien encadrée pendant ces trois ans. Merci de m'avoir permis de faire cette thèse sur le sujet passionnant que sont les champs magnétiques des étoiles chaudes, de m'avoir guidée et conseillée sur le chemin de la recherche, et de m'avoir accueillie dans vos équipes respectives. Vous m'avez appris la rigueur scientifique, à devenir autonome. Merci pour vos relectures attentives, votre bienveillance et vos soutiens qui ont été si importants pour moi. Merci à tous les deux d'avoir cru en moi, sûrement plus que moi-même. Grâce à vous j'ai eu l'opportunité d'aller observer au Pic du Midi (j'y ai sans doute vu plus de nuages que d'étoiles, mais j'en garde des souvenirs inoubliables) et à La Silla qui, de par la beauté de la voûte céleste, reste pour moi une des plus belles expériences que j'ai vécues.

Miguel, Sophie et Lisa merci d'avoir endossé le rôle de représentants des étudiants du LESIA et d'avoir consacré de votre temps et de votre énergie à l'organisation des repas des étudiants, évènements fédérateurs propices aux échanges et qui nous ont permis de mieux nous connaître. Je tiens aussi à remercier les filles du bâtiment 14, Sophie, Charlotte et Carolina. Merci pour toutes nos discussions autour d'un thé ou dans les couloirs à propos de tout et de rien. Raphaël, tu es parfois exaspérant mais sans toi il n'y aurait pas eu l'ambiance qu'il y avait dans le groupe et c'est sûr que ça nous aurait manqué. Merci à toi pour ce matériel que tu m'as prêté et qui m'a permis de faire de magnifiques photos du ciel étoilé au Chili. Bram, nous avons partagé le même bureau et étudié la même étoile, et je tenais à te dire merci pour toutes ces discussions passionnantes que l'on a eues à propos de ζ Ori A. Merci aussi pour ces chocolats belges que tu avais ramenés. La prochaine fois c'est moi qui en apporterai! Sonny merci pour ta bonne humeur à chaque fois que l'on se voyait.

Thank you Mary for your cheerfulness during your two years in the MagMaS team and for your delicious cupcakes.

Merci aussi à l'ensemble des membres du club astro (Miguel, Sophie, Clément, Lucas, Melody, Lucien,...), grâce à qui j'ai pu continuer à observer le ciel, malgré la pollution

de Paris, dans la joie et la bonne humeur et avec des télescopes historiques. Pendant ma thèse, j'ai aussi fait partie du comité d'organisation d'Elbereth pendant deux ans. Il serait trop long d'en citer tous les membres ici, mais je tenais à vous dire que j'ai été ravie d'avoir partagé cette expérience avec vous tous.

Si j'en suis arrivée là c'est aussi grâce à mes parents, Catherine et François. Vous m'avez permis d'assouvir ma passion en m'achetant mon premier télescope. Grâce à vous, je suis partie à la découverte des nébuleuses, galaxies et autres objets célestes. Merci Papa de m'avoir donné le goût des sciences et de m'avoir fait découvrir l'astronomie à travers la venue de la comète Hale-Bopp, les éclipses lunaires et celle du Soleil en 1999, ainsi que les soirs d'été où on scrutait le ciel à la recherche d'étoiles filantes. Merci Maman d'avoir consacré ton temps à notre education, de nous avoir fait de bons petits plats, amenés chez nos amis et à nos activités sportives. Je tiens aussi à remercier ma grande soeur Mélanie, d'avoir toujours été là pour moi et de m'avoir soutenue dans mon choix de carrière. Ainsi que mon frère, qui a pris le temps malgré son travail très prenant de venir partager des repas avec moi et de passer de bons moments loin de mes préocupations de thèsarde. Afin de n'oublier personne et parce qu'il serait trop long de les lister toutes, je remercie toutes les personnes qui ont de près ou de loin contribué à ma thèse.

Enfin et non des moindres, je tenais à dire un immense merci à mon mari, Louis-Marie, qui m'a supportée pendant ces trois ans et qui me supportait déjà aussi avant! Cela n'est pas toujours facile de partager sa vie avec une thésarde, surtout pendant les derniers mois de thèse où la pression est à son comble. Merci à toi de m'avoir écoutée divaguer sur mon sujet de thèse, même si tu comprenais à moitié ce que je te racontais. Merci surtout pour ta présence à mes cotés et ton soutien. Je ne suis pas sûre que je serais là où j'en suis aujourd'hui si tu n'avais pas été là.

Contents

Acknowledgements iii

Contents v

List of Figures ix

List of Tables xi

1 Introduction 1
- 1.1 Hot stars . . . 1
- 1.2 Magnetic fields in hot stars . . . 1
- 1.3 Origin of the magnetic field in hot stars . . . 3
  - 1.3.1 The dynamo hypothesis . . . 3
  - 1.3.2 The mergers hypothesis . . . 3
  - 1.3.3 The fossil field origin . . . 4
- 1.4 The dichotomy between strong and weak fields . . . 5
  - 1.4.1 Bifurcation between stable and unstable configurations . . . 6
  - 1.4.2 Failed fossil field . . . 7
- 1.5 Goal of the thesis . . . 7

2 Detecting magnetic fields 11
- 2.1 Polarization . . . 11
- 2.2 Zeeman effect . . . 14
- 2.3 Measuring polarization . . . 16
- 2.4 The spectropolarimeter Narval . . . 18
- 2.5 Data analysis . . . 19
  - 2.5.1 Data reduction with Libre-Esprit . . . 19
  - 2.5.2 Least Square Deconvolution technique . . . 20
  - 2.5.3 Detection probability . . . 24
  - 2.5.4 Longitudinal magnetic field . . . 24
  - 2.5.5 Oblique rotator model . . . 25

I Strong magnetic fields **27**

3 The supergiant ζ Ori A **29**
3.1 Introduction . . . 29
3.2 Observations . . . 33
3.2.1 Narval spectropolarimetric observations . . . 33
3.2.2 Archival spectroscopic observations . . . 33
3.3 Checking for the presence of a magnetic field . . . 34
3.4 Separating the two components . . . 35
3.4.1 Identifying the lines of each component . . . 35
3.4.2 Spectral disentangling of Narval data . . . 37
3.4.3 Disentangling using the archival spectroscopic data . . . 38
3.5 Measuring the longitudinal magnetic field of ζ Ori Aa . . . 38
3.5.1 Using the Narval data and correcting for the companion . . . 40
3.5.2 Using synthetic intensity profiles . . . 40
3.5.3 Using disentangled spectroscopic data . . . 40
3.6 No magnetic field in ζ Ori Ab . . . 41
3.6.1 Longitudinal magnetic field values for ζ Ori Ab . . . 41
3.6.2 Upper limit on the non-detected field in ζ Ori Ab . . . 44
3.7 Magnetic field configuration . . . 47
3.7.1 Rotational modulation . . . 47
3.7.2 Field strength and geometrical configuration . . . 48
3.7.3 Stokes V modeling . . . 50
3.8 Magnetospheres . . . 52
3.8.1 Magnetospheric parameters . . . 52
3.8.2 H_α variations . . . 52
3.9 Discussion and conclusions . . . 53

4 The upper limit of the magnetic desert **55**
4.1 Introduction . . . 55
4.1.1 Choice of targets . . . 56
4.2 Data Analysis and longitudinal field measurements . . . 58
4.2.1 HD12447 . . . 58
4.2.2 HD19832 . . . 60
4.2.3 HD22470 . . . 62
4.2.4 HD28843 . . . 62
4.2.5 HD32650 . . . 64
4.2.6 HD96707 . . . 65
4.3 Dipolar magnetic field . . . 66
4.3.1 HD19832 . . . 67
4.3.2 HD32650 . . . 67
4.3.3 HD96707 . . . 68
4.3.4 HD22470 . . . 69

4.3.5 HD28843 . . . 70
4.4 Conclusion . . . 71

II Ultra-weak magnetic fields 73

5 The magnetic field of normal stars 75
5.1 Vega . . . 76
5.1.1 Introduction . . . 76
5.1.2 Observations . . . 76
5.1.3 Data Analysis . . . 77
5.1.4 Conclusion . . . 80
5.2 UZ Lyn . . . 80
5.2.1 Introduction . . . 80
5.2.2 Observations . . . 81
5.2.3 Data Analysis . . . 81
5.2.4 Conclusions . . . 85
5.3 B stars . . . 86
5.3.1 Introduction . . . 86
5.3.2 Choice of targets . . . 86
5.3.3 Observations . . . 87
5.3.4 ι Her . . . 88
5.3.5 γ Peg . . . 89
5.3.6 Conclusion for B stars . . . 93
5.4 Conclusion . . . 94

6 Weak magnetic fields in chemically peculiar stars 95
6.1 The Am stars: β UMa and θ Leo . . . 95
6.1.1 Introduction . . . 95
6.1.2 Selected targets . . . 95
6.1.3 Data analysis . . . 96
6.1.4 Results . . . 99
6.1.4.1 LSD profiles with complete line mask . . . 99
6.1.4.2 Possible instrumental artifacts at high SNR . . . 100
6.1.4.3 Establishing the Zeeman origin of Stokes V signatures . . . 101
6.1.5 Discussion . . . 106
6.1.5.1 Peculiar Stokes V signatures in Am stars . . . 106
6.1.5.2 Origin of the magnetism of Am stars . . . 109
6.1.5.3 Towards a systematic exploration of weak magnetic fields in Am stars . . . 110
6.2 The Am star of Alhena . . . 110
6.2.1 Introduction . . . 110
6.2.2 Observations . . . 111
6.2.3 Magnetic analysis . . . 111
6.2.4 Discussion and conclusion . . . 116

6.3 The HgMn star: α And . . . 117
6.3.1 Introduction . . . 117
6.3.1.1 The target: α And . . . 118
6.3.2 Observations and data analysis . . . 118
6.3.3 Data Analysis . . . 118
6.3.4 The secondary: α And B . . . 124
6.3.5 Conclusion . . . 125
6.4 Conclusion . . . 126

7 Conclusions and perspectives **127**

A Paper on the magnetic field of ζ Ori A **133**

B Paper on magnetic field on β Uma and θ Leo **147**

C Letter on the discovery of the magnetic field of Alhena **158**

D Other refereed publications **163**

Bibliography **164**

List of Figures

1.1 Illustration of the origin of fossil magnetic field in hot stars 5
1.2 Illustration of the dichotomy between strong and weak magnetic field in hot stars 6

2.1 Illustration of the different kinds of polarization. 12
2.2 Schematic description of the Stokes parameters 13
2.3 Zeeman effect on the atomic level 14
2.4 Polarization properties of the Zeeman effect 17
2.5 Schematic description of the Narval polarimeter 19
2.6 Drawing of Narval spectrograph 20
2.7 Example of a Narval spectrum 21
2.8 Illustration of the LSD technique 23
2.9 Illustration of the oblique rotator model 25
2.10 Illustration of the rotational modulation of the Stokes V profile 26

3.1 The Stokes parameter of ζ Ori A of Bouret et al. (2008) 30
3.2 The magnetic confinement-rotation diagram 31
3.3 Example of the result of the LSD technique for ζ Ori A 35
3.4 Comparison between the LSD mask used by Bouret et al. (2008) and my LSD mask 36
3.5 Orbital phase distribution of the spectra of ζ Ori A 38
3.6 LSD profiles of ζ Ori A 39
3.7 Disentangling thanks to FD3Binary 41
3.8 Examples of LSD results for ζ Ori Aa 42
3.9 Examples of LSD results for the secondary component ζ Ori Ab 44
3.10 Upper limit of the non-detected magnetic field in the secondary component of ζ Ori Ab 46
3.11 Rotational modulation of the longitudinal magnetic field of ζ Ori Aa . . . 49
3.12 Best dipolar model fit of the observed Stokes V profiles 51
3.13 Dynamic plot of l H_α 53

4.1 Relation between the field strength and the rotation of Ap stars 57
4.2 Results of the LSD for HD12447 59
4.3 LSD profiles for HD19832 61
4.4 LSD profiles for HD22470 62
4.5 LSD profiles for HD28843 63

4.6 LSD profiles for HD32650 . . . 65
4.7 LSD profiles for HD96707 . . . 66
4.8 Rotational modulation of the longitudinal magnetic field of HD19832 . . 68
4.9 Rotational modulation of the magnetic field of HD32650 . . . 69
4.10 Rotational modulation of the longitudinal magnetic field of HD96707 . . 70
4.11 Upper limit on the non-detected magnetic field in HD28843 . . . 71
4.12 Relation between the field strength and the rotation of Ap stars . . . 72

5.1 Yearly average Stokes V LSD profiles . . . 78
5.2 Yearly averaged Stokes I LSD profiles . . . 79
5.3 Intensity of the Fe line at 518.3nm and Mg line at 518.3 nm . . . 80
5.4 mean LSD profiles of UZ Lyn for 12 October 13 . . . 83
5.5 Co-added LSD profiles of UZ Lyn . . . 84
5.6 Upper limit of the non-detected magnetic field of UZ Lyn . . . 85
5.7 mean LSD profiles of ι Her . . . 90
5.8 Upper limit of the non-detected magnetic field of ι Her . . . 91
5.9 The mean LSD profiles of γ Peg . . . 92
5.10 Upper limit of the non-detected magnetic field of γ Peg . . . 93

6.1 Coadded LSD profiles of *beta* UMa and θ Leo . . . 99
6.2 Comparison of the Stokes V profiles obtained by selecting photospheric lines of low and high magnetic sensitivity . . . 104
6.3 Comparison of the Stokes V profiles obtained by selecting photospheric lines of red and blue wavelength . . . 105
6.4 Comparison of the Stokes V profiles obtained by selecting photospheric lines of large and weak depth . . . 106
6.5 LSD tests for Sirius A . . . 107
6.6 Mean Stokes V profiles of Am stars for the different years of observation 109
6.7 LSD profiles of Alhena A . . . 112
6.7 continued . . . 113
6.8 LSD profiles of the companion Alhena B . . . 115
6.9 Mean LSD profiles of α And A . . . 120
6.10 Mean LSD profiles of α And A for each phase . . . 122
6.11 Upper limit of the non-detected magnetic field in α And A . . . 123
6.12 Mean LSD profiles of α And B . . . 124
6.13 Upper limit of the non-detected magnetic field in α And B . . . 125

List of Tables

3.1 Journal of Narval observations 32
3.2 Journal of archival spectroscopic observations of ζ Ori A 34
3.3 Longitudinal magnetic field of the magnetic primary star ζ Ori Aa 43
3.4 Longitudinal magnetic field measurements for the secondary ζ Ori Ab . . 45

4.1 Stellar parameters of the Ap/Bp stars 57
4.2 Journal of observations of HD12447 58
4.3 Journal of observations of HD19832 60
4.4 Journal of observations of HD22470 62
4.5 Journal of observations of HD28843 64
4.6 Journal of observations of HD32650 64
4.7 Journal of observations of HD96707 66

5.1 journal of observations 77
5.2 longitudinal magnetic field of Vega 79
5.3 Journal of observations of UZ Lyn 82
5.4 Parameters of the possible targets 87
5.5 Journal of observations of the B stars 88

6.1 Fundamental parameters of β UMa and θ Leo 96
6.2 Journal of observations of β UMa and θ Leo 97
6.3 Mean and normalization parameters of the original mean LSD line profiles for β UMa, θ Leo, and α^2 CVn. 102
6.4 Fundamental parameters of the Am stars Alhena and θ Leo. 111
6.5 Journal of observations of Alhena 114
6.6 Longitudinal magnetic field of Alhena 116
6.7 Journal of observations of α And 119
6.8 Measurement of the longitudinal magnetic field of α And 121

Chapter 1

Introduction

1.1 Hot stars

Although quite rare, hot stars (O, B and A-type stars) play a fundamental role in the universe. They have an impact on most astrophysical domains, such as the evolution of galaxies or stellar formation. Stellar magnetic fields have an influence on the transport of energy and mass in the star, on the structure of stars, and on the circumstellar environment. Magnetic fields are present during all stellar evolution stages, and their presence can modify significantly the stellar evolution and fate. During stellar formation, the magnetic field hampers the gravitational collapse (Hennebelle & Fromang 2008) and brakes the protostar. During the whole life of the star, the magnetic field influences the angular momentum, the transport of energy and mass inside the star, and its wind. At its death, it plays a role in the mass loss and in the expulsion of the envelope. For hot stars, the consequences of the presence of a magnetic field are important: these stars, during their entire life and at their death, enrich the interstellar medium with heavy elements such as iron. The irradiation from the most massive stars also influences the environment. However, the magnetic properties of hot stars are poorly known due to a lack of observational constraints. Understanding the magnetism of hot stars is crucial to improve our global understanding of hot stars and in particular stellar evolution theories.

1.2 Magnetic fields in hot stars

Magnetic fields are known to be present in various kinds of stars: on young protostars, on all main sequence stars from very low-mass M dwarfs to massive O stars, and on evolved stars such as white dwarfs and neutron stars. They have a strong influence on all evolutionary stellar stages, from the stellar birth when the molecular cloud collapses to the stellar death (e.g., Mestel 1999). In hot stars, magnetic fields are found to play a significant role on a number of physical processes operating within and in the immediate

vicinity of stars, such as the accretion, diffusion, mass-loss, turbulence and fundamental quantities such as the rotation rate by magnetic braking during the pre-main sequence (PMS) (Ferreira et al. 2000) and chemical composition thanks to the stabilization of the stellar atmosphere that lead to a stratification of the chemical elements by diffusion (Michaud 1970).

The first detection of a magnetic field in a star was obtained by Hale (1908) on the Sun in 1908, thanks to the magnetic polarization of spectral lines in sunspots and he deduced a magnetic field of nearly 3 kGauss. This was the first astrophysical application of the Zeeman effect (Zeeman 1897), discovered by Zeeman 12 years before the discovery of the magnetic field of the Sun by Hale.

The second discovery of a stellar magnetic field was performed by Babcock (1947) at the surface of an Ap star: 78 Virginis in 1947, by searching for magnetic stars other than the Sun. The Ap/Bp stars are chemically peculiar stars that show abundance anomalies in their spectra compared to the solar abundances. Generally, the rotation velocity of Ap/Bp stars is slower than the one of normal A stars. The result by Babcock (1947) was the first magnetic detection in intermediate-mass stars (mass between 1.8 M$\odot$ and 8 M$\odot$). Before this discovery, astronomers thought that magnetic field did not exist in this kind of stars because, contrary to cool stars like the Sun, they do not have a convective envelop where a dynamo can take place. Between 1947 and the early 90's, all magnetic field detections in hot stars concerned Ap/Bp stars. The presence of a magnetic field, or its strength, show no dependence with fundamental stellar parameters, such as radius, temperature, mass, or rotation rate. Even though the observations showed a temporal variability, this variability was attributed to the rotation of the stars and not to an intrinsic variability of the magnetic field. These stars exhibit strong magnetic fields which, in contrast to the fields in cool stars, are dominated by structure on large scales, with a dominant dipolar component. The geometrical characteristics can be well reproduced by the oblique rotator model (Stibbs 1950), that represents the magnetic field of the star like a dipole with a magnetic axis inclined by a tilt angle β with respect to the rotation axis. Even if the dipolar oblique rotator model is a good approximation of the global magnetic field in Ap/Bp stars, the new generation of instruments has shown that the magnetic field on Ap/Bp stars can be more complex (e.g Wade et al. 2000). Smaller scale field structures can exist at the surface. The occurrence of Ap/Bp stars among A/B-type stars and the recent demonstration that all Ap/Bp stars are magnetic (Aurière et al. 2007) leads to an estimate of 5-10 % magnetic stars among main-sequence intermediate-mass stars (Aurière et al. 2007).

The first discovery of magnetic fields in more massive stars was obtained by Donati et al. (2002) for the O star θ^1 Ori C, which hosts a magnetic field of 1 kG. In the last decades, thanks to new instruments and technique, magnetic fields have been discovered in several dozens of massive stars: O and early B-type stars. In particular, a large spectropolarimetric survey of massive stars, MiMeS (Magnetism in Massive Stars) was performed to investigate the occurrence and properties of magnetic fields in massive stars. Around 550 O and early B stars have been observed in this project with a detection threshold of a few tens of Gauss (Wade et al. 2016). MiMeS detected a similar 7% fraction of magnetic stars (Grunhut & Neiner 2015), with similar characteristics as Ap/Bp stars, such as the simple topology (except for the early-B type star τ Sco

which hosts a complex magnetic field, Kochukhov & Wade 2016) and the intrinsic time invariance, suggesting a common origin for the intermediate-mass and massive star magnetism.

1.3 Origin of the magnetic field in hot stars

1.3.1 The dynamo hypothesis

In cool stars, such as the Sun, the magnetic field is generated by a dynamo in the convective envelope. The dynamo is due to the convective motion and the differential rotation by converting the mechanical energy in magnetic field. Such a dynamo generates a complex magnetic field that changes over time.

The envelope of hot stars is radiative, thus the mechanisms that generate the dynamo in the Sun cannot take place in this kind of envelope. Hot stars have a convective core and this is a place where a dynamo could take place. However, even if a dynamo can occur in the core, the time required for this field to reach the surface through diffusion is longer than the lifetime of the star (Charbonneau & MacGregor 2001; MacGregor & Cassinelli 2003). Therefore, even if such a core dynamo exists, it is not the explanation for the magnetic field that we observe at the surface of hot stars.

Hot stars have a very thin convective layer very close to their surface caused by a peak in the opacity due to the iron recombination. A dynamo may develop in this convective layer (Cantiello & Braithwaite 2011). The time needed by the field to reach the surface is shorter (a few years) due to the short distance between the bottom of convective layer and the stellar surface. However, such fields would produce small-scaled field structures and not a large scale structure as observed in magnetic hot stars. Moreover, the magnetic field strength at the surface would be 10 to 100 times weaker than the one observed. Furthermore, the observed fields are stable while a magnetic field produced by sub-surface convection would be time-dependent. As a result, even if such a sub-surface layer dynamo exists, it cannot produce the observed magnetic field in hot stars. Moreover, in the intermediate-mass stars the iron convective layer is deeper than in massive stars. Therefore, this explanation is less probable in the intermediate-mass stars, while the similar characteristics of the magnetic field in massive and intermediate-mass stars suggest a common origin.

1.3.2 The mergers hypothesis

Another explanation to generate a magnetic field in hot stars is the merging of two pre-main sequence stars. During the merging of young proto-stars, a magnetic field can be generated through a dynamo process due to the strong shears (Ferrario et al. 2009). Mergers of stars are rare and that could explain the observed small fraction of magnetic hot stars. This scenario predicts that no magnetic field exists in close binaries (Schneider et al. 2016) and that the produced merger star shows significant nitrogen enrichment at

its surface (Glebbeek et al. 2013). However, a double magnetic close binary system, ϵ Lupi, was discovered by Shultz et al. (2015). Moreover, no observational proofs could confirm this scenario.

1.3.3 The fossil field origin

Fossil magnetic fields are products of a seed field (Mestel 1999). In the fossil field theory, the magnetic field observed at the surface of hot stars is a remnant of the magnetic field of the molecular cloud from which the star was formed. During the early stages of stellar formation, the proto-star is fully convective, a dynamo can enhance and sustain the seed field. As the radiative core appears and the convective zone disappears in the center of the star, the magnetic field relaxes onto a large-scale dipole, like the ones observed at the surface of hot stars. In addition, it is possible that the appearance of the convective core, just at the end of the stellar formation, produces a tilt of the dipole and explains why we observed oblique dipoles in basically all hot stars (Featherstone et al. 2009). Figure 1.1 shows a scheme of the fossil field scenario.

One of the issue of this theory was the survival of the magnetic field: it is difficult to find a magnetic field that is stable enough to survive during the lifetime of the stars. Indeed, a magnetic field is only stable on the Alfvén timescale, that corresponds to the time needed for a magnetic Alfvén wave to cross the star. This time depends on the magnetic strength, but for a typical magnetic hot star it is around a few years. However, Braithwaite & Spruit (2004) and Duez & Mathis (2010) demonstrated thanks to simulations and analytical work that magnetic fields can be stable over the stellar lifetime if it is a mix between toroidal and poloidal components. They modeled a star without rotation with a random magnetic field. At the beginning, the field decreases rapidly. However at some point, the decreasing stops and the field reaches a stable configuration that is the same whatever the initial conditions. The configuration is approximatively axisymmetric and made of toroidal and poloidal components. At the stellar surface, it appears as a dipole, just like the ones observed on hot stars.

In addition, Alecian (2012) showed that Herbig Ae/Be stars, which are the precursors of the magnetic Ap/Bp stars, host magnetic fields with a similar occurrence rate and configuration as main sequence hot stars. This indicates that the fields observed in hot stars are already present at the pre-main sequence phase. It thus provides support for the fossil field theory.

Therefore, it is now well established that the magnetism in hot stars is of fossil origin. However, the creation and evolution of these fields are not known in detail, during the stellar formation, and require further investigations. One remaining problem of the fossil magnetic field theory is that it does not explain why only 7% of hot stars host a magnetic field (Grunhut & Neiner 2015).

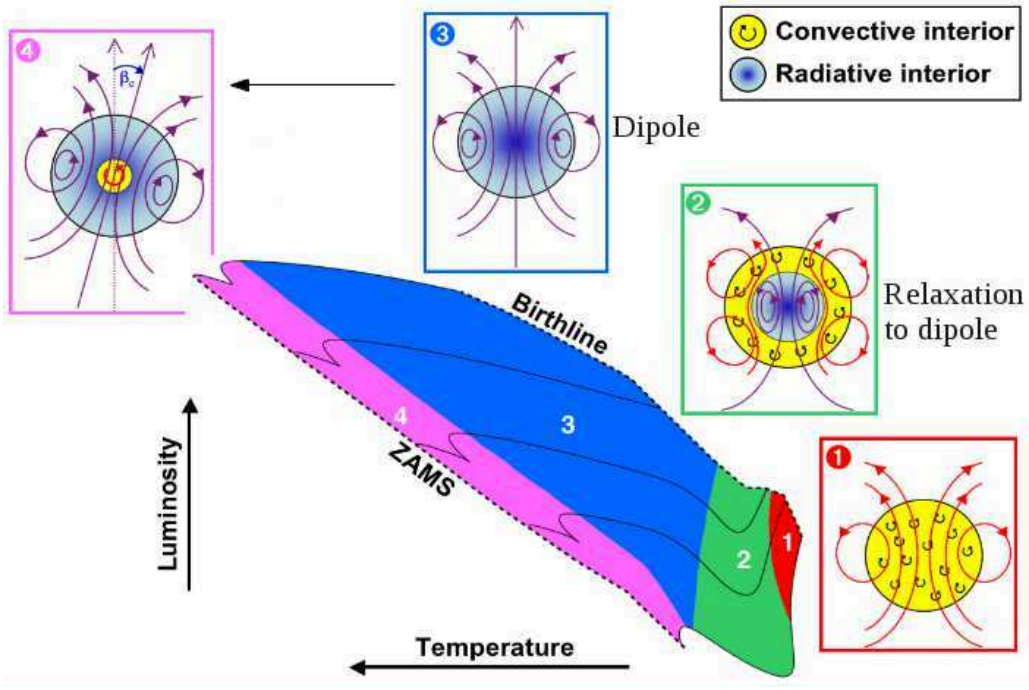

FIGURE 1.1: **Illustration of the origin of fossil magnetic field in hot star**: The diagram is divided in 4 parts indicated with colours, showing 4 stages of the evolution of the structure of the stars and of their fossil magnetic field (Neiner et al. 2015b).

1.4 The dichotomy between strong and weak fields

All magnetic massive and intermediate-mass stars discovered until recently have a strong dipolar magnetic field, with a typical strength 3of kG (Power et al. 2007). These fields are stable over time. The fossil field origin is well established for these fields.

Recently, Lignières et al. (2009) discovered an ultra-weak magnetic field in the normal A star Vega. The spectropolarimetric time series was interpreted in terms of a surface magnetic field distribution using the Zeeman-Doppler Imaging technique (ZDI, Petit et al. 2010), unveiling a peak local field strength of about 7 G (Petit et al. 2014a). The results of that study support the view that Vega is a rapidly rotating star seen nearly pole-on, and the reconstruction of the magnetic topology at two epochs revealed a magnetic region of radial field orientation, closely concentrated around the rotation pole. Another ultra-weak magnetic field was discovered in the chemically peculiar Am star Sirius (Petit et al. 2011). However, the shape of the signature in Sirius is peculiar with a prominent positive lobe without negative lobe. This signature is not expected in the normal Zeeman theory. These two stars may well be the first confirmed members of a much larger, as yet unexplored, class of weakly magnetic hot stars.

What is the origin of these weak magnetic fields? Two different theories can explain the dichotomy between strong fields and ultra-weak fields: the first one assumes that the two types of magnetic fields are produced by two different processes and have different properties. The second assumes that the strong and weak fields have a common origin but, during the stellar evolution, there is a bifurcation between weak and strong

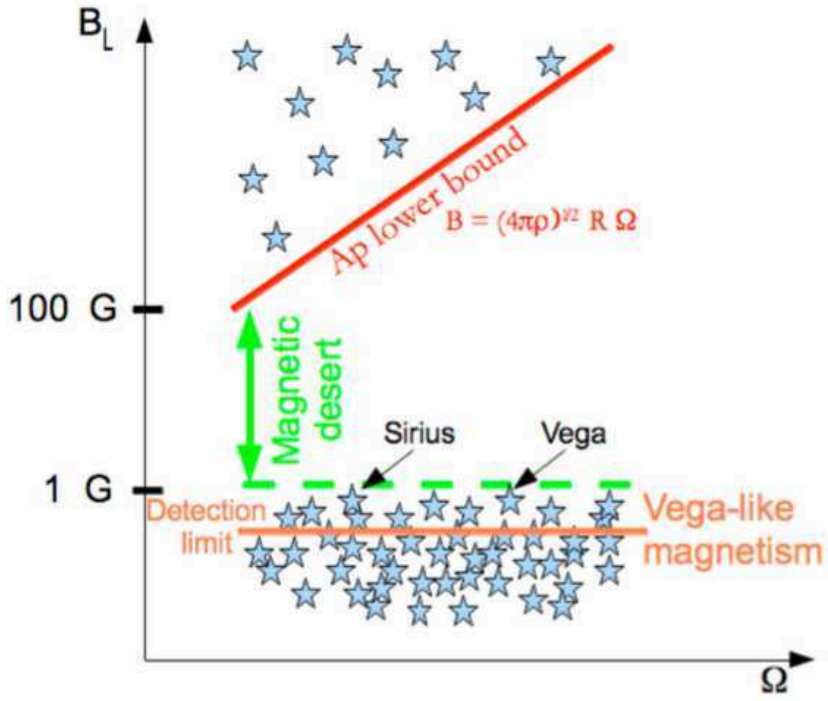

FIGURE 1.2: **Scheme of the dichotomy between strong and weak magnetic field in hot stars** (courtesy F. Lignières).

magnetic fields. The latter explanation was used in various scenarios to explain the dichotomy between strong and weak magnetic fields.

1.4.1 Bifurcation between stable and unstable configurations

To explain the dichotomy between strong and weak magnetic fields, Aurière et al. (2007) proposed a scenario based on the stability of large scale magnetic configurations in differentially rotating stars. If the magnetic field is weak enough, it cannot prevent the winding-up of the poloidal field into a toroidal field. The increasingly toroidal configuration is expected to become unstable to a pinch-type instability, called the Tayler instability, that replaces the large scale field configuration by a new configuration structured at the length scale of the instability. On the contrary, if the initial magnetic field is strong enough, Maxwell stresses will tend to impose uniform rotation and eventually lead to a stable configuration. Starting with an initial distribution of magnetic fields ranging from low to high dipolar strengths, this mechanism predicts a sharp decrease of the longitudinal field - i.e. the surface averaged of the line-of-sight field component - between stable and unstable configurations. An order of magnitude estimate of the critical field separating the stable and unstable configuration yields: $B_c = (4\pi\rho)^{1/2} r\Omega$. This estimate turns out to be quite close to the observed minimum field of Ap stars and the predicted increase of the critical field with the rotation is also compatible with the few existing data. See Figure 1.2 for an illustration of this scenario.

Regarding the 7% occurrence issue, Aurière et al. (2007)'s scenario does not assume that at the end of their formation process some stars are magnetic and others not. It proposes instead that all stars are initially magnetic and that the differentiation leading to the 7% incidence rate is due to a subsequent bifurcation between stable and unstable configurations.

Models of a magnetic field in a differentially rotating radiative zone (Gaurat et al. 2015; Jouve et al. 2015) show that instabilities destroy the large scale magnetic field when the poloidal field is weaker than a critical value. These models are compatible with the scenario developed by Aurière et al. (2007).

1.4.2 Failed fossil field

Braithwaite & Cantiello (2013) also proposed a scenario to explain the dichotomy. In this scenario, called failed fossil field, the magnetic fields evolve dynamically toward an equilibrium in absence of any driving from differential rotation, convection or meridional circulation. At first, the magnetic field is not in equilibrium, and evolves on its own dynamic timescale. As it does so, magnetic energy is lost and the field strength drops. While in the strongly magnetic stars an equilibrium is quickly reached and the field essentially stops evolving (a fossil field), in weakly magnetic stars the field is still evolving. If the time to reach equilibrium is shorter than the age of the star, it is called a failed fossil field. The time to reach the stable configuration depends on the rotation of the star. For slow rotators, this time is longer than for fast rotators. This theory predicts that this kind of unstable magnetic field exist in the fraction of massive stars that do not have strong magnetic fields, younger stars should tend to have stronger fields and faster rotators have stronger fields.

For both theories presented above, there is a lack of observational constraints. New observations are needed to provide constraints to differentiate between theories to explain the bifurcation between strong and weak magnetic fields.

1.5 Goal of the thesis

Understanding the magnetism of massive and intermediate-mass stars is critical to make progress in stellar evolution theory. Magnetic fields are key actors in the evolution of all stellar objects. Although the influence of magnetic fields on stellar evolution has been recognized for a long time, progress have been challenged by a lack of observational constraints combined with the difficulty in modeling magnetohydrodynamics processes. This is particularly true in the range of intermediate-mass and massive stars. Until recently, only a small ($\sim$7%) fraction of hot stars were known to be magnetic (Grunhut & Neiner 2015) usually with a simple topology (i.e. dipolar) and their magnetic fields are stable in time. To explain these properties, the current theory, the fossil field theory, describes this magnetism as remnant of an early phase of the star's life, but leaves many basic questions unanswered, such as the small fraction of magnetic stars, and in practice provides no constraint to stellar evolution theory.

In last decades, progress was achieved to understand this magnetism thanks to a new generation of spectropolarimeters. First, the similar detection rate of strong magnetic fields among intermediate-mass and massive stars suggest a common origin to the magnetic fields of all hot stars. Then, the observations of Ap/Bp stars revealed the lower limit to the magnetic fields of intermediate-mass stars and the existence of a magnetic desert between the strong magnetic fields and the weak magnetic fields like the one detected on Vega. The scenarios to explain this dichotomy are based on the stability of magnetic fields. The strong and weak fossil magnetisms originate from the bifurcation between stable and unstable magnetic configurations (Aurière et al. 2007; Braithwaite & Cantiello 2013). However, more observational and numerical works are needed in order to discriminate between the different scenarios.

Understanding the origin of the weak magnetism is an exciting new challenge of stellar magnetism and can provide new constraints for theory. Do all supposed non-magnetic stars actually host a weak magnetic field? For example, the detection of low frequency modulation of the light-curve compatible with a rotational modulation found in ∼70% of the A-type Kepler stars could be explained by the presence of star spots or other magnetic co-rotating features (Balona 2011; Böhm et al. 2015). A large occurrence of weak magnetic fields in hot stars would also have a direct impact on stellar evolution models by providing the first direct constraints on the value of the magnetic field of a typical intermediate-mass or massive star.

My PhD was undertaken in this context as part of the ANR Imagine project (Investigating MAGnetism of IntErmediate-mass and massive stars, PI:F. Lignières). The aims of this project is to investigate the magnetism of hot stars thanks to observations and modeling, to reach a better understanding of the properties of the magnetic hot stars and the physical processes that occur in these stars.

My PhD thesis consisted in analyzing observational data taken with high-resolution spectropolarimeters, principally with Narval installed at the Pic du Midi Observatory, to detect magnetic fields. This instrument and the techniques I have used are presented in Chapter 2. One part of my thesis was dedicated to the study of strong magnetic fields and my work is described in chapters 3 and 4. I analyzed the observations of a massive O star: ζ Ori A (see chapter 3) because only a few O stars are known to be magnetic and each new discovery of a magnetic O star helps to understand the magnetic properties of massive stars. While we know that a magnetic desert exists among intermediate-mass stars, we did not know if it extends to massive stars. Bouret et al. (2008) claim that ζ Ori A hosts a weak dipolar magnetic field ($\sim$ 100 G). Confirming or refuting this result would bring constraints on the existence of the magnetic desert in massive stars. I was also involved in a project to determine the upper limit of the magnetic desert thanks to observations of Ap/Bp stars. The goal of this project is to test the dependence of the upper limit with rotation (see chapter 4). The other part of my thesis is dedicated to the search for ultra-weak fields like the one of Vega or Sirius in hot stars, to bring constraint to the various scenarios that explain the dichotomy and to have a better understanding of the magnetic properties of this kind of fields. The results are presented in chapters 5 and 6. I present the results of the spectropolarimetric study of normal stars (see chapter 5): Vega, UZ Lyn and some B stars. Then, I present the result for chemically peculiar stars (see chapter 6). I studied three Am stars: β UMa, θ Leo and Alhena,

and one HgMn star: α And. In chapter 7 I then summarize the conclusions of my work and present the perspectives for future studies.

Chapter 2

Detecting magnetic fields

We use an indirect method to detect magnetic fields thanks to the emitted light of the stars. The detection of a magnetic field is based on the Zeeman effect, that influences the lines in the spectrum of the star. Indeed, a spectral line that is sensible to the magnetic field is divided in several components when it is formed in a magnetic environment. However, this splitting is difficult to detect in stars due to their weak magnetic field and to line broadening by stellar rotation. Nevertheless, the components of a Zeeman triplet are polarized, and we can use this polarization to diagnose the field.

2.1 Polarization

Light can be represented by the superposition of two plane electromagnetic waves. Each electromagnetic wave can be described by its electric field $\vec{E}$ and magnetic field $\vec{B}$ that are in a plane perpendicular to the wave propagation direction $\hat{e_z}$. If this plane is described by an orthonormal basis $\{\hat{e_x}, \hat{e_y}, \hat{e_z}\}$, $\hat{e_x}$ and $\hat{e_y}$ define the polarization plane. So, in any point in space, the electric field can be described by:

$$\vec{E}(t) = \begin{pmatrix} E_x \\ E_y \end{pmatrix} = \begin{pmatrix} A_x e^{i(\delta_x - \omega t)} \\ A_y e^{i(\delta_y - \omega t)} \end{pmatrix}, \tag{2.1}$$

where A_x and A_y are respectively the amplitude of the components of the electric field on the axis $\hat{e_x}$ and $\hat{e_y}$, ω is the angular frequency, and $(\delta_x - \delta_y) = \delta$ is the temporal phase shift between the oscillations of the two components. If $\delta = 0$ or $\delta = \pi$, the light is linearly polarized: the vector of the electric field oscillates along a line in the polarization plane (see left panel of Fig. 2.1). If $\delta = \frac{\pi}{2}$ or $\delta = \frac{3\pi}{2}$ and the two amplitudes A_x and A_y are equal, the light is circularly polarized: the electric field vector turns around the propagation axis. If the rotation is in the clockwise direction, the polarization is right circular and in the counterclockwise direction, the polarization is left circular (see middle panel of Fig. 2.1). In the general case, the wave is elliptically polarized, the amplitude of the components are not identical and the vector of the electric field describes an ellipse (see right panel of Fig. 2.1)

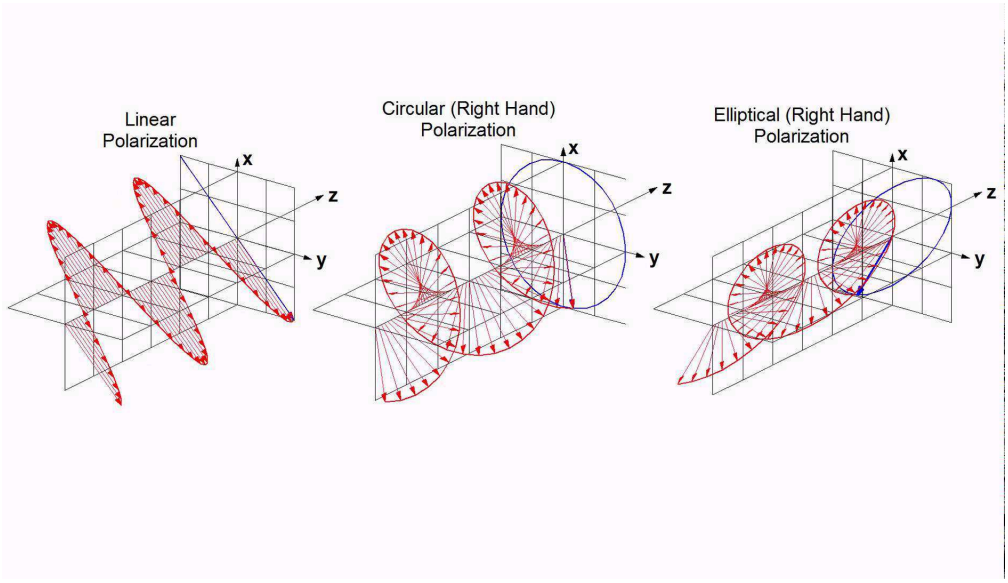

FIGURE 2.1: **Illustration of the different kinds of polarization**. The left panel shows an example of linear polarization. The electric field oscillations are contained in a plane. The middle panel shows an example of circular polarization: the electric field turns around the propagation axis and the amplitude of the components are equal. Finally, the right panel shows the elliptical polarization case: the electric field turns around the propagation axis and the amplitude of the components are not equal. This figure was generated thanks to the video available at: https://www.youtube.com/watch?v=Q0qrU4nprB0

In practice, we cannot observe the electric field of a wave directly. Unfortunately, detectors (CCD,...) are only sensitive to the energy transported by the electromagnetic wave and not to the electric field itself. However, the transported energy is a function of the electric field and its conjugated complex is:

$$E_i^*(t)E_j(t) = A_i A_j e^{i(\delta_j - \delta_i)} \tag{2.2}$$

For the superposition of plane waves, we must average this quantity on all waves. We define the polarization tensor, so that its components are:

$$I_{ij} = \langle E_i^*(t)E_j(t)\rangle, \tag{2.3}$$

where the symbol $\langle ...\rangle$ is the average on the set of plane waves. We can rewrite this tensor under the form of a matrix:

$$\mathbf{I} = \begin{pmatrix} \langle E_x^* E_x\rangle & \langle E_y^* E_x\rangle \\ \langle E_x^* E_y\rangle & \langle E_y^* E_y\rangle \end{pmatrix} = \begin{pmatrix} A_x^2 & A_x A_y e^{i\delta} \\ A_x A_y e^{-i\delta} & A_y^2 \end{pmatrix} \tag{2.4}$$

The diagonal elements represent the intensity of the two components on the $\hat{e}_x$ and $\hat{e}_y$ axis and the other elements describe the phase relation. While the diagonal elements are real and measurable, it is not the case for the other elements. If the non-diagonal

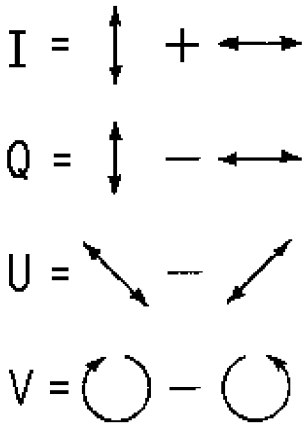

FIGURE 2.2: **Schematic description of the Stokes parameters**: I is the addition of the two linear orthogonal polarization states. Q and U are the subtractions between two linear orthogonal polarization states. V is the difference between the right circular polarization and the left circular polarization (https://kicp.uchicago.edu/research/cosmology_glossary.html).

elements are null, the light is not polarized. In the opposite case, we use a linear combination of the elements to describe the polarized light, the Stokes parameters (see Fig. 2.2):

$$\begin{aligned} I &= (I_{11} + I_{22}) = A_x^2 + A_y^2 \\ Q &= (I_{11} - I_{22}) = A_x^2 - A_y^2 \\ U &= (I_{12} + I_{21}) = 2A_x A_y cos(\delta_x - \delta_y) \\ V &= i(I_{12} - I_{21}) = 2A_x A_y sin(\delta_x - \delta_y), \end{aligned} \tag{2.5}$$

where i is the imaginary number. These parameters have the advantage to be measurable quantities by combining the diagonal elements of the polarization tensor.

I is the addition of the two linear orthogonal polarization states and represent the total intensity of the radiation. Q and U represent the linear polarization of the light. More exactly, the Stokes Q parameter is the subtraction between the two linear orthogonal polarization states that are perpendicular, and U is the subtraction between the two linear orthogonal polarization states with an angle of 45 ° with the ones of Q. V is the difference between the right circular polarization and the left circular polarization.

Several phenomena can polarize and depolarize the light emitted by atoms, for example the Rayleigh diffusion, the birefringent properties of some material, refraction... However, only the polarization due to Zeeman and Hanle effects are linked to the presence of a magnetic field. The Zeeman effect is easier to measure for stars than the Hanle effect, and it is the one I used in this thesis.

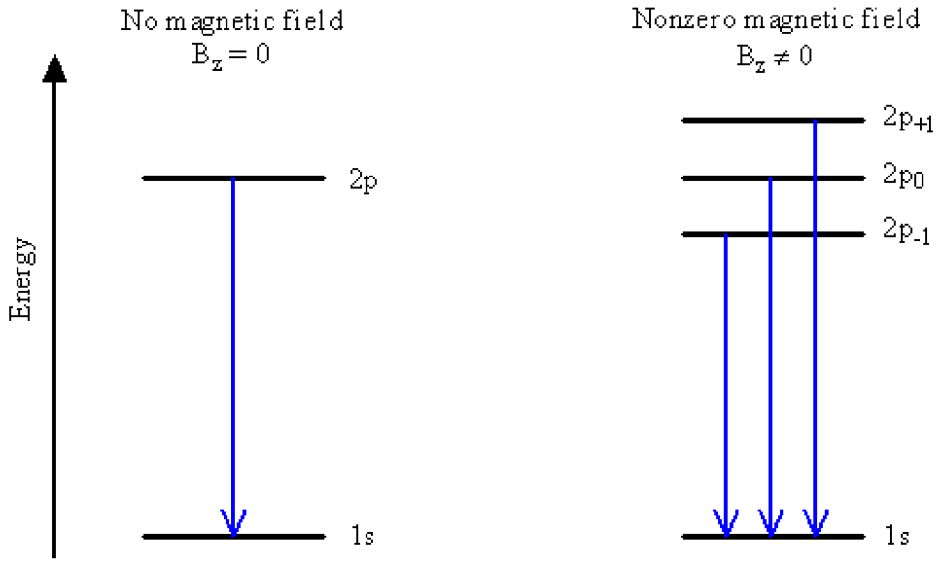

FIGURE 2.3: **Zeeman effect on the atomic level**: Without magnetic field (B=0, left panel), we observe only one transition at a frequency ν_0 or at a wavelength $\lambda = \frac{c}{\nu_0}$. With a magnetic field (right panel), the upper level are split in three sublevels equidistant in energy. The component σ_b is the line at frequency $\nu_0 + g\nu_L$, the component σ_r is the line at frequency $\nu_0 - g\nu_L$, and the component π is the line at frequency ν_0 (http://chem.libretexts.org).

2.2 Zeeman effect

The Zeeman effect is the splitting of spectral lines in presence of a magnetic field. This effect was predicted by H. L. Lorentz in the classical electromagnetic theory and discovered by P. Zeeman in 1896.

In the presence of a magnetic field, some atomic energy levels are split in sublevels equidistant in energy (see Fig. 2.3). Without magnetic field (B=0), we observe only one transition. With a magnetic field, the upper level is split in several transitions.

According to the theory of atomic structure, the presence of a uniform magnetic field modifies the spectrum. This modification can be described by adding a magnetic Hamiltonian to the unperturbed Hamiltonian:

$$H_B = \frac{e_0 h}{4\pi mc}(\vec{L} + 2\vec{S}).\vec{B} + \frac{e_0^2}{8mc^2}(\vec{B} \times \vec{r}), \tag{2.6}$$

where e_0 is the absolute value of the electron charge, h is the Planck constant, m is the electron mass, and c is the speed of light. $\vec{L}$ and $\vec{S}$ are the total orbital angular momentum and total spin of the electronic cloud, $\vec{B}$ is the magnetic field vector, and $\vec{r}$:

$$\vec{r} = \sum_i \vec{r_i}, \tag{2.7}$$

where $\vec{r_i}$ corresponds to the position of the i-th electron relative to the nucleus. The second term of Equation 2.6 is called the diamagnetic term. In case of a weak magnetic field, this term can be ignored because it is negligible compared to the first term of Equation 2.6. So, in case of a weak magnetic field, which corresponds to the case of magnetic main sequence hot stars, the magnetic Hamiltonian is:

$$H_B = \frac{e_0 h}{4\pi mc}(\vec{L} + 2\vec{S}).\vec{B} = \mu_0(\vec{L} + 2\vec{S}).\vec{B}, \tag{2.8}$$

where μ_0 is the Bohr magneton that can be calculated by the L-S coupling or measured in a laboratory.

If the magnetic field is weak enough, the magnetic Hamiltonian H_B is small compared to the unperturbed Hamiltonian H_0. In this case, the effect related to H_B can be treated as a perturbation of H_0 and the eigenvalues of $H_0 + H_B$ are:

$$E_{J,M} = E_{J0} + \mu_0 g B M, \tag{2.9}$$

where M is the magnetic quantum number, E_{J0} is the energy of the level J without perturbation, and g is the Landé factor.

Thus the degeneracy is removed by the Hamiltonian H_B, and the level of quantum number J is split into $(2J + 1)$ equally spaced sublevels, the splitting depends on the Landé factor g and on the magnetic field. The sublevels characterized by the magnetic quantum number M take all the integral values between $-J$ and J.

If we consider a transition between two atomic levels, in presence of a magnetic field, with J and J' respectively the angular quantum numbers of the lowest and highest level, and g and g' the corresponding Landé factors, the spectral line originating from the transition between the two levels splits, owing to the magnetic field, into a collection of components whose frequencies are given by:

$$\nu_{MM'}^{JJ'} = \nu_0 + \nu_L(g'M' - gM), \tag{2.10}$$

where ν_0 is the frequency of the line without magnetic field, M and M' are the respective magnetic quantum numbers of the lowest and highest levels, and ν_L is the Larmor frequency:

$$\nu_L = \frac{e_0 B}{4\pi mc} = 1.3996 \times 10^6 B, \tag{2.11}$$

where B is in G and ν_L in s^{-1}.

The wavelength shift can be written as:

$$\lambda_{MM'}^{JJ'} = \lambda_0 - \Delta\lambda_B(g'M' - gM), \tag{2.12}$$

where $\lambda_0 = C/\nu_0$ is the wavelength of the unperturbed line and where:

$$\Delta\lambda_B = \lambda_0^2 \frac{\nu_L}{c} = \frac{\lambda_0^2 e_0 B}{4\pi m c^2}. \tag{2.13}$$

If $\Delta\lambda_B$ is expressed in $m\mathring{A}$, λ_0 in $\mathring{A}$, and B in G, we obtain:

$$\Delta\lambda_B = 4.6686 \times 10^{-10} \lambda_0^2 B. \tag{2.14}$$

Among the possible wavelengths in Equation 6.3, the only authorized transitions are the ones such as:

$$\Delta M = M' - M = 0, \pm 1 \tag{2.15}$$

Finally, three families of Zeeman components exist:

The transitions having $\Delta M = -1$ and $\Delta M = 1$, called respectively the σ_r and σ_b components, are generally shifted respectively towards the red part and the blue part of the spectrum from the unperturbed line. If we consider an orthonormal reference frame with the z-axis along the magnetic field vector, the σ component produces circular polarization along the z-axis, and linear polarization, perpendicular to the z-axis (see Fig. 2.4).

Finally, the transitions having $\Delta M = 0$, called π components, are at the same wavelength as the unperturbed line. The π components produce linear polarization whose direction is parallel to the magnetic field (see Fig. 2.4).

The normal Zeeman effect, occurs when the angular momentum of any of the two levels involved in the transition is zero ($J = 0$ or $J' = 0$), or when both levels have the same Landé factor ($g = g'$). In both cases only three components are left: a σ_r component at the wavelength $(\lambda_0 + g\Delta\lambda B)$, a σ_b component at the wavelength $(\lambda_0 - g\Delta\lambda B\ )$, and a π component at the wavelength λ_0.

In the other cases, called anomalous Zeeman effect, more complex patterns occur.

2.3 Measuring polarization

Polarization can be measured thanks to two optical systems: a polarizer and a retarder. A polarizer filters the light. The light of a specific polarization passes and the light of other polarizations are blocked. It can convert light of undefined or mixed polarization into a beam of light with well-defined polarization. It works by dichroism, birefringence, reflection, or scattering. Only the component E_θ of an electric field along the optical axis of the polarizer can pass through the polarizer. If an electric field $\vec{E}$ passes through

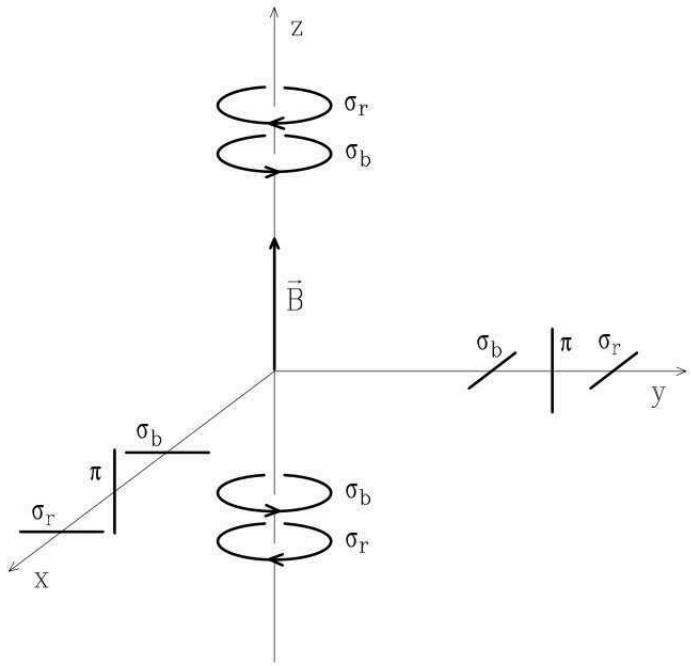

FIGURE 2.4: **Polarization properties of the Zeeman effect**: The polarization properties of the radiation emitted by different Zeeman components depend on the type of components and on the angle between the observing direction and the magnetic field vector (see (Landi Degl'Innocenti & Landolfi 2004)

a polarizer which has an optical axis angle θ, the components of the output electric field are:

$$\begin{aligned} E'_x &= E_x cos\theta \\ E'_y &= E_y sin\theta \end{aligned} \tag{2.16}$$

A retarder is a system that introduces a phase shift δ to one of the component of $\vec{E}$ with respect to the other. The retarded axis is called slow axis and the other axis is called fast axis. If an electric field $\vec{E}$ passes through a retarder that has an optical axis $\hat{e_x}$, the new components of the electric field at the output of the retarder are:

$$\begin{aligned} E'_x &= E_x \\ E'_y &= E_y e^{i\delta}. \end{aligned} \tag{2.17}$$

If we consider a light ray that crosses first a retarder and then a polarizer, the intensity of the light ray at the output of the system is a function of the phase shift δ induced by the retarder and of the angle θ of the optical axis of the polarizer. The amplitudes of the electric field at the output then becomes:

$$E_\theta(t,\theta) = E_x cos\theta + E_y sin\theta e^{i\delta}. \tag{2.18}$$

The intensity of the output light ray is :

$$\begin{aligned} I_{mes}(\theta,\delta) &= \langle E_\theta(t,\theta)E_\theta^*(t,\theta)\rangle \\ &= \langle E_x E_y^* cos^2\theta + E_y E_y^* sin^2\theta + \tfrac{1}{2}E_x E_y^* e^{-i\delta} sin(2\theta) + \tfrac{1}{2}E_x^* E_y e^{i\delta} sin(2\theta)\rangle \end{aligned} . \tag{2.19}$$

Finally, if we use the definition of the Stokes parameters, we find that:

$$I_{mes}(\theta,\delta) = \frac{1}{2}(I + Qcos2\theta + Ucos\delta sin(2\theta) + Vsin\delta sin(2\theta)) \tag{2.20}$$

With different combinations of optical axis θ of the polarizer and the phase shift δ of the retarder, it is possible to measure the Stokes parameters:

$$\begin{aligned} I &= I_{mes}(0,0) + I_{mes}(\pi/2,0) \\ Q &= I_{mes}(0,0) - I_{mes}(\pi/2,0) \\ U &= I_{mes}(\pi/4,0) - I_{mes}(3\pi/4,0) \\ V &= I_{mes}(\pi/4,\pi/2) - I_{mes}(3\pi,\pi/2) \end{aligned} \tag{2.21}$$

The combination of a retarder and a polarizer thus allows us to measure the Stokes parameters thanks to the measurement of intensity only.

2.4 The spectropolarimeter Narval

To detect the polarization in spectral lines due to the Zeeman effect, we use high-resolution spectropolarimeters. The three performant instruments are: ESPaDOnS installed at the CFHT (Canada France Hawaii Telescope) on the Mauna Kea Observatory (Hawaii), Narval installed at the TBL (Télescope Bernard Lyot) on the Pic du Midi Observatory (France), and HarpsPol installed at the 3.6m telescope at La Silla Observatory (Chili). The TBL is the only telescope in the world fully dedicated to stellar spectropolarimetry. Almost all data presented in this thesis were taken with Narval.

Narval is installed on the 2-meter TBL since 2006. Its sensitivity is 20 times that of Musicos, its predecessor. It is a copy of the high-resolution spectropolarimeter ESPaDOnS at CFHT. Narval provides complete coverage of the optical spectrum (from 370 to 1050 nm) in a single exposure, except three gaps of a few nm in the red part of the spectrum, with a resolving power of $\sim$ 65000 in its spectropolarimetric mode.

As the name indicates, a spectropolarimeter is composed of a polarimeter and a spectrograph. Narval's polarimeter receives the light from the Cassegrain focus of the telescope. The light passes trough an atmospheric dispersion corrector and a 1.6 arcsec hole drilled in a tilted mirror. Then, the light is collimated thanks to an objective composed of 3 lenses. The polarization of the light is analyzed thanks to a retarder and a Wollaston prism. The retarder is composed of three Fresnel rhombs: one quarter-wave and two half-wave (see Fig. 2.5). Fresnel rhombs provide a very achromatic polarization analysis of the stellar light without producing the usual spectral interference patterns. By

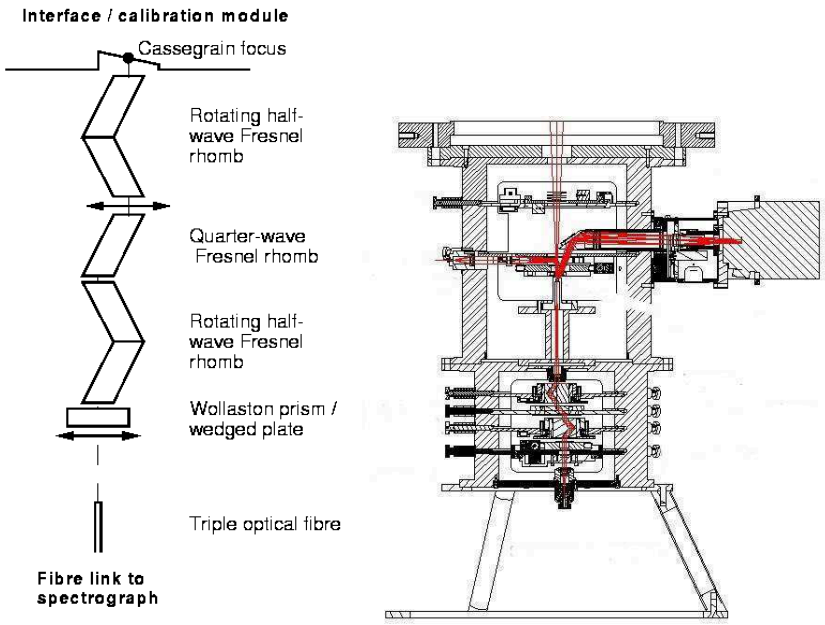

FIGURE 2.5: **Schematic description (left) and drawing (right) of the Narval polarimeter**: the light comes from the Cassegrain focus and crosses the Fresnel rhombs and the Wollaston prism before it is sent to the spectrograph. ©TBL

rotating the two half-wave rhombs with respect to the fixed quarter-wave rhomb, we can achieve either a circular or linear polarization analysis of the stellar light. After the Wollaston prism, the light is sent to the echelle spectrograph thanks to optical fibers.

The light brought by the optical fibers gets to the spectrograph's tunable image slicer. Then the resulting light arrives on the blazed grating thanks to a collimator. Finally, the 40 orders of the spectrum are separated thanks to a cross dispersion prism before being imaged on a CCD detector (see Fig. 2.6).

The spectrograph thermal stability is kept to within 0.1K, thanks to the use of a double layer thermal enclosure. The final 2D CCD image is composed of two times 40 orders, corresponding to the two orthogonal polarization states (see Fig. 2.7).

2.5 Data analysis

2.5.1 Data reduction with Libre-Esprit

To minimize systematic errors, one complete Stokes V sequence consists of four successive sub-exposures taken with the half-wave rhombs oriented at different angles. This follows the method of Semel et al. (1993) to reduce the amplitude of possible spurious signatures of instrumental origin. This strategy also provides a strong test to discard the possibility of a spurious signal by computing a "null" polarization spectrum. This

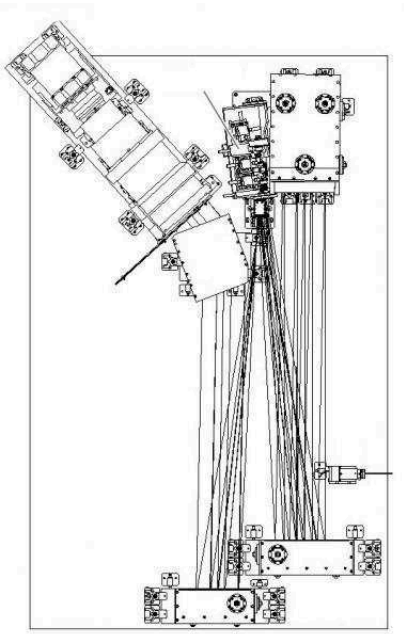

FIGURE 2.6: **Schematic description of the spectrograph of Narval**: the light comes from the polarimeter unit. ©TBL

is calculated from a different combination of the four sub-exposures constituting the polarimetric sequence (Donati et al. 1997) that should not display any signal. This "null" check parameter is automatically produced for each Stokes V sequence.

The data are reduced by Libre-Esprit, a dedicated and fully automated software (Donati et al. 1997) specifically developed for reducing echelle spectropolarimetric data and optimized for Narval. Libre-Esprit proceeds in 3 steps: the first stage consists of performing a geometrical analysis from a sequence of calibration exposures; the position and shape of orders are derived from a mean flat-field image, while the details of the wavelength to pixel relation along and across each spectral order is obtained from comparison frames from a Thorium-Argon lamp and a Fabry-Perot setup. The second step performs spectrum optimal extraction (Horne 1986; Marsh 1989), using the geometrical information derived in step 1. A last step consists of refining the wavelength calibration using telluric lines recorded in the reduced spectrum, therefore reaching a radial velocity accuracy close to 30 $m.s^{-1}$ (Moutou et al. 2007). Spectra processed with Libre-Esprit include the flux and polarization information, as well as the "null" spectrum computed from two different combinations and error bars at each wavelength point in the spectrum.

2.5.2 Least Square Deconvolution technique

As explained above, a magnetic field induces a polarization of the spectral lines of the star. However, this polarization is weak and difficult to detect in individual lines. The expected amplitude of the signal for a typical magnetic field in hot stars is less than 0.1% of the continuum. To detect it, we need a high signal-to-noise ratio (S/N). To reach it,

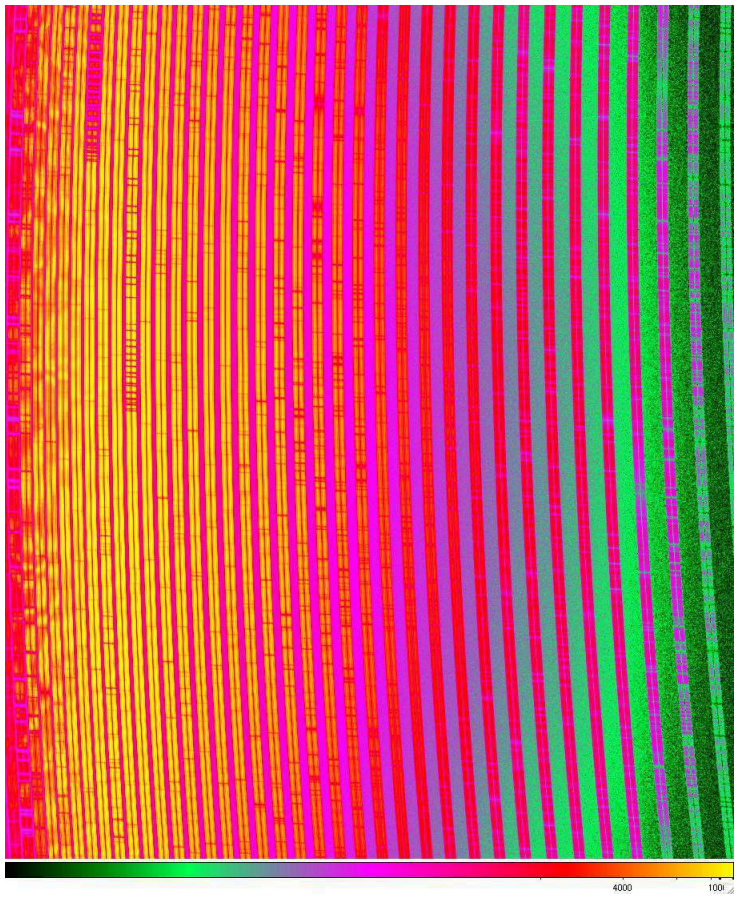

FIGURE 2.7: **Example of an echelle spectrum**: A part of a raw spectrum of the Sun taken with Narval with red and blue orders appearing respectively on the left and right sides of the frame. Each order is divided into two orthogonal polarization states (http://www.ast.obs-mip.fr/projets/narval/v1/spec.html).

one solution would be to increase the observing time, but this solution is not viable for two reasons: first, the amount of observing time per measurement would be prohibitive; second, the star or the observing conditions would vary during an observation and thus the magnetic measurement would be meaningless.

However, a spectropolarimeter records a large spectral domain containing many lines. Semel et al. (1993) proposed to extract the information of all available lines at the same time, under the hypothesis that the Zeeman profile of all lines are similar, by averaging all the lines. Donati et al. (1997) developed a cross correlation technique based on this idea called Least Square Deconvolution (LSD).

This technique assumes a weak field regime, which is indeed the case for the field of hot stars. In the approximation of the weak field regime, the Stokes V line profile is:

$$V(v) \propto g\lambda \frac{\partial I(v)}{\partial v}, \tag{2.22}$$

where v is the velocity, λ is the wavelength, g is the effective Landé factor (the magnetic sensitivity), and I is the intensity of the line. Assuming that all spectral lines in intensity have the same shape, V(v) becomes :

$$V(v) \propto g\lambda dk_B(v), \tag{2.23}$$

where $k_B(v)$ is the profile shape function for all lines. Here, we thus suppose that the broadening processes are the same for all the lines (natural, microturbulence, rotation,...). This implies that we reject hydrogen lines from the average and use only metallic lines. We also reject the lines blended with hydrogen.

To obtain the total output stellar flux, we need to integrate the profile on the stellar surface S. The Stokes I and V parameters of one line become :

$$\begin{array}{l} I_i(v) = w_{int,i} Z_{int}(v) \\ V_i(v) = w_{pol,i} Z_{pol}(v), \end{array} \tag{2.24}$$

where Z_{int} and Z_{pol} correspond to the LSD profile in intensity and polarization, and w_{int} and w_{pol} are the weights for each line in the averaged line in intensity and polarization.

$M(v)$ is defined as a line mask. $M(v)$ can be seen as a Dirac comb where each peak position corresponds to the position of the line and the intensity of the peak is proportional to the line strength :

$$M(v) = \sum_i w_i \delta(v - v_i). \tag{2.25}$$

To interpret the LSD profiles in terms of magnetism, the line weights w_{int} and w_{pol} must be linked to the line parameters of the mask M. The mean profile amplitude depends on this normalization of the line weights.

The weight of an individual line of the mask is given by:

$$w_{int,i} = \frac{d_i}{d_0} w_{pol,i} = \frac{\lambda_i d_i g_i}{\lambda_0 d_0 g_0}, \tag{2.26}$$

where λ_i, d_i, and g_i are respectively the wavelength, the depth and the Landé factor of the line, and λ_0, d_0, and g_0 are the corresponding normalization factor. λ_0 is arbitrarily fixed to 500 nm and d_0 and g_0 are adjusted so that the average of the weights are equal to 1.

The observed spectrum is the convolution of the mask $M(v)$ with the mean profile $Z(v)$. In the case of the Stokes V profile:

$$\begin{array}{rl} V(v) & = M_{pol}(v) * Z_{pol}(v) \\ & = \sum_{k=0}^{m} Z_{k-m} M(v-k). \end{array} \tag{2.27}$$

A similar equation exists for the I profile :

$$I(v) = M_{int}(v) * Z_{int}(v). \tag{2.28}$$

A template line mask is provided by the Vienna Atomic Line Database (VALD, Kupka & Ryabchikova 1999). It collects the atomic and molecular transition parameters. This database allows us to extract the parameters of the lines present in a spectrum of a star of a certain temperature T_{eff} and surface gravity log g.

The aim of the LSD technique is to inverse Equations 2.27 and 2.28 to find the mean LSD profile of Stokes I and V by using the LSD. The concept of this method is illustrated in Fig. 2.8. The depth of the lines provided by VALD is calculated thanks to the ATLAS code with an ETL atmosphere model. These depths can tailored to the actual depths of the lines in the observed spectra.

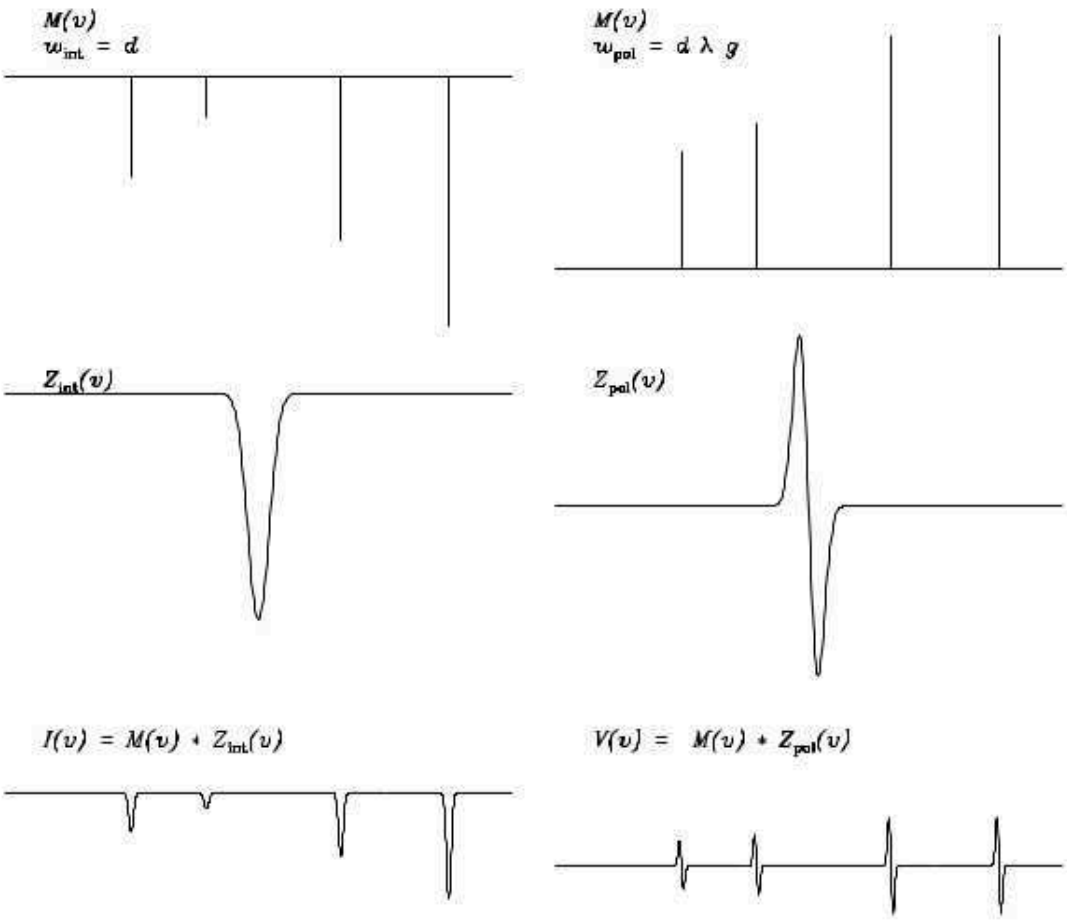

FIGURE 2.8: **Illustration of the LSD technique**: At the bottom, the observed spectra in Stokes I (left) and Stokes V (right) can be represented by the convolution of a line mask (top) and a mean profile (center) (Petit 2011).

2.5.3 Detection probability

To diagnose the presence of a magnetic signal in Stokes V, we use the χ^2 test proposed by Donati et al. (1992) that consists in calculating the probability that the signal in the Stokes V is not null (V(v)=0):

$$\chi^2 = \frac{1}{n}\sum_{i=1}^{n}\left[\frac{V(v_i)}{\sigma_i}\right]^2, \tag{2.29}$$

where n is the number of points in the Stokes V profile V(v) and σ_i is the error bar at the point i.

The χ^2 quantifies the deviation of the Stokes V profile from a flat profile.

The false alarm probability (FAP) then gives the probability that there is signal in the Stokes V profile while the star is not magnetic. If there is a signature in Stokes V but the FAP is low, the signature is considered magnetic.

$$FAP(\chi^2,\nu) = 1 - \frac{1}{\Gamma(\frac{\nu}{2})2^{\frac{\nu}{2}}}\int_0^{\chi^2} t^{\frac{\nu}{2}-1}e^{-\frac{t}{2}}dt, \tag{2.30}$$

where Γ is the gamma function and ν is the number of pixels in the profile.

We apply this diagnostic on the Stokes V profiles inside and outside the averaged stellar line. If inside the line FAP $< 0.001\%$, the magnetic detection is definite (DD); if it is $0.001\% <$ FAP $< 0.1\%$ the detection is marginal (MD), otherwise there is no detection (ND).

2.5.4 Longitudinal magnetic field

The spectropolarimetric data give us access to the longitudinal magnetic field. The longitudinal magnetic field is the component of the magnetic field parallel to the line of sight averaged over the stellar hemisphere visible at the time of observation. To measure it, I use the center-of-gravity method (Rees & Semel 1979):

$$B_l(G) = -2.14\times10^{11}\frac{\int vV(v)dv}{\lambda_0 gc\int(1-I(v))dv} \tag{2.31}$$

It depends strongly on the angles between line of sight, rotation axis, magnetic axis, as well as on the rotation phase. Thus, it is very useful to follow the rotational modulation of the longitudinal magnetic field and characterize the configuration of the field (see Fig. 2.10). This variation can then be modeled by an oblique rotator model (Stibbs 1950).

2.5.5 Oblique rotator model

The oblique rotator model considers a dipole inclined by an angle β, called the obliquity angle, with respect to the rotational axis (see Fig. 2.9). The angle i corresponds to the inclination of the star, i.e. the angle between the rotational axis and the line-of-sight.

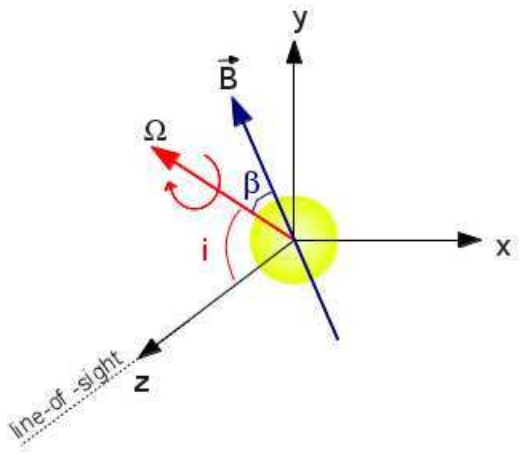

FIGURE 2.9: **Illustration of the oblique rotator model**: the reference frame (x,y,z) corresponds to the one of the observer and the z axis is the line-of-sight. Ω is the rotational axis of the star and i corresponds to the inclination. $\vec{B}$ is the magnetic axis and β the obliquity angle.

As the star rotates, the dipole is seen under various angles and the longitudinal magnetic field value changes, thus the Stokes V profile also changes (see Fig. 2.10).

We can use an oblique rotator model to fit the LSD Stokes V profiles observed at various rotational phases of the star and determine the dipolar magnetic field. The fit includes five parameters: i, β, $B_{\rm pol}$, a phase shift ϕ, and a possible off-centering distance d_d of the dipole with respect to the center of the star (d_d=0 for a centered dipole and d_d=1 if the center of the dipole is at the surface of the star).

We can calculate a grid of Stokes SV profiles for each phase of observation for various sets of five parameters mentioned above and apply a χ^2 minimization to obtain the set of parameters that best fits all observations simultaneously. More details of the modeling technique can be found in Alecian et al. (2008).

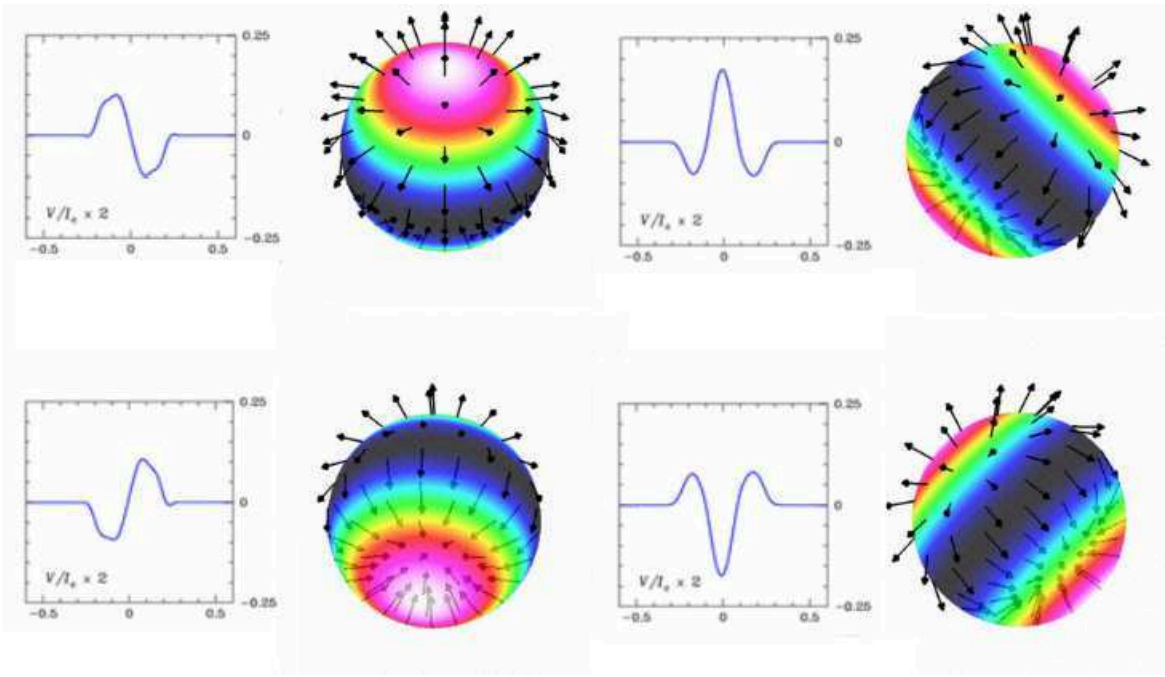

FIGURE 2.10: **Illustration of the rotational modulation of the Stokes V profile** at different phases of observations: for each phase the Stokes V profile it shown, as well as the orientation of the field on the surface of the star. This figure was generated thanks to the applet available at: http://star.arm.ac.uk/highlights/sba1.html

Part I

Strong magnetic fields

Chapter 3

The supergiant ζ Ori A

3.1 Introduction

Magnetic fields play a significant role in the evolution of hot massive stars. However, the basic properties of the magnetic fields of massive stars are poorly known. As I said in the introduction, about 7% of massive stars are found to be magnetic at a level that is detectable with current instrumentation (Grunhut 2015). In particular, only 11 magnetic O stars are known. Detecting magnetic fields in O stars is particularly challenging because they only have few, often broad, lines from which to measure the field. There is therefore a deficit in the knowledge of the basic magnetic properties of O stars and any new detection of a magnetic field in an O star helps us to progress.

Here I study the O star ζ Ori A. A magnetic field seems to have been detected in this star by Bouret et al. (2008) but the signatures are weak and not very clear (see Fig. 3.1). Their detailed spectroscopic study of the stellar parameters led to the determination of an effective temperature of $T_{\rm eff}$ = 29500±1000 K and log g = 3.25±0.10 with solar abundances. This makes ζ Ori A the only known magnetic O supergiant. Moreover, Bouret et al. (2008) found a magnetic field of 61±10 G, which makes it the weakest ever reported field in a hot massive star (typically ten times weaker than those detected in other magnetic massive stars). They found a rotational period of ∼7 days from the temporal variability of spectral lines and the modulation of the Zeeman signatures. To derive the magnetic properties, they used six lines that are not or only weakly affected by the wind. The rotation period they obtained is compatible with their measured $v \sin i$=100 km s^{-1}.

In addition, the measurement of the magnetic field provided by Bouret et al. (2008) allows to characterize the magnetosphere of ζ Ori A and to locate it in the magnetic confinement-rotation diagram (Petit et al. 2013). This diagram compares the Alfvén radius, that corresponds to the radius of the last closed magnetic loop, to the Keplerian co-rotation radius and allows us to determine what kind of magnetosphere the star hosts. ζ Ori A is the only known magnetic massive star with a confinement parameter below 1, that is, without a magnetosphere (see Fig. 3.2).

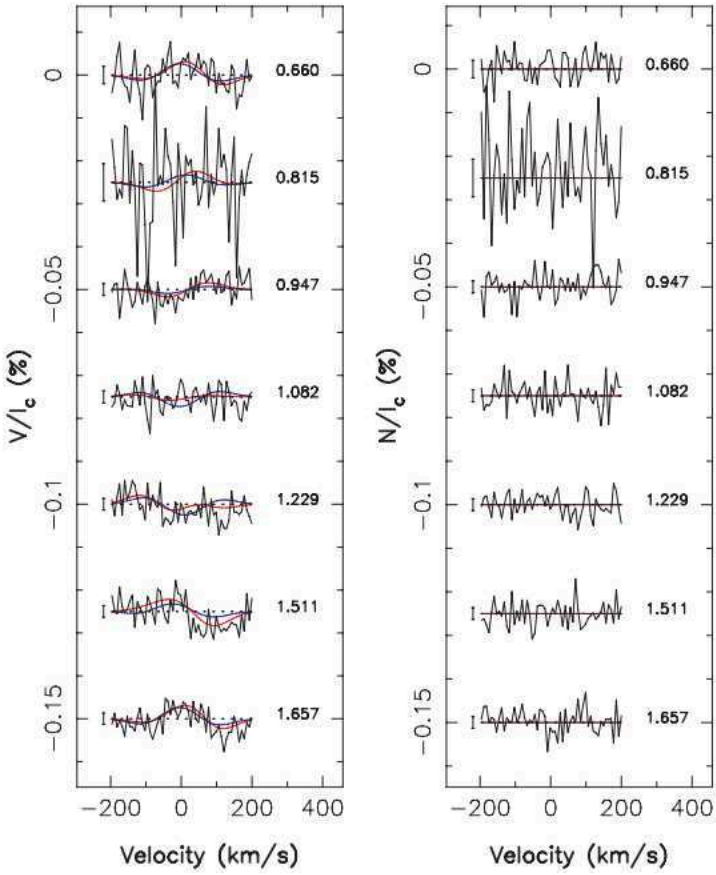

FIGURE 3.1: **The Stokes parameters of ζ Ori A of Bouret et al. (2008)**: Stokes V profiles (left) and null polarization (right) for each night of observations. The blue line corresponds to a simple dipole, while the red one corresponds to a more complex field.

For all these reasons, the study of the magnetic field of ζ Ori A is of the highest importance. Each massive star that is detected to be magnetic moves us closer to understanding the stellar magnetism of hot stars. Studying this unique magnetic massive supergiant is also of particular relevance for our understanding of evolution of the magnetic fields in hot stars.

ζ Ori A has a known B0III companion, ζ Ori B. In addition, Hummel et al. (2013) found that ζ Ori A consists of two companion stars (Aa and Ab) located at 40 mas of each other, orbiting with a period of 2687.3±7.0 days. To determine a dynamical mass of the components, Hummel et al. (2013) analyzed archival spectra to measure the radial velocity variations. The conclusions reached are presented below. The primary ζ Ori Aa is a O9.5I supergiant star, whose radius is estimated to 20.0±3.2 $R_\odot$ and whose mass is estimated to 33±10 $M_\odot$. The secondary ζ Ori Ab is a B1IV with an estimated radius of 7.3±1.0 $R_\odot$ and an estimated mass of 14±3 $M_\odot$. Moreover, ζ Ori A is situated at a distance of 387 pc. Initial estimates of the elements of the apparent orbit were obtained by Hummel et al. (2013) using the Thiele-Innes method. The estimation provided a value of the periastron epoch of JD 2452734.2±9.0 with a longitude of 24.2±1.2°. The eccentricity is estimated to be 0.338±0.004.

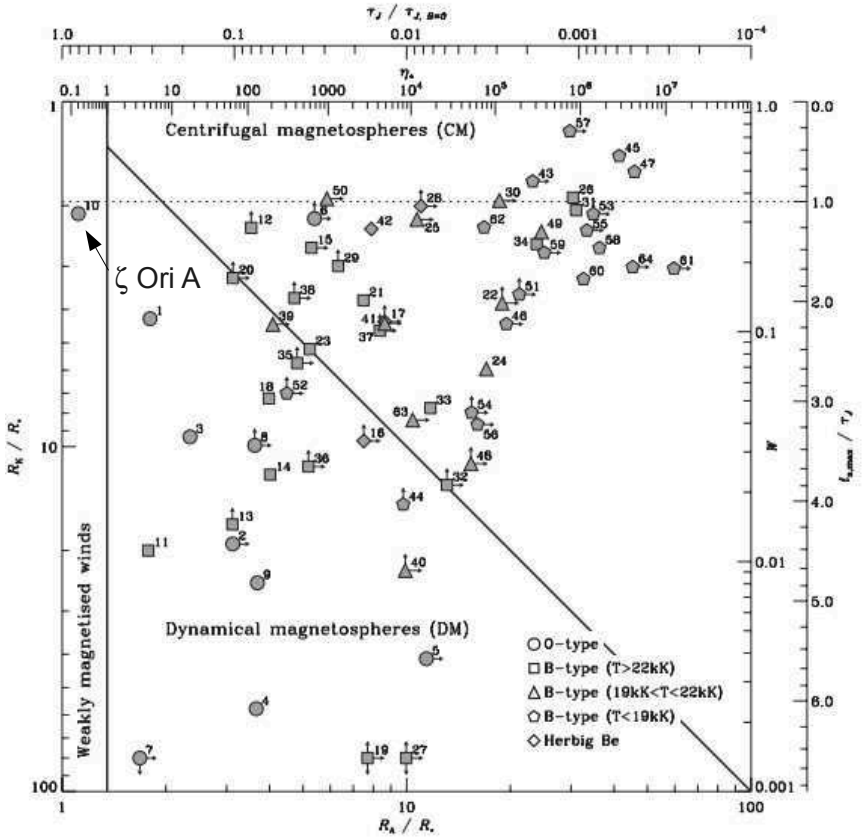

FIGURE 3.2: **The magnetic confinement-rotation diagram (Petit et al. 2013)**: a log–log plot with the Kepler radius R_K increasing downwards and the Alfén radius R_A increasing to the right. The right and upper axes give, respectively, the corresponding rotation fraction W and magnetic confinement parameter η_*. When $R_K > R_A$, the star hosts a dynamical magnetosphere, when $R_K < R_A$ the magnetosphere is centrifugally supported and when $\eta_* < 1$, the star does not have a magnetosphere.

Bouret et al. (2008) considered ζ Ori A as a single star of 40 $M_\odot$ with a radius equal to 25 $R_\odot$, seen from Earth at an inclination angle of 40°. Taking into account that the star is a binary could strongly modify the magnetic field value derived for only one of the binary components. In their analysis, the magnetic signature was normalized by the full intensity of the lines from both components, and if only one of the two stars is magnetic, the field was thus underestimated. Moreover, the position in the magnetic confinement-rotation diagram will be modified as a result of the new magnetic strength value, but also as a consequence of the new stellar parameters.

TABLE 3.1: **Journal of Narval observations.** The columns list the date and the heliocentric Julian date (HJD) for the middle of observation, the number of sequences and the exposure time per individual subexposure, the signal-to-noise ratio in the I profiles, and the orbital phase.

#	Date	mid-HJD	T_{exp} (s)	S/N	$\phi_{\rm orb}$
1	17oct07	2454391.559	48 × 4 × 20	4750	0.617
2	18oct07	2454392.719	8 × 4 × 40	2220	0.617
3	19oct07	2454393.570	44 × 4 × 40	6940	0.617
4	20oct07	2454394.491	48 × 4 × 40	6860	0.618
5	21oct07	2454395.518	48 × 4 × 40	7070	0.618
6	23oct07	2454397.496	48 × 4 × 40	7180	0.619
7	24oct07	2454398.526	48 × 4 × 40	7270	0.619
8	22oct08	2454762.644	40 × 4 × 50	6660	0.755
9	23oct08	2454763.645	38 × 4 × 50	5530	0.755
10	24oct08	2454764.654	36 × 4 × 50	6790	0.756
11	25oct08	2454765.639	37 × 4 × 50	6140	0.756
12	26oct08	2454766.635	38 × 4 × 50	6420	0.756
13	04oct11	2455839.688	12 × 4 × 90	5810	0.156
14	05oct11	2455840.670	12 × 4 × 90	5790	0.156
15	10oct11	2455845.608	12 × 4 × 90	2040	0.158
16	11oct11	2455846.632	12 × 4 × 90	3450	0.158
17	30oct11	2455865.712	12 × 4 × 90	5610	0.165
18	07nov11	2455873.557	5 × 4 × 90	2700	0.168
19	11nov11	2455877.626	12 × 4 × 90	4860	0.170
20	12nov11	2455878.565	12 × 4 × 90	4830	0.170
21	24nov11	2455890.673	12 × 4 × 90	4180	0.175
22	25nov11	2455891.660	12 × 4 × 90	4900	0.175
23	26nov11	2455892.502	12 × 4 × 90	4490	0.175
24	29nov11	2455895.667	12 × 4 × 90	5400	0.176
25	30nov11	2455896.600	6 × 4 × 90	2030	0.177
26	14dec11	2455910.477	12 × 4 × 90	1360	0.182
27	08jan12	2455935.555	12 × 4 × 90	5630	0.191
28	13jan12	2455940.536	12 × 4 × 90	5060	0.193
29	14jan12	2455941.539	12 × 4 × 90	5350	0.193
30	15jan12	2455942.475	12 × 4 × 90	4680	0.194
31	16jan12	2455943.367	12 × 4 × 90	4520	0.194
32	25jan12	2455952.529	12 × 4 × 90	5120	0.198
33	26jan12	2455953.431	8 × 4 × 90	3200	0.198
34	08feb12	2455966.472	12 × 4 × 90	3900	0.203
35	09feb12	2455967.402	11 × 4 × 120	4340	0.203
36	10feb12	2455968.343	12 × 4 × 90	2198	0.203

3.2 Observations

3.2.1 Narval spectropolarimetric observations

Spectropolarimetric data of ζ Ori A were collected with Narval in the frame of the MiMeS project (see e.g. Neiner et al. 2011). This is the same instrument with which the magnetic field of ζ Ori A was discovered by Bouret et al. (2008).

ζ Ori A was first observed in October 2007 during 7 nights (PI: J.-C. Bouret) and these data were used in Bouret et al. (2008). Then, this star was observed again in October 2008 during 5 nights (PI: J.-C. Bouret) and in October 2011 and February 2012 during 24 nights by the MiMeS collaboration (PI: C. Neiner). This provides a total number of 36 nights of observations. The observations were taken in circular polarimetric mode, that is, measuring Stokes V.

Since ζ Ori A is very bright (V=1.77), only a very short exposure time could be used to avoid saturation. To increase the total S/N, we thus obtained a number of successive measurements each night, which were co-added. The exposure time of each subexposure of each measurement varies between 20 and 120 s, and the total integration time for a night varies between 1280 and 7680 s (see Table 3.1).

Data were reduced at the telescope using the Libre-Esprit reduction package (Donati et al. 1997). I then normalized each of the 40 echelle orders of each of the 756 spectra with the continuum task of IRAF[1]. Finally, I co-added all the spectra obtained within each night to improve the S/N, which varies between 1360 and 7270 in the intensity spectra (see Table 3.1). I therefore obtained 36 nightly averaged measurements.

3.2.2 Archival spectroscopic observations

In addition to the spectropolarimetric data, I used archival spectroscopic data of ζ Ori A taken with various echelle spectrographs. These data were kindly put at my disposal by Thomas Rivinius.

In 1995, 1997 and 1999, spectra were obtained with the HEROS instrument, installed at the ESO Dutch 0.9 m telescope at the La Silla Observatory. The spectral resolution of HEROS is 20000, with a spectral domain from about 350 to 870 nm. In addition, in 2006, 2007 and 2009, data were taken with the FEROS spectrograph installed at the ESO 2.2 m at the La Silla observatory. The spectral resolution of FEROS is about 48000 and the spectral domain ranges from about 370 to 900 nm. Finally, in 2010, spectra were taken with the UVES spectrograph (Dekker et al. 2000) installed at the VLT at the Paranal Observatory. Its spectral domain ranges from about 300 to 1100 nm with a spectral resolution of 80000 and 110000 in the blue and red domains respectively.

[1]IRAF is distributed by the National Optical Astronomy Observatories, which are operated by the Association of Universities for Research in Astronomy, Inc., under cooperative agreement with the National Science Foundation.

I co-added spectra collected for each year to improve the final S/N. I therefore have seven spectra for seven different years, with a S/N of between about 100 and 2000 (see Table 3.2).

TABLE 3.2: **Journal of archival spectroscopic observations of ζ Ori A** obtained with HEROS, FEROS and UVES, showing the date, Julian date, instrument used, exposure time, signal-to-noise ratio, and orbital phase.

Date	JD	Instrument	T_{exp}	S/N	ϕ_{orb}
1995	2449776.024	HEROS	57×1200	1200	0.90
1997	2450454.379	HEROS	16×1200	1000	0.15
1999	2451147.333	HEROS	64×1200	1200	0.41
2006	2453738.159	FEROS	60	100	0.37
2007	2454501.018	FEROS	2×20	250	0.66
2009	2454953.970	FEROS	5×10	200	0.84
2010	2455435.373	UVES	36×2	2000	0.01

3.3 Checking for the presence of a magnetic field

The magnetic field of ζ Ori A claimed by Bouret et al. (2008) has not been confirmed by independent observations so far and one of the goals of this study is to confirm or disprove its existence using additional observations.

To test whether ζ Ori A is magnetic, I applied the LSD technique (Donati et al. 1997 and see Sect. 2.5.2). I first created a line mask for ζ Ori A. I started from a list of lines extracted from VALD (Kupka & Ryabchikova 1999; Piskunov et al. 1995) for an O star with $T_{\rm eff}$=30000 K and log g=3.25, with their Landé factors and theoretical line depths. I then cleaned this line list by removing the hydrogen lines, the lines that are blended with hydrogen lines, and those that are not visible in the spectra. I also added some lines visible in the spectra that were not in the original O-star mask. Altogether, I obtained a mask of 210 lines. I then adjusted the depth of these 210 lines in the mask to fit the observed line depths.

Using the final line mask, I extracted LSD Stokes I and V profiles for each night. I also extracted null (N) polarization profiles to check for spurious signatures. The LSD I, Stokes V, and the null N profiles are shown in Fig. 3.3 for 8 of the 36 nights. Zeeman signatures are clearly seen for these 8 nights and some others as well, but are not systematically observed for all nights. The existence of Zeeman signatures confirms that ζ Ori A hosts a magnetic field, as previously reported by Bouret et al. (2008).

The previous study of the magnetic field of ζ Ori A (Bouret et al. 2008) only used a few lines that were not affected by the wind. However, I need to use as many lines as possible to improve the S/N. I therefore checked whether our results were modified by using lines that might be affected by the wind. I compared the LSD results obtained with the mask used by Bouret et al. (2008) and my own mask (see Fig. 3.4). The signatures in Stokes V are similar with both masks and the measurements of the longitudinal magnetic field

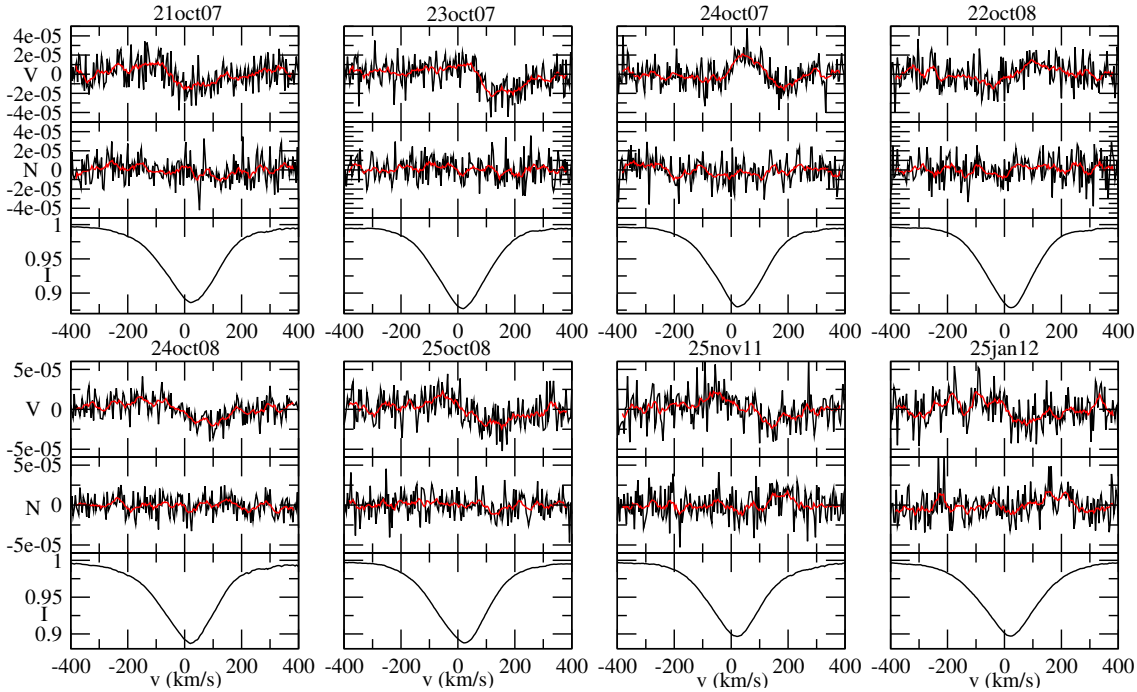

FIGURE 3.3: **Example of the result of the LSD technique for ζ Ori A:** LSD Stokes I (bottom), Stokes V (top), and null N (middle) profiles, normalized to Ic, for 8 selected nights. The red line is a smoothed profile.

are consistent (e.g., 44.5±19.6 G with the mask of Bouret et al. (2008) and 35.8±7.2 G with our mask for measurement # 11, see Fig. 3.4). However, the S/N is better with our mask (the S/N of Stokes V is 57624) than with the mask of Bouret et al. (2008) (the S/N of Stokes V is 27296). Therefore, I used all available lines for this study.

However, the line mask used in this first analysis includes lines from both components of ζ Ori A. I thus do not know which component of the binary is magnetic or whether both components are magnetic. To provide an answer to this question, I must separate the composite spectra.

3.4 Separating the two components

3.4.1 Identifying the lines of each component

I first created synthetic spectra of each component. The goal was to identify which lines come from the primary component, the secondary component, or both. To this aim, I used TLUSTY (Hubeny & Lanz 1995). This program calculates plane-parallel, horizontally homogeneous stellar atmosphere models in radiative and hydrostatic equilibrium. One of the most important features of the program is that it allows for a fully consistent, non-LTE metal line blanketing. However, TLUSTY does not take winds into account, which can be important in massive stars, especially in supergiants.

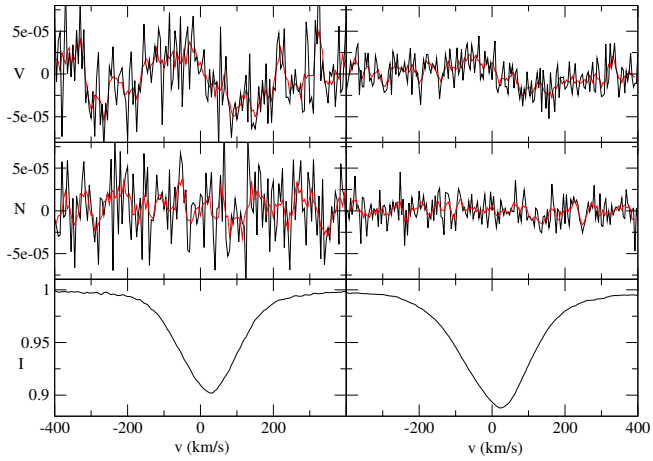

FIGURE 3.4: **Comparison between the LSD mask used by Bouret et al. (2008) (left) and my LSD mask (right:** Stokes I (bottom), Stokes V (top), and null N (middle) profiles, normalized to Ic, for the night of 25 October 2008. The red line is a smoothed profile.

For the primary component ζ Ori Aa, I computed a model with an effective temperature $T_{\rm eff}$=29500 K and logg=3.25, corresponding to the spectral type of the primary as given by Hummel et al. (2013). For the secondary, I computed a model with an effective temperature $T_{\rm eff}$=29000 K et logg=4.0, again following Hummel et al. (2013). I used solar abundances, for both stars. The emergent spectrum from a given model atmosphere was calculated with SYNSPEC[2]. This program is complemented by the program ROTINS, which calculates the rotational and instrumental convolutions for the net spectrum produced by SYNSPEC.

Comparing these two synthetic spectra to the observed spectra of ζ Ori A, I identified which lines belong only to ζ Ori Aa, only to ζ Ori Ab, and which are a blend of the lines of both components. If one observed line only existed in one synthetic spectrum, I considered that this line is only produced by one component of the binary. If it existed in both synthetic spectra, I considered this line to be a blend of both components. I then created line lists containing lines from the three categories (only Aa, only Ab, or both).

In addition, I gathered archival spectra of ζ Ori A taken with the spectrographs FEROS, HEROS and UVES (see Sect. 3.2.2). While these spectra do not include polarimetric information, they cover the orbital period much better than our Narval data (see Table 3.2 and Fig. 3.5). In particular, some spectra were obtained close to the maximum or minimum of the radial velocity (RV) curve.

I compared the spectrum taken close to the maximum and minimum RV, because the line shift is maximum between these two spectra. I arbitrarily decided to use the spectra taken close to the maximum as reference. Depending on the shift, I determined the origin of the lines. If the lines of the spectrum taken at minimum RV are shifted to the

[2]Synspec is a general spectrum synthesis program developed by Ivan Hubeny and Thierry Lanz: http://nova.astro.umd.edu/Synspec49/synspec.html

blue (respectively red) side compared to the spectrum at maximum RV, the line comes from the primary Aa (respectively secondary Ab) component. When lines from the two components are blended, the core of the lines are shifted to the red side and the wings to the blue side.

The identification of lines made this way resulted in similar line lists as those obtained by comparing the observed spectra with synthetic ones.

I then ran LSD again on the observed Narval spectra, once with the mask containing the 13 lines only belonging to ζ Ori Aa and once with the mask only containing the 51 lines from ζ Ori Ab. I observe magnetic signatures in the LSD V profiles of ζ Ori Aa that are similar to those obtained in the original LSD analysis presented in Sect. 3.3. In contrast, I do not observe magnetic signatures in the LSD Stokes V profiles of ζ Ori Ab. I conclude that ζ Ori Aa is magnetic and ζ Ori Ab is not.

However, the LSD profiles of ζ Ori Aa obtained this way are very noisy, because of the low number of lines in the mask, and they cannot be used to precisely estimate the longitudinal magnetic field strength. To go further, it is necessary to disentangle the spectra, so that more lines can be used.

3.4.2 Spectral disentangling of Narval data

I first attempted to use the Fourier-based formulation of the spectral disentangling (hereafter, SPD) method (Hadrava 1995) as implemented in the FDBinary code (Ilijic et al. 2004) to simultaneously determine the orbital elements and the individual spectra of the two components Aa and Ab of the ζ Ori A binary system. The Fourier-based SPD method is superior to the original formulation presented by Simon & Sturm (1994) that is applied in the wavelength domain in that it is less time-consuming. In particular, this increases the technique's efficiency when it is applied to long time-series of high-resolution spectroscopic data.

One of the pre-conditions for the SPD method to work efficiently is a homogeneous phase coverage of the orbital cycle with the data. In particular, covering the regions of maximum/minimum radial velocity (RV) separation of the two stars is essential, because these phases provide key information about the RV semi-amplitudes of both stellar components.

Fig. 3.5 illustrates the phase distribution of our Narval spectra according to the orbital period of 2687.3 days reported by Hummel et al. (2013). Obviously, the spectra provide very poor phase coverage; no measurements exist at phases $\sim$0.0 and 0.4, corresponding to a maximum RV separation of the components (also see Fig. 5 in Hummel et al. 2013). This prevents determining accurate orbital elements from our Narval spectra.

Our attempt to use the orbital solution obtained by Hummel et al. (2013) to separate the spectra of the individual components also failed: although all regions in which I disentangled the spectra indicate the presence of lines from the secondary in the composite spectra, the separated spectra themselves are unreliable.

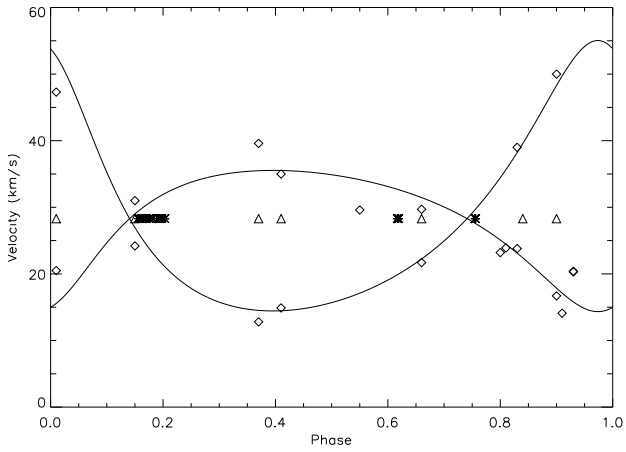

FIGURE 3.5: **Orbital phase distribution of the spectra of ζ Ori A.** The diamonds indicate the radial velocity measured by Hummel et al. (2013). The lines correspond to the best fit of the radial velocity of each component. The crosses correspond to our Narval observations and the triangles to the archival spectroscopic data. Phase zero corresponds to the time of periastron passage (T_0 = 2452734.2 HJD) as reported by Hummel et al. (2013).

3.4.3 Disentangling using the archival spectroscopic data

Since the SPD method failed in disentangling the Narval spectra because of the poor phase coverage, I again used the spectroscopic archival data obtained with FEROS, HEROS, and UVES. The orbital coverage of these spectra is much better than the one of the Narval data (see Fig. 3.5). I have seven spectra taken at different orbital phases, including phases of maximum RV separation of the components (see Table 3.5). I first normalized the spectra with IRAF. I used the orbital parameters given by Hummel et al. (2013) for the disentangling.

The coverage of these spectra enables the disentangling using FDBINARY. As an illustration of the results, a small part of the disentangled spectra is shown in Fig. 3.7. The results confirms the origin of the lines that were determined in Sect.3.4.1, and also the spectral types of the components given by Hummel et al. (2013).

3.5 Measuring the longitudinal magnetic field of ζ Ori Aa

Following these results, I assume that ζ Ori Ab is not magnetic and that the Stokes V signal only comes from ζ Ori Aa. Therefore, I ran the LSD technique on the Narval spectra with a mask containing all lines (157 lines) produced by ζ Ori Aa, even those that are blended with the ones of ζ Ori Ab, to obtain the LSD Stokes V profile of ζ Ori Aa. The contribution of ζ Ori Ab to this Stokes V signal is null, as the magnetic signal is only provided by ζ Ori Aa. The Stokes V and "null" profiles are shown in Fig. 3.6.

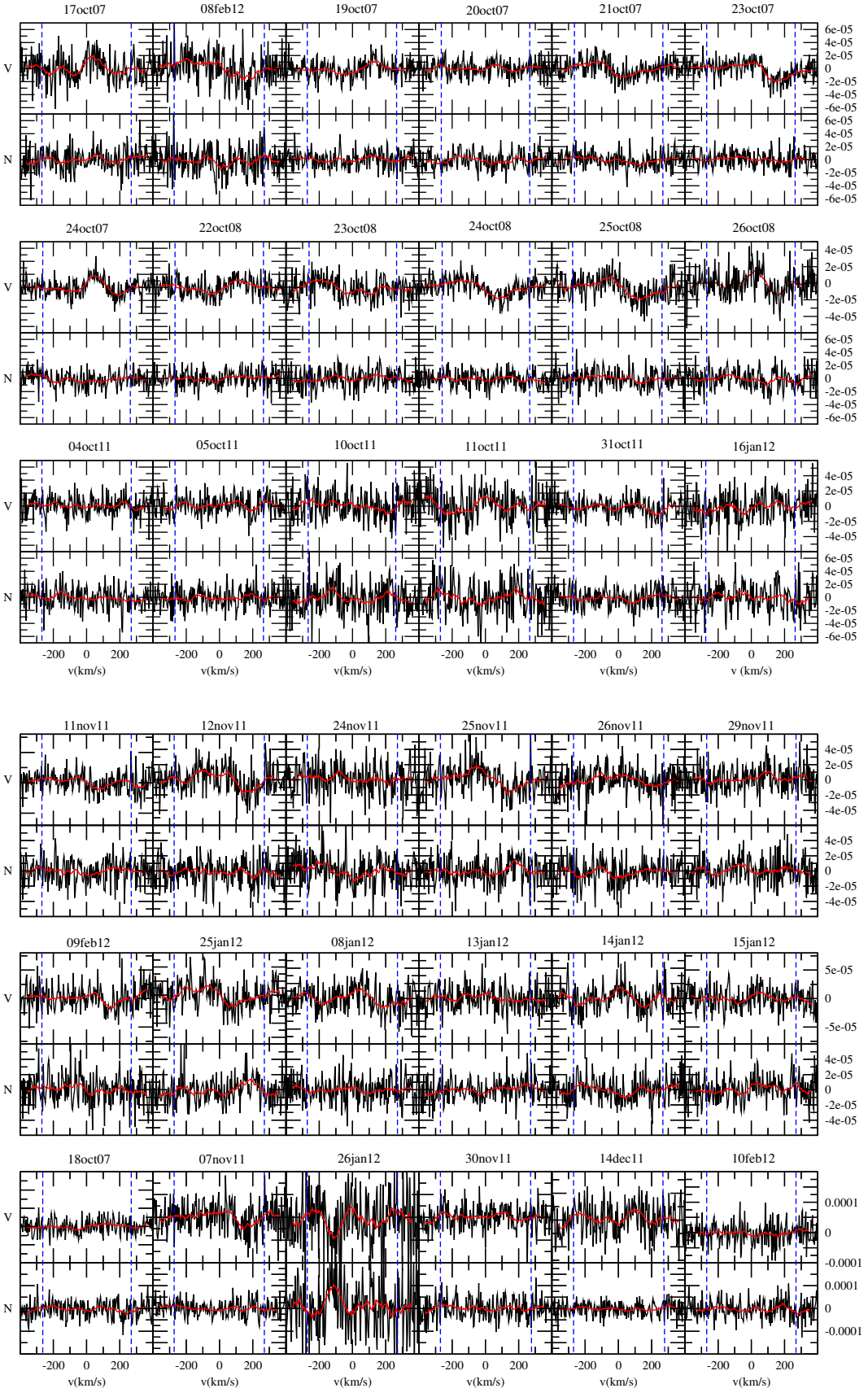

FIGURE 3.6: LSD Stokes I profiles (bottom) computed from the disentangled spectroscopic data, Stokes V (top) and null N (middle) profiles, normalized to Ic, from the Narval data, for ζ Ori A. The red line is a smoothed profile.

However, I was unable to disentangle the Narval data (see Sect. 3.4.2), therefore the LSD Stokes I spectra of ζ Ori Aa could not be computed in the same way as the LSD Stokes V spectra. As a consequence, I attempted to compute the LSD Stokes I profiles in several ways.

3.5.1 Using the Narval data and correcting for the companion

For the I profiles, I first proceeded in the following way: I computed the LSD Stokes I profiles with different masks that only contained the lines of ζ Ori Aa, only the lines of ζ Ori Ab, and only the blended lines. I subtracted the LSD Stokes I profiles obtained for the lines of ζ Ori Ab alone from the LSD Stokes I profiles obtained for blended lines to remove the contribution from the Ab component. I then averaged the LSD Stokes I profiles obtained this way and the one obtained for the lines of ζ Ori Aa alone. In this way the same list of lines (those of Aa alone and the blended ones) are used in the final LSD Stokes I profiles as in the LSD Stokes V profiles calculated above.

This allowed us to use more lines than in Sect. 3.4.1 (i.e., to include the blended lines) and to improve the resulting S/N. I obtained magnetic signatures similar to those derived in Sects. 3.3 and 3.4.1 (see Fig. 3.3). However, the S/N remained low, and some contribution from the Ab component is probably still present in the LSD Stokes I profile. Longitudinal field values extracted from these LSD profiles may thus be unreliable.

3.5.2 Using synthetic intensity profiles

To improve the LSD I profiles, I attempted to use the synthetic TLUSTY/SYNSPEC spectra calculated in Sect. 3.4.1 for ζ Ori Aa. I ran the LSD tool on the synthetic spectra to produce the synthetic LSD Stokes I profiles of ζ Ori Aa with the same line mask as the one used for the LSD Stokes V profiles above.

I then computed the longitudinal magnetic field values from the observed LSD Stokes V profiles and the synthetic LSD Stokes I profiles. I calculated the longitudinal magnetic field B_l for all observations with the center-of-gravity method (see Eq. 2.31 in Sect. 2.5.4).

I obtained longitudinal magnetic field values between -144 and +112 G with error bars between 20 and 100 G.

3.5.3 Using disentangled spectroscopic data

Although I was unable to disentangle the Narval data, I obtained disentangled spectra from the purely spectroscopic archival data. To derive the longitudinal magnetic field values more accurately, I therefore used the disentangled spectra obtained from the purely spectroscopic data.

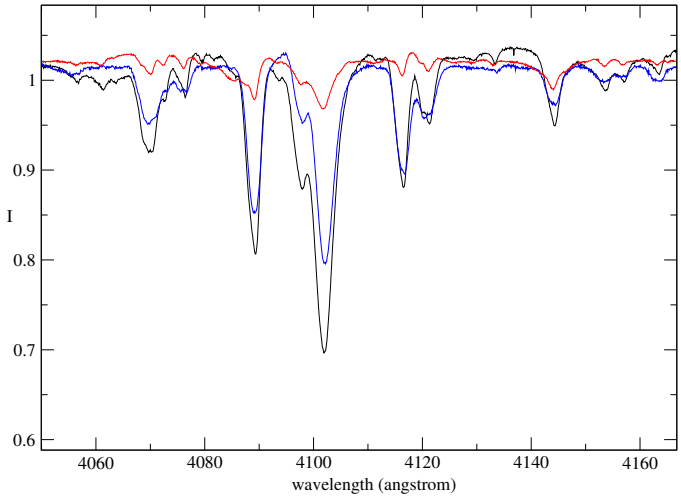

FIGURE 3.7: **Disentangling thanks to FD3Binary**: Small part of the spectrum of ζ Ori A showing the composite observed spectrum (black), the spectrum of ζ Ori Aa (blue) and that of ζ Ori Ab (red).

I ran the LSD technique on the disentangled archival spectra obtained for ζ Ori Aa using the same line list as I used for Stokes V. Thus, I obtained the observed mean intensity profile for ζ Ori Aa alone. I then computed the longitudinal magnetic field values from the observed LSD Stokes V profiles from Narval and the observed LSD Stokes I profiles from the disentangled spectroscopic spectra.

The shape of the magnetic signatures in LSD Stokes V profiles (Fig. 3.8) is similar to the shapes obtained for the combined spectra (Fig. 3.3) and the various methods presented above. The LSD Stokes I spectra now better represent the observed ζ Ori Aa spectrum, however. I therefore adopted these LSD profiles in the remainder of this work. I calculated the FAP (see Sect. 2.5.3). Table 3.3 indicates the detection status obtained for each of the night. Fifteen of the 36 measurements are DD or MD (see Sect. 2.5.3).

As above, I calculated the longitudinal magnetic field B_l for all observations with the center-of-gravity method (see Eq. 2.31 in the Sect. 2.5.4). Results are given in Table 3.3. The longitudinal field B_l varies between about -30 and +50 G, with typical error bars below 10 G. N values are systematically compatible with 0 within 3σN, where σN is the error on N, while B_l values are above $3\sigma B_l$ in seven instances, where σB_l is the error on B_l.

3.6 No magnetic field in ζ Ori Ab

3.6.1 Longitudinal magnetic field values for ζ Ori Ab

To confirm the non-detection of a magnetic field in ζ Ori Ab, I ran the LSD technique with a mask that only contained lines emitted from ζ Ori Ab, that is 62 lines. This

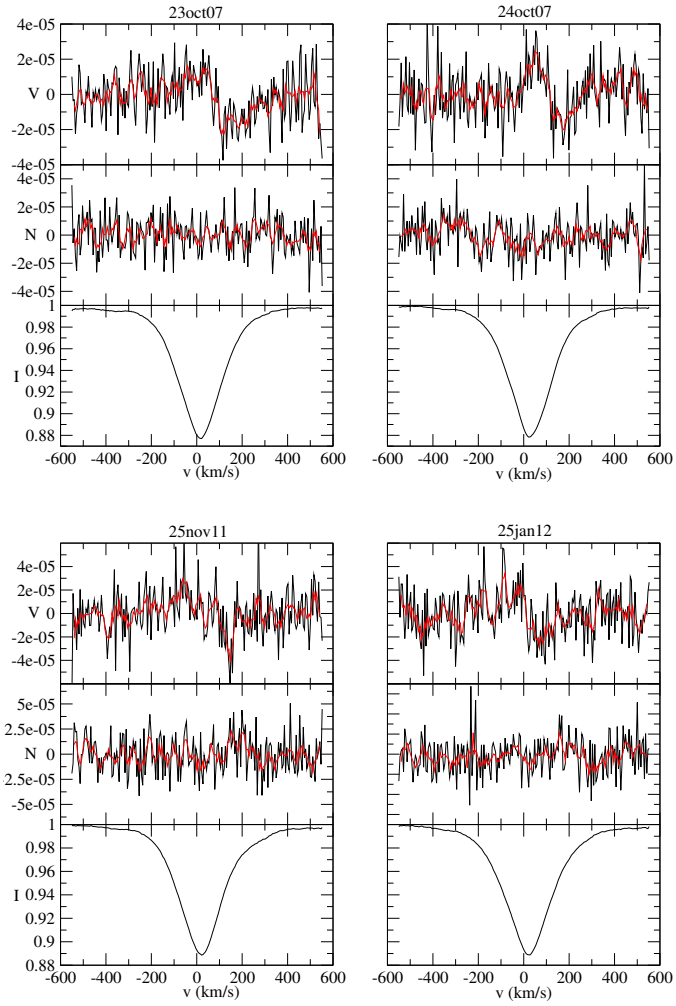

FIGURE 3.8: **Examples of LSD results for ζ Ori Aa :** LSD Stokes I profiles (bottom) computed from the disentangled spectroscopic data, Stokes V (top), and null N (middle) profiles, normalized to Ic, from the Narval data for the primary component ζ Ori Aa for a few nights of observations. The red line is a smoothed profile.

ensures that the LSD Stokes V profiles are not polluted by the magnetic field of ζ Ori Aa. Signatures in the LSD Stokes V profiles are not detected in any of the profiles (all ND), as shown in Table 3.4 and in Fig. 3.9 for selected nights when a signal is detected in ζ Ori Aa.

Using these LSD profiles and the center-of-gravity method, I calculated the longitudinal field value, the null polarization, and their error bars for ζ Ori Ab. I find that both B_l and N are compatible with 0 within 3σ for all nights (see Table 3.4). However, the error bars on the longitudinal field values of ζ Ori Ab are much higher (typically 70 G) than those for ζ Ori Aa (typically 10 G), because far fewer lines could be used to extract the signal for ζ Ori Ab.

TABLE 3.3: **Longitudinal magnetic field of the magnetic primary star ζ Ori Aa.** The columns list the heliocentric Julian dates (HJD) for the middle of observation, the longitudinal magnetic field and its error in Gauss, the detection status: definite detection (DD), marginal detection (MD) and no detection (ND), and the "null" polarization and its error in Gauss.

#	mid-HJD	B_l	σB_l	Detect.	N	σN
1	2454391.559	-5.7	7.7	MD	-3.9	7.7
2	2454392.719	-26.9	16.6	ND	37.2	16.6
3	2454393.570	-9.3	5.5	ND	3.6	5.5
4	2454394.491	-0.3	5.4	ND	6.3	5.4
5	2454395.518	18.1	5.2	MD	12.4	5.4
6	2454397.496	25.5	5.1	MD	3.9	5.1
7	2454398.526	4.7	5.1	MD	-3.7	5.1
8	2454762.644	-15.1	5.5	MD	-6.9	5.5
9	2454763.645	12.8	6.6	ND	-5.4	6.6
10	2454764.654	28.0	5.3	MD	3.6	5.3
11	2454765.639	32.8	6.3	DD	11.1	6.3
12	2454766.635	10.9	6.4	MD	12.7	6.4
13	2455839.688	-3.9	6.5	ND	2.9	6.5
14	2455840.670	3.9	6.5	ND	-6.7	6.6
15	2455845.608	21.3	9.4	ND	4.8	9.4
16	2455846.632	-9.7	11.0	ND	-1.8	11.0
17	2455865.712	12.4	6.5	ND	-0.9	6.6
18	2455873.557	25.2	13.5	MD	-3.6	13.5
19	2455877.626	13.6	7.5	ND	-13.5	7.5
20	2455878.565	7.7	7.5	ND	6.8	7.5
21	2455890.673	6.1	8.7	ND	11.0	8.7
22	2455891.660	24.0	7.4	MD	-6.7	7.4
23	2455892.502	6.0	8.1	ND	-11.4	8.1
24	2455895.667	1.3	6.9	ND	-8.0	6.9
25	2455896.600	-22.6	22.3	ND	22.3	22.5
26	2455910.477	4.1	13.8	ND	13.6	13.8
27	2455935.555	-7.2	7.0	MD	4.2	7.0
28	2455940.536	5.9	7.2	ND	-10.1	7.2
29	2455941.539	-3.1	6.8	MD	4.5	6.8
30	2455942.475	-5.3	8.0	ND	-4.4	8.0
31	2455943.367	4.8	8.4	ND	4.3	8.4
32	2455952.529	25.2	7.3	MD	-12.5	7.3
33	2455953.431	72.3	59.1	DD	-60.4	59.1
34	2455966.472	51.0	9.5	MD	-0.3	9.5
35	2455967.402	1.7	8.5	ND	11.3	8.4
36	2455968.343	10.7	16.7	ND	-13.7	16.6

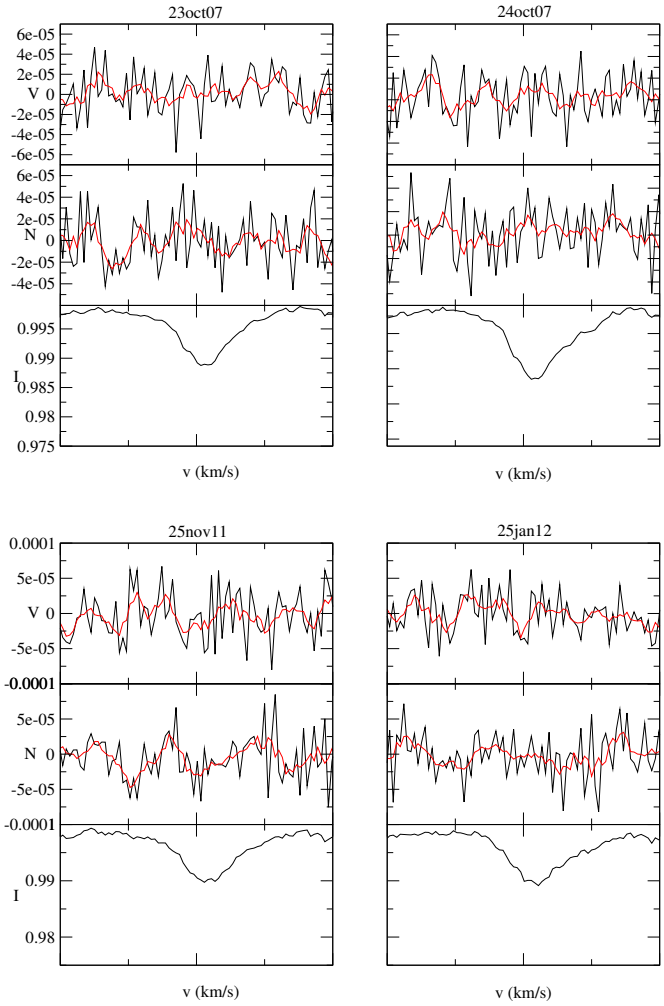

FIGURE 3.9: **Examples of LSD results for ζ Ori Ab :** LSD Stokes I (bottom), Stokes V (top), and null N (middle) profiles, normalized to Ic, for the secondary component ζ Ori Ab for a few nights of observations, computed from Narval data using only the 62 lines belonging to the secondary component. The red line is a smoothed profile. No magnetic signature is observed.

3.6.2 Upper limit on the non-detected field in ζ Ori Ab

The signature of a weak magnetic field might have remained hidden in the noise of the spectra of ζ Ori Ab. To evaluate its maximum strength, I first fitted the LSD I profiles computed above for ζ Ori Ab with a double Gaussian profile. This fit does not use physical stellar parameters, but it reproduces the I profiles as well as possible. I then calculated 1000 oblique dipole models of each of the LSD Stokes V profiles for various values of the polar magnetic field strength $B_{\rm pol}$. Each of these models uses a random inclination angle i, obliquity angle β, and rotational phase, as well as a white Gaussian noise with a null average and a variance corresponding to the S/N of each observed profile. Using the fitted LSD I profiles, the code calculates local Stokes V profiles assuming the weak-field case, and integrates over the visible hemisphere of the star. I obtained synthetic Stokes V profiles, normalized to the intensity of the

TABLE 3.4: **Longitudinal magnetic field measurements for the secondary ζ Ori Ab.** The columns list the heliocentric Julian dates (HJD) for the middle of observation, the longitudinal magnetic field and its error in gauss, the detection status: no detection (ND) in all cases, and the "null" polarization and its error in gauss.

#	mid-HJD	B_l	σB_l	Detect.	N	σN
1	2454391.559	-62.9	74.5	ND	46.5	74.4
2	2454392.719	-80.4	132.7	ND	91.9	132.8
3	2454393.570	26.0	54.8	ND	-60.6	54.9
4	2454394.491	31.0	56.7	ND	24.1	56.6
5	2454395.518	86.7	47.6	ND	101.4	47.7
6	2454397.496	-49.4	45.5	ND	14.3	45.9
7	2454398.526	14.2	46.0	ND	44.6	46.1
8	2454762.644	-14.2	50.8	ND	73.0	50.6
9	2454763.645	-24.1	65.4	ND	43.3	65.5
10	2454764.654	-40.1	49.2	ND	80.0	49.4
11	2454765.639	-32.9	73.5	ND	47.2	73.6
12	2454766.635	7.9	60.5	ND	-26.5	60.6
13	2455839.688	-62.3	53.2	ND	-30.5	53.6
14	2455840.670	-8.3	58.3	ND	3.4	58.2
15	2455845.608	-19.1	92.2	ND	-21.9	91.1
16	2455846.632	-126.4	91.9	ND	-102.1	91.2
17	2455865.712	35.7	63.2	ND	173.4	63.9
18	2455873.557	141.5	112.7	ND	-224.0	113.0
19	2455877.626	55.7	60.0	ND	2.5	60.0
20	2455878.565	34.8	68.3	ND	75.0	68.7
21	2455890.673	-105.9	106.6	ND	-154.9	107.5
22	2455891.660	8.7	82.6	ND	86.6	82.8
23	2455892.502	77.1	84.3	ND	-63.7	84.8
24	2455895.667	-27.0	75.2	ND	-63.8	75.5
25	2455896.600	-33.7	289.4	ND	-113.7	296.7
26	2455910.477	171.0	183.7	ND	129.3	183.4
27	2455935.555	-82.4	70.1	ND	-58.6	69.9
28	2455940.536	-12.3	63.5	ND	-55.8	63.7
29	2455941.539	20.3	67.3	ND	116.9	67.8
30	2455942.475	31.8	70.6	ND	-97.2	71.1
31	2455943.367	-6.2	78.8	ND	-27.7	79.2
32	2455952.529	-72.4	71.0	ND	1.1	71.3
33	2455953.431	173.6	478.5	ND	-152.6	480.7
34	2455966.472	52.9	79.9	ND	-32.1	79.8
35	2455967.402	-57.8	74.6	ND	62.8	74.3
36	2455968.343	-152.8	186.5	ND	-92.9	187.2

continuum. These synthetic profiles have the same mean Landé factor and wavelength as the observations.

I then computed the probability of detecting a dipolar oblique magnetic field in this

set of models by applying the Neyman-Pearson likelihood ratio test (see e.g. Helstrom 1995; Kay 1998; Levy 2008). This allowed us to decide between two hypotheses: the profile only contains noise, or it contains a noisy Stokes V signal. This rule selects the hypothesis that maximizes the detection probability while ensuring that the FAP is not higher than 10^{-3} for a marginal magnetic detection. I then calculated the rate of detections in the 1000 models for each of the profiles depending on the field strength (see Fig. 3.10).

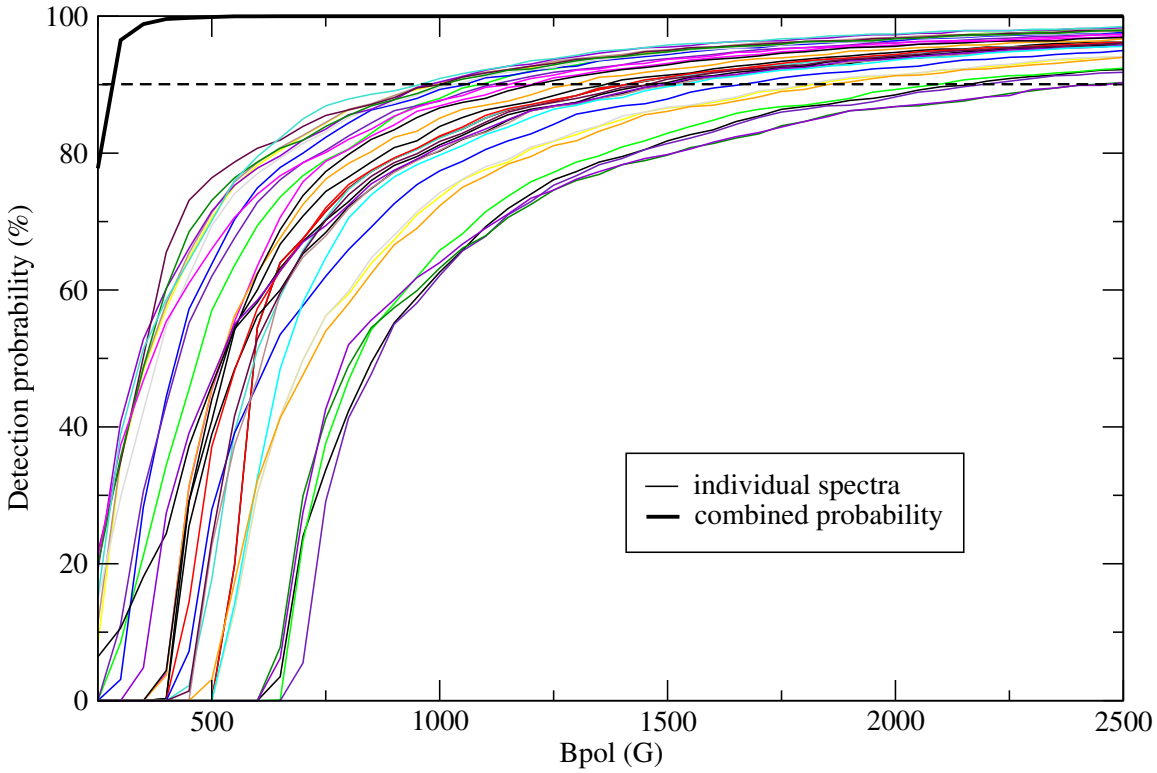

FIGURE 3.10: **Upper limit of the non-detected magnetic field in the secondary component ζ Ori Ab :** Detection probability of a magnetic field in each spectrum of the secondary component of ζ Ori Ab (thin color lines) as a function of the magnetic polar field strength. The horizontal dashed line indicates the 90% detection probability, and the thick black curve (top left corner) shows the combined probability.

I required a 90% detection rate to consider that the field would statistically be detected. This translates into an upper limit for the possible undetected dipolar field strength for each spectrum, which varies between ∼900 and ∼2350 G (see Fig. 3.10).

Since 36 spectra are at our disposal, statistics can be combined to extract a stricter upper limit taking into account that the field has not been detected in any of the 36 observations (see Neiner et al. 2015a). The final upper limit derived from this combined probability for ζ Ori Ab for a 90% detection probability is ∼300 G (see the thick line in Fig. 3.10).

3.7 Magnetic field configuration

3.7.1 Rotational modulation

I searched for a period of variation in the 36 longitudinal magnetic field measurements of ζ Ori Aa with the clean-NG algorithm (see Gutiérrez-Soto et al. 2009). I obtained a frequency $f = 0.146421$ c d^{-1}, which corresponds to a period of 6.829621 days. This value is consistent with the period of ∼7 days suggested by Bouret et al. (2008). Assuming that the magnetic field is a dipole with its axis inclined to the rotation axis, as is found in the vast majority of massive stars, this period corresponds to the rotation period of the star.

I used this period and plotted the longitudinal magnetic field as a function of phase. For the data taken in 2007 and 2008, the phase-folded field measurements show a clear sinusoidal behavior, as expected from a dipolar field model (see top panel of Fig. 3.11). A dipolar fit to the data, that is, a sine fit of the form $B(x) = B_0 + B_a \times sin(2\pi(x+\phi_d))$, resulted in B_0=6.9 G and B_a=19.2 G. A quadrupolar fit to the phase-folded data only shows an insignificant departure from the dipolar fit.

However, the period of ∼6.829 days does not match the measurements collected in 2011 and 2012 very well (see middle panel of Fig. 3.11). None of the dipolar or quadrupolar fits to these data provide a reasonable match. A further search for a different period in these 2011-2012 data alone provided no significant result.

The magnetic fields of main-sequence massive stars are of fossil origin. These fields are known to be stable over decades and are only modulated by the rotation of the star. A change of period in the field modulation between the 2007-8 and 2011-12 epochs is thus not expected in ζ Ori Aa.

ζ Ori Aa has a companion, therefore I investigated the possibility that the magnetic field has been affected by the companion. Indeed, in 2011 and 2012, ζ Ori Ab was close to periastron, which means that the distance between the two stars was smaller than in 2007 and 2008. I calculated this distance to check whether some binary interactions might have occurred.

To calculate the distance between the two components, I used the photometric distance of ζ Ori A, d=387 pc (Hummel et al. 2013). From Hummel et al. (2013), I know the orbital parameters of the binary. The shortest distance between the two stars is $r_{\rm min} = a - \sqrt{a^2 - b^2} = 23.8$ mas, where a is the semi-major axis and b the semi-minor axis. From the distance of ζ Ori A, I can compute $r_{\rm min} = \sin(\theta)/d$ in pc, where θ is the parallax in radian. I obtained a distance of 81 R_*, where R_* is the radius of ζ Ori Aa.

The distance between the two stars at periastron therefore appears too large for interactions between the two stars to occur. In addition, the binary system is still significantly eccentric (0.338, Hummel et al. 2013), even though ζ Ori Aa has already evolved into a supergiant. Tidal interactions have apparently not been able to circularize the system yet, which would confirm that these interactions are weak (Zahn 2008).

However, in addition to ζ Ori Aa and Ab, a third star ζ Ori B may also interfere with the ζ Ori A system. Correia et al. (2012) showed that when a third component comes into play, tidal effects combined with gravitational interactions may increase the eccentricity of ζ Ori A, which would otherwise have circularized. I thus cannot exclude that tidal interactions are stronger than they seem in the ζ Ori A system.

3.7.2 Field strength and geometrical configuration

Assuming that the period detected in Sect. 3.7.1 is the rotation period of the star, I can determine the inclination angle i of the star by measuring $v \sin i$. In massive stars, line broadening does not come from rotational broadening alone, but also from turbulence and stellar wind. This is particularly true for supergiant stars.

Based on the synthetic spectra calculated in Sect. 3.4.1 and the lines identified to belong to only one of the two components, I determined the broadening needed in the synthetic spectra to fit the observations. For ζ Ori Aa, a broadening of 230 km s^{-1} was necessary to provide a good fit to the observed lines, while for ζ Ori Ab I needed 100 km s^{-1}. These broadening values are upper limits of the $v \sin i$ values because they include all physical processes that broaden the lines. In fact, with a period of 6.829 days and a radius of 20 R$_\odot$ as given by Hummel et al. (2013), the maximum possible $v \sin i$ for ζ Ori Aa is 148 km s^{-1}.

In addition, Bouret et al. (2008) determined $v \sin i$ through a Fourier transform of the average of the 5801 and 5812 Å CIV and 5592 Å OIII line profiles. They found a $v \sin i$ of 110$\pm$10 km s^{-1}. From our disentangling of the spectra, I know that the two CIV lines originate from ζ Ori Aa, but the OIII 5590 Å line is partly ($\sim$10%) polluted by ζ Ori Ab. As a consequence, I applied the Fourier transform method to the LSD Stokes I profiles I calculated from the lines that only originate from ζ Ori Aa. I obtained $v \sin i$= 140 km s^{-1}. However, it is known that $v \sin i$ values determined from LSD profiles might be overestimated.

Finally, taking macroturbulence into account but not binarity, for example, Simón-Díaz & Herrero (2014) found that $v \sin i$ for ζ Ori A is between 102 and 127 km s^{-1}, depending on the method they used.

In the following, I thus consider that $v \sin i$ is between 100 km s^{-1}and 148 km s^{-1}for ζ Ori Aa. In addition, I adopt the radius of 20 R$_\odot$ given by Hummel et al. (2013) and the rotation period of 6.829 d. Using $v \sin i$= [100-148] km s^{-1}, I obtain $i \sim [42 - 87]^\circ$.

Using the dipolar fit to the 2007-2008 longitudinal field measurements and the inclination angle i, I can deduce the obliquity angle β of the magnetic field with respect to the rotation axis. To this aim, I used the formula $r = B_{\rm min}/B_{\rm max} = \cos(i - \beta)/\cos(i + \beta)$ (Shore 1987). The dipolar fit of the longitudinal field values gives r=0.47. With $i \sim [42 - 87]^\circ$, I obtain $\beta \sim [71 - 8]^\circ$.

In addition, from the dipolar fit to the longitudinal field values and the angles i and β determined above, I can estimate the polar field strength with the formula $B_0 \pm B_a = 0.296 \times B_{\rm pol} \cos(\beta \pm i)$, where the limb-darkening coefficient is assumed to be 0.4 (see

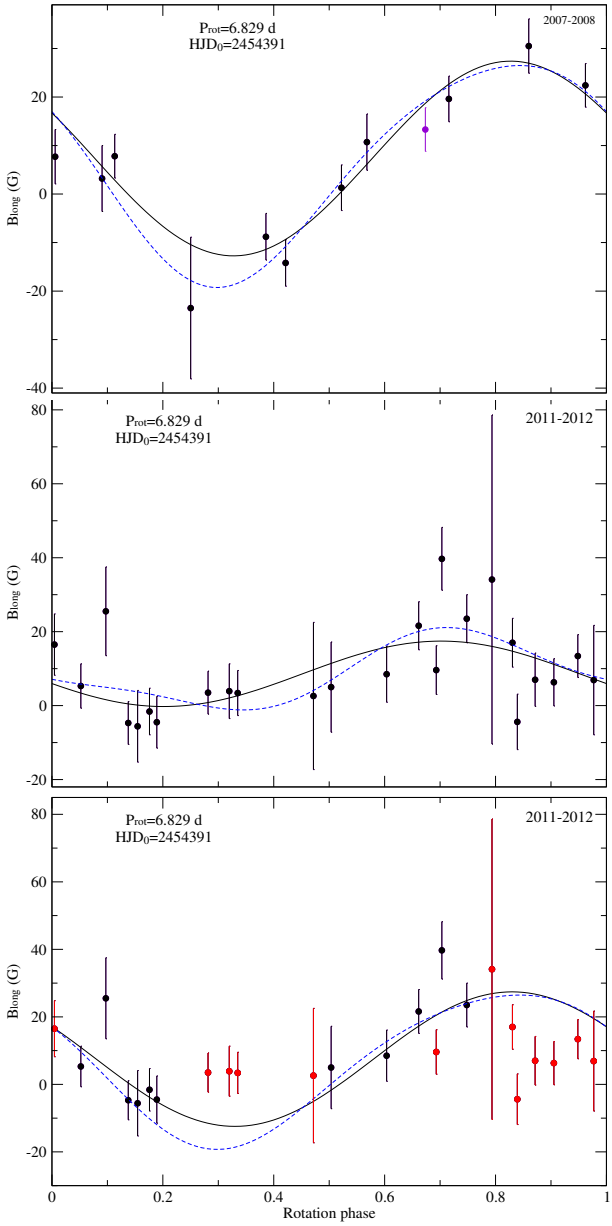

FIGURE 3.11: **Rotational modulation of the longitudinal magnetic field of ζ Ori Aa** for the observations taken in 2007-2008 (top) and 2011-2012 (center). The black line corresponds to the best dipolar fit, while the dashed blue line corresponds to the best quadrupolar fit. The bottom panel compares the fit of the dipole and the quadrupole obtained from the 2007-2008 data with the observations obtained in 2011-2012 (see Sect. 3.7.3). The data for which the Stokes V model matches the observed LSD V profiles are shown in black, while the data for which the Stokes V model does not match are in red. We see that the observed B_l match with the fit when the Stokes V models also match.

Borra & Landstreet 1980). I found $B_{\rm pol} = [110 \pm 5 - 524 \pm 65]$ G. The dipolar magnetic field that I find is thus higher than the one found by Bouret et al. (2008).

In 2011-2012, the maximum measured B_l is 51 G and the minimum polar field strength is thus $B_{\rm pol} \geq 3.3 B_{l,max} = 168 \pm 33$ G. This value is compatible with the range derived from the 2007-2008 data.

3.7.3 Stokes V modeling

Since the B_l data taken in 2007-2008 point towards the presence of a dipole field, I used an oblique rotator model to fit the LSD Stokes V and I profiles.

I used Gaussian local intensity profiles with a width calculated according to the resolving power of Narval and a macroturbulence value of 100 $\mathrm{km\,s^{-1}}$ determined by Bouret et al. (2008). I fit the observed LSD I profiles by Gaussian profiles to determine the depth, $v \sin i$ and radial velocity of the intensity profile. I used the weighted mean Landé factor and wavelength derived from the LSD mask applied to the Narval observations and the rotation period of 6.829 days. The fit includes five parameters: i, β, $B_{\rm pol}$, a phase shift ϕ, and a possible off-centering distance d_d of the dipole (see Sect. 2.10).

I calculated a grid of V profiles for each phase of observation by varying the five parameters mentioned above and applied a χ^2 minimization to obtain the best fit of all observations simultaneously. More details of the modeling technique can be found in (Alecian et al. 2008 and Sect. 2.10). The parameters of the best fit are i=79.89°, β=21.5°, ϕ=0.68, $B_{\rm pol}$=142.2 G and d_d=0.0. The values for the angles i and β are within the error boxes derived in Sect. 3.7.2, and the value for the polar field strength $B_{\rm pol}$ fits the B_l results well. Moreover, the best fit is obtained for d_d=0, which confirms that no quadrupolar component is found.

The 36 Stokes V profiles for this best fit are shown in Fig. 3.12 overplotted on the observations. As expected, for the nights in 2007-2008, the model fits the observations well. For some nights in 2011-2012, the observations are too noisy to see whether the model fits well. Considering the nights in 2011-2012 for which the S/N is sufficient, the model fits some of the observations but not all. For those nights for which the model fitted well the observations, I compared the values of the longitudinal magnetic field B_l to the dipolar fit obtained for the B_l measurements of 2007-2008 (see bottom panel of Fig. 3.11). The 2011-2012 data that match the Stokes V models also match the B_l dipolar fit curve. Therefore, it seems that at least part of the 2011-2012 data show the same rotational modulation and dipole field as in 2007-2008. Only part of the 2011-2012 dataset does not match the rest of the observations.

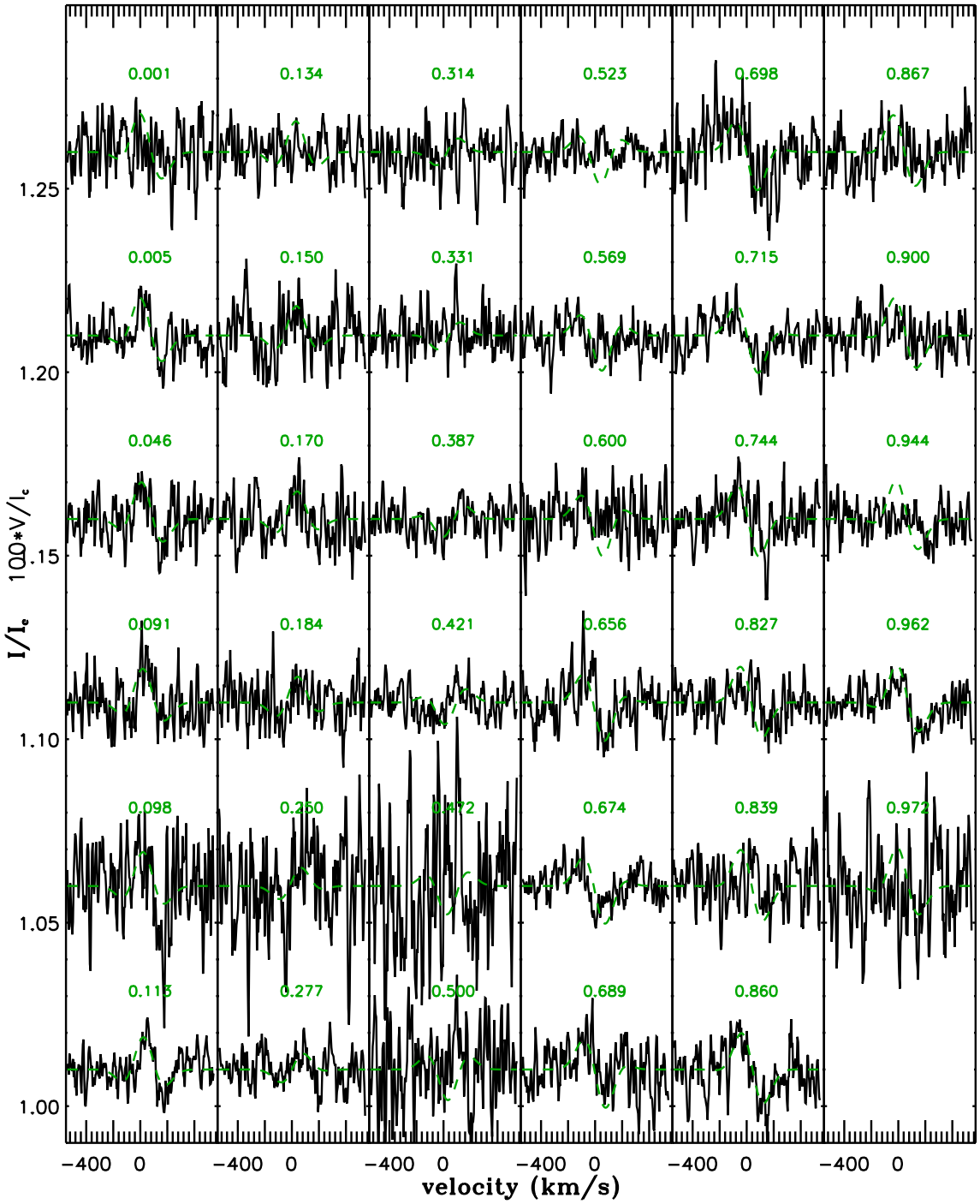

FIGURE 3.12: **Best dipolar model fit (green) of the observed Stokes V profiles (black).** The green numbers correspond to the rotational phase. The very noisy observation at phase 0.793 is not shown.

3.8 Magnetospheres

3.8.1 Magnetospheric parameters

With the polar magnetic field strength $B_{\rm pol}$ = 142.2 G determined with the Stokes V model, I calculated the wind confinement parameter η_*, which characterizes the ability of the magnetic field to confine the wind particles into a magnetosphere (ud-Doula & Owocki 2002). If $\eta_* \leq 1$, ζ Ori Aa is located in the weakly magnetized winds region of the magnetic confinement-rotation diagram and it does not have a magnetosphere (see Fig. 3.2). However, for $\eta_* > 1$, wind material is channeled along magnetic field lines toward the magnetic equator and ζ Ori Aa hosts a magnetosphere.

To calculate η_*, I first used the fiducial mass-loss rate $\dot{M}_{B=0} = 1.4 \times 10^{-6} M_\odot\ yr^{-1}$ and the terminal speed $V_\infty = 2100$ km s^{-1} determined by Bouret et al. (2008). They measured the mass-loss rate from the emission of Hα and used archival International Ultraviolet Explorer (IUE) spectra to measure the wind terminal velocity from the blueward extension of the strong UV P Cygni profile. I obtained $\eta_* = 0.9$.

I then recalculated η_* but this time using the mass-loss rate of $\dot{M} = 3.4 \times 10^{-7} M_\odot\ yr^{-1}$ and $V_\infty = 1850$ km s^{-1} determined by Cohen et al. (2014). This gives $\eta_* = 4.2$.

A magnetosphere can only exist below the Alfvén radius R_A, which is proportional to η_*, with $R_A = \eta_*^{1/4} R_*$. For ζ Ori Aa, using the two above determinations of η_*, $R_A = [0.98 - 1.43] R_*$. Moreover, the magnetosphere can be centrifugally supported above the corotation Kepler radius R_K. $R_K = (2\pi R_*/P_{\rm rot}\sqrt{(GM/R_*)})^{2/3}$, thus for ζ Ori Aa $R_K = 2.8 R_*$. Since $R_K > R_A$, no centrifugally supported magnetosphere can exist.

Therefore, ζ Ori Aa is either in the weakly magnetized winds region of the magnetic confinement-rotation diagram, meaning that ζ Ori Aa does not have a magnetosphere ($\eta_* < 1$), or it hosts a dynamical magnetosphere ($1 < \eta_* < 4.2$).

3.8.2 H_α variations

The H_α line shows significant variability in emission and absorption. For stars that have a magnetosphere, we expect magnetospheric emission at H_α, which varies with the rotation period (see e.g. Grunhut 2015).

To check whether there is a signature of the presence of a magnetosphere around ζ Ori Aa, I studied the variation of its H_α line in the archival spectra (see Sect. 3.2.2). I confirm that the emission in H_α does indeed vary. While most of the variations are problably related to variations in the stellar wind of the supergiant, the signature of a weak rotationally modulated dynamical magnetosphere is observed in H_α (see Fig. 3.13).

The ratio $\log R_A/R_K$ gives a measure of the volume of the magnetosphere. For ζ Ori Aa, $\log R_A/R_K$ is very small ($<$ -0.3), and it is thus not surprising that H_α only weakly reflects magnetic confinement.

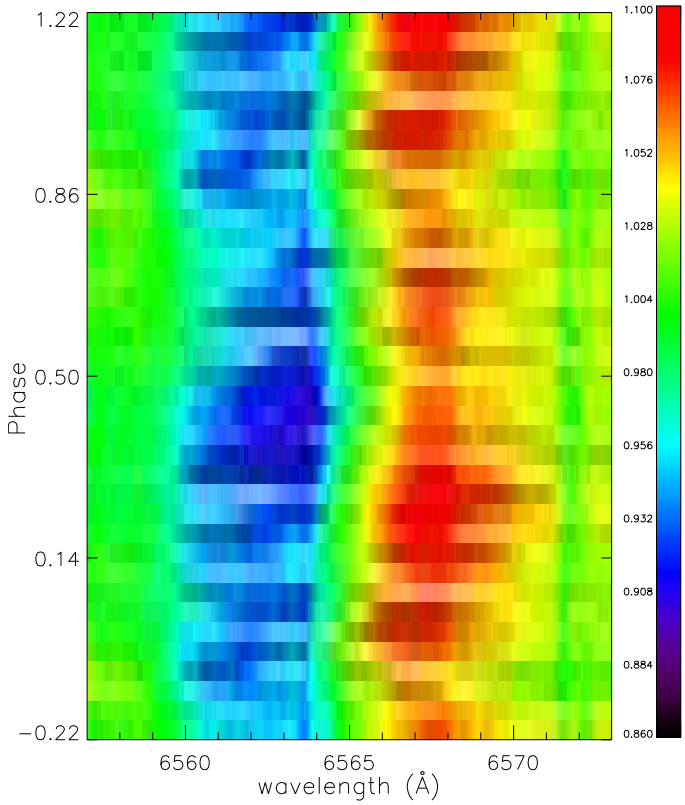

FIGURE 3.13: **Dynamic plot of each individual archival H_α spectrum** in phase with the rotation period (P_{rot}=6.829d).

3.9 Discussion and conclusions

Based on archival spectrocopic data and Narval spectropolarimetric data, I confirm the presence of a magnetic field in the massive star ζ Ori A, as initially suggested by Bouret et al. (2008). However, Bouret et al. (2008) did not know that ζ Ori A is a binary star, which was subsequently shown by Hummel et al. (2013) with interferometry.

I disentangled the spectra and could thus show that the primary O supergiant component ζ Ori Aa is the magnetic star, while the secondary ζ Ori Ab is not magnetic at the achieved detection level. ζ Ori Aa is the only magnetic O supergiant known as of today.

The magnetic field of ζ Ori Aa is a typical oblique dipole field, similar to those observed in main-sequence massive stars. From Stokes modeling, the polar magnetic field strength $B_{\rm pol}$ of ζ Ori Aa is found to be about 140 G. If I assume field conservation during the evolution of ζ Ori Aa, because the stellar radius increased from ∼10 to ∼20 $R_\odot$, the surface magnetic polar field strength decreased by a factor ∼4. This implies that the polar field strength of ζ Ori Aa when it was on the main sequence was about 600 G. This is similar to what is observed in other main-sequence magnetic O stars.

The current field strength and rotation rate of ζ Ori Aa are too weak, with respect to the wind energy, for the star to be able to host a centrifugally supported magnetosphere. However, it seems to host a dynamical magnetosphere. All other ten known magnetic O stars host dynamical magnetospheres, except for the complicated system of Plaskett's

star, which has a very strong magnetic field and hosts a centrifugally supported magnetosphere (see Grunhut et al. 2013). However, these other magnetic O stars are not supergiants.

Although ζ Ori A is one of the brightest O star in the X-ray domain, Cohen et al. (2014) found that it resembles a non-magnetic star, with no evidence for magnetic activity in the X-ray domain and a spherical wind. This probably results from the weakness of the magnetosphere around ζ Ori Aa.

The rotation period of ζ Ori Aa, $P_{\rm rot} = 6.829$ d, was determined from the variations of the longitudinal magnetic field. This period is clearly seen in the data obtained in 2007-2008, but only part of the spectropolarimetric measurements obtained in 2011 and 2012 seem to follow that rotational modulation. The reason for the lack of periodicity for part of the magnetic measurements of 2011-2012 was not identified. Although passage at the binary periastron occurred between 2008 and 2011, the distance between the two companions seems too large for the companion to have perturbed the magnetic field of the primary star, unless it is ζ Ori B which has maintained the two components of ζ Ori A at a distance (see Sect. 3.7.1). A recent study of BRITE observations of ζ Ori (Buysschaert et al., in prep.) shows that this star undergoes short episodes of brightening, possibly due to sporadic ejection of matter. Such variations could perturb the spectropolarimetric measurements.

ζ Ori A therefore remains an interesting star that needs to be studied further. More spectropolarimetric observations should be collected at appropriate orbital phases to allow for a more accurate spectral disentangling. This would allow to obtain stronger constraints on the magnetic field strength and configuration, to study the field as a function of orbital phase, and to better understand the magnetic field perturbations that seem to have occurred during the observations in 2011-2012.

Chapter 4

The upper limit of the magnetic desert

4.1 Introduction

As explained in the introduction (see chapter 1), a magnetic desert exists between ∼300 G and ∼3 G. Knowing the properties of this magnetic desert is crucial to bring constraints on the scenarios that attempt to explain the dichotomy between strong and weak magnetic fields in hot stars.

What could be the origin of the magnetic dichotomy between Ap/Bp and Vega-like magnetism? The scenario of Aurière et al. (2007) suggested that an initially continuous distribution of fields bifurcated into two separated groups. If the magnetic field of the stars is too weak to prevent the growth of a strong toroidal component by differential rotation, the field configurations then became unstable to a Tayler instability. As a result, the surface integrated longitudinal field strongly decreased due to polarity cancellation effects. By contrast, the stars that host strong enough dipolar magnetic fields reacted back efficiently on the differential rotation leading to the present strong magnetic field in hot stars in stable configurations. In support to this scenario, the order of magnitude estimate of the critical dipolar field separating the stable and unstable configurations, B_c, is:

$$B_c = (4\pi\rho)^{1/2} r\Omega \tag{4.1}$$

where ρ is the volumetric mass density, r is the stellar radius, and Ω is the angular velocity.

The lower limit and the way it depends on stellar rotation carries crucial information about the origin of magnetism of hot stars. In addition, even if the scenario developed by Aurière et al. (2007) is not the correct one, the relation between B_c and the stellar parameters would provide very important constraints.

To test the relation between B_c and stellar rotation, I participated in an observational program to study the upper limit of the magnetic desert (PI: F. Lignières) thanks to Ap/Bp stars, with the spectropolarimeter Narval during the semester 2014B. This observational program is the sequel of the study performed by Aurière et al. (2007). Ap/Bp stars are chemically peculiar stars and one of the properties of these stars is that they host a strong magnetic field contrary to the other intermediate-mass stars, making them good targets to determine the upper limit of the magnetic desert.

The goal of this project is to determine B_c, the minimum dipolar field strength of Ap/Bp stars for various interval of rotation periods. This requires to gather, for each period range, a large enough sample of dipolar field strength measurements. As in the Aurière et al. (2007) survey, we have selected Ap/Bp stars with weak or marginally detected longitudinal fields, for which the rotational period is known. The lowest dipolar field stars are expected to be among such stars, although the relation between the dipolar strength B_d and the observed longitudinal field depends on the line of sight inclination and of the magnetic axis inclination. As a first estimate, $B_d \geq 3.3 B_{l,max}$ (for more details see Aurière et al. 2007) where $B_{l,max}$ is the maximum value of the longitudinal field during one rotation period. However, to determine the dipolar strength more precisely thanks to the oblique rotator model (see section 2.10), we need to obtain the longitudinal magnetic field measurements at different rotational phases.

4.1.1 Choice of targets

As shown in Figure 4.1, the lowest dipolar fields $B_c \approx 300$G of the 28 stars in Aurière et al. (2007) were found in the 2-to 4-day period range. However, there is a lack of observations, in the 0-to 2-day period range, that is why we choose to observe Ap/Bp stars in this period range. We used the Bychkov et al. (2005) Ap/Bp star catalog that contains 32 stars in this period range to extract a list of 6 stars with the lowest known longitudinal field. The stars are also chosen in a narrow domain of temperature, in order not to be influenced by the temperature, because we do not know if the upper limit of the magnetic desert depends on the temperature. The existing data for the target stars clearly do not allow to fit an oblique rotator model, nor to retrieve dipolar strengths with a significant accuracy (see Bychkov et al. 2005 and comments therein). We thus plan to obtain spectra with a S/N of ~ 800 at 15 different rotational phases for each of these 7 stars and then to determine the dipolar strengths by fitting oblique rotator models (see section 2.10). From this, we will determine whether B_c increases in the 0-to 2-days period range and we will test whether this increase is compatible with the model proposed in Aurière et al. (2007). In addition, we plan to observe again one star of the Aurière et al. (2007) survey, HD96707, for which they obtained only marginal detection of a magnetic field. The survey of Aurière et al. (2007) was performed mainly with the Musicos spectropolarimeter, which was the predecessor of Narval. The sensitivity of Narval is 30 times higher than the one of Musicos, so we expect to detect the magnetic field of this star with Narval. Table 4.1 describes the stellar parameters of the targets.

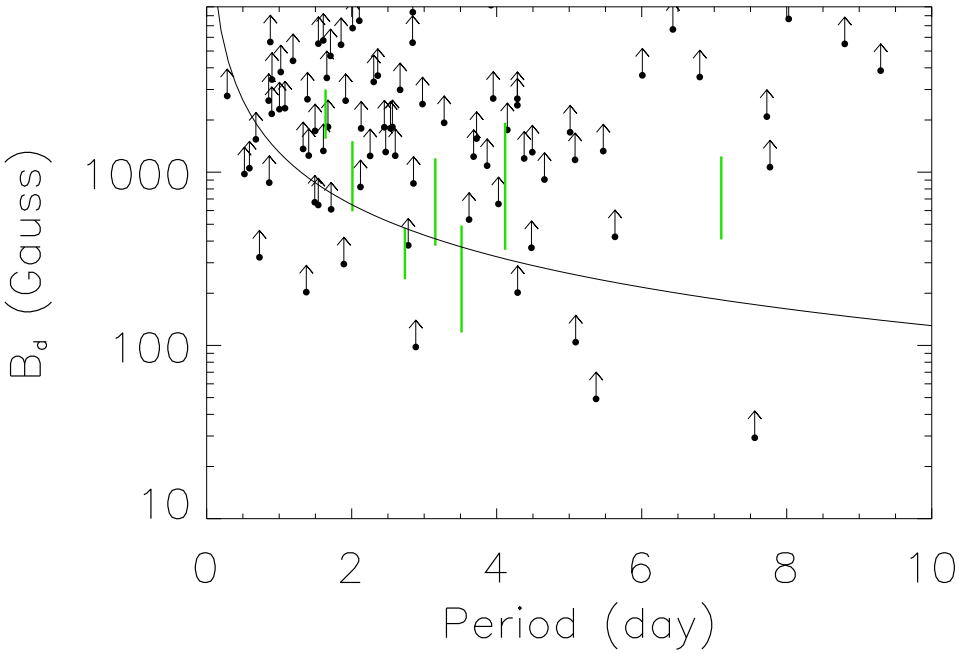

FIGURE 4.1: Relation between the field strength and the rotation of Ap stars from data published in the literature. The black arrows correspond to the lower limit of the dipolar strength deduced from the maximum longitudinal field. In green are determinations of the dipolar strength from the oblique rotator model done by Aurière et al. (2007). The black curve is a $B_c \propto \Omega$ relation.

TABLE 4.1: **Stellar parameters of the Ap/Bp stars used in this study:** the columns list the name of the star, its magnitude, spectral type, $v \sin i$, rotational period, effective temperature, and gravity.

star	m_v	Sp. type	vsini ($km\,s^{-1}$)	P_{rot} (d)	$T_{\rm eff}$ (K)	log g
HD12447	4.11	A0p	81	1.49070	9900	3.99
HD12767	4.69	B9p	44	1.892	10956	3.85
HD19832	5.8	B9p	110	0.727893	12800	4.0
HD22470	5.2	B9p	75	0.6785	12400	3.97
HD28843	5.8	B9p	100	1.373813	10778	4.33
HD32650	5.32	A0p	30	2.7347	11920	4.15
HD96707	6.0	F0p	42	3.515	7780	4.0

4.2 Data Analysis and longitudinal field measurements

The target HD12767 was not observed, the other targets were observed at least 3 times. For each observation, I used the LSD technique (see section 2.5.2) with a mask adapted to the temperature and log g of the target, extracted from VALD (Kupka & Ryabchikova 1999; Piskunov et al. 1995). I cleaned the masks by removing lines that were not visible in the spectra, the hydrogen lines, and the lines that were blended with the hydrogen lines.

4.2.1 HD12447

HD12447 (α Piscium A) is the primary of a long period binary system and it is classified as A0p star. Due to the separation of 3.6" between the two components, the secondary HD12446 (an Am star) was not recorded in the Narval fiber. However, HD12447 is also suspected to be a multiple system. HD12447 was observed 14 times between September 2014 and December 2014 (see Table 4.2).

TABLE 4.2: **Journal of observations of HD12447:** the columns list the date, heliocentric Julian date (HJD) at the middle of the exposure (2450000+), exposure time, mean S/N of the Stokes V profiles, and detection status (see Sect. 2.5.3).

date	MHJD	T_{exp}(s)	S/N	Detect.
05 Sep. 14	6906.603	4 × 60	13955	DD
24 Sep. 14	6925.561	4 × 60	13255	DD
17 Oct. 14	6948.450	4 × 60	12844	DD
18 Oct. 14	6949.588	4 × 60	11699	DD
19 Oct. 14	6950.556	4 × 60	8871	DD
23 Oct. 14	6954.496	4 × 60	7244	MD
24 Oct. 14	6955.421	4 × 60	9836	DD
25 Oct. 14	6956.573	4 × 60	12213	DD
26 Oct. 14	6957.410	4 × 60	12785	DD
29 Oct. 14	6960.428	4 × 60	13190	DD
30 Oct. 14	6961.432	4 × 60	11642	DD
31 Oct. 14	6962.441	4 × 60	13507	DD
01 Nov. 14	6963.494	4 × 60	14037	DD
03 Dec. 14	6995.326	4 × 60	13412	DD

For HD12447, the final mask for the LSD technique contains 900 lines. I obtained definite detection of a Zeeman signature for all nights, except on 23 October 2014. For this night, I obtained a marginal detection (see Table 4.2) due to the lower S/N in the Stokes V profiles. As seen in the Stokes I profiles (see Fig. 4.2), HD12447 is in fact a triple system. The broadest line corresponds to the primary and the narrow lines to the secondary and tertiary components. The radial velocity of the components varies

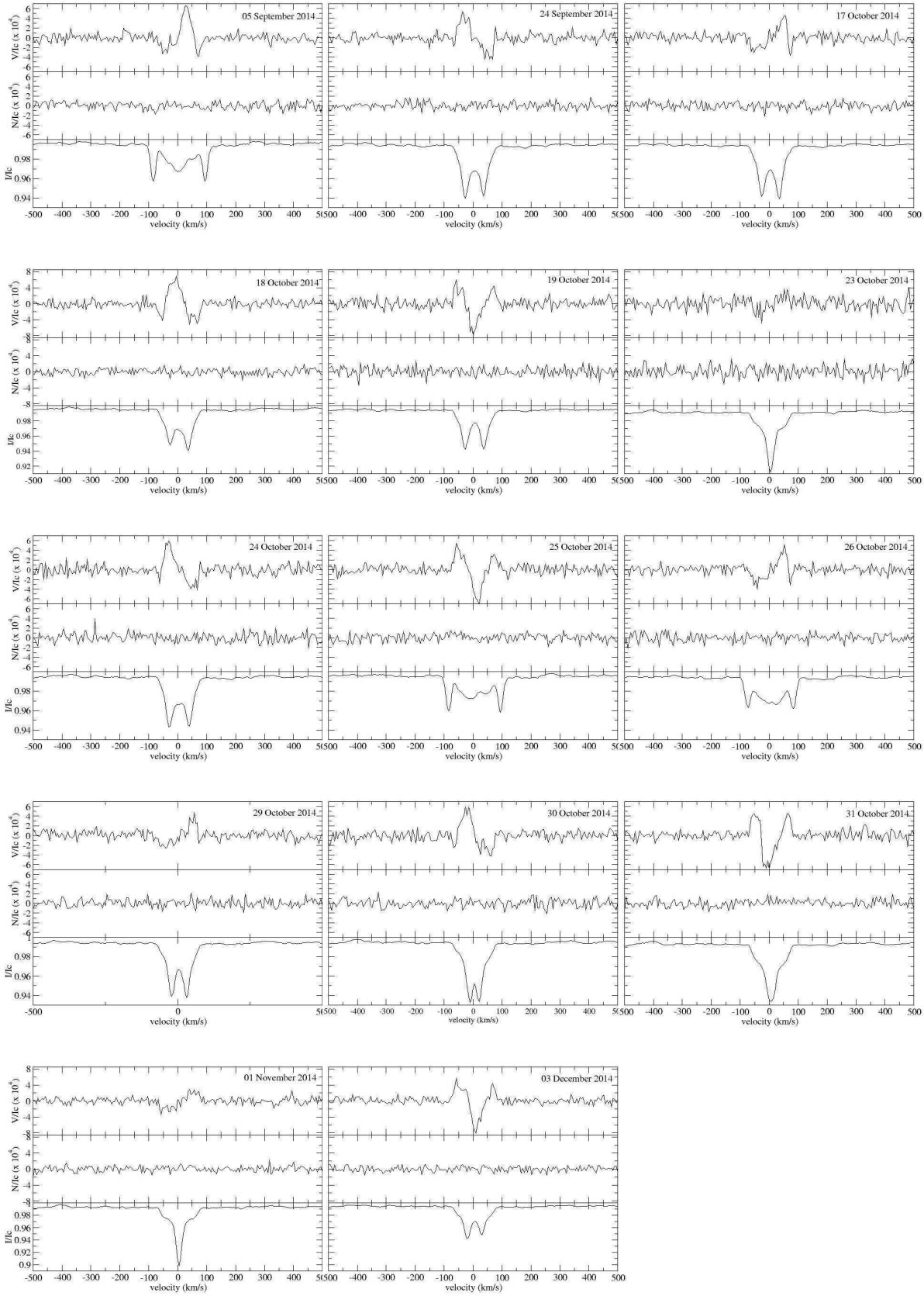

FIGURE 4.2: **Results of the LSD for HD12447** The LSD Stokes I profiles (bottom), Stokes V (top) and null N profiles for each observation.

rapidly over the observation run, which implies that the orbital period is short (less than 2 months).

The Zeeman signatures in the Stokes V profiles are spread over the line of the primary, thus I concluded that they come from the primary, the Ap star. However, I cannot exclude that the secondary and the tertiary are also magnetic. To determine the longitudinal magnetic field, we would need to disentangle the spectra of the three components. To do this however, a careful normalization of all Narval orders is needed, as well as a detailed orbital solution. This is beyond the scope of this thesis. For this star, it is therefore not possible at this stage to determine a polar field strength.

4.2.2 HD19832

HD19832 is a fast rotator, therefore it is difficult to detect Zeeman signatures in the Stokes V profiles. That is why, instead of the default spectral bin spanning 1.8 $\mathrm{km\,s^{-1}}$, used for Narval, I used for HD19832 a spectral bin of 18 $\mathrm{km\,s^{-1}}$ which leaves us with about 20 velocity bins in the pseudo line profile. After the cleaning of the initial mask, the mask contains 247 lines. The number of lines in the mask of HD19832 is lower than for HD12447 although they have a close spectral type. Due to the high $v \sin i$ of HD19832, some spectral lines are not visible in the spectra of HD19832. Therefore, I tested a mask containing also the invisible lines however the result of the LSD with this mask is worse than with the cleaned mask.

TABLE 4.3: **Journal of observations of HD19832:** The columns list the date, the heliocentric Julian dates (HJD) at the middle of the observation (2450000+), the exposure time, the mean S/N of the Stokes V profiles, the detection status (MD means Marginal Detection and ND means No Detection), the longitudinal magnetic field, and its error and the "null" polarization and its error.

date	MHJD	T_{exp}	S/N	detect.	$B_l \pm \sigma B_l$	$N \pm \sigma N$
03 Sep. 14	6904.655	4 × 275	14961	MD	-471.5±223.6	12.8±220.3
12 Sep. 14	6913.579	4 × 275	15739	MD	439.9±224.2	75.6±221.3
23 Sep. 14	6924.656	4 × 275	17764	ND	265.1±172.7	-27.5±172.0
17 Oct. 14	6948.482	4 × 275	15809	MD	670.7±261.1	-210.5±254.8
18 Oct. 14	6949.621	4 × 275	15870	MD	-513.9±214.8	98.5±208.7
19 Oct. 14	6950.571	4 × 275	13325	ND	-419.9±337.9	-63.6±335.2
23 Oct. 14	6954.567	4 × 275	10059	ND	487.5±290.4	-1065.0±297.8
24 Oct. 14	6955.436	4 × 275	12362	MD	-412.0±274.9	89.7±271.6
26 Oct. 14	6957.426	4 × 275	13477	ND	414.9±228.9	32.2±226.6
27 Oct. 14	6958.451	4 × 275	13184	MD	-737.9±279.5	-44.0±273.6
28 Oct. 14	6959.421	4 × 300	11217	ND	404.5±305.9	327.1±304.6

I obtained marginal detections of a magnetic field for 6 of the 11 observations (see Table 4.3). For the other observations, the S/N is too low to detect the Zeeman signatures in Stokes V. For the observation taken on 23 October 2014, the "null" polarization is not consistent with 0 (see Table 4.3). The "null" polarization is a check for spurious

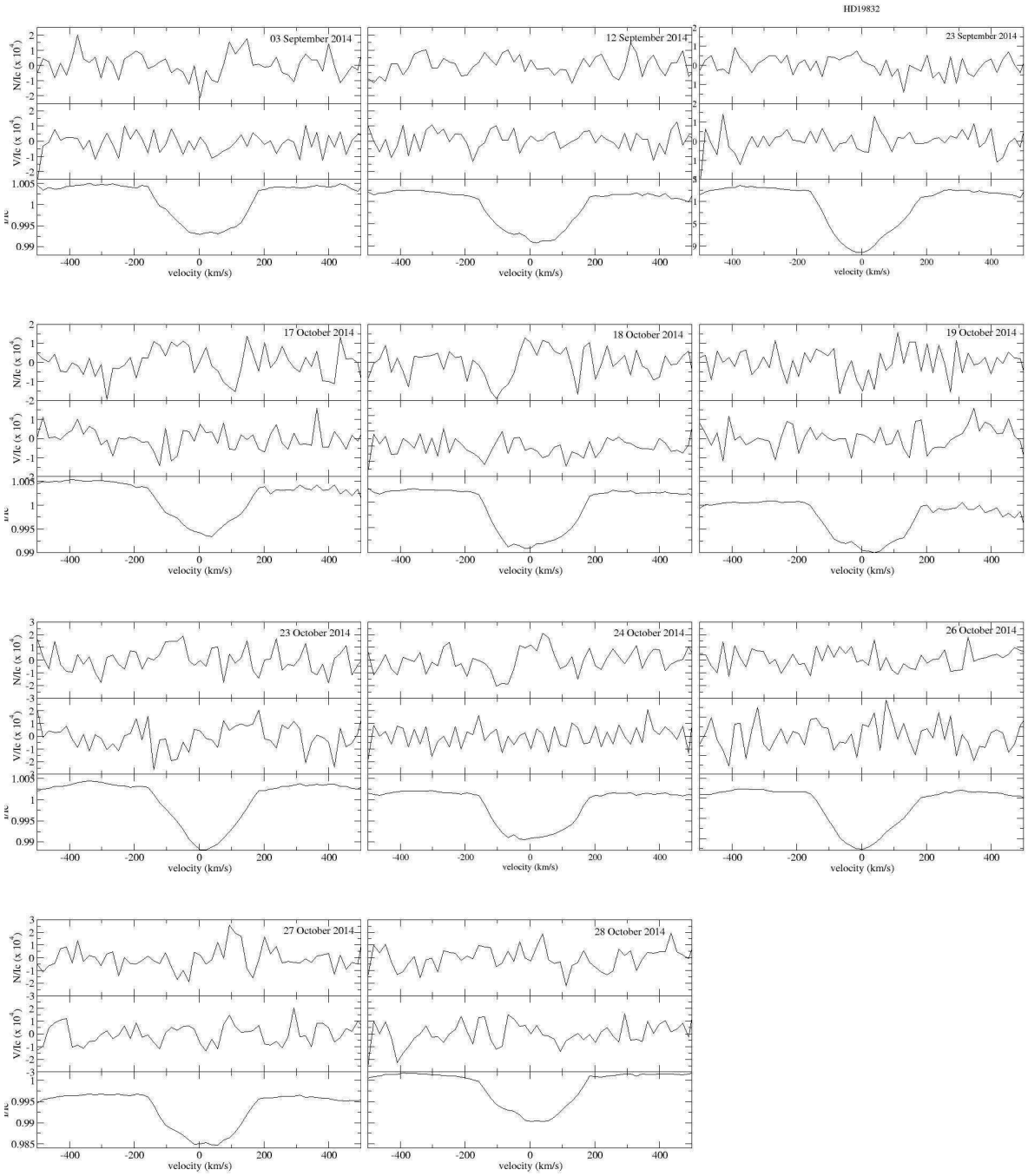

FIGURE 4.3: **LSD profiles for HD19832:** LSD Stokes I profiles (bottom), Stokes V (top), and null N profiles for each observation.

signature, that is why I do not consider the result of this night to determine the dipolar magnetic field in Sect. 4.3.1 below.

4.2.3 HD22470

Due to bad weather, I obtained only 3 observations of the Ap star HD22470 (see Table 4.4).

The final mask for HD22470 contains 666 lines. For all nights, I have a clear Zeeman signatures in the Stokes I profiles (see Fig. 4.4). These signatures appear rather complex, probably due to the presence of strong chemical spots visible as deformations in the I profiles. However, 3 observations is not enough to determine the dipolar magnetic field of HD22470 with an oblique dipolar model and only an estimate using $B_{l,max}$ will be possible (see Sect. 4.3.4).

TABLE 4.4: **Journal of observations of HD22470 :** The columns list the date, the heliocentric Julian dates (HJD) at the middle of the observations (2450000+), the exposure time, the mean S/N of the Stokes V profiles, the detection status, the longitudinal magnetic field and its error, and the "null" polarization and its error.

date	MHJD	Times	S/N	Detect.	$B_l \pm \sigma B_l$	$N \pm \sigma N$
30 Oct. 14	6961.511	4 × 175	8187	DD	-868.5 ± 97.3	4.6±78.6
31 Oct. 14	6962.537	4 × 175	9435	DD	1575.4 ± 132.4	-16.0 ± 84.0
11 Jan. 15	7034.314	4 × 175	6394	DD	-602.9 ± 118.5	103.4 ± 102.5

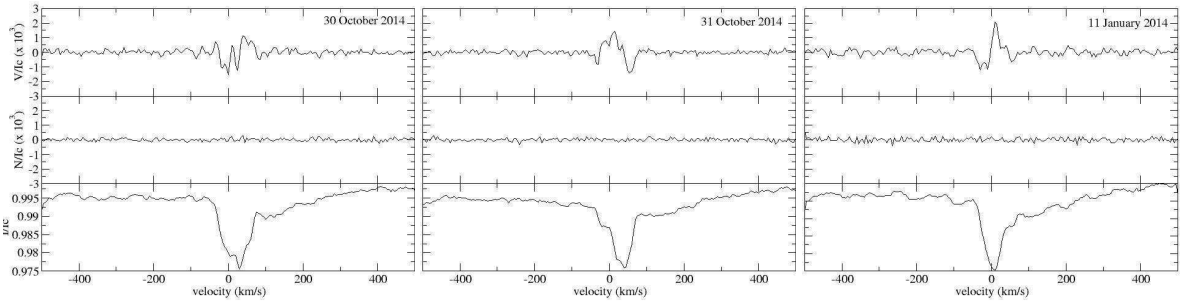

FIGURE 4.4: **LSD profiles for HD22470:** LSD Stokes I profiles (bottom), Stokes V (top), and null N profiles for each observation.

4.2.4 HD28843

HD28843 was observed 11 times (see Table 4.5). The mask of HD28843 contains only 376 lines because, due to the high $v \sin i$ some spectral lines are not visible in the spectra. However, due to bad weather, the S/N is too low to detect a magnetic field. HD28843 is a fast rotator (see Table 4.1) therefore, to increase the S/N, instead of using the default spectral bin of 1.8 $\mathrm{km\,s^{-1}}$ of Narval, I used a step of 9 $\mathrm{km\,s^{-1}}$. Despite that, I cannot clearly detect the signature of the magnetic field of HD28843 in the Stokes V profiles (see Table 4.5 and Figure 4.5). The mask of HD28843 contains 376 lines.

Some observations (e.g. Oct. 17) nevertheless seem to indicate the possible presence of a field. Better data will be required for this star.

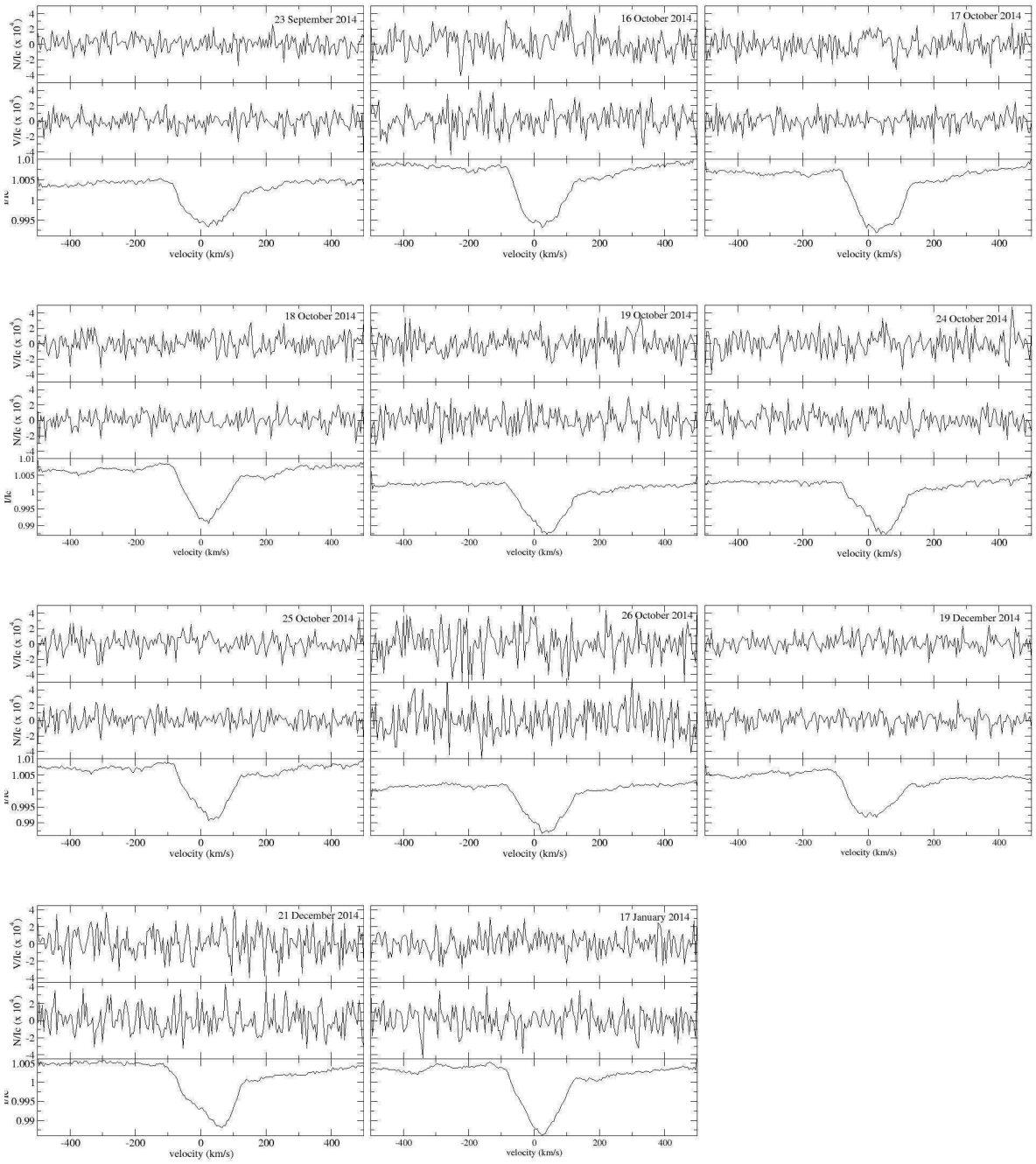

FIGURE 4.5: **LSD profiles for HD28843:** LSD Stokes I profiles (bottom), Stokes V (top),S and null N profiles for each observation.

TABLE 4.5: **Journal of observations of HD28843** The columns list the date, the heliocentric Julian dates (HJD) at the middle of the observation (2450000+), the exposure time, the mean S/N of the Stokes V profiles, the detection status, the longitudinal magnetic field and its error bar, and the "null" polarization and its error bar.

date	MHJD	T_{exp}	S/N	Detect.	B$-l$ $\pm\sigma$B$_l$	N $\pm$ σN
23 Sep. 14	6924.706	4 × 260	8859	ND	31.3 ± 180.5	-161.7 ± 177.4
16 Oct. 14	6947.668	4 × 260	5971	ND	50.7 ± 195.6	-213.8 ± 196.3
17 Oct. 14	6948.531	4 × 260	8353	ND	-12.4 ± 151.2	-84.7 ± 151.8
18 Oct. 14	6949.649	4 × 260	8271	ND	59.2 ± 173.8	-58.1 ± 173.8
19 Oct. 14	6950.601	4 × 260	6505	ND	209.3 ± 213.1	194.6 ± 212.6
24 Oct. 14	6955.568	4 × 260	7135	ND	-38.4 ± 186.3	78.9 ± 187.1
25 Oct. 14	6956.618	4 × 260	8330	ND	253.5 ± 161.9	-25.9 ± 159.1
26 Oct. 14	6957.465	4 × 260	4952	ND	654.3 ± 288.2	-66.4 ± 283.9
19 Dec. 14	7011.346	4 × 260	8875	ND	217.2 ± 175.8	349.8 ± 178.8
21 Dec. 14	7013.328	4 × 260	6034	ND	-208.1 ± 192.9	93.1 ± 193.0
17 Jan. 14	7040.356	4 × 260	6982	ND	97.8 ± 148.2	-138.7 ± 175.3

4.2.5 HD32650

For HD32650, I obtained only 4 observations, however this star was observed 5 times by Aurière et al. (2007) with Narval in 2007. I can thus use all 9 observations.

The final LSD mask contains 522 lines. I have 4 definite detections, 2 marginal detections and 3 non detections. The longitudinal magnetic is weak, it is between 20 and 70 G (see Table 4.6).

TABLE 4.6: **Journal of observations of HD32650:** The columns list the date, the heliocentric Julian dates (HJD) at the middle of the observations (2450000+), the exposure time, the mean S/N of the Stokes V profiles, the detection status, the longitudinal magnetic field and its error bar, and the "null" polarization and its error bar.

date	MHJD	T_{exp}	S/N	Detect.	B$_l$ $\pm\sigma$B$_l$	N $\pm$ σN
27 Oct. 14	6958.638	4 × 225	9332	ND	48.2 ± 26.8	-6.6 ± 26.7
30 Oct. 14	6961.446	4 × 225	8527	ND	39.0 ± 29.7	23.4 ± 29.8
19 Dec. 14	7011.322	4 × 225	9707	DD	32.4 ± 24.2	-24.2 ± 23.4
10 Jan. 15	7033.565	4 × 225	9778	DD	69.9 ± 22.5	36.0 ± 22.4
Archival data						
11 Mar. 07	4171.342	4 × 800	12854	DD	31.4 ± 13.4	-7.2 ± 13.4
12 Mar. 07	4172.390	4 × 800	11621	MD	24.5 ± 17.3	-20.2 ± 18.0
13 Mar. 07	4173.344	4 × 800	14323	DD	53.2 ± 10.2	-1.0 ± 10.1
14 Mar. 07	4174.385	4 × 800	12148	ND	23.7 ± 14.0	0.7 ± 13.6
15 Mar. 07	4175.378	4 × 800	11852	MD	26.7 ± 20.4	17.6 ± 20.4

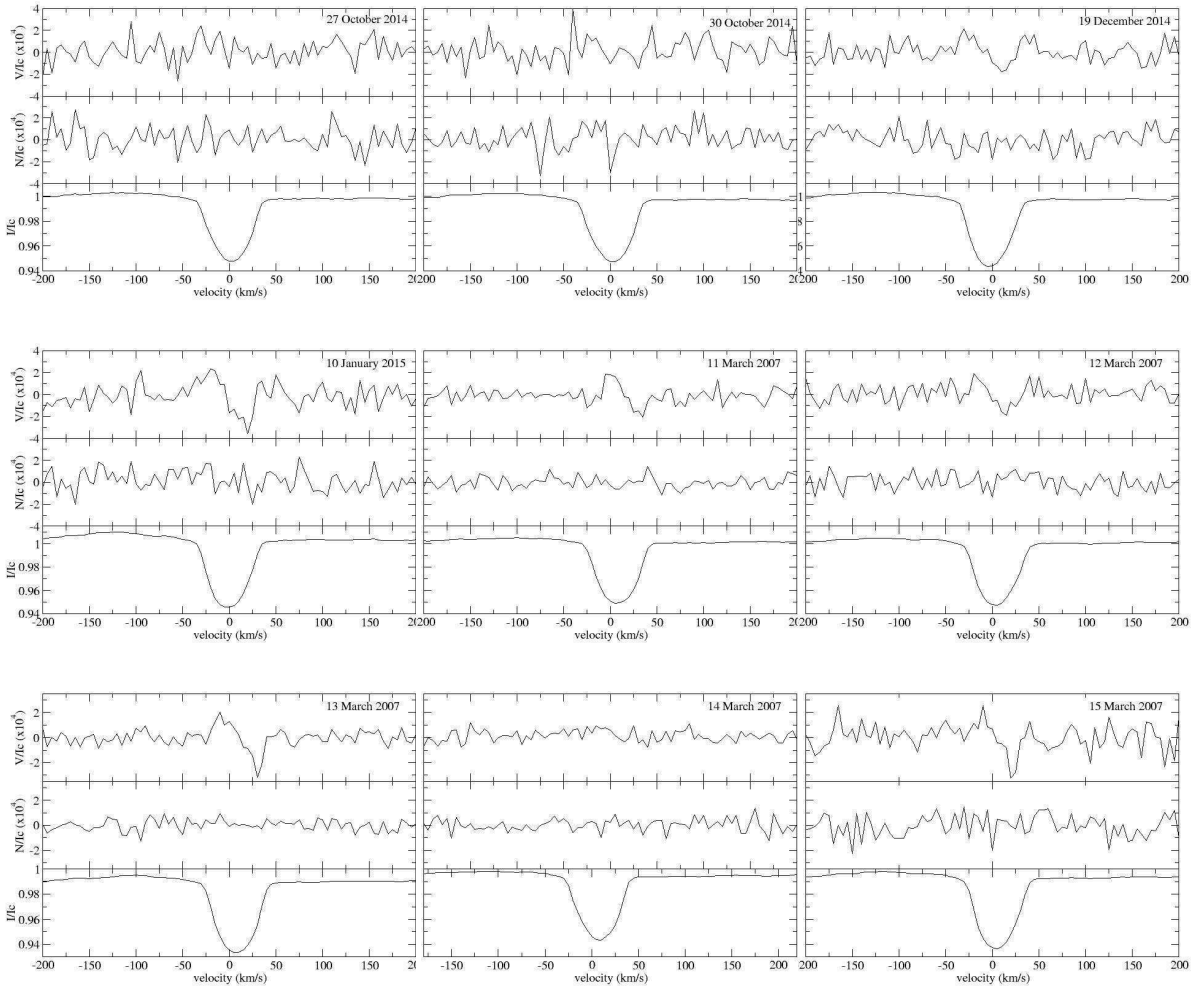

FIGURE 4.6: **LSD profiles for HD32650**: the LSD Stokes I profiles (bottom), Stokes V (top), and null N profiles for each observation.

4.2.6 HD96707

HD96707 is the coolest star of the sample, it is a F0p star. Aurière et al. (2007) obtained marginal detections of a magnetic field in this star. So, it is an interesting target to constraint the upper limit of the magnetic desert.

The LSD mask contains 3687 lines. I obtained definite detections for all 6 observations and clear Zeeman signatures in the Stokes V profiles (see Fig. 4.7). The longitudinal magnetic field of HD96707 is the weakest detected in this study. It is between -45 G and 35 G (see Table 4.7). The shape of the intensity profiles varies (see Fig. 4.7) due to chemical spots at the surface of HD96707, and this also produces structures in the Stokes V signatures.

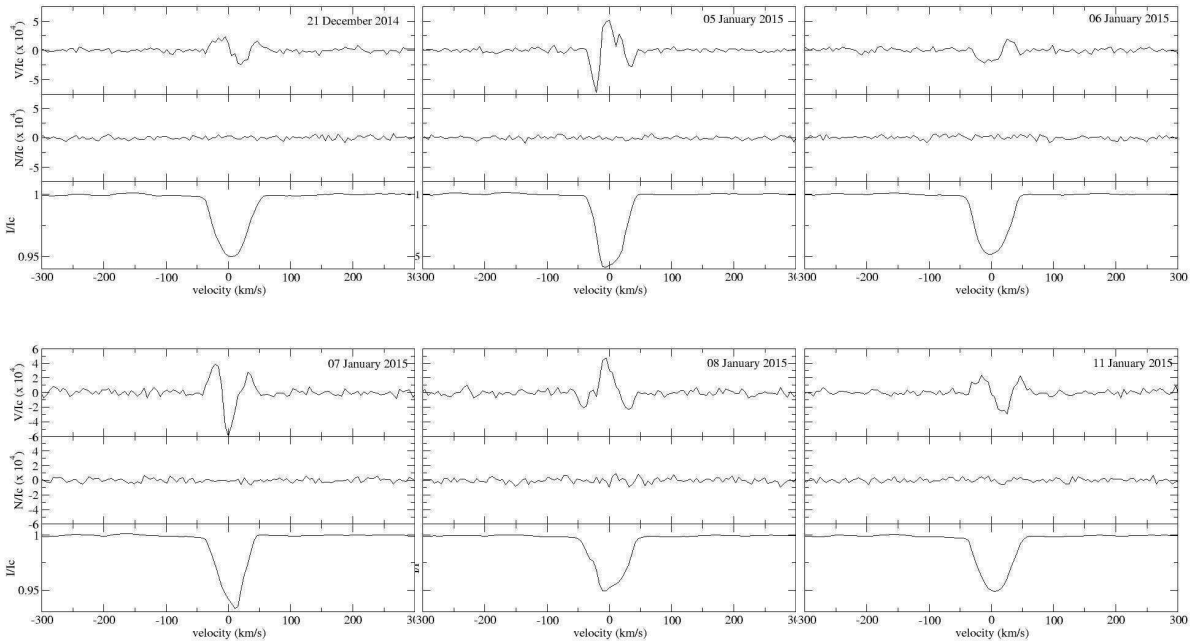

FIGURE 4.7: **LSD profiles for HD96707**: the LSD Stokes I profiles (bottom), Stokes V (top), and null N profiles for each observation.

TABLE 4.7: **Journal of observations of HD96707** The columns list the date, the heliocentric Julian dates (HJD) at the middle of the observations (2450000+), the exposure time, the mean of the Stokes V profiles, the detection status, the longitudinal magnetic field and its error bar, and the "null" polarization and its error bar.

date	MHJD	T_{exp}	S/N	Detect.	$B_l \pm \sigma B_l$	$N \pm \sigma N$
21 Dec. 14	7013.657	4 × 375	29406	DD	35.8 ± 7.7	2.6 ± 2.6
05 Jan. 15	7028.708	4 × 375	32142	DD	-30.1 ± 6.9	7.3 ± 6.9
06 Jan. 15	7029.696	4 × 375	27333	DD	-45.1 ± 8.6	-1.5 ± 8.5
07 Jan. 15	7030.662	4 × 375	29153	DD	27.8 ± 7.3	5.0 ± 7.3
08 Jan. 15	7031.654	4 × 375	27611	DD	4.1 ± 8.2	6.2 ± 8.2
11 Jan. 15	7034.687	4 × 375	30996	DD	29.1 ± 7.1	0.8 ± 7.1

4.3 Dipolar magnetic field

To characterize the dipole components of the magnetic fields of the sample stars for which we have enough high-quality B_l measurements (HD19832, HD32650, HD96707), I use the oblique rotator model (see section 2.10). This model provides a good first approximation of the large scale magnetic field of Ap stars. Each phased longitudinal field variation B_l was then fit using a sine fit of the form:

$$B_l = B_0 + B_1 \times sin(2\pi(x + \phi_d)) \tag{4.2}$$

Considering a tilted, centered magnetic dipole, we derived the surface polar field strength B_d from the variation of the longitudinal magnetic field B_l with rotational phase ϕ using

Preston (1967) relation:

$$B_d = B_{l,max}\left(\frac{15+u}{20(3-u)}cos\beta cosi + sin\beta sini\right)^{-1} \tag{4.3}$$

where u is the limb-darkening, β is the magnetic obliquity angle, and i the inclination.

$$tan\beta = \frac{1-r}{1+r}coti, \tag{4.4}$$

where $r = (|B_0| - B_1)/(|B_0| + B_1)$

We have determined the inclination i for each of our stars assuming rigid rotation:

$$sini = \frac{P_{rot}vsini}{50.6R}, \tag{4.5}$$

where P_{rot} is the rotational period in days, $v \sin i$ is the projected rotational velocity in $\mathrm{km\,s^{-1}}$, and R is the stellar radius in solar units.

4.3.1 HD19832

To plot the longitudinal magnetic field of HD19832 as a function of phase, I use the rotational period of 0.7278893 d from Stepien & Czechowski (1993) (see Figure 4.8). The dipolar fit (see Equation 4.2) resulted in B_0=-43 ± 76 G and B_1=611 ± 103 G. A quadrupolar fit to the phase-folded data only shows an insignificant departure from the dipolar fit.

Using the period of 0.727893 d, I can determine the inclination angle of the star i by using the $v \sin i$ of 110 $\mathrm{km\,s^{-1}}$ and the radius of 2.1 $R_\odot$ (Babu & Shylaja 1981). I obtained an inclination of 49°.

Using the dipolar fit to the longitudinal field measurements and the inclination angle i, I can deduce the obliquity angle β= 85°.

In addition, from the dipolar fit to the longitudinal field values and the angles i and β determined above, I can estimate the polar field strength. I found that B_{pol} is between 1522 and 3350 G.

4.3.2 HD32650

I used the period of 2.7347 d (Adelman 1997) and plotted the longitudinal magnetic field of HD32650 as a function of phase (see Fig. 4.10). The dipolar fit is compatible

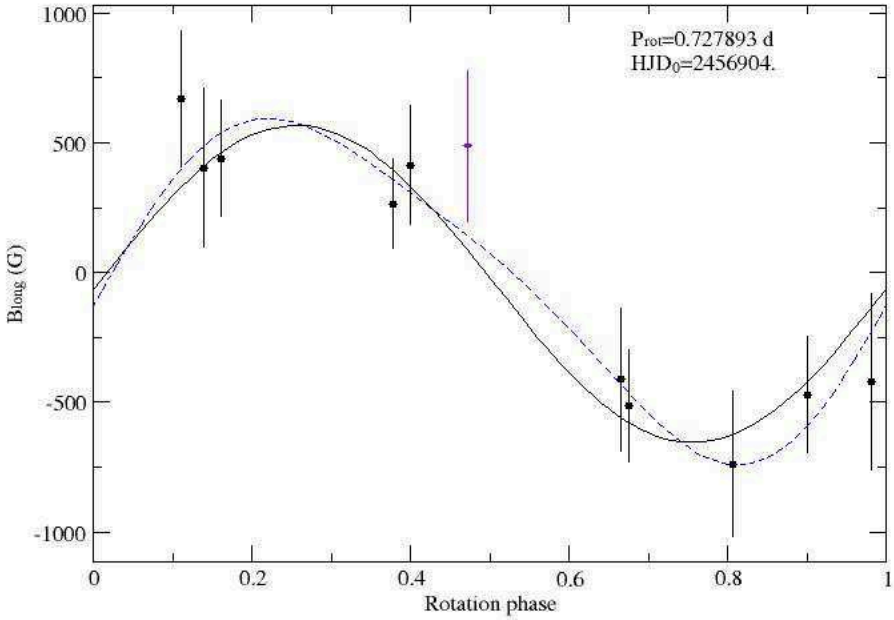

FIGURE 4.8: **Rotational modulation of the longitudinal magnetic field of HD19832**: the black points correspond to the longitudinal magnetic field values with their error bars. The purple point correspond to an observation with a non-null N, which is discarded. The black curve correspond to the best fit for a dipole and the dash blue curve is the best fit for a quadrupole.

with the measured weak longitudinal magnetic field values, however the error bars are large. I obtained B_0=-36 ± 4 G and B_1=14 ± 5 G.

Using the period of 2.7347 d, I can determine the inclination angle of the star i by using the $v \sin i$ of 30 km s^{-1} and the radius of 2.7 R$_\odot$. I obtain an inclination of 37°. I can then deduce the obliquity angle β= 28°. Finally, from the dipolar fit to the longitudinal field values and the angles i and β determined above, I can estimate the polar field. I found that $B_{\rm pol}$ is between 177 and 351 G.

4.3.3 HD96707

I used the period of 3.515 d (Aurière et al. 2007) and plotted the longitudinal magnetic field of HD96707 as a function of phase. The phase-folded field measurements show a clear sinusoidal behavior, as expected from a dipolar field model (see Figure 4.10). For the dipolar fit, I found that B_0=-36 ± 4 G and B_1=14 ± 5 G. A quadrupolar fit to the phase-folded data only shows an insignificant departure from the dipolar fit.

Using the period of 3.515 d, I can determine the inclination angle i of the star by using the $v \sin i$ of 42 km s^{-1} and the radius of 3.2 R$_\odot$. I obtained an inclination of 40° with this inclination angle i, I deduced the obliquity angle β= 79°. In addition, from the dipolar fit to the longitudinal field values and the angles i and β, I can estimate the

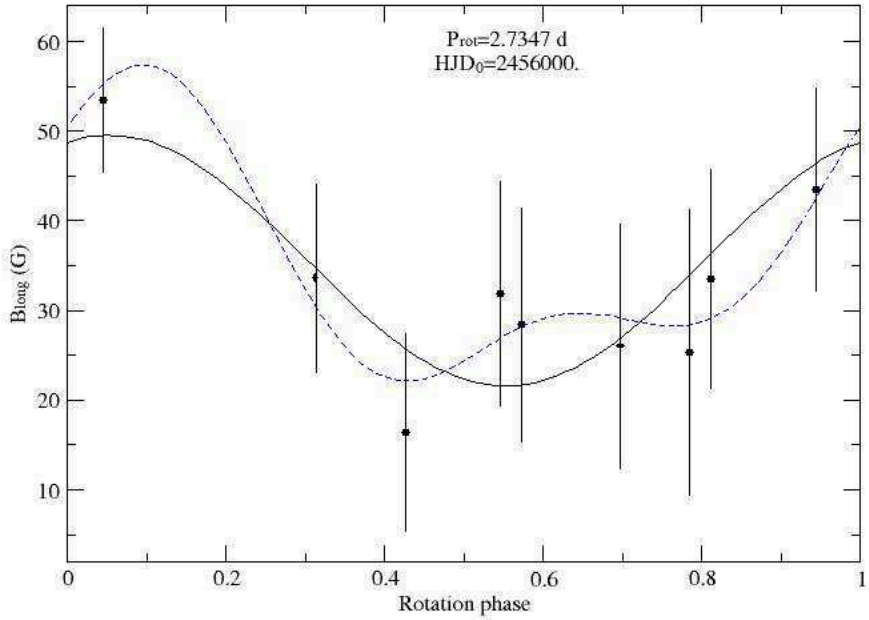

FIGURE 4.9: **Rotational modulation of the magnetic field of HD32650**: the black points correspond to the longitudinal magnetic for all observations. The black curve correspond to the best fit for a dipole and the dash blue curve is the best fit for a quadrupole

polar field. I found that B_{pol} is between 114 and 210 G, which is weaker than the values derived by Aurière et al. (2007).

4.3.4 HD22470

Even if I do not have enough observations to determine the dipolar magnetic field from an oblique dipole fit, I can determine a lower limit of the dipolar magnetic field. If we consider Equation 4.2, we see that:

$$B_d \geq \frac{20(3-u)}{15+u} B_{l,max} \tag{4.6}$$

For a typical limb darkening of Ap/Bp stars (u$\approx$ 0.5), we obtain:

$$B_d \geq 3.23 B_{l,max} \tag{4.7}$$

For HD22470, $B_{l,max}$ is 1575.4 $\pm$ 132.4 G, so the dipolar magnetic field $B_d \geq$ 4762 G . This lower limit of the dipolar magnetic field is higher than to the one predicted by the correlation of Aurière et al. (2007) for the rotational period of 0.6785 days (Borra et al. 1983). Therefore, this star is not useful for constraining the $B_c \propto \Omega$ relation.

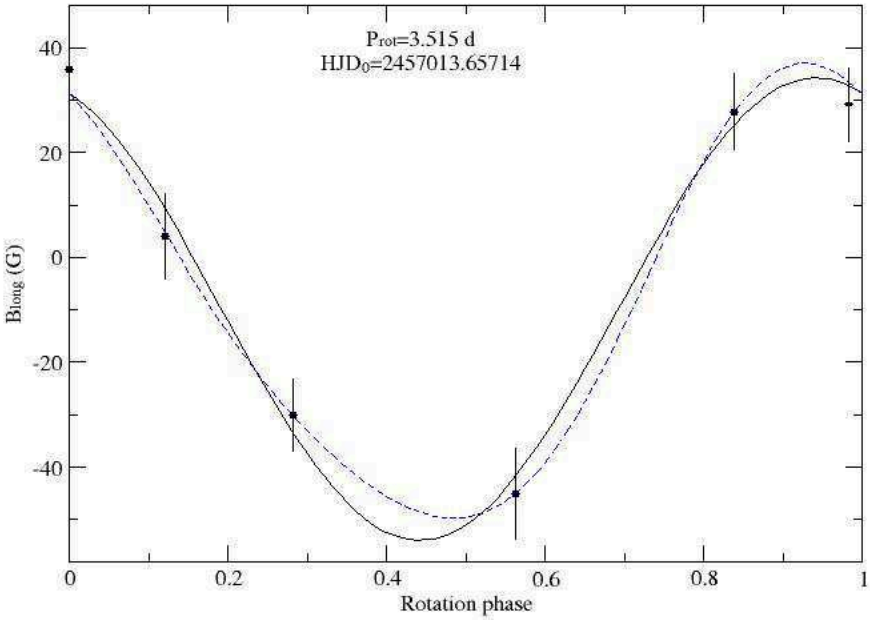

FIGURE 4.10: **Rotational modulation of the longitudinal magnetic field of HD96707**: the black points correspond to the longitudinal magnetic field values with their error bars for all observations. The black curve corresponds to the best fit for a dipole and the dash blue curve is the best fit for a quadrupole.

4.3.5 HD28843

The signature of the magnetic field of HD28843 is hidden in the noise of the spectra. To evaluate the maximum strength of this magnetic field, I used the same method as for ζ Ori Ab (see Section 3.6.2).

I required a 90% detection rate to consider that the field would statistically be detected. This translates into an upper limit for the undetected dipolar field strength for each spectrum, which varies between ∼19000 and ∼36000 G (see Fig. 4.11).

Since 11 spectra are at our disposal, statistics can be combined to extract a stricter upper limit taking into account that the field has not been detected in any of the 9 observations (see Neiner et al. 2015a). The final upper limit derived from this combined probability for HD28843 for a 90% detection probability is ∼6000 G (see thick line in Fig. 4.11). As a consequence, the magnetic field of HD28843 is less than 6000 G. This large upper limit is not constraining for our purpose. Reobserving this star in the future with a higher S/N would be useful.

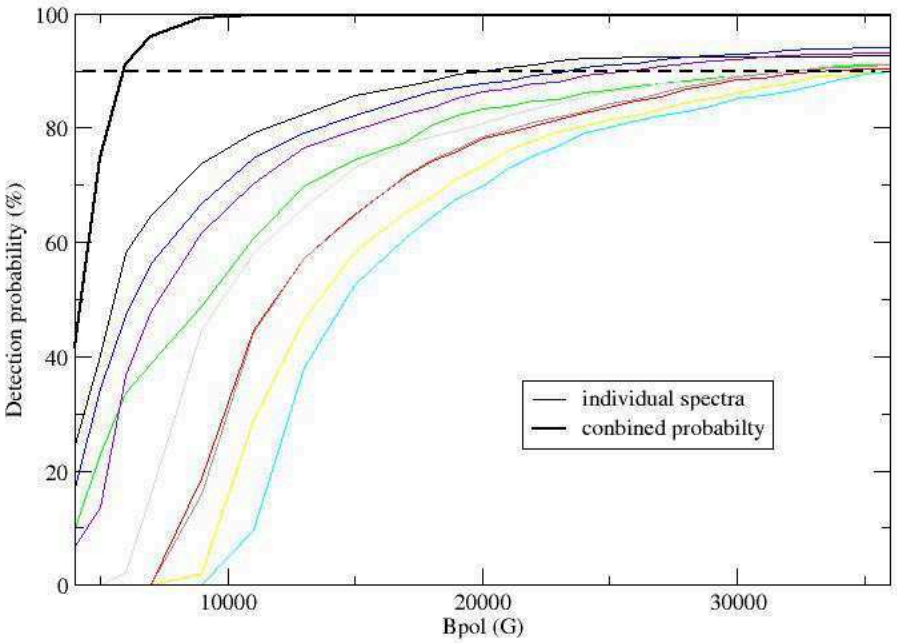

FIGURE 4.11: **Upper limit on the non-detected magnetic field in HD28843:** Detection probability of a magnetic field in each spectrum of HD28843 (thin color lines) as a function of the magnetic polar field strength. The horizontal dashed line indicates the 90% detection probability, and the thick black curve (top left corner) shows the combined probability.

4.4 Conclusion

On the 7 targets of the observational program, I was able to determine the dipolar magnetic field B_d for 3 stars: HD19832, HD32650 and HD96707. Due to bad weather, I do not have data for HD12767 and I do not have enough data for HD22470, so only a lower limit on B_d could be derived. In addition HD12477 is a triple system. To determine the dipolar magnetic field of the Ap star, I would need to disentangle the spectra of its components. For HD28843, the S/N of the Stokes V profiles is not sufficient to detect Zeeman signatures and only an upper limit of its dipolar field could be computed. For this star, new observations are needed with a better S/N to detect the magnetic field and add constraints to the upper limit of the magnetic desert for the fast rotators.

On Fig. 4.12, the dipolar magnetic field of HD32650 and HD96707 are lower than the limit predicted by Aurière et al. (2007). However, we need to determine the dipolar magnetic field of more Ap/Bp stars to improve this limit.

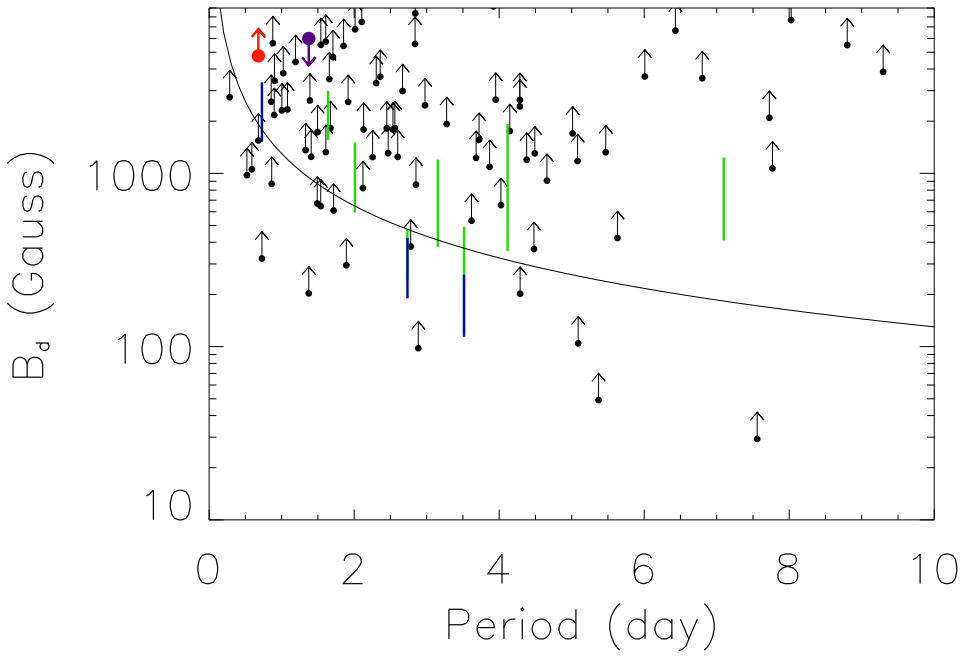

FIGURE 4.12: Relation between the field strength and the rotation of Ap stars from data published in the literature and derived here. The black arrows correspond to the lower limit of the dipolar strength in measuring the maximum longitudinal field. In green are the dipolar magnetic fields determined by Aurière et al. (2007) and in blue are the ones determined in this study. The red arrow correspond to the lower limit of the dipole strength for HD22470 and the purple arrow to the upper limit of the dipolar strength for HD28843. The black curve is a $B_c \propto \Omega$ relation.

Part II

Ultra-weak magnetic fields

Chapter 5

The magnetic field of normal stars

As I mentionned in the introduction (see Sect. 1.4), until recently the only type of magnetic fields known in hot stars were the strong magnetic fields, with a longitudinal field strength above 100 G (Aurière et al. 2007; Wade et al. 2014b) associated with a quite simple and stable topology (e.g, Lüftinger et al. 2010; Silvester et al. 2014).

In 2009, a longitudinal magnetic field much weaker than any previous detection in hot stars has been measured in the normal A star Vega (Lignières et al. 2009; Petit et al. 2010). The measurement leads to a longitudinal magnetic field value less than 1 Gauss. This field is much weaker than the lower limit of $\sim$ 100 G of the strong magnetic fields. Some scenarios was developed to explain the dichotomy between strong and weak magnetic fields (Aurière et al. 2007; Braithwaite & Cantiello 2013). They predict that the new kind of weak magnetic field exists in all hot stars that do not host a strong magnetic field (see Sect. 1.4). Vega may thus well be the first confirmed member of a new family of magnetic stars: the weakly magnetic hot stars.

The motivation to progress on this topic is strong because the discovery of a new, potentially widespread class of weakly magnetic A stars offers important new information about the dichotomy between strong and weak magnetic fields in tepid stars. In an attempt to interpret this division, Aurière et al. (2007) proposed a scenario based on the stability of a large scale magnetic configuration in a differentially rotating star, leading to estimating a critical field strength above which magnetic fields can remain stable on long time scales, while magnetic fields below this limit would likely be destroyed by the internal shear. More detailed models including 2D and 3D numerical simulations (Gaurat et al. 2015; Jouve et al. 2015) tend to confirm the existence of a critical field in such configurations, where the pre-main sequence contraction is a possible way to force differential rotation. On the other hand, the magnetic dichotomy might simply be the result of two different magnetic field generation processes. Braithwaite & Cantiello (2013) proposed that Vega-like magnetic stars are the result of the slow evolution of magnetic configurations characterized by weak initial magnetic helicity and argue that it should be widespread among most intermediate-mass and massive stars. Meanwhile, Ferrario et al. (2009) proposed that the small fraction of strong magnetic fields could be produced in early stellar merging events.

Studying stars with the same precision as Vega can confirm or disprove the prediction of the scenarios to explain the dichotomy and bring constraints for these theories. In particular, studying the weakly magnetic hot stars can help us to understand the origin and the properties of this kind of magnetism.

5.1 Vega

5.1.1 Introduction

Vega is a normal bright A0V star (V=0.03). Since it is often used as a standard star, it is well studied and its spectral and stellar parameters are thus well known. It is a fast rotator, however due to its inclination ($i \sim 7^o$) its $v \sin i$ is low: $v \sin i$ =22 km s^{-1} (Takeda et al. 2008). Its temperature is T_{eff}=9519 K and its log g is 3.88. Due to the flattening at the pole, T_{eff} increases from the pole to the equator. In this study, we have taken the temperature of the pole as a reference for T_{eff}.

The longitudinal magnetic field of Vega is very weak (less than 1 Gauss) and the magnetic map of the surface of Vega obtained thanks to Zeeman-Doppler Imaging technique (ZDI, Petit et al. 2010) revealed a magnetic spot concentrated around the rotational pole of Vega with a strength of about 7 G (Petit et al. 2014a).

Böhm et al. (2015) found temporal variabilities with a period similar to the rotational period of Vega. This rotational modulation reveals the existence of spots on the surface of Vega close to the equator. These spots can have different explanations: they can be chemical spots or magnetic spots (like the ones of the Sun). However, due to the high rotational velocity, the atmosphere of Vega is not stable enough to generate chemical spots. Therefore, the weak magnetic field of Vega is a likely explanation for this spot. This confirms the finding of the ZDI map, which shows weak magnetic spots close to the equator. The magnetic field of Vega is more complex than the one of the strongly magnetic stars.

In addition,Butkovskaya et al. (2011) found a long periodic variation of Vega, with a period of 21 years, by measuring the equivalent width and the flux density of various lines. This variability may also be due to the weak magnetic field of Vega, for example if it undergoes a magnetic cycle. Studying the evolution of the magnetic field of Vega over several years can help us to understand the origin of this variability.

5.1.2 Observations

The data were obtained with the spectropolarimeters Narval and ESPaDOnS and were collected in the polarimetric mode measuring Stokes V (circular polarization). Vega was observed over several years: 2008, 2009, 2010, 2011, 2014, and 2015 (see Table 5.1), to determine if its magnetic field changes over the years. Due to a mechanical problem on one rhomboedra, the data taken on 21 and 22 August 2011 are not exploitable in

TABLE 5.1: **Journal of observations :**the columns correspond to the year of observations, the mean heliocentric julian days (2450000+), the spectropolarimeter used to acquire the data, and the number of sequence and exposure time.

year	MHJD	Instrument	T_{exp} (s)
2008	4675.0	Narval	278 × 4 × 6
2009	5084.8	ESPaDOnS	322 × 4 × 4
2009	5048.5	Narval	238 × 4 × 6
2010	5403.2	Narval	410 × 4 × 13
2011	5786.7	Narval	227 × 4 × 13
2014	6853.7	Narval	316 × 4 × 13
2015	7250.5	Narval	120 × 4 × 12

polarization. This unfortunately corresponds to 42% of the total data gathered that year.

5.1.3 Data Analysis

In the absence of any detectable polarized signatures in individual spectral lines of Vega, I applied the LSD procedure (see Sect. 2.5.2) to each spectrum. The line list is extracted from the VALD atomic data base (Kupka & Ryabchikova 1999; Piskunov et al. 1995) using the respective effective temperature and log g of Vega. This line list is extracted using $T_{\rm eff}$=10000K and log g=4.0. I rejected the lines whose depth is less than 1% of the continuum and the lines blended with the hydrogen lines. The final mask contains 1041 lines.

Due to the weakness of the signatures of the magnetic field on Vega, we co-added the observations taken each year to reach a high S/N ratio. To coadd the LSD profiles, I weighted each individual spectra proportionally to its squared S/N:

$$w_i = S/N_i^2 / \sum_{i=0}^{n} S/N_i^2$$

where w_i and S/N_i are the weight and S/N of the i^{th} spectrum.

I renormalized the yearly averaged spectra with the continuum task of IRAF, because the automatic spectral normalization of Libre ESprit is not sufficiently precise. If the continuum is not very flat, it can influence the LSD profiles.

I obtained a definite detection of a magnetic field for the yearly averaged profiles of 2008, 2009, and 2010 (see Table 5.2). For these years, the FAP is less than 3.603×10^{-6}. For 2011 and 2014, I obtained marginal detections (see Table 5.2) with a FAP of $\sim 3\times10^{-5}$. Due to the low S/N in the Stokes V profiles (see Table 5.2), I obtained a non-detection for 2015 with a detection probability of ∼50% and a FAP of 4.791×10^{-1}. Nevertheless, a Stokes V signature is visible every year (see Fig. 5.1) When comparing the results

obtained for each year, I find no significant variability in the Zeeman signatures in the Stokes V profiles (see Fig. 5.1). The magnetic field of Vega seems stable over the years of observations. Thanks to the center-of-gravity method (Semel et al. 1993), I calculated the longitudinal magnetic field for each yearly averaged profile using a mean Landé Factor of 1.27 and a mean wavelength of 500 nm corresponding to the normalization of the LSD profiles. The 6 values of the longitudinal magnetic field are coherent, with a precision of 0.2-0.5 G (see Table 5.2).

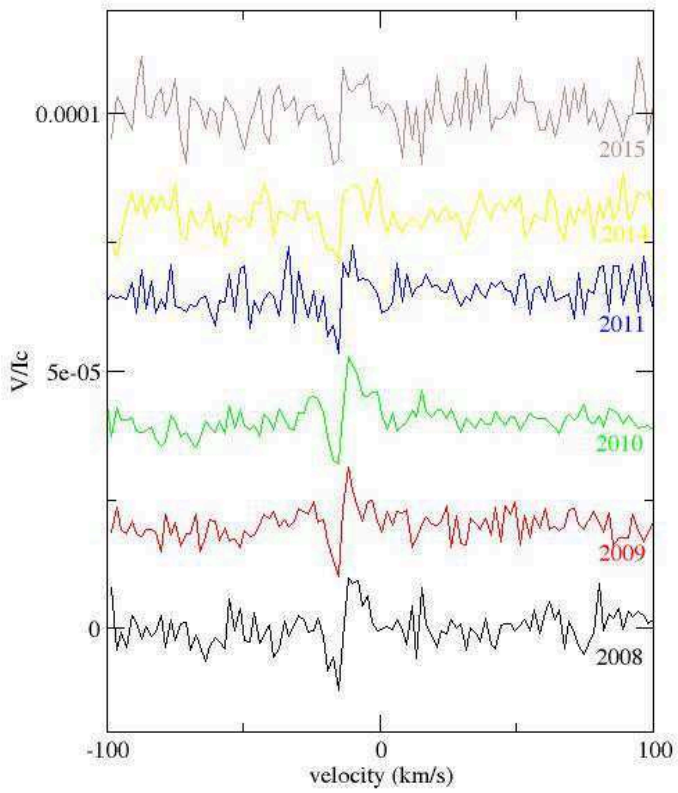

FIGURE 5.1: **Yearly average Stokes V LSD profiles:** in black for 2008, in red for 2009, in green for 2010, in blue for 2011, in yellow for 2014, and in brown for 2015.

This stability of the magnetic field of Vega is in agreement with the scenario that explains the dichotomy between strong and weak fields, which argues that the origin of the weak field is the same as the strong fields, i.e. it is a fossil origin and not a dynamo origin.

Butkovskaya et al. (2011) find variation in the intensity of the lines of Vega with a period of 21 years. I compared the depth of the intensity LSD profiles for each year. No significant variability is detected in the intensity LSD profiles (see Fig. 5.2) between 2008-2015, contrary to Butkovskaya et al. (2011)'s claim. Even if the observations did not cover the full period of 21 years, if I follow the modulation of the lines found by Butkovskaya et al. (2011), the depth of the intensity profiles should decrease between 2008 and 2011 and increase between 2011 and 2015. I do not observe this behaviour in the intensity LSD profiles (see Fig. 5.2).

However, the LSD technique can influence the shape of the intensity profiles. To further check if there is a variation in the depth of the lines of Vega, I compared the depth of

TABLE 5.2: **Longitudinal magnetic field of Vega:** the columns correspond to the year of observations, the mean S/N of the Stokes V profile, the detection status, the longitudinal magnetic field and its error bar, and the "null" polarization and its error bar

years	S/N	Detection	$B_l \pm \sigma B_l$	N$\pm\sigma$N
2008	332658	DD	-0.5 ± 0.3	-0.2 ± 0.3
2009	495451	DD	-0.1 ± 0.2	0.3 ± 0.2
2010	549236	DD	-0.3 ± 0.2	0.0 ± 0.2
2011	270685	MD	-0.3 ± 0.3	-0.3 ± 0.3
2014	368568	MD	-0.2 ± 0.3	0.2 ± 0.3
2015	223964	ND	0.0 ± 0.5	-0.3 ± 0.5

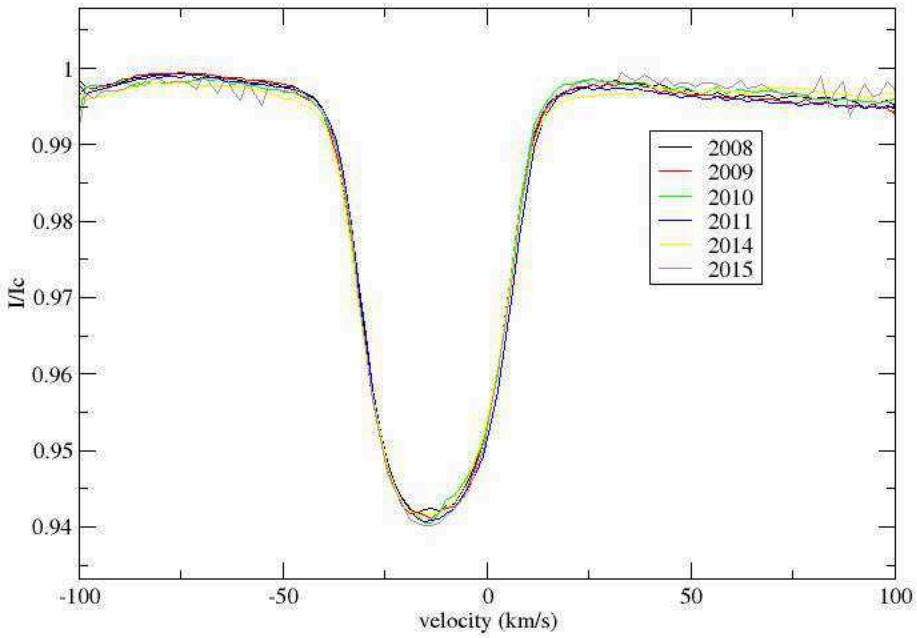

FIGURE 5.2: **Yearly averaged Stokes I LSD profiles:** in black for 2008, in red for 2009, in green for 2010, in blue for 2011, in yellow for 2014 and in brown for 2015.

the individual lines used by Butkovskaya et al. (2011), i.e. Fe at 516.7 nm and Mg at 518.3 nm for each year of observations(see Fig. 5.3).

For the Fe line at 516.9 nm Butkovskaya et al. (2011) found between their observations in 2008 and 2010 a depth variation of $\sim$ 6% and for the Mg line at 518.3 nm a depth variation of 3%. I found no significant variability in these two lines (see Fig. 5.3). For the Fe line at 516.9 nm I obtained a depth variations of 4% however this variations did not follow the behavior predicted by Butkovskaya et al. (2011). The deepest Fe line is the one of 2015 instead of the one of 2011. The Fe line for the other years of observations

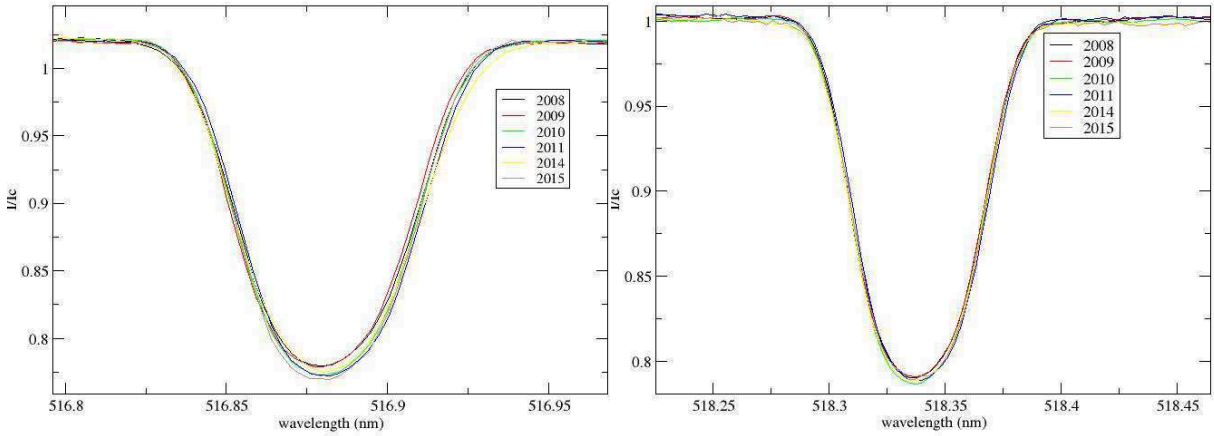

FIGURE 5.3: **Intensity of the Fe line at 518.3nm (left) and Mg line at 518.3 nm (right)** in black for 2008, in red the one for 2009, in green for 2010, in blue for 2011, in yellow for 2014, and in brown 2015.

seems to follow the variability predicted by Butkovskaya et al. (2011). For the Mg line at 518.3 nm, the variation is $\sim 1.5\%$.

5.1.4 Conclusion

I did not find long-term variability in the magnetic field of Vega, nor in its intensity LSD profiles. However, the observations did not cover the whole period found by (Butkovskaya et al. 2011), we should to observe again Vega during the next years.

The stability in the magnetic field of Vega is in favor of a fossil origin of the field, as predicted by the scenarios to explain the dichotomy. These scenarios are based on a common origin of strong and weak magnetic fields, but during the evolution the magnetic field distribution splits into two distinct families.

5.2 UZ Lyn

5.2.1 Introduction

It is probable that Vega is the first detection of a new type of magnetic stars among intermediate-mass stars. The scenarios to explain the dichotomy (Aurière et al. 2007; Braithwaite & Cantiello 2013) predict that this kind of ultra-weak fields exists in all stars that do not host a strong magnetic field. Confirming that this new type of magnetism is common among intermediate-mass stars will provide important constraints on the magnetic field of a typical intermediate-mass star. Compared to strong fossil

magnetism, which only concerns a small fraction of stars, such constraints would have a strong impact for stellar evolution models. It is therefore important to perform deep spectropolarimetric studies of chemically normal A stars to determine if ultra-weak magnetic fields are typical of A stars. It is however challenging, due to the high S/N required to detect these weak fields and thus the large amount of observing time spent per target. As a consequence, we need to carefully choose the targets for such studies.

One good target for this study is UZ Lyn. UZ Lyn is a bright star and it is a long-period spectroscopic binary (Lehmann et al. 2003) with an orbital period of 3.6 years. The primary is a normal A2V star with a temperature $T_{\rm eff}$=9310±100 K and log g=4.1 ± 0.1 (Lehmann et al. 2003). Therefore, its stellar parameters are close to the ones of Vega. UZ Lyn is only slightly cooler than Vega. The spectral type of the secondary component is not known, but Lehmann et al. (2003) estimated its mass to 0.46 $M_{\odot}$. The chemical abundances of the primary are close to the solar ones (Caliskan & Adelman 1997; Lehmann et al. 2003), like for Vega (Takeda et al. 2008).

UZ Lyn is thus a good target to test if ultra-weak magnetic fields like the one of Vega are common in normal A-star type or if Vega is a peculiar case.

5.2.2 Observations

UZ Lyn was observed 39 times with the Narval spectropolarimeter in circular polarization mode during semester 2013B, 6 times during semester 2014A, and 20 times during semester 2014B, in the frame of a program to search for ultra-weak magnetic fields in A stars (PI: F. Lignières), for a total of 65 observations. UZ Lyn was also observed twice in the frame of the Binarity and Magnetic Interactions in various classes of Stars (BinaMIcS) project (a project to study the magnetic field of close binaries, PI: E. Alecian, see Neiner et al. 2015a) with Narval (PI: C. Neiner). I thus have a total of 67 observations.

5.2.3 Data Analysis

I ran the LSD technique (see Sect. 2.5.2) on the individual spectra using a line mask corresponding to the temperature and log g of the primary. The mask contains 879 lines after removing the hydrogen lines, the lines blended with the hydrogen lines and the ones that I did not see in the spectra. I used a velocity bin of 5.4 km s^{-1} to improve the S/N and to have around 20 velocity bins in the line profile.

The S/N of the individual Stokes V profiles is around 30000-40000 except for some nights during which the weather was not good enough. This S/N is not high enough to detect a Zeeman signature in the individual LSD profiles, therefore I co-added the spectra taken on the same night, when possible, to improve the S/N. I obtained non-detections for the nightly-averaged LSD profiles, expect for the observation taken on 12 October 2013. For this night I obtained a marginal detection with a detection probability of 99.03% inside the stellar lines and a detection probability of 25% outside the stellar lines. The

TABLE 5.3: **Journal of observations of UZ Lyn:** the columns contain the date for each Stokes V sequence, the heliocentric Julian date corresponding to the middle of the observation time (2450000+), the number of sequences and the exposure time per individual subexposure, and the averaged S/N in the individual LSD Stokes V pseudo-line profile (± rms when there are multiple sequences).

Date	Mid-HJD	T_{exp} (s)	S/N
03sep13	6539.691	1 × 4 × 143	24873
22sep13	6558.657	3 × 4 × 500	46608 ± 927
23sep13	6559.665	3 × 4 × 500	49436 ± 1130
06oct13	6572.625	1 × 4 × 500	47405
07oct13	6573.559	3 × 4 × 500	48997 ± 318
08oct13	6574.650	3 × 4 × 500	49426 ± 215
09oct13	6575.665	3 × 4 × 500	41608 ± 3156
10oct13	6576.578	3 × 4 × 500	32903 ± 4231
10oct13	6576.704	1 × 4 × 500	19500
12oct13	6578.662	3 × 4 × 500	47701 ± 1870
16oct13	6582.667	3 × 4 × 500	32970 ± 3064
31oct13	6597.642	3 × 4 × 500	22991 ± 1867
16dec13	6643.694	3 × 4 × 500	31682 ± 3159
17dec13	6644.571	2 × 4 × 500	37376 ± 6483
10jan14	6668.539	3 × 4 × 500	27265 ± 12724
11jan14	6669.506	3 × 4 × 500	48026 ± 1696
09apr14	6757.312	1 × 4 × 500	48722
12apr14	6760.327	1 × 4 × 500	46993
13apr14	6761.323	1 × 4 × 500	46835
14apr14	6762.363	1 × 4 × 500	40022
15apr14	6763.331	1 × 4 × 500	45904
16apr14	6764.325	1 × 4 × 500	46634
19oct14	6950.677	3 × 4 × 500	32193 ± 4993
24oct14	6955.653	2 × 4 × 500	43413 ±19
26oct14	6957.620	3 × 4 × 500	42245 ± 577
03dec14	6995.461	3 × 4 × 500	37767 ± 2837
05jan15	7028.571	3 × 4 × 500	43081 ± 604
06jan15	7029.568	3 × 4 × 500	43046 ± 182
11jan15	7030.564	3 × 4 × 500	32834 ± 4061

result of the nightly-averaged LSD profiles on 12 October 2013 is shown in Fig. 5.4. The signature is more prominent on the blue side of the line profile (see Fig. 5.4).

Using the centre-of-gravity method (Rees & Semel 1979) with a mean wavelength of 500 nm and a mean Landé factor of ∼ 1.234 corresponding to the normalization parameters used in the LSD, I calculated the longitudinal field value (B_l) corresponding to these Zeeman signatures over the velocity range [-50:50] km s^{-1}. The measured longitudinal magnetic field is -4.3 ± 4.2 G. The Null polarization is 5.2 ± 4.1 G for the night of 12 October 2013.

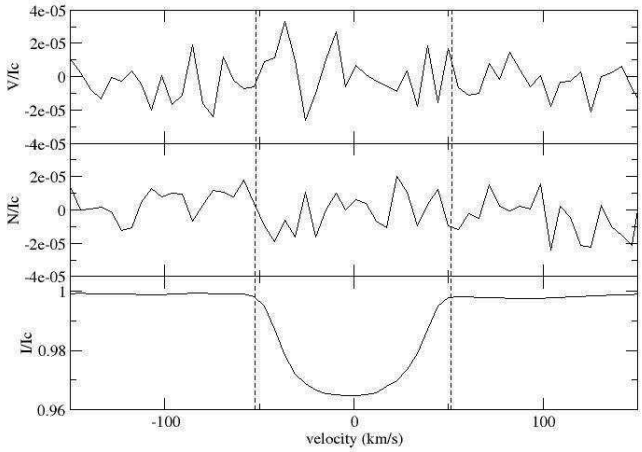

FIGURE 5.4: **The LSD profiles of UZ Lyn for 12 October 2013:** in Stokes I (bottom), V (top) and N (center).

For the other nightly-averaged LSD profiles, the detection probability is between 5% and 88% inside the stellar lines, which corresponds to a non-detection. Therefore, on 36 nights of observations, I obtained one marginal detection and 35 non-detections.

To improve the S/N further, I co-added all LSD profiles, even the ones with a low S/N because they have a low influence in the grand-average profile due to their low weight. Due to the binary, the radial velocity changes over the observations. To co-add the LSD profiles, I thus realigned the LSD profiles on the same radial velocity. To know the radial velocity of the observation, I fitted the core of the intensity profile by a Gaussian.

At first, I only had the data taken during the semester 2013B. In the mean Stokes V LSD profiles of all the data taken in 2013B, a signature seemed to emerge from the noise in the profiles in the same velocity range as the intensity profile. However it is not significant: the detection probability of a signal inside the stellar line is 98.4% which is not sufficient for a formal detection. We require a detection probability of 99% for a marginal detection and 99.99% to claim a definite detection.

To known if UZ Lyn is magnetic or not, I needed more data to increase the S/N, that is why we observed UZ Lyn again in 2014A and 2014B. When I added the data taken during the semester 2014A, the detection probability decreased (67%) and when I co-added all the observations up to 2014B the detection probability decreased even more and I obtained a detection probability of 46%, which corresponds to a non-detection. The LSD profiles are presented in Fig. 5.5. The measured longitudinal magnetic field is 1.0 ± 1.0 G over the integration domain [-54:54] $\mathrm{km\,s^{-1}}$, with a mean Landé factor of 1.25 and a mean wavelength of 500 nm. The achieved precision is however not sufficient to detect a magnetic field like the one of Vega.

However, I co-added data taken at random rotational phases and I thus lost the phase information. If this method worked for Vega, it is because Vega is seen pole-on and has a polar magnetic spot, so the same hemisphere is observed all the time. For UZ Lyn,

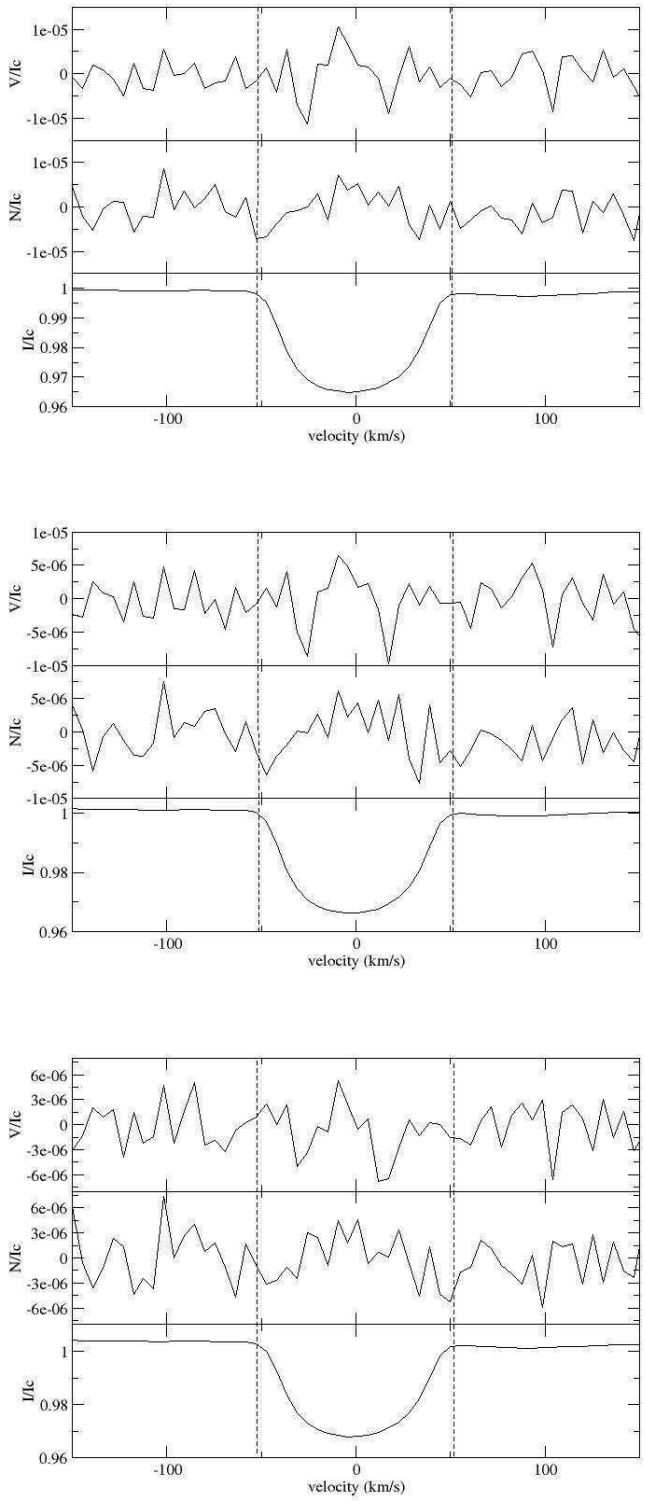

FIGURE 5.5: **Co-added LSD profiles of UZ Lyn:** for the observations of semester 2013B (top), of semesters 2013B and 2014A (center), and all observations (bottom).

the inclination is not known. Even if UZ Lyn hosts an ultra-weak field, the Zeeman signatures are not visible in the nightly-averaged LSD profiles because of the too low

S/N and the addition of LSD profiles taken at different phases can destroy the Zeeman signature since the signature shape changes along the rotational phase. So, I cannot exclude that the longitudinal magnetic field has been averaged out over the stellar surface and over the rotation.

A non-detected dipolar magnetic field could have remained hidden in the noise of the grand average LSD profile. To know the upper limit of its strength, I used the same method as for ζ Ori Ab (see Sect. 3.6.2). If a magnetic field exists on the surface of UZ Lyn, its strength is less than $\sim$ 145 G (see Fig. 5.6)

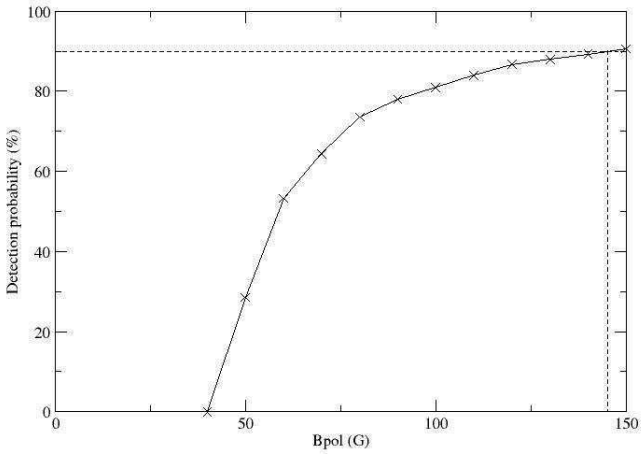

FIGURE 5.6: **Upper limit of the non-detected magnetic field of UZ Lyn :** Detection probability of a magnetic field in the grand average profile of UZ Lyn as a function of the magnetic polar field strength. The horizontal dashed line indicates the 90% detection probability.

5.2.4 Conclusions

I suspected that UZ Lyn is a magnetic star. I obtained a marginal detection for one nightly-averaged LSD profiles and the grand average LSD profile of the 2013B data seems to show a signature in the Stokes V profile as well. However, this signature disappears when I add the new observations of 2014A and 2014B. The data were taken at random rotational phases and I cannot exclude that the longitudinal magnetic field has been averaged out over the stellar rotation when performing the average

In the future it will be important to observe UZ Lyn again to confirm or disprove the magnetism of this star, by changing the observational strategy: take more data on the same night to avoid serious phase smearing and improve the S/N of the nightly-averaged LSD profiles.

Moreover, the achieved precision (1 G) of the grand average LSD profile obtained by co-adding all observations is not sufficient to detect an ultra-weak magnetic field like the one of Vega. Therefore, it would be useful to obtain the future observations on a

bigger telescope, i.e. with ESPaDOnS at CFHT rather than Narval at TBL. However, read-out time will quickly dominate the exposure time and the S/N will be limited in all cases by the duration of the night.

5.3 B stars

5.3.1 Introduction

The different scenarios to explain the dichotomy between strong and weak magnetic fields (Aurière et al. 2007; Braithwaite & Cantiello 2013) predict that weak magnetic fields exist in the ∼90% of massive stars that do not host a strong magnetic field, younger stars should have stronger fields, and faster rotators have stronger fields. These scenarios apply to all hot stars, not only to A stars. Therefore, I have set up an observational program to search for Vega-like magnetism in B stars. For both theories, there is a lack of observational constraints. The aims of this observational program are to determine whether or not weak Vega-like magnetic fields exist in stars hotter and more massive than A-type stars, and to provide observational constraints to differentiate between theories to explain the bifurcation of strong and weak magnetic fields.

Two previous studies were performed to try to find a weak magnetic field in two B stars: γ Peg (Neiner et al. 2014b), which is a very bright B2IV star, and ι Her (Wade et al. 2014b), which is a bright B3IV star. Neither study detected a magnetic field in spite of reaching an accuracy of 0.4 G for γ Peg and 0.3 G for ι Her. The precision they reached is thus similar to that used for the field detection in A stars. However, to check the detectability of Vega-like fields in early B stars, Wade et al. (2014b) compared the observations of ι Her with synthetic Stokes V profiles corresponding to the surface magnetic maps of Vega (Petit et al. 2010) but computed for the spectral characteristics of ι Her and a range of inclination angles and (Neiner et al. 2014a) did the same for γ Peg. In these studies they concluded that it is unlikely we would have detected a magnetic field identical to the one of Vega on γ Peg or ι Her with the achieved precision. To detect a magnetic field like the one of Vega on γ Peg and ι Her, we need a precision around 0.1 G.

The aim of this project is thus to determine whether weak magnetic fields exist in B stars by increasing the number of stars in which this has been tested in addition to the two B stars mentioned above and by reaching a very high signal-to-noise ratio, with high-resolution spectropolarimetric data. The detection of ultra-weak magnetic fields in B stars is challenging, therefore the targets must be carefully selected.

5.3.2 Choice of targets

I chose bright potential targets with a magnitude in the V band below 4 and low $v \sin i$ ($v \sin i < 50$ km/s) and I excluded those that are in a binary system. I found 7 potential targets observable with Narval that correspond to these criteria. I plan to reach an

accuracy of 0.3 G, i.e. a precision similar to the one used for the field detection of the Vega, for the late-B stars because the stellar parameters of the late-B stars are close to the one of A-type stars, and 0.1 G for the early B stars as discussed above.

In addition, I added ι her and γ Peg on the list of targets. The precision of 0.3-0.4 G reached so far makes it impossible to detect a magnetic field like the one of Vega on these stars. To make sure I can detect such a field, I plan to observe again the early B stars ι Her and γ Peg with an accuracy of 0.1 G. Whatever the results of this study, they will provide important qualitative and quantitative constraints on current ideas about the magnetic desert (absence of magnetic stars with a longitudinal magnetic field between 1 G and 100 G). If we detect weak magnetic fields in B stars, we will support the theoretical prediction and provide new observational constraints to improve these theories. If we do not detect weak magnetic fields in B stars, we will need to develop new theories to explain why this kind of magnetic fields exist in A stars and not in B stars, and why only $\sim$7% of hot stars are strongly magnetic.

The field detection limit that can be reached for a star depends on several parameters: the peak S/N of the data, the projected rotational velocity of the star (the uncertainty scales approximately as $(v \sin i)^2$), and the number of lines available in the spectra that can be used in the LSD technique to extract the average Zeeman signature, i.e. the spectral type of the star. Therefore, I have tailored the exposure times to meet the required field limit for each star. For all stars, the required time is more than one night (1 night=7 hours for Narval). I eliminated the potential targets for which the required time is more than 1 week of observations. In the end, I have 5 possible targets including ι Her and γ Peg (see Table 5.4).

TABLE 5.4: **Parameters of the possible targets:** the columns contain the name of the stars, the spectral type, the magnitude, the projected rotational velocity, and the required exposure time

Star	Sp. Type	V_{mag}	$v \sin i$ (km s^{-1})	T_{exp}
γ Crv	B8III	2.58	33	259272
γ Peg	B3IV	3.8	6	40392
ι Her	B2IV	2.83	3	54320
μ Lep	B9IV	3.29	18	28231
θ Aql	B9.5IV	3.22	47	114492

5.3.3 Observations

The observational strategy was to observe the stars over consecutive nights to avoid serious phase smearing. However, due to the fact that the weather was variable at the Pic du Midi Observatory, this strategy was not fully applied (see Table 5.5).

Only, ι Her and γ Peg have been observed so far with the Narval spectroplarimeter. For ι Her I have a total of 38 observations and for γ Peg, a total of 83 observations (see Table 5.5)

TABLE 5.5: **Journal of observations of the B stars:** the columns contain the name of the star, the date for each Stokes V sequence, the heliocentric Julian date corresponding to the middle of the observation time, the number of sequences and the exposure time per individual subexposure, and the averaged S/N in the individual LSD Stokes V pseudo-line profile (± rms).

Star	Date	Mid-HJD	T_{exp} (s)	S/N
ι Her	09 March 2015	7091.681	06 × 4 × 280	11744 ± 973
ι Her	14 April 2015	7127.489	05 × 4 × 280	7159 ± 1586
ι Her	05 June 2015	7179.490	16 × 4 × 280	13244 ± 273
ι Her	06 June 2015	7180.429	11 × 4 × 280	13337 ± 373
γ Peg	31 October 2015	7327.489	26 × 4 × 120	17748 ± 1486
γ Peg	01 November 2015	7328.412	33 × 4 × 120	15124 ± 3760
γ Peg	10 November 2015	7337.340	18 × 4 × 120	16129 ± 476
γ Peg	11 November 2015	7338.290	6 × 4 × 120	16551 ± 375

5.3.4 ι Her

ι Her is a bright B3IV star (V=3.80). The spectral lines of ι Her are sharp, its $v \sin i$ = 6 ± 1 km s^{-1} (Nieva 2013)), indicating that ι Her is either a slow rotator or a fast rotator seen pole-on. The stellar parameters of ι Her are well known thanks to many spectroscopic studies of this star (e.g. Lefever et al. 2010; Nieva 2013). The effective temperature and log g of ι Her are respectively 17500 ± 200 K and 3.80 ± 0.05 (Nieva 2013).

ι Her is a slowly pulsating B-type star with a period of ∼3.5 days (Chapellier et al. 2000). ι Her is also a single-lined spectroscopic binary system. The period of the binary is estimated to ∼ 113 days and the mass of the secondary is estimated to 0.4 $M_\odot$ (Chapellier et al. 2000).

As mentionned above, ι Her was already observed with the ESPaDOnS spectropolarimeter by Wade et al. (2014b). They reached a precision of 0.32 G by co-adding all their observations. This precision is close to the one obtained for Vega but they did not detect an ultra-weak magnetic field in ι Her. However, they demonstrated that due to the spectral characteristics of ι Her, the precision required to detect a magnetic field like the one of Vega is 0.1 G. That is why, I observed ι Her again with the Narval spectropolarimeter with the aim to reach a precision of 0.1 G.

I ran the LSD technique (see Sect. 2.5.2) on the individual spectra with a mask adapted to the temperature and log g of ι Her. I removed the hydrogen lines, the lines blended with the hydrogen lines, and the ones that I did not observe in the spectra. The final mask contains 381 lines. As a comparison, the mask used by Wade et al. (2014b) contains only 130 lines. Therefore, since with I have more lines in my mask than in the mask of Wade et al. (2014b), I improve the S/N of the LSD profiles.

As expected, I did not obtain a detection of a Zeeman signature in the Stokes V profiles of the individual observations, the S/N (see Sect. 5.5) is not enough to detect a weak magnetic field. Therefore, I applied the same method as for e.g. Vega : I co-added all

the LSD profiles to obtain a grand-average LSD profile (shown in Fig. 5.7). Due to the binarity and the pulsations of the star, the radial velocity change over the observations. To co-add the LSD profiles, I realigned the LSD profiles on the same radial velocity. To this aim, I fitted the core of the individual intensity profile by a Gaussian to deduce the radial velocity. The mean S/N on the grand-average profile is 782669. At the radial velocity of the intensity line, a signature seems to emerge from the noise, however it is not statistically significant. The detection probability of a signal inside the stellar line is ∼86%, it is not sufficient to have a detection. Moreover outside the stellar line the detection probability is ∼89%. As a consequence, I conclude that I did not obtain a detection of a magnetic field in ι Her. Thanks to the center-of-gravity method (Semel et al. 1993), and using a mean Landé factor of 1.6 and a mean wavelength of 500 nm, I nevertheless calculated the longitudinal magnetic field over the velocity range of [32:0] $\mathrm{km\,s^{-1}}$, B_l=-0.6 ± 0.3 G with a null polarization of 0.0 ± 0.3 G. This measurement is not null but remains below 3σ.

Due to bad weather during semester 2015A, not all observations planned to reach the accuracy of 0.1 G were gathered. The S/N of the observed spectra is thus lower than expected. To compensate for this problem, I used the archival data of ι Her (PI: G. Wade) taken with the ESPaDOnS spectropolarimeter in 2012.

I ran the LSD technique with my own mask on the ESPaDOnS data and I co-added the LSD profiles. The S/N of this average Stokes V profile for ESPaDOnS is similar to the one of the Narval data : 76295. In this grand-average Stokes V profile, a signal similar to the one obtained with the data taken with Narval is visible at the radial velocity of the stellar line (see Fig. 5.7). However, the detection probability inside the stellar line is ∼ 53%, which is lower than the one of the average profile of the Narval data. I calculated the longitudinal magnetic field, B_l=-0.1 ± 0.3 G with a null polarization of -0.6 ± 0.3 G. This measurement is compatible with 0.

Finally, I co-added all Narval and ESPaDOnS profiles. The final S/N of this grand-average Stokes V profile is 109304. The detection probability of a signal inside the stellar line is ∼74%, corresponding to a non-detection. I calculated the longitudinal magnetic field, B_l=-0.2 ± 0.2 G with a null polarization of -0.1 ± 0.2 G. This measurement is compatible with 0.

I then estimated the upper limit on the non-detected dipolar magnetic field which could have remained hidden in the noise of the grand-average LSD profile, using the same method as for ζ Ori Ab (see Sect. 3.6.2). If a magnetic field exists on the surface of ι Her, its strength is less than ∼ 54 G (see Fig. 5.8)

5.3.5 γ Peg

γ Peg is a bright B2IV star (V=2.83) and a variable star of β Cephei type (Handler et al. 2009). Like ι Her, γ Peg has a low $v \sin i$ close to 0 $\mathrm{km\,s^{-1}}$ (Telting et al. 2006) and it is either a slow rotator or a fast rotator seen pole-on. The effective temperature and log g of γ Peg are respectively 20454 K and 3.79 (Prugniel et al. 2011).

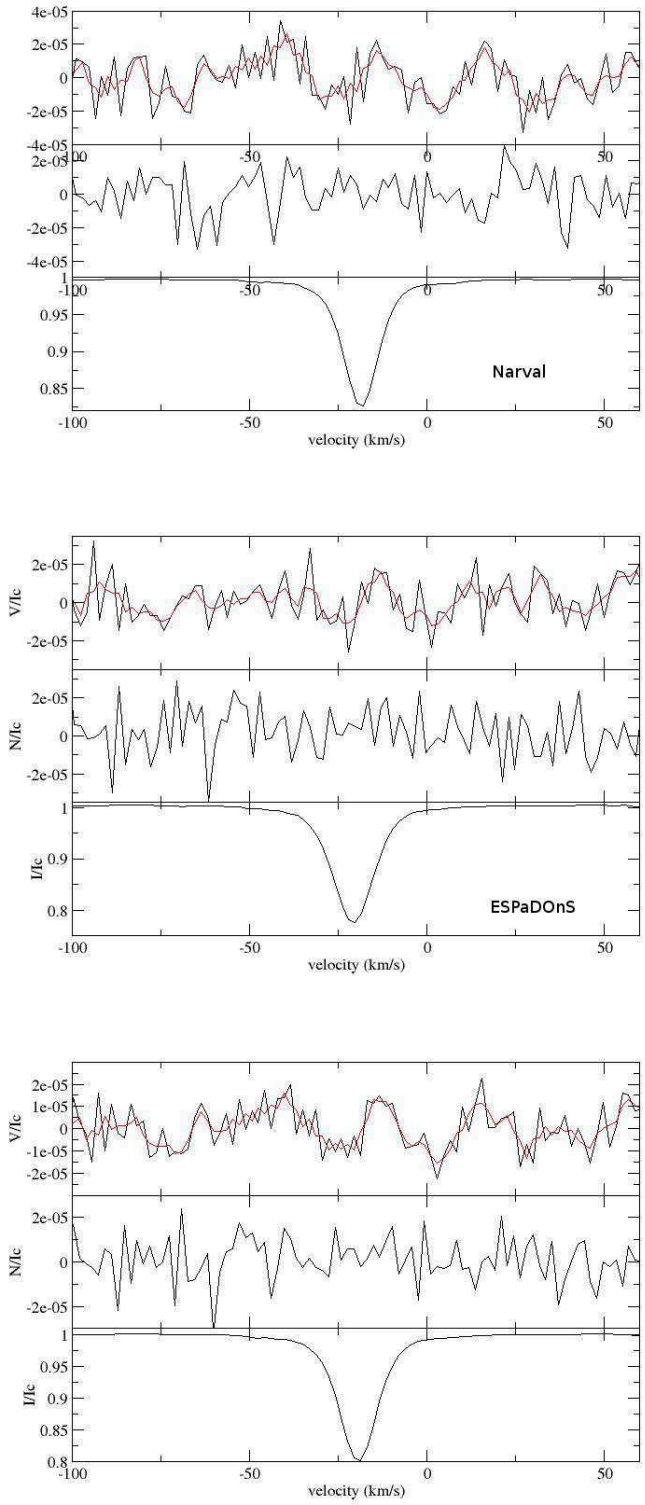

FIGURE 5.7: **The LSD profiles of ι Her:** on the top the averaged LSD profile of the data taken in 2015, on the center the averaged LSD profile of the data taken in 2012 and on the bottom the grand-averaged LSD profile of all data.

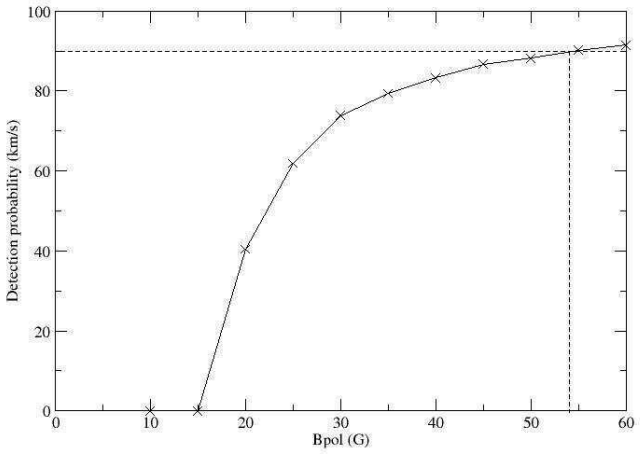

FIGURE 5.8: **Upper limit of the non-detected magnetic field of ι Her:** Detection probability of a magnetic field in the grand average profile of ι Her as a function of the magnetic polar field strength. The horizontal dashed line indicates the 90% detection probability.

A deep spectropolarimetric study of γ Peg was performed by Neiner et al. (2014b) using Musicos and Narval data. They reached a precision of 0.4 G. However, Neiner et al. (2014a) demonstrated that due to the spectral characteristics of γ Peg, to detect a magnetic field like the one of Vega on γ Peg, the required precision is 0.1 G. That is why, I observed γ Peg again with the Narval spectropolarimeter in 2015. I planned to reach a precision of 0.1 G.

I ran the LSD technique (see Sect. 2.5.2) on the individual spectra with the same mask as used by Neiner et al. (2014b). This mask contains 1012 lines.

As expected, in the Stokes V profiles of the individual observations, no signature is detected. Therefore, I applied the same method as above, I co-added all the LSD profiles to obtain an averaged LSD profile (shown in Fig. 5.9). Due to the pulsations, the radial velocity of γ Peg changes over the observations. I fitted the core of the intensity profile by a Gaussian to measure the radial velocity to realign the LSD profiles on the same velocity. Then, I co-added the LSD profiles. The mean S/N on the Stokes V of the averaged profile is 144011. At the radial velocity of the intensity line, a signature seems to emerge from the noise, however it is not statistically significant. The detection probability of a signal inside the stellar line is $\sim$55%, it is not sufficient to have a detection, even though outside the stellar line the detection probability is $\sim$2%.

As a consequence, I do not get a detection of a magnetic field in γ Peg. Thanks to the center-of-gravity method (Semel et al. 1993) and using a mean Landé factor of 1.23 and a mean wavelength of 500 nm corresponding to the normalization parameters used in the LSD, I calculated the longitudinal magnetic field, B_l=-0.6 $\pm$ 0.3 G with a null polarization of 0.1 $\pm$ 0.3 G over the velocity domain [-20,20] km s^{-1}. This measurement is not null, but also not above 3σ.

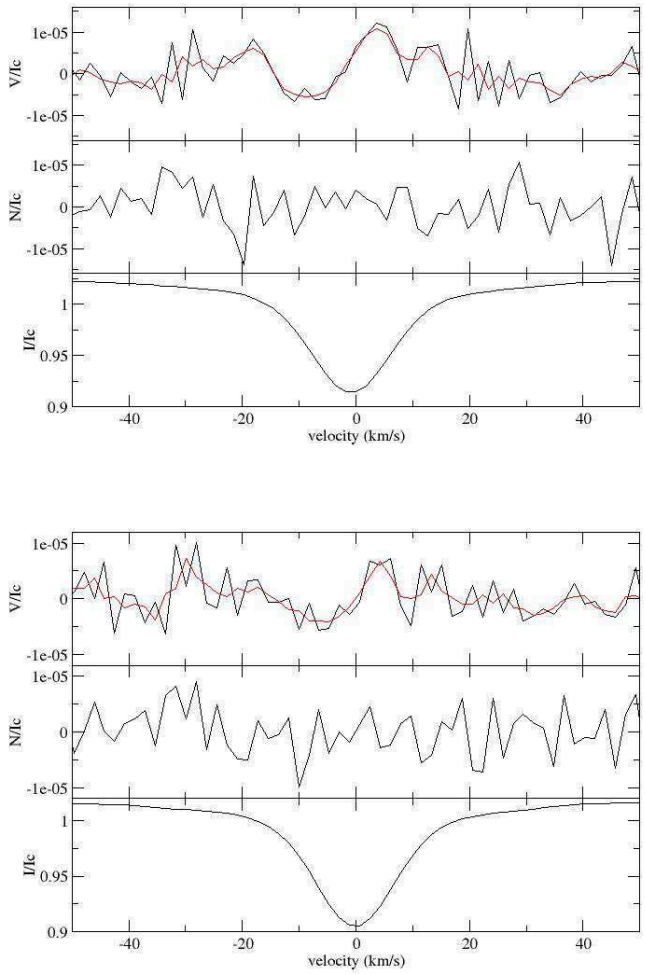

FIGURE 5.9: **The mean LSD profiles of γ Peg** for the data taken in 2015 (top) and for all Narval data (bottom).

To improve the S/N, I co-added my own LSD profiles with the LSD profiles of Neiner et al. (2014b). The final S/N on this grand-average Stokes V profile is 183224. The detection probability of a signal inside the stellar line is ∼24%, corresponding to a non detection. The profile is similar to the one of the 2015 because it is dominated by the 2015 profile. Again, I calculated the longitudinal magnetic field, B_l=-0.3 ± 0.2 G with a null polarization of 0.0 ± 0.2 G.

Finally,I estimated the upper limit on the non-detected dipolar magnetic field which could have remained hidden in the noise of the grand-average LSD profile, using the same method as for ζ Ori Ab (see Sect. 3.6.2). If a magnetic field exists on the surface of γ Peg, its strength is less than ∼37 G (see Fig. 5.10)

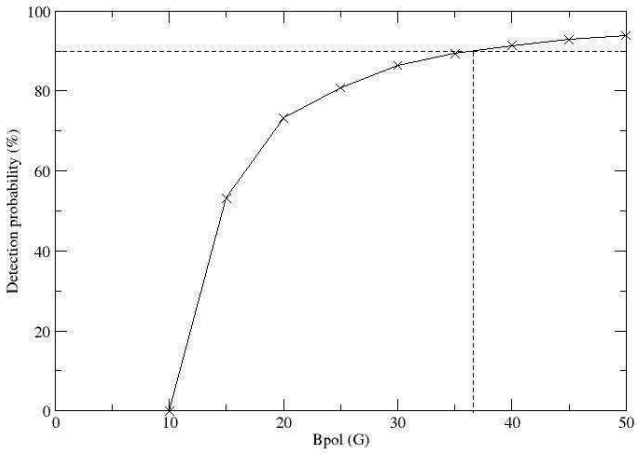

FIGURE 5.10: **Upper limit of the non-detected magnetic field of γ Peg:** Detection probability of a magnetic field in the grand-average profile of γ Peg as a function of the magnetic polar field strength. The horizontal dashed line indicates the 90% detection probability

5.3.6 Conclusion for B stars

To conclude, I did not detect ultra-weak magnetic fields in ι Her and γ Peg. However, due to the bad weather at the Pic du Midi Observatory, the accuracy of 0.1 G was not reached. (Wade et al. 2014b and Neiner et al. 2014b) demonstrated that if these stars host a magnetic field like the one of Vega, to detect it, a precision of 0.1 G is required. I would need even more observations to increase the S/N of the grand-average profiles. In spite of the lack of formal detections, hints for the possible presence of a weak Zeeman signature exists in some of the data. In particular, the fact that the Stokes V profile of ι Her is very similar for the Narval and ESPaDOnS data is encouraging. Therefore, ι Her will indeed be observed again during the summer 2016 and observing time for γ Peg got allocated at TBL for next semester. Thanks to these new observations, I hope to reach the accuracy of 0.1 G and determine if an ultra-weak field exists on B stars in the future.

Whatever the results of this study, they will provide important qualitative and quantitative constraints on current ideas about the magnetic desert. If I detect weak magnetic fields in B stars, that will support the prediction of the theories and provide new observational constraints to improve these theories, developed by Aurière et al. (2007) and Braithwaite & Cantiello (2013)). If I do not detect weak magnetic fields in B stars, we will need to develop new theories to explain why this kind of magnetic fields exist in A stars and not in B stars.

5.4 Conclusion

The discovery of an ultra-weak magnetic field in Vega by Lignières et al. (2009) raised the issue of the existence of this kind of magnetic fields in all hot stars that do not host a strong magnetic field. Studying the magnetism of Vega over several years brings constraints on the properties and origin of this field. Thanks to the observations taken between 2008 and 2015, I find that the magnetism of Vega did not change, which indicates a probable fossil origin rather than a dynamo.

Detecting ultra-weak magnetic fields in hot stars is very challenging, due to the weakness of the signal expected in the Stokes V profiles, and requires a large amount of observing time. The co-addition of all data is a working strategy for Vega thanks to the fact that Vega is seen pole-on. However, this strategy is not necessary the best one for other stars, for which we do not know the inclination and the rotation period, because we add observations taken at different rotational phases at which the signature of a potential magnetic field differs, and thus the co-addition of these signatures can destroy them.

For the moment, Vega is the only confirmed normal star that hosts an ultra-weak magnetic field. However, I suspect that UZ Lyn is a strong candidate to host a similar magnetic field, because I obtained a marginal detection for one night of observations. Nevertheless, I did not get a detection of a signature in the grand-average profile. For the B stars, to detect an ultra-weak magnetic field like the one of Vega in these stars, we would need a precision of 0.1 G. At the time of writing, this precision has not been reached and I cannot conclude on the existence or not of an ultra-weak magnetic field in B stars.

Only few normal stars are observed with the precision required to detect an ultra-weak magnetic field. Continuing to perform deep spectropolarimetric studies of hot stars is the only way to bring information on the existence of this kind of magnetism and helps us to know its properties. Good targets for such studies are the stars known to be see pole-on or the ones for which the rotational period is known.

Chapter 6

Weak magnetic fields in chemically peculiar stars

6.1 The Am stars: β UMa and θ Leo

6.1.1 Introduction

A weak Stokes V detection in spectral lines has been reported for the bright Am star Sirius A (Petit et al. 2011). For this object, however, the polarized signature observed in circular polarization is not a null integral over the width of the line profile, as expected in the usual description of the Zeeman effect. Instead, the Stokes V line profile exhibits a positive lobe dominating the negative one (in amplitude and integrated flux). The interpretation of a Zeeman origin was favored by Petit et al. (2011), in particular after excluding the possibility of an instrumental crosstalk from linear to circular polarization. However, the abnormal shape of the polarized profile remained a puzzle and required further investigation.

6.1.2 Selected targets

Here, I present the results of deep spectropolarimetric campaigns carried out for two bright Am stars in which magnetic fields were previously undetected (Aurière et al. 2010). Am stars are chemically peculiar stars exhibiting overabundances of iron-group elements such as zinc, strontium, zirconium, and barium and deficiencies of a few elements, particularly calcium and scandium. Most Am stars also feature low projected rotational velocities, as compared to normal A stars (Abt 2009). The targets of this study are β Ursa Majoris (HD 95418) and θ Leonis (HD 97633). Abundances measured for β UMa place this star among targets featuring weak Am characterictics with noticeable overabundance in VII, MnII, NiI, NiII, ZnI, SrII, YII, ZrII, and BaII and underabundances in HeI, CI, CII, and ScII (for more details, see Adelman et al. 2011). The

star θ Leo is also on the weak side of Am abnormality, with large reported overabundance in SiI, VII, CrII, SrII, YII, ZrII and BaII and underabundance in AlI, CaII, ScII, MnII, and NiI (Adelman et al. 2015a).

TABLE 6.1: **Fundamental parameters of β UMa and θ Leo**

	β UMa	θ Leo
Spectral type	A1V	A2V
$T_{\rm eff}$	9480K±10K[a]	9280±10K[a]
log g	3.82[b]	3.65[c]
Mass	2.64±0.01$M_\odot$[a]	2.94±0.2$M_\odot$[a]
Radius	3.021±0.038 $R_\odot$[d]	4.03± 0.10 $R_\odot$[e]
$v \sin i$	46±3 km/s[f]	23±3 km/s[f]
$L_\odot$	72±11[a]	127±13[a]
Frac. age	0.778[a]	0.943[a]
Metallicity	-0.03[g]	-0.13[g]

[a] Zorec & Royer (2012) [b] Allende Prieto et al. (1999)
[c] Adelman et al. (2015a) [d] Boyajian et al. (2012)
[e] Maestro et al. (2013) [f] Royer et al. (2002)
[g] Anderson & Francis (2012)

The fundamental parameters of both targets are presented in Table 6.1. The two objects are early A-type targets. Both of them benefit from an interferometric estimate of their radius, which is distinctly larger than the radius of main sequence stars of similar spectral types. Accordingly, their surface gravities are found to be below main sequence values. High luminosity values complete this picture, confirming that both targets are already on their way off the main sequence. Using evolutionary models matching the position of both stars in the H-R diagram, Zorec & Royer (2012) found that the fractional age on the main sequence of β UMa and θ Leo are equal to 0.778 and 0.943, respectively, giving further support to the idea that both stars have completed most of their path on the main sequence. That β UMa is reported to belong to the Ursa Majoris association gives another constraint on the age, which is estimated to be around 500 Myr for this group of stars (Monier 2005). Based on Spitzer measurements of IR excess, Ballering et al. (2013) attribute ages of 310 Myr and 500 Myr to β UMa and θ Leo, respectively, which is too young to be reconciled with other stellar parameters, but may provide an additional hint that θ Leo is more evolved than β UMa.

The projected rotational velocities estimated for both stars are fairly typical of values reported for Am stars (Abt 2009). In the absence of any direct estimate of the rotation period of our targets, it cannot be determined whether the higher $v \sin i$ value reported for β UMa compared to θ Leo is linked to a faster rotation or higher inclination angle.

6.1.3 Data analysis

Data were taken with the Narval spectropolarimeter (Aurière 2003, Silvester et al. 2012) in operation at TBL. The data are collected in the polarimetric mode measuring Stokes V (circular polarization).

β UMa was observed in March/April 2010 and March/April 2011 for a total of 149 spectra. For its part, θ Leo was observed in January/March/April 2012, March/April 2013, and May/June 2014 for a total of 171 spectra (see Table 6.2 for the detailed distribution of observations among individual nights). For each star, the exposure time was adjusted to reach a peak S/N throughout the Stokes V spectrum between 1,000 and 2,000 per 1.8 km s^{-1} bin, depending on weather conditions. These relatively high values are safely away from the saturation level of the EEV detector used in fast readout mode.

TABLE 6.2: **Journal of observations.** The columns contain the date for each Stokes V sequence, the heliocentric Julian date corresponding to the middle of the observation time, the object name, the number of sequences and exposure time per individual subexposure, and the averaged S/N in the individual LSD Stokes V pseudo-line profile (±rms).

Date	Mid-HJD	Star	T_{exp} (s)	S/N
17 Mar 2010	2455273.520	β UMa	16×4×107	52707±6090
06 Apr 2010	2455293.412	β UMa	17×4×107	49436±22333
10 Apr 2010	2455297.444	β UMa	19×4×107	76493±1960
11 Apr 2010	2455298.397	β UMa	19×4×107	32500±7752
25 Mar 2011	2455646.426	β UMa	25×4×107	56378±24444
31 Mar 2011	2455652.504	β UMa	25×4×107	45963±4907
02 Apr 2011	2455654.379	β UMa	03×4×107	53964±8998
04 Apr 2011	2455656.462	β UMa	24×4×107	69029±6099
22 Jan 2012	2455949.644	θ Leo	05×4×180	44503±1018
23 Jan 2012	2455950.628	θ Leo	05×4×180	39774±5090
24 Jan 2012	2455951.624	θ Leo	05×4×180	41547±3889
25 Jan 2012	2455952.640	θ Leo	05×4×180	41737±3134
14 Mar 2012	2456001.579	θ Leo	05×4×180	43929±1810
15 Mar 2012	2456002.524	θ Leo	10×4×180	47360±698
24 Mar 2012	2456011.526	θ Leo	05×4×180	44880±1487
25 Mar 2012	2456012.502	θ Leo	05×4×180	47392±506
27 Mar 2012	2456013.400	θ Leo	10×4×180	40883±1229
21 Mar 2013	2456373.488	θ Leo	09×4×180	25542±4619
23 Mar 2013	2456375.465	θ Leo	09×4×180	29220±2557
16 Apr 2013	2456399.444	θ Leo	09×4×180	23751±3600
17 Apr 2013	2456400.492	θ Leo	09×4×180	45010±1529
22 Apr 2013	2456405.512	θ Leo	09×4×180	42777±1707
23 Apr 2013	2456406.454	θ Leo	09×4×180	42064±2815
24 Apr 2013	2456407.502	θ Leo	09×4×180	39578±2497
14 Apr 2014	2456762.445	θ Leo	05×4×180	25433±8566
07 May 2014	2456785.408	θ Leo	05×4×180	42839±3748
08 May 2014	2456786.411	θ Leo	05×4×180	39435±2842
09 May 2014	2456787.416	θ Leo	05×4×180	44236±617
14 May 2014	2456792.471	θ Leo	05×4×180	42041±543
15 May 2014	2456793.413	θ Leo	05×4×180	44653±1052
07 Jun 2014	2456816.408	θ Leo	05×4×180	29599±1530
10 Jun 2014	2456819.415	θ Leo	05×4×180	29931±3928

In the absence of any detectable polarized signatures in individual spectral lines of β UMa and θ Leo, I applied the LSD procedure (see Sect. 2.5.2) to each spectrum of both stars. Our line lists are taken from the VALD atomic data base (Kupka & Ryabchikova 1999; Piskunov et al. 1995) using the respective effective temperature and log g of both stars (Table 6.1). Our line lists are extracted using $T_{\rm eff} = 9,500K$ and log g=4.0 for β UMa and $T_{\rm eff} = 9,250K$ and log g=3.5 for θ Leo. I rejected the lines whose depth is less than 1% of the continuum. By doing so, I obtained a mask of 1173 lines and 1133 lines for β UMa and θ Leo, respectively. Then, I adjusted the depth of the lines in the mask to fit the observed line depths. To reduce the noise per spectral bin further, I decreased the spectral resolution of the LSD line profiles. Instead of the default spectral bin spanning 1.8 $\mathrm{km\,s^{-1}}$ at a spectral resolution of 65,000, I used 9 $\mathrm{km\,s^{-1}}$ for β UMa and 5.4 $\mathrm{km\,s^{-1}}$ for θ Leo, which leaves us with about ten velocity bins in the pseudo-line profile. With this modification of the spectral resolution, the additional gain in the S/N is a factor of 2.1 for β UMa and 1.7 for θ Leo. The nightly averaged S/N of the resulting Stokes V LSD profiles (i.e., the average of the S/N of individual profiles) was between 45000 and 77000 for β UMa and between 25000 and 48000 for θ Leo (see Table 3.1). The dispersion of the S/N between individual Stokes V sequences of a given night is often the lowest during nights featuring the highest average S/N, because of the excellent (and stable) sky transparency.

Polarized signals remain undetected in individual LSD Stokes V pseudo-profiles of our two targets. However, their typical S/N remains far too low to detect polarized signatures as weak as the one previously reported for Sirius A (Petit et al. 2011). To further improve the S/N, I coadded all available LSD profiles for each star, resulting in one "grand average" pseudo-line profile. This method was successfully used for Vega (Lignières et al. 2009, Petit et al. 2010) and Sirius A (Petit et al. 2011) to detect signatures with amplitudes as low as about 10^{-5} of the continuum level. To coadd the LSD profiles, I used the same technique as in Chapter 5 (see Sect. 2.5.2).

I choose here to keep all profiles in this process, even those with the lowest S/N (LSD profiles with S/N lower than 10000 represent 16 observations for β UMa and 2 for θ Leo), because this systematic rejection was found to provide us with nothing more than a marginal modification of the result and no noticeable improvement. The grand average LSD profiles are presented in Fig. 6.1. With the large number of spectra collected here, the coaddition of all profiles increases the S/N by a factor ≈ 10, compared to individual profiles. The resulting S/N of the grand average V profiles is 653640 for β UMa and 512370 for θ Leo.

One limitation of this rough co-addition method is that we average together observations taken at different rotational phases. In the absence of any known rotation period, we assume our data are distributed over all rotation phases with the same probability. I therefore lose any phase-resolved information, and the axisymmetric surface structures (i.e., structures symmetric about the spin axis) are the most likely to survive the coaddition process and actually contribute to the grand average. This strategy is, however, successful at reducing the noise level enough to permit the detection of circularly polarized signatures in both stars (see Fig. 6.1), while the null profiles remain free of any feature above noise level.

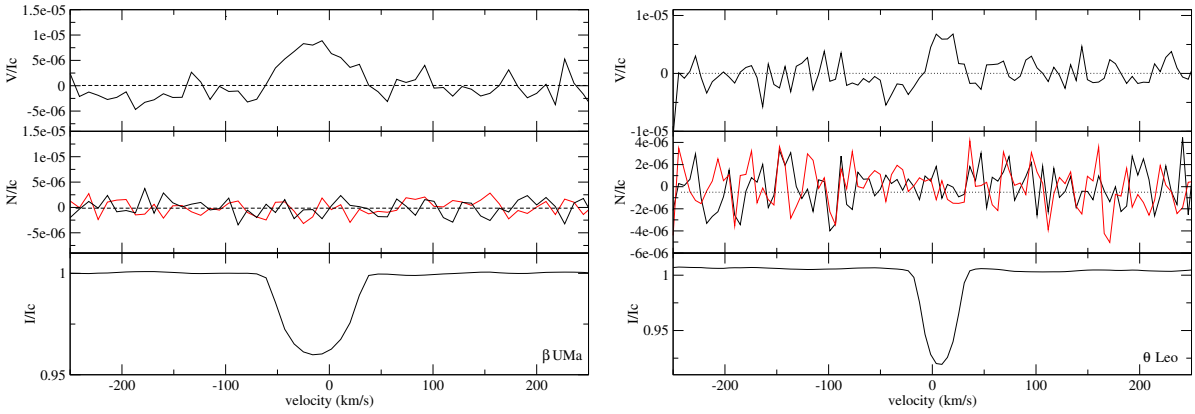

FIGURE 6.1: **Coadded LSD profiles** in Stokes I (bottom) and V (top). The two available "null" control parameters Null1 and Null2 are shown in the middle panel. Left: β UMa observations. Right: θ Leo observations. All profiles are normalized to the continuum level.

Reduced spectra are provided by Libre-Esprit with a normalized continuum, although the actual resulting continuum typically deviates by up to 15% from unity, especially in the bluest orders of the spectra. To test the impact of this imperfect automated processing on the result of our LSD analysis, I normalized each of the 40 echelle orders for each spectrum with the continuum task of IRAF. The new normalization improves the S/N of the individual LSD profiles by about 5%. I notice that the upgraded normalization changes the resulting LSD profiles slightly, however the improvement is very marginal, even at the extremely high S/N of our grand average profiles. In spite of the limited quality of the default continuum normalization, the robustness of LSD is mainly due to the large number of lines taken into account in the LSD process, compared to hotter stars for which the improved normalization is more useful. As a consequence, I simply consider here the spectra normalized with Libre-Esprit for consistency with the previous studies on Vega (Lignières et al. 2009, Petit et al. 2010) and Sirius (Petit et al. 2011) in which the default normalization was used.

6.1.4 Results

6.1.4.1 LSD profiles with complete line mask

The Stokes I, V, Null1 and Null2 co-added LSD profiles of β UMa and θ Leo are shown in Fig. 6.1. They display clear Stokes V signatures at the radial velocity of the Stokes I line profiles. The circularly polarized signal observed for both stars covers most of the width of the line and is mostly symmetric about the line centroid. In both cases, a positive lobe dominates the signal. No detectable signal is seen in the Null1 and Null2 control profiles. I computed the detection probability of the Stokes V signal by using the χ^2 test (see Sect. 2.5.3), getting a detection probability of ∼100 % for both stars

with a FAP below 10^{-11} for β UMa and equal to 6.5×10^{-6} for θ Leo. Outside of the stellar lines, I obtained a marginal signal detection for β UMa, due to the negative bump in the Stokes V continuum showing up at a radial velocity of around -200 $\mathrm{km\,s^{-1}}$. This continuum feature, not observed for θ Leo, may be due to residuals of line blends (Kochukhov et al. 2010).

I note that the Stokes V signatures detected in the co-added LSD profiles probably stem from a significant fraction of the individual LSD profiles, as various subsets from our complete data set (e.g., observations taken during a given year, see Fig. 6.6) display the same signal when co-added separately, although with a higher noise level. The single-epoch subsets are obtained over a timespan that is much longer than the longest possible rotation period of the two targets, so that the co-addition process of many individual rotational phases should result, in all cases, in a filtering of any signatures resulting from non-axisymmetric magnetic structures.

6.1.4.2 Possible instrumental artifacts at high SNR

The very high S/N achieved to detect weak polarimetric signatures in intermediate-mass stars raises the question of possible instrumental effects that could contribute to generate spurious signatures in Narval Stokes V sequences. All spectra obtained for our study display a peak S/N below 2000, and the majority of them are kept below 1500. At such S/N values, we safely stay away from the saturation regime of the detector (S/N above 2000 for standard early-type stars). I note that subsets extracted from our complete time-series display consistent signatures, regardless of the S/N of the subset, as highlighted by, e.g., Fig. 6.6. In any case, most spurious signatures generated by nonlinear behavior of the detector are expected to show up in the Null1 and Null2 check profiles (especially if the S/N is fluctuating from one subexposure to the next), which is not seen here.

From an empirical point of view, I stress that the signatures recorded so far for Sirius A (Kochukhov 2014; Petit et al. 2011) display a similar shape using three different instrumental setups (ESPaDOnS, Narval, HARPSpol), three different models of CCD detector, and two different reduction pipelines, giving strong confidence in a stellar origin of the polarized signature. We finally emphasize that a number of stars belonging to several classes were previously observed at a comparable S/N, which resulted in no Stokes V detection in two normal B stars (Neiner et al. 2014c; Wade et al. 2014a) with a similar level of accuracy, in a definite Stokes V detection (with a standard Zeeman shape) for the star Vega (Lignières et al. 2009), and in a definite Zeeman detection (again with a standard shape) for the cool giant Pollux (Aurière et al. 2009), using a strictly identical instrumental setup. The reducing process can thus not explain the peculiar signatures.

Another potential source of instrumental artifacts, especially for very weak Stokes V signatures, is possible crosstalk from linear to circular polarization. This effect is documented for Narval and ESPaDOnS (e.g., Silvester et al. 2012). Stokes Q and U spectra were obtained for Sirius A by Petit et al. (2011), featuring no polarimetric signal at a level that could significantly contribute to the Stokes V signal. So, the crosstalk from

linear to circular polarization is not a possible explanation of the signatures detected in the Stokes V profiles of Sirius A, β UMa and θ Leo . The same profile shape obtained for Sirius A using three instruments affected by different crosstalk levels is, in itself, an independent evidence that linear polarization did not contaminate the Stokes V signature.

Considering this context as a whole, I conclude that a convincing body of evidence now exists to safely conclude that the Stokes V signal observed for β UMa and θ Leo most likely has a stellar origin.

6.1.4.3 Establishing the Zeeman origin of Stokes V signatures

The shapes of the signatures in the Stokes V profiles (mainly constituted of a positive lobe) are not expected in the standard theory of the Zeeman effect, which predicts that lobes of positive and negative signs should be observed, resulting in a zero-integral Stokes V profile. This surprising observation, and the extremely low amplitude of the recorded signatures, raise natural concerns about possible artifacts that may contribute to the observed polarized signal. Considered all together, the standard series of tests detailed in Sect. 6.1.4.2 provides us with strong evidence that the recorded signatures are stellar in origin.

Even if instrumental effects can be safely excluded, the physical origin of the signal still requires further investigation. I propose here a series of tests to ascertain the Zeeman origin of the recorded signal. The basic idea is that the amplitude of Zeeman signatures is expected to depend on various line parameters (Landé factor, wavelength, line depth), so that a careful selection of spectral lines for the LSD procedure should confirm or refute this dependence in our data. We therefore ran again the LSD process using a number of new line lists, extracted from our original list but featuring a selection of lines where one line parameter has been restricted to a given range. In the weak field approximation, Stokes V signals are related to line parameters according to the following equation:

$$V \propto g.\lambda_0^2.B_l.\partial I/\partial\lambda \tag{6.1}$$

where λ_0 represents the wavelength of the line profile, $B_\parallel$ the line-of-sight projection of the magnetic field vector, and g the effective Landé factor. At a given value of B_l, the amplitude of Stokes V is therefore expected to follow simple variations with λ_0, g, and with the line depth.

As a reference, I use here the standard Ap star α^2 CVn and a Narval observation downloaded from PolarBase (Petit et al. 2014b) and already used by Silvester et al. (2014). The star α^2 CVn is a bright and variable A0p with $v \sin i$=18 $\pm$ 0.5 km s^{-1}, an effective temperature of 11600 $\pm$ 500 K, and a logarithmic surface gravity equal to 3.9 $\pm$ 0.1 (Silvester et al. 2014). Its spectral properties are therefore reasonably similar to β UMa and θ Leo, except its slightly higher surface temperature. The interesting characteristic of α^2 CVn is its strong and organized surface magnetic field (locally up to 2 kG), resulting in very large circularly polarized signatures. We applied our series

of tests to this reference star to better highlight the expected results in the presence of a strong magnetic field, with negligible noise in the polarized profile.

The average line parameters for all submasks used to compute the new LSD profiles are listed in Table 6.3. They vary slightly from one star to the next mostly because of the different VALD models employed. The largest star-to-star differences are observed when we define the line sublists according to a wavelength threshold. I also list in Table 6.3 the normalization parameters used for the LSD procedure, forcing a normalized wavelength of 500 nm everywhere, except when we set a wavelength threshold, in which case we force a normalized Landé factor equal to 1.2. Finally, we correct for any difference in the depth of Stokes I profiles, except when the submasks are defined with a line depth threshold.

TABLE 6.3: Mean and normalization parameters of the original mean LSD line profiles for β UMa, θ Leo, and α^2 CVn.

	β UMa	θ Leo	α^2 CVn
Original Mask			
Mean Landé factor g	1.207	1.206	1.218
Mean wavelength (nm)	475.72	489.05	493.34
Mean line depth	0.322	0.311	0.297
Normalized Landé factor	1.216	1.227	1.241
Normalized wavelength (nm)	500.00	500.00	500.00
Normalized depth	0.450	0.433	0.410
Low$g$LSD			
Mean Landé factor g	0.941	0.956	0.971
Mean wavelength (nm)	472.22	488.71	494.91
Mean line depth	0.311	0.317	0.308
Normalized Landé factor	0.939	0.957	0.992
Normalized wavelength (nm)	500.00	500.00	500.00
Normalized depth	0.464	0.441	0.421
High$g$LSD			
Mean Landé factor g	1.529	1.516	1.533
Mean wavelength (nm)	479.95	489.48	491.27
Mean line depth	0.310	0.305	0.283
Normalized Landé factor	1.469	1.463	1.489
Normalized wavelength (nm)	500.00	500.00	500.00
Normalized depth	0.436	0.4253	0.397
Low wavelength LSD			
Mean Landé factor g	1.219	1.217	1.229
Mean wavelength (nm)	419.88	420.29	400.88
Mean	0.381	0.361	0.049
Normalized Landé factor	1.2	1.2	1.2

Normalized wavelength (nm)	450.03	457.57	464.26
Normalized depth	0.522	0.495	0.465
High wavelength LSD			
Mean Landé factor g	1.197	1.195	1.206
Mean wavelength (nm)	573.3	604.7	713.43
Mean line depth	0.275	0.267	0.256
Normalized Landé factor	1.2	1.2	1.2
Normalized wavelength	593.28	606.06	623.95
Normalized depth	0.375	0.358	0.333
Low depth LSD			
Mean Landé factor g	1.219	1.209	1.226
Mean wavelength (nm)	505.58	507.28	512.475
Mean line depth	0.214	0.212	0.203
Normalized Landé factor	1.328	1.358	1.405
Normalized wavelength (nm)	500.00	500.00	500.00
Normalized depth	0.253	0.252	0.238
High depth LSD			
Mean Landé factor g	1.170	1.192	1.193
Mean wavelength (nm)	480.14	481.97	480.45
Mean line depth	0.628	0.643	0.588
Normalized Landé factor	1.205	1.141	1.208
Normalized wavelength (nm)	500.00	500.00	500.00
Normalized depth	0.646	0.649	0.599

As a first test, I ran LSD for two submasks containing lines with an average Landé factor g lower (respectively greater) than the mean Landé factor of the original line list: 1.207 for β UMa, 1.207 for θ Leo, and 1.218 for α^2 CVn. Hereafter, I consider the normalizing Landé factors used as part of the LSD procedure, since it is the relevant quantity for direct comparison of different LSD profiles. (The normalizing g values follow the same trend as the average Landé factors of the submasks.) The resulting Stokes V profiles are plotted in Fig. 6.2 for the two Am stars and the control Ap star. The Stokes V profiles are corrected for a ∼10% difference in equivalent width observed in their associated Stokes I profile. Because of a higher noise level than obtained with the complete line mask, the high-g and low-g profiles of β UMa and θ Leo do not display any statistically conclusive differences. The overplotted running average helps to improve the situation, showing that the high-g signals possess higher amplitudes than their low-g counterparts. We note that their amplitude ratio is roughly consistent with the g ratio, although this point is difficult to establish with high accuracy (even with the running average) because of the level of noise.

As a second test, two sublists were defined from our original list by containing lines with a wavelength lower (respectively greater) than the mean wavelength of the original list: 475.72 nm for β UMa, 489.05 nm for θ Leo and 493.34 nm for α^2 CVn. For a given star, the Stokes V profiles were corrected for the ∼30% difference in equivalent width observed in their associated Stokes I profiles. The outcome of this test is shown in Fig. 6.3, which illustrates a marginally larger amplitude of the Stokes V signal when the wavelength increases. As for the previous test, we computed a moving average of

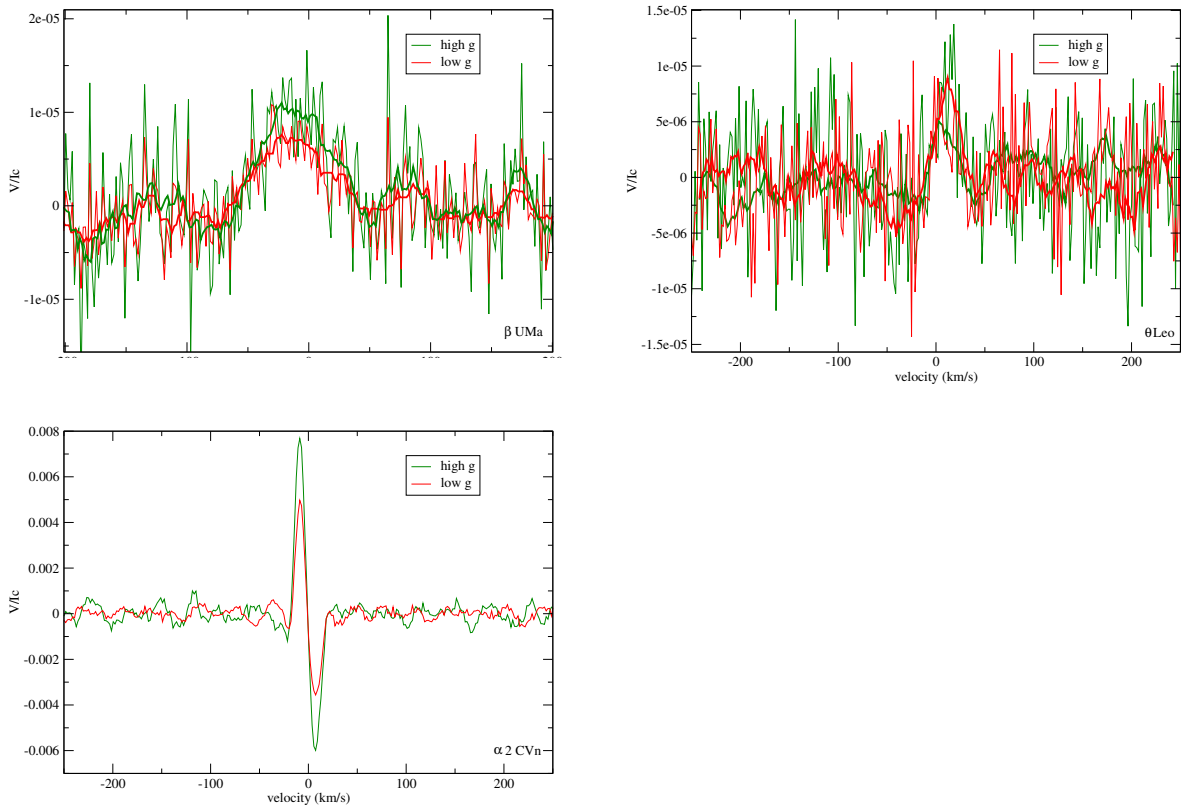

FIGURE 6.2: **Comparison of the Stokes V profiles obtained by selecting photospheric lines of low and high magnetic sensitivity**Top left: Comparison of the Stokes V profiles obtained by selecting photospheric lines of low (red thin line) and high (green thin line) magnetic sensitivity for β UMa. The thick red and green lines represent a moving average over three spectral bins of the thin lines. Top right: same figure for θ Leo. Bottom: same figure for α^2 CVn. All profiles are normalized to the continuum level.

the signal to confirm the trend that is otherwise completely hidden in the noise and to check that the trend observed in both Am stars is consistent with the outcome obtained for α^2 CVn.

As a last test, I defined two sublists using spectral lines with an average depth lower (respectively greater) than the mean depth of the original list: 0.45 for β UMa, 0.433 for θ Leo and 0.410 for α^2 CVn. The Stokes V LSD profiles obtained from the sublists are displayed in Fig. 6.4 and, for our two Am stars and our reference star, clearly show a lower amplitude whenever the average line depth is smaller. This outcome is expected in the case of a signature of magnetic origin, but also for most instrumental artifacts.

From the series of tests presented here, only the one with low versus high Landé factors was performed by Petit et al. (2011) for Sirius A. For consistency, we used their observing material to reproduce with Sirius A the three tests applied to β UMa and θ Leo. The result shown in the Figure 6.5, is fully consistent with the conclusions reached in the present study. Considered together, this series of tests strongly suggests that the

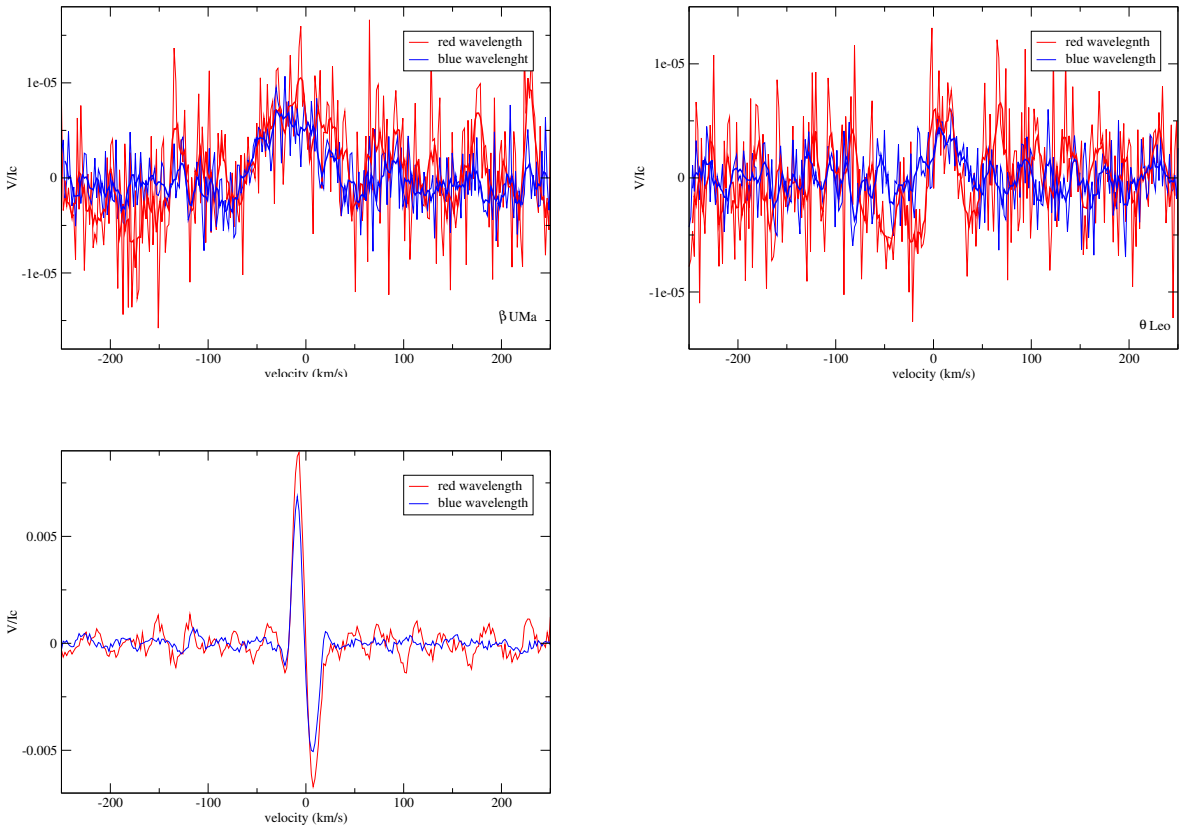

FIGURE 6.3: **Comparison of the Stokes V profiles obtained by selecting photospheric lines of red and blue wavelength.** Same as Fig. 6.2 for photospheric lines of high (thin red line) and low (thin blue line) wavelength.

circularly polarized signatures obtained for the three bright Am stars observed so far have a Zeeman origin.

Based on this conclusion, it is tempting to estimate the surface field strength from our set of measurements, using the classical center of gravity (or first moment) method (Rees & Semel 1979). I must stress, however, that this widely used technique is based on the standard assumption that the Stokes V signature is anti-symmetric about the line center, which is very far from the actual shape of our Stokes V signatures. A purely symmetric signature (closer to what is obtained for β UMa and θ Leo) will be interpreted as a zero longitudinal field strength, regardless of the amplitude of the Stokes V signal, similarly to dipolar fields observed at the rotational phase of a crossover configuration (e.g., Aurière et al. 2007). The situation here is obviously different, because the large time span of data collection is very unlikely to be restricted to a crossover phase. Nevertheless, such a measurement (and in particular its error bar) provides us with a quality measure of the sensitivity of the magnetic diagnosis that can be compared to similar studies. The first moment estimate of the magnetic field provides us with a field strength of -1 ± 0.8 G for β UMa and -0.4 ± 0.3 G for θ Leo that is unsurprisingly consistent with zero (as previously reported with Sirius A). As an attempt to propose a more relevant proxy of the field strength, I calculated the equivalent width (EW) of the Stokes V signature

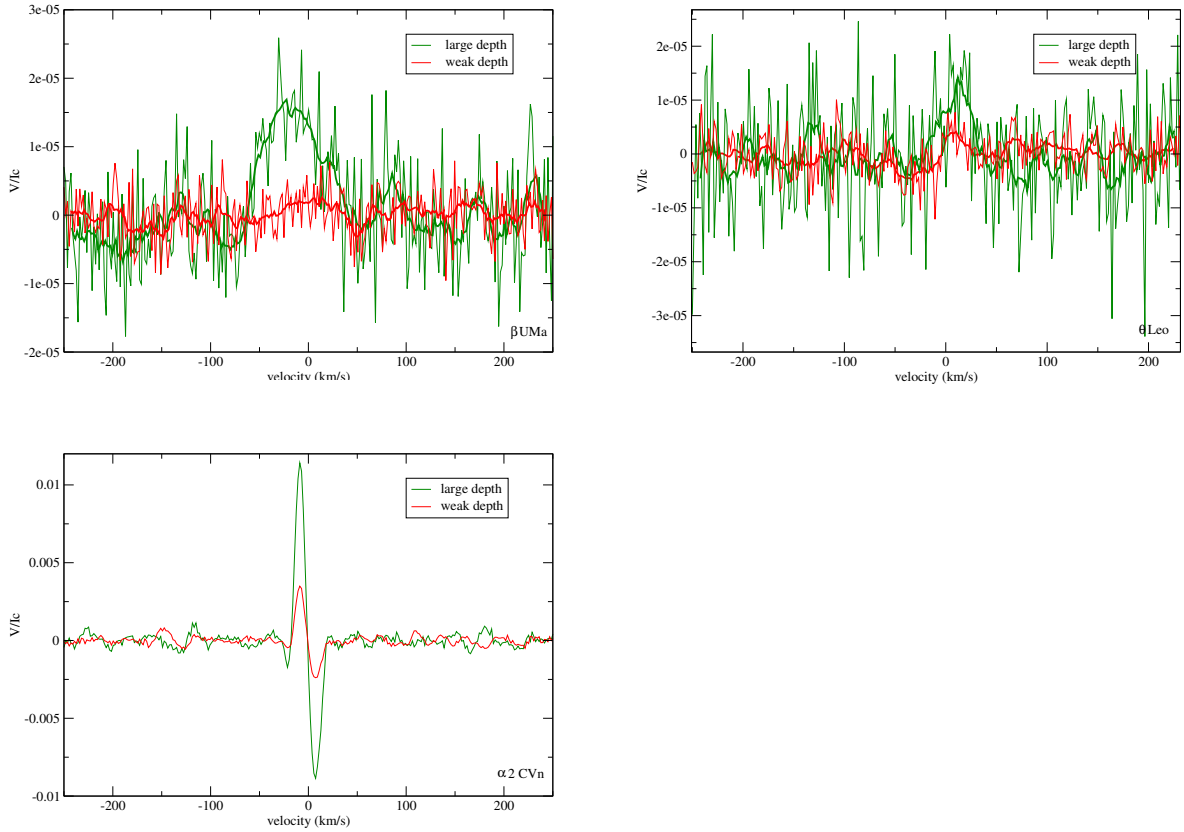

FIGURE 6.4: Same as Fig. 6.2 for photospheric lines of weak (thin red line) and large(thin green line) central depth.

and normalized this EW by the one of the Stokes I profile. By doing so, I obtained a normalized EW equal to 1.96×10^{-4} for β UMa, and 5.44×10^{-5} for θ Leo. For Sirius A, the normalized EW is equal to 6.68×10^{-5}.

6.1.5 Discussion

6.1.5.1 Peculiar Stokes V signatures in Am stars

The observations presented in Sect. 6.1.4 provide new clues to the weak polarized signatures produced in the photospheres of intermediate-mass stars. I report the detection of weak Stokes V signatures in two of the brightest Am stars, which complements the previous detection of a similar polarized signal for Sirius A (Petit et al. 2011)[1]. Considered together, the three polarimetric detections constitute a 100% detection rate so far in our sample of bright Am stars, suggesting widespread similar signatures in this stellar class.

All signals observed up to now possess roughly the same shape, with one positive lobe roughly symmetric about the line center and occupying most of the width of the line

[1] an observation confirmed by independent HARPSpol observations carried out by Kochukhov (2014).

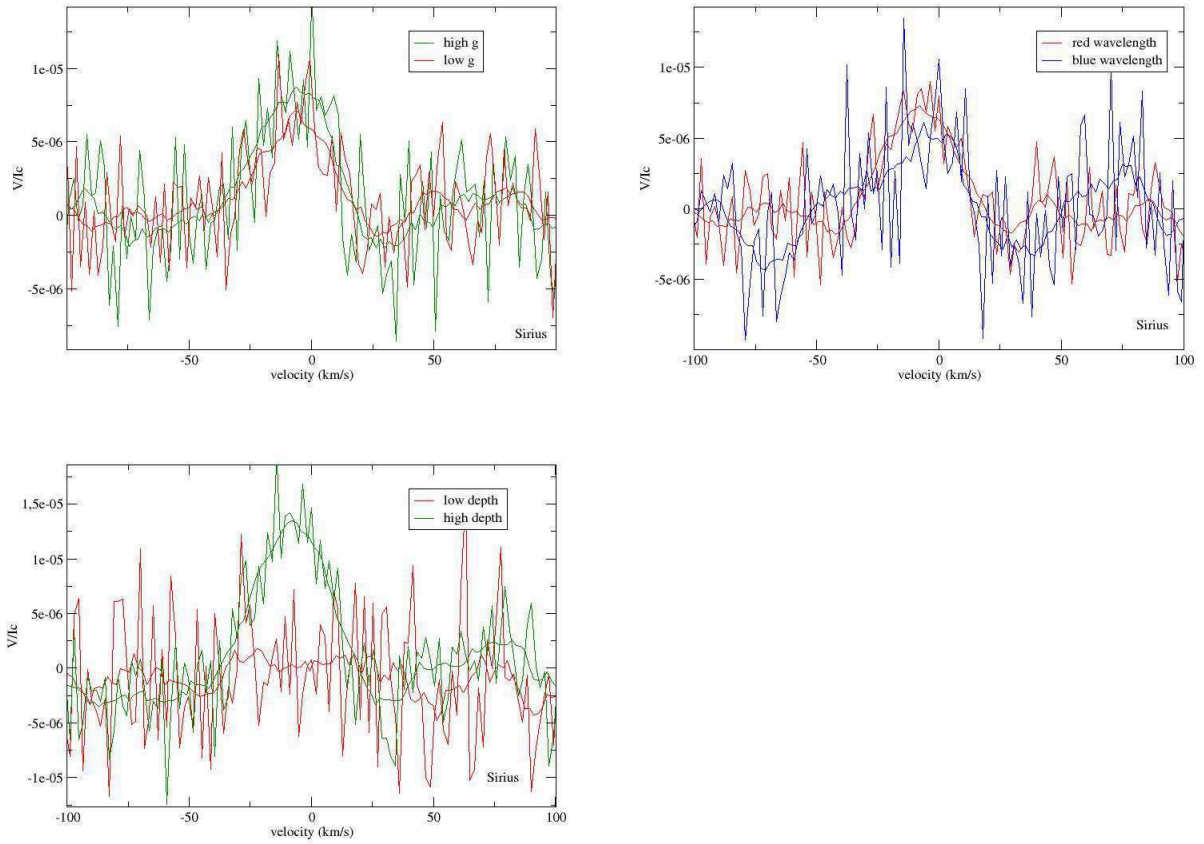

FIGURE 6.5: **LSD test for Sirius A.** On the top left: comparison of the Stokes V profiles obtained by selecting photospheric lines of low (red thin line) and high (green thin line) magnetic sensitivity. The thick red and green lines represent a moving average over three spectral bins of the thin lines. On the top right, same figure for photospheric lines of low (thin blue line) and high (thin red line) wavelength and on the bottom same figure for photospheric lines of low (thin red line) and high (thin green line) central depth.

profile. Negative lobes surrounding the positive one, if they exist, do not exceed the noise level in the data sets available to us. These profile shapes displaying net circular polarization are atypical of Zeeman signatures observed in other classes of magnetic stars, where the integral of the Stokes V profile is generally close to null. This peculiar shape naturally prompts questions about the origin of these polarized spectral features. The tests conducted in this study show that these unexpected signatures depend on spectral line parameters (wavelength, Landé factor, line depth), as expected from a Zeeman signal.

Stokes V profiles that are nearly symmetric about the line center are common. These patterns are temporarily observed when two magnetic poles of an inclined dipole are seen on the visible hemisphere of a star, close to the limb, and therefore with different radial velocities (at the so-called crossover rotational phases). This simple interpretation is, however, very unlikely here since our co-added LSD profiles mix data collected over timespans much longer than the typical rotation periods of Am stars, merging a large

number of random rotation phases. A dominant toroidal magnetic field component is also able to generate symmetric Stokes V profiles (Donati et al. 2005), although this specific type of magnetic geometry should not produce any net circular polarization, as observed here. In any case, a purely geometric explanation is not able to account for the absence of negative lobes in the Stokes V profiles.

A number of cool active stars were reported to display weak net circular polarization after integration over LSD line profiles (Aurière et al. 2011, 2008; Lèbre et al. 2014; Morgenthaler et al. 2012; Petit et al. 2005; Tsvetkova et al. 2013). However, no similar findings have been reported so far in strongly magnetic massive stars or intermediate-mass stars, and the very subtle effect reported for cool stars is nowhere near the extreme situation reported here. For cool stars, the proposed interpretation was adapted from solar physics, where abnormal Stokes V are routinely described (e.g., Solanki 1993) and attributed to simultaneous vertical gradients in velocities and magnetic field strengths (López Ariste 2002 and references therein). Single-lobed signatures resembling those recorded for Am stars can be locally observed in solar magnetic elements (Sainz Dalda et al. 2012; Viticchié & Sánchez Almeida 2011), but they are more difficult to justify in the case of disk-integrated measurements (as obtained for unresolved stars) because of the organized flows and magnetic fields invoked to justify their shape. Relatively strong magnetic fields are also involved in asymmetric solar Stokes V profiles, although the very weak disk-integrated signatures reported here do not tell much about local magnetic strengths, which could potentially be rather large in the case of a very tangled field geometry.

The absence of any similar phenomenon in Ap stars (in spite of masses roughly identical to those of Am stars) may simply be related to the lack of any significant surface turbulence due to the strong magnetic fields permeating their photosphere (Folsom et al. 2013) and, in the case of Bp stars, to a photospheric temperature too high to allow for a thin convective shell, even in the absence of their magnetic field. The situation is different for Am stars, for which high-resolution spectra have revealed stronger micro-turbulence than for normal A stars (Landstreet et al. 2009), as long as their effective temperature remains below about 10000 K, a condition fulfilled by our two targets and by Sirius A. The very shallow convective shell producing this turbulent velocity field may host supersonic convection flows (Kupka et al. 2009). This could provide the source of sharp velocity and magnetic gradients needed to produce strongly asymmetric profiles. Shocks traveling in this superficial turbulent zone may also contribute to amplify any existing magnetic field, as previously proposed in the context of the Mira star χ Cygni (Lèbre et al. 2014).

In any case, a physical model able to produce a convincing reproduction of the peculiar polarized signatures reported for Am stars still needs to be developed. Preliminary simulations of Stokes V profiles with velocity and field gradients show that signatures such as those observed in β UMa, θ Leo, and Sirius A can be reproduced (C. Folsom, priv. comm.). Without such a tool at our disposal, any quantitative description of the associated surface magnetic fields is out of reach, since techniques commonly used to estimate stellar magnetic field strengths (like the center-of-gravity method) are not suited to model Stokes V profiles following such unexpected shape. In practice, magnetic strengths derived for β UMa and θ Leo by applying the usual methods can only provide

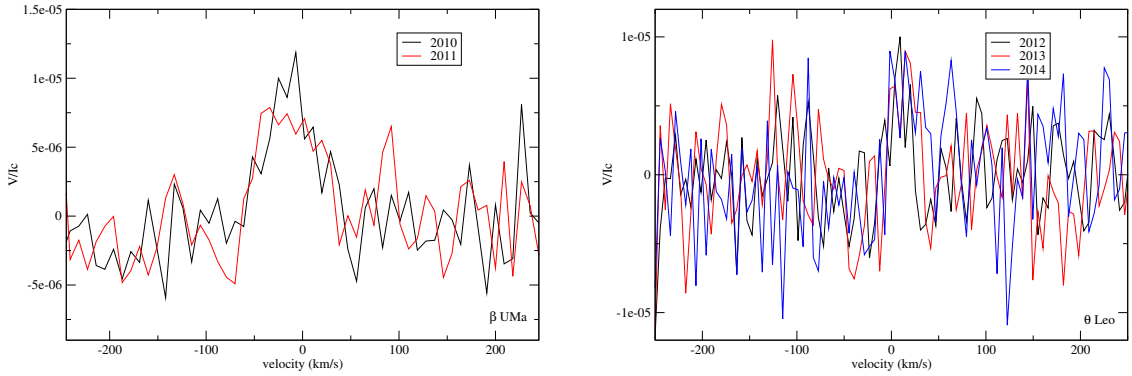

FIGURE 6.6: **Mean Stokes V profiles of Am stars for the different years of observation.** Left for β UMa. Right for θ Leo.

us with a lower limit of a few tenths of a gauss on the surface axisymmetric field component, which is consistent with the estimate available for Sirius A.

6.1.5.2 Origin of the magnetism of Am stars

With only small number of objects observed so far and polarimetric signatures close to the detection limit, our observations only offer a few hints to the physical ingredients involved in the generation of the weak surface magnetic fields observed in Am stars.

An important clue to distinguishing between a dynamo-generated field and most other scenarios is the long-term evolution of the observed magnetic field, because a dynamo-generated field is likely to experience some temporal variability on a secular timescale. By splitting our data sets into subsets limited to a given year of observation, we are able to get a first glimpse at the stability of the polarimetric signal (Fig. 6.6). We find that signatures recovered one year apart are consistent with each other, showing that any variability over this timespan remains below the noise level. This outcome is consistent with similar attempts for Sirius A and Vega (see Sect. 5.1).

Surface brightness inhomogeneities are usually associated with the structured magnetic field produced by a global dynamo. The lack of any rotation period estimate available in the literature for β UMa and θ Leo suggests that any such brightness patches must take place on relatively small spatial scales or be limited to a very low contrast. We note that the recent discovery of rotational modulation in Am stars of the Kepler field by Balona et al. (2015) was limited to targets that are significantly cooler than the objects of our study. A possibility is that the deeper convective envelope of stars in the Kepler sample may be more favorable to the onset of a large-scale dynamo. A very sensitive method, such as the one employed by Böhm et al. (2015) to detect very faint starspots on Vega, may be the key to unveiling surface features on weakly magnetic Am stars like those studied here. We also note the lack of documented flaring events for these bright and well-studied stars, again in contrast to claims for cooler intermediate-mass stars observed with Kepler (Balona 2013; Balona et al. 2015).

6.1.5.3 Towards a systematic exploration of weak magnetic fields in Am stars

The ultra-deep polarimetric campaign carried out for three bright Am stars is far from exhausting the exploration of this stellar class. The most noticeable difference between these stars is that β UMa and θ Leo seem to be located near the end of the main sequence, while Sirius A is a more standard main sequence object. One conclusion of our study is that these differences in the evolutionary status do not affect the recorded polarimetric signatures in any obvious way.

While Sirius A and θ Leo share a low projected rotational velocity, β UMa displays a higher $v \sin i$ value, although it is not possible to distinguish between the contribution of rotational and inclination effects in this parameter. The larger normalized EW of the polarimetric signal reported for β UMa may be a first hint of a rotational dependence of the weak magnetism of Am stars, although a much larger sample is required to seriously test this hypothesis.

Finally, all three objects discussed here were confined to a quite narrow band in effective temperature. The active behavior of cooler Am stars (Balona 2013; Balona et al. 2015) is a strong motivation to expand the available sample to Am stars of late-A spectral types. Since the peculiar polarized signatures observed up to now are proposed to be indirect tracers of surface convective motions, gathering observations in cooler stars is an obvious way to test this hypothesis by considering the effects of varying the surface turbulent flows on the polarized signature.

6.2 The Am star of Alhena

6.2.1 Introduction

Alhena (γ Gem) was observed in the frame of the BRITE (BRIght Target Explorer) spectropolarimetric survey. The BRITE constellation of nano-satellites performs asteroseismology of stars with V$\leq$4 (Weiss et al. 2014). In this context, we are performing a high resolution, high S/N, high sensitivity, spectropolarimetric survey of all stars brighter than V=4, with the ultimate aim to combine seismic and spectropolarimetric studies of bright stars (see Neiner & Lèbre 2014).

Alhena is a bright (V=1.90) spectroscopic binary, in which the primary is a subgiant A0IVm star (Gray 2014) and the secondary is a cool G star (Thalmann et al. 2014). The orbital elements of the binary have been measured thanks to interferometry (Drummond 2014). The orbital period is 12.63 years and the orbit is very eccentric with e=0.89. The mass of the primary is estimated to 2.84 $M_\odot$ and the one of the secondary to 1.07 $M_\odot$. The primary, Alhena A, is a weakly Am star (Adelman et al. 2015b), similar to the three known magnetic Am stars discussed in Sect. 6.1. The stellar parameters of Alhena A are actually very close to the ones of θ Leo, which exhibits peculiar magnetic signatures in its Stokes V profiles (see Table 6.4).

TABLE 6.4: Fundamental parameters of the Am stars Alhena and θ Leo.

	Alhena A	θ Leo
Spectral type	A0IVm	A2Vm
$T_{\rm eff}$ (K)	9260±10[a]	9280±10[b]
log g	3.6[a]	3.65[c]
Mass ($M_\odot$)	2.84±0.01[b]	2.94±0.2[b]
Radius ($R_\odot$)	3.9±0.1 [d]	4.03± 0.10 [e]
$v \sin i$ (km s^{-1})	15±3[f]	23±3[f]
Luminosity ($L_\odot$)	123±11[b]	127±13[b]
Age (Myr)	484[g]	436[g]
Microturb. (km s^{-1})	2[a]	1[b]

[a] Adelman et al. (2015b) [b] Zorec & Royer (2012)
[c] Adelman et al. (2015a) [d] Pasinetti Fracassini et al. (2001)
[e] Royer et al. (2007) [f] Royer et al. (2002)
[h] David & Hillenbrand (2015)

6.2.2 Observations

Data were collected with the Narval spectropolarimeter (Aurière 2003, Silvester et al. 2012) in polarimetry mode to measure the circular polarization (Stokes V). Alhena was observed on October 27, 2014, and 19 times between September 2015 and April 2016. The journal of observations is provided in Table 6.5.

6.2.3 Magnetic analysis

To test whether Alhena is magnetic, I used the LSD technique (see Sect. 2.5.2). I first created a line mask corresponding to the primary component of Alhena. I started from a list of lines extracted from VALD (Kupka & Ryabchikova 1999; Piskunov et al. 1995) for an A star with $T_{\rm eff}$=9250 K and log g=3.5, with their Landé factors and theoretical line depths. I then cleaned this line list by removing the hydrogen lines, the lines that are blended with hydrogen lines, as well as those that are not visible in the spectra. I also added some lines visible in the spectra that were not in the original A-star mask. Altogether I obtained a mask of 1044 lines. I then adjusted the depth of these 1044 lines in the mask to fit the observed line depths.

The results of the LSD analysis are shown in Fig. 6.7. The Stokes V profiles show clear Zeeman signatures for almost all observation nights. I computed the detection probability of the Stokes V signal by using the χ^2 test (see Sect. 2.5.3), getting a detection probability of 100% for all observations except the ones taken on 31 October 2015 and on 9 November 2015, with a FAP always smaller than 1.117×10^{-7} inside the stellar line. For the observations of 31 October 2015 and 9 November 2015, I obtained marginal detections due to the weakness of the amplitude of the signature for these observations. I note that the magnetic signatures are strong enough to be detected in individual LSD Stokes V profiles, while for other magnetic Am stars co-addition of many Stokes V profiles was necessary to extract a magnetic signature (see Sect. 6.1).

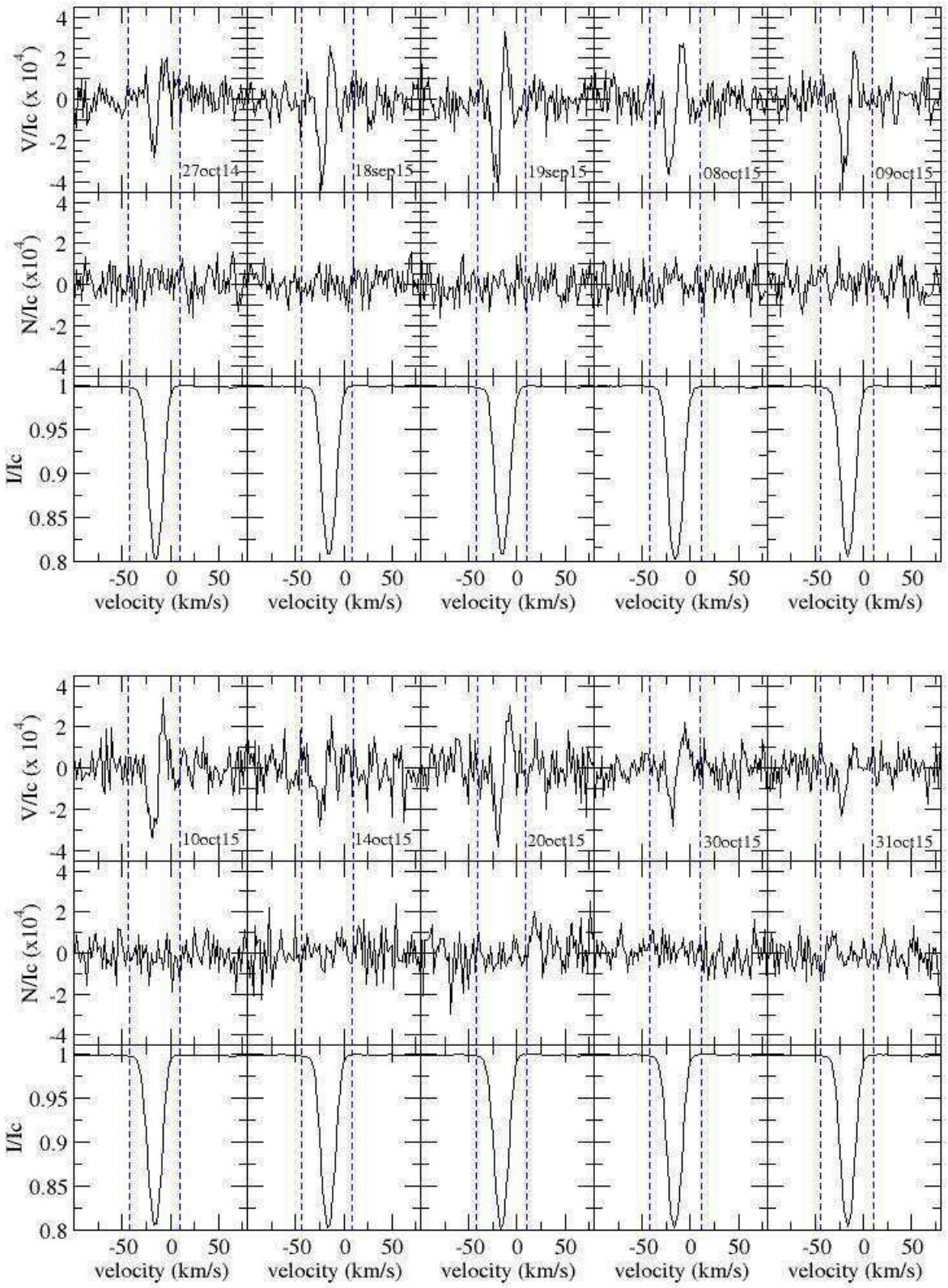

FIGURE 6.7: **LSD profiles of Alhena A** for Stokes I (bottom), the null N polarization (center), and Stokes V (top). The vertical blue dashed lines indicate the domain of integration used to determine the longitudinal field values.

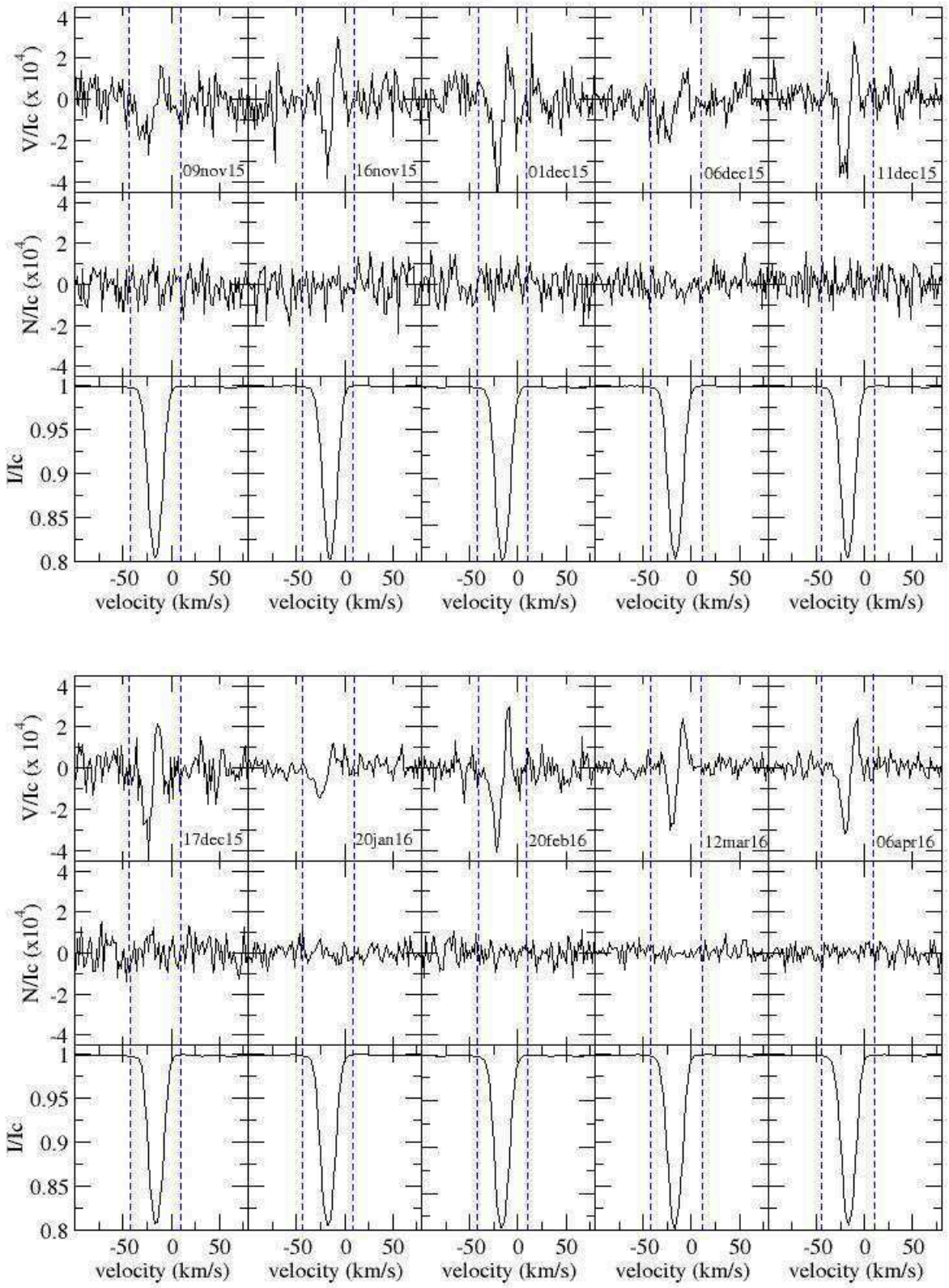

FIGURE 6.7: continued

TABLE 6.5: **Journal of observations of Alhena** indicating the date of observation, Heliocentric Julian Date at the middle of the observations (mid-HJD - 2450000), the number of sequences and exposure time in seconds, and the mean S/N of the intensity spectrum at ∼500 nm.

#	date	MHJD	$T_{\rm exp}$	S/N
1	27 Oct. 14	6958.65307	4 × 25	986
2	18 Sep. 15	7284.69538	4 × 35	1016
3	19 Sep. 15	7285.69435	4 × 35	1093
4	20 Oct. 15	7304.72039	4 × 35	1152
5	09 Oct. 15	7305.72662	4 × 35	1194
6	10 Oct. 15	7306.71038	4 × 35	961
7	14 Oct. 15	7310.58949	4 × 35	938
8	20 Oct. 15	7316.66823	4 × 35	832
9	30 Oct. 15	7326.72888	4 × 35	1157
10	31 Oct. 15	7327.73536	4 × 35	1149
11	09 Nov. 15	7336.73000	4 × 35	935
12	16 Nov. 15	7343.63519	4 × 35	917
13	01 Dec. 15	7358.61184	4 × 35	951
14	06 Dec. 15	7363.66416	4 × 35	1320
15	11 Dec. 15	7368.62637	4 × 35	1170
16	17 Dec. 15	7374.60852	4 × 35	1057
17	20 Jan. 16	7408.60778	3 × 4 × 42	2246
18	20 Feb. 16	7439.44522	3 × 4 × 42	1323
19	20 Mar. 16	7460.40347	3 × 4 × 42	2307
20	06 Apr. 16	7485.32998	3 × 4 × 42	2173

Outside the stellar line, I obtained a detection probability between 10% and 60% and a FAP between 7.356×10^{-1} and 5.351×10^{1}, that corresponds to a non-detection outside the stellar lines.

Since the diameter of the fiber of Narval is 2.8 arcsec, the two components of the binary have been recorded in the observations. However, the secondary is 5-6 magnitudes fainter than the primary, so only ∼2% of the received light comes from the G-type secondary component. Moreover, the secondary is not visible in the spectra. Thus, the contribution of the lines of the secondary are considered negligible unless its radial velocity is very close to the one of the primary. In addition, we ran the LSD analysis with a mask corresponding to a main sequence G star and the signatures in the Stokes V profiles disappeared (see an example in Fig. 6.8). I thus confirm that the signatures in the Stokes V profiles come from the primary star, i.e. that the Am star is magnetic.

Using the centre-of-gravity method (Rees & Semel 1979) with a mean wavelength of 500 nm and a mean Landé factor of ∼1.46 corresponding to the normalization parameters used in the LSD, I calculated the longitudinal field value (B_l) corresponding to these Zeeman signatures over the velocity range [-40:8] $\mathrm{km\,s^{-1}}$.

The longitudinal magnetic field value for the three observations, and the corresponding null values, are shown in Table 6.6. The values of the longitudinal magnetic field are

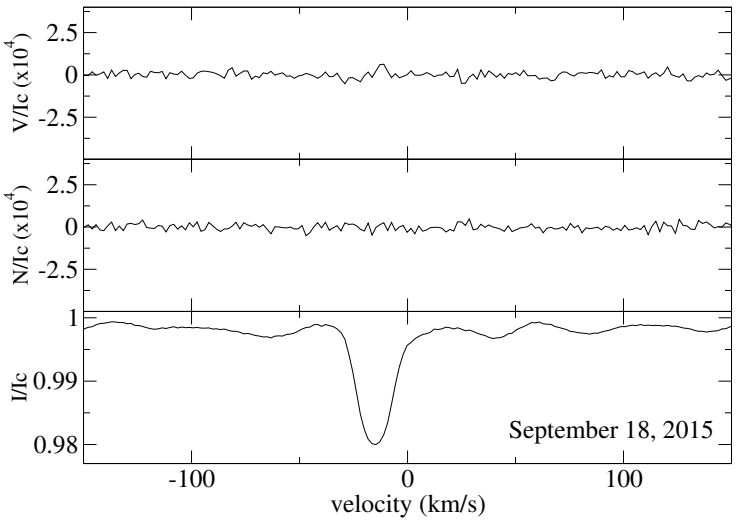

FIGURE 6.8: **LSD profiles of the companion Alhena B** for Stokes I (bottom), the null N polarization (center), and Stokes V (top) for September 18, 2015.

between -10 G and -2.0 G, with error bars smaller than 3 G. The values extracted from the N profiles are compatible with 0 G (see Table 6.6).

The shape of the Zeeman signatures in the Stokes V profiles only slightly changed between the observation obtained in 2014 and the ones from 2015-2016. However, the amplitude of the signature changed during the observations of 2015-2016. This could be due to a rotational modulation of the longitudinal magnetic field, if the field is oblique compared to the rotation axis, as observed in most hot stars (Grunhut & Neiner 2015). In 2014, the signature would look like a cross-over signature, while in 2015 and 2016 the negative pole may be observed.

On the contrary, the signatures obtained over two or three consecutive nights did not change. This suggests that either Alhena is an intrinsically slow rotator or the rotational modulation is small because the star is seen under a specific geometrical configuration with an inclination or obliquity angle close to 0.

With the $v \sin i$ of 15 $\mathrm{km\,s^{-1}}$and the radius of 3.9 $\mathrm{R_\odot}$, I calculated the upper limit of the rotational period. I found that the period P_{rot} is less than ∼13 days. That is less long than the observation period. So, I conclude that Alhena is seen close to pole-on or with an obliquity angle close to 0.

Even if the signatures change slightly, the longitudinal magnetic field values I measured are similar for all nights. Signatures with different amplitude give the same longitudinal magnetic field value, because it is compensated by a change in profile shape. The signatures with low amplitude are spread over the entire intensity profile and the the ones with high amplitude are more concentrated over the core of the intensity profile. It is thus possible that the signature is due to a magnetic spot located close to the pole, like for Vega.

TABLE 6.6: **Longitudinal magnetic field of Alhena** (B_l) and null (N) measurements with their respective error bars and magnetic detection status.

#	$B_l \pm \sigma B_l$ (G)	N$\pm\sigma$N (G)	Detection
1	-5.1±2.7	-1.5 ±2.7	DD
2	-5.6± 2.7	1.6 ± 2.7	DD
3	-5.5 ± 2.5	-2.6 ± 2.5	DD
4	-7.6 ±2.5	-1.7± 2.5	DD
5	-6.8 ±2.4	-2.5±2.4	DD
6	-4.9 ±2.8	2.3±2.8	DD
7	9.1±2.9	-0.9±2.9	DD
8	-10.7±3.3	-0.3±3.3	DD
9	-6.6 ± 2.6	2.8 ± 2.6	DD
10	-6.0±2.4	4.5± 2.3	MD
11	-8.9 ±2.9	-1.3± 2.9	MD
12	-2.5 ±2.9	0.4 ± 2.9	DD
13	-2.0±2.9	0.5±2.1	DD
14	-6.9±2.1	-1.9±2.4	DD
15	-6.4±2.4	2.1±2.8	DD
16	-7.6±2.8	-1.7±2.2	DD
17	-7.8±1.3	1.1± 1.3	DD
18	-8.0±2.1	1.1±1.3	DD
19	-5.5±1.2	-0.1±1.2	DD
20	-5.5±1.3	-0.6±1.3	DD

6.2.4 Discussion and conclusion

The results obtained for Alhena correspond to the first detection of a magnetic field in an Am star with a normal Zeeman signature, i.e. with a positive and negative lobe as seen in the ultra-weakly magnetic A star Vega and in all strongly magnetic hot stars. On the contrary, all the other Am stars studied in spectropolarimetry with a high accuracy exhibit peculiar magnetic signatures with only a prominent positive lobe (see Sect. 6.1)

The difference between the field of Alhena and the other Am stars is thus puzzling. In particular, Alhena has very similar stellar parameters to the ones of the magnetic Am star θ Leo. However, the signatures in the Stokes V profiles are very different. θ Leo shows peculiar signatures, while Alhena shows normal signatures. Considering the oblique rotator model, the dipolar magnetic field B_d is at least 3.3 times the maximum observed B_l value (Aurière et al. 2007; Preston 1967). Therefore, the longitudinal field values measured for Alhena point towards a polar magnetic field strength of the order of 30 G, i.e. weak but much stronger than what is observed in the other magnetic Am stars.

An explanation to the difference between the characteristics of the magnetic field observed in Alhena and in other Am stars may be found in their microturbulence value. The microturbulence of Alhena A is ~ 1 km s^{-1}(Adelman et al. 2015b), while the one of θ Leo, β UMa, and Sirius A is ~ 2 km s^{-1}(Adelman et al. 2015a, 2011; Landstreet et al.

2009). Indeed, the peculiar shape of the magnetic signatures of the latter 3 Am stars is thought to be related to their stronger microturbulence, compared to normal A stars. The very shallow convective shell producing this turbulent velocity field may host supersonic convection flows (Kupka et al. 2009), which could be the source of sharp velocity and magnetic gradients producing strongly asymmetric Zeeman profiles. Alhena A may have a too weak microturbulence to undergo this effect.

Another difference between Alhena and θ Leo is that Alhena is a binary star with a G-type companion, while θ Leo is a single star. However, Sirius is also a binary star and Sirius A does present peculiar magnetic signatures like θ Leo. The distance between the two components of Sirius is larger ($P_{\rm orb}$=50.1 years) than the one of Alhena, nevertheless Alhena is a wide binary as well ($P_{\rm orb}$=12.63 years). However, the orbit of Alhena B is more eccentric (e=0.89) than the orbit of Sirius B (e=0.59), and there could thus be more tidal interactions between the 2 components of Alhena than between the components of Sirius.

Alhena is thus a very interesting star to understand the magnetism of Am stars and ultra-weak magnetic fields in general.

6.3 The HgMn star: α And

6.3.1 Introduction

Mercury-Manganese (HgMn) stars are an other type of chemically peculiar intermediate-mass stars, showing notable overabundance of Hg, Mn, Y, Sr, and other, mostly heavy, chemical elements. HgMn stars are typically slow rotators compared to normal intermediate-mass stars that are rapid rotators.

A deep spectropolarimetric study of HgMn stars could bring constraints on the existence or not of magnetic fields on the surface of HgMn stars. Some HgMn stars show Hg line variations (Adelman et al. 2002) and they were interpreted as a consequence of a non-uniform photospheric abundance distribution.

On Ap/Bp stars, the explanation for non-uniform surface abundance distributions is the strong magnetic field that these stars host(see e.g., Aurière et al. 2004). Similarly, some Am stars (see Sects. 6.1 and 6.2) have been found to host an ultra-weak magnetic field and this magnetic field may be linked to the chemical peculiarity of these stars. Therefore, it is important to check if HgMn stars host an ultra-weak field that could explain the non-uniform abundance distribution in these stars.

Moreover, some scenarios to explain the chemical spots detected for some HgMn stars predict that they could be explained by a weak magnetic field (less than 100 G, Alecian 2012).

In the past several studies already tried to detect magnetic fields in HgMn stars but without success (e. g. Shorlin et al. 2002). However, the precision that they reached is

too high to detect ultra-weak magnetic fields like the one of Vega or of the Am stars. I thus made a new detection attempt using much deeper spectropolarimetric observations.

6.3.1.1 The target: α And

To test if an ultra-weak magnetic exists on HgMn stars, we choose α And as our target, because it is a typical HgMn star with Hg line variations. Adelman et al. (2002) find that the period of Hg line variation on α And is 2.38236 $\pm$ 0.00011 days. This period is similar to the rotational period found by Ryabchikova et al. (1999), P_{rot}=2.53 $\pm$0.4 days, using a solid rotator model. Adelman et al. (2002) mapped the distribution of the Hg at the surface of α And thanks to Doppler Imaging. They deduced that the Hg abundance is higher close to the rotational equatorial regions.

α And is a bright star (Vmag=1.9 mag) and it is a binary system. The primary is a B8IV HgMn star and the secondary is classified as an A3V star (Tomkin et al. 1995). It is a close binary with an orbital period P_{orb}=96.7 days (Ryabchikova et al. 1998; Tomkin et al. 1995).

Previous studies of the magnetic field of α And exist (Borra & Landstreet 1980, Glagolevskii et al. 1985, Chountonov 2001, Wade et al. 2006)but they did not detect a magnetic field. The best precision was obtained by Wade et al. (2006) with an error bar of $\sim$6 G. However, this was not sufficient to detect an ultra-weak field on α And.

6.3.2 Observations and data analysis

α And was observed 397 times between August 2011 and February 2012 with the Narval spectropolarimeter (see Table 6.7) in circular polarization mode.

6.3.3 Data Analysis

As for all previous stars presented in this thesis, I applied the well-known and commonly used LSD procedure (see Sect. 2.5.2) to each spectrum. Our line list is taken from the VALD atomic data base (Kupka & Ryabchikova 1999; Piskunov et al. 1995) using the respective effective temperature $T_{\rm eff}$=13800 K and log g=4.0 of the primary of α And (Ryabchikova et al. 1999). I rejected the lines whose depth is less than 1% of the continuum, the H lines, and the ones blended with the H lines. By doing so, I obtained a mask of 315 lines. Then, I adjusted the depth of the lines in the mask to fit the observed line depths. To decrease the noise per spectral bin further, I reduce the spectral resolution of the LSD line profiles. Instead of the default spectral bin spanning 1.8 km s^{-1} at a spectral resolution of 65,000, I used a step of 3.6 km s^{-1} which leaves us with about 20 velocity bins in the pseudo-line profile.

I did not obtain a detection of a Zeeman signature in the individual LSD Stokes V profiles of α And. However, their typical S/N remains far too low to detect ultra-weak

TABLE 6.7: **Journal of observations of α And:** the columns contain the date for each Stokes V sequence, the heliocentric Julian date corresponding to the middle of the observation, the number of sequences and the exposure time per individual subexposure, and the averaged S/N in the individual LSD Stokes V pseudo-line profiles ($\pm$ rms).

Date	Mid-HJD	T_{exp} (s)	S/N
09 August 2011	5783.65144	10 × 4 × 40	13341 ± 301
10 August 2011	5784.61910	10 × 4 × 40	13512 ± 156
11 August 2011	5785.64703	10 × 4 × 40	14815 ± 304
16 August 2011	5790.55807	10 × 4 × 40	13070 ± 143
18 August 2011	5792.59612	10 × 4 × 40	10473 ± 455
19 August 2011	5793.56584	10 × 4 × 40	12057 ± 239
20 August 2011	5794.55027	03 × 4 × 40	12743 ± 7299
21 August 2011	5795.58978	07 × 4 × 40	5527 ± 2762
22 August 2011	5796.57960	11 × 4 × 40	12474 ± 777
27 August 2011	5801.65944	10 × 4 × 40	11619 ± 787
28 August 2011	5802.68719	10 × 4 × 40	13953 ± 231
04 October 2011	5839.49693	11 × 4 × 75	18591 ± 273
05 October 2011	5840.49221	11 × 4 × 75	19995 ± 173
09 October 2011	5844.47340	11 × 4 × 75	13856 ± 1226
10 October 2011	5845.36225	10 × 4 × 75	16396 ± 1139
11 October 2011	5846.37076	11 × 4 × 75	12776 ± 637
13 October 2011	5848.36627	11 × 4 × 75	21134 ± 379
14 October 2011	5849.54243	11 × 4 × 75	19171 ± 495
30 October 2011	5865.35945	11 × 4 × 75	15515 ± 3939
31 October 2011	5866.33234	11 × 4 × 75	16859 ± 952
10 November 2011	5876.42637	11 × 4 × 75	14200 ± 5135
12 November 2011	5878.41248	11 × 4 × 75	17436 ± 1152
25 November 2011	5891.34752	11 × 4 × 75	18128 ± 928
26 November 2011	5892.29450	10 × 4 × 75	13500 ± 1526
27 November 2011	5893.34266	11 × 4 × 75	15227 ± 684
28 November 2011	5894.36610	11 × 4 × 75	18479 ± 657
29 November 2011	5895.37864	11 × 4 × 75	17095 ± 6328
30 November 2011	5896.33456	11 × 4 × 75	19484 ± 307
08 December 2011	5904.35069	11 × 4 × 75	16074 ± 1599
10 December 2011	5906.40472	11 × 4 × 75	18963 ± 330
13 January 2012	5940.26348	11 × 4 × 75	19278 ± 714
14 January 2012	5941.26325	11 × 4 × 75	20152 ± 575
15 January 2012	5942.25550	11 × 8 × 75	15900 ± 1031
17 January 2012	5944.27414	11 × 4 × 75	14565 ± 3056
18 January 2012	5945.27492	14 × 4 × 75	14181 ± 1801
23 January 2012	5950.27870	11 × 4 × 75	12903 ± 3065
24 January 2012	5951.27608	11 × 4 × 75	17723 ± 353
25 January 2012	5952.27845	11 × 4 × 75	18985 ± 1368

polarized signatures. I therefore adopted the same strategy as for Vega and the Am stars: I co-added all LSD profiles, resulting in one "grand average" pseudo-line profile. This method was successfully used for Vega (Lignières et al. 2009, Petit et al. 2010) and the Am stars (Petit et al. 2011 and see previous sections) to detect signatures with amplitudes as low as about 10^{-5} of the continuum level. To co-add the LSD profiles, I used the same method as for the Am stars β UMa and θ Leo (see Sect. 6.1.3).

Due to the binarity, the radial velocity of the primary changes over the observations. To co-add the LSD profiles, I thus measured the radial velocity of the primary ($r_{v,p}$) of each intensity profiles that correspond to the primary to shift all LSD profiles by -$r_{v,p}$ before I co-added the LSD profiles. The observations are taken over more than one orbital period. The velocity of the secondary also changes, so co-adding the shifted LSD profiles averaged out the intensity profiles of the secondary with the continuum of the primary. Therefore, the line in the I profiles mainly comes from the primary, α And A.

With the large number of spectra collected here, the co-addition of all profiles increases the S/N by a factor ≈ 30, compared to individual profiles. The resulting S/N of the grand average V profiles is 461720, close to the value I obtained for θ Leo (see Sect. 6.1.3).

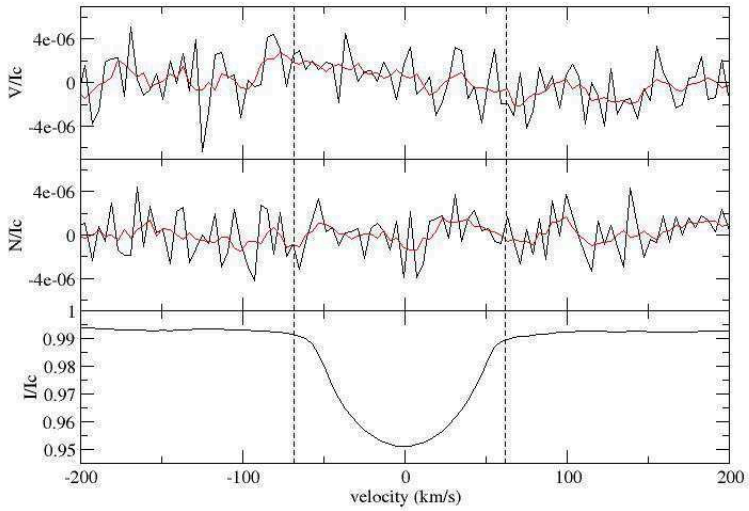

FIGURE 6.9: **Mean LSD profiles of α And A** for Stokes I (bottom), the null N polarization (center), and Stokes V (top). Dashed lines delimit the width of the line profile.

The Stokes I, V, and Null co-added LSD profiles of α And are shown in Fig. 6.9. It does not display a clear Stokes V signature at the radial velocity of the Stokes I line profiles. I computed the detection probability of the Stokes V signal by using the χ^2 (see Sect. 2.5.3), getting a detection probability of $\sim$40% with a FAP around 6 $\times 10^{-1}$. That corresponds to a non-detection of a Zeeman signature inside the stellar lines.

By co-adding all LSD profiles taken at random phases, I lose any phase-resolved information, and the axisymmetric surface structures (i.e., structures symmetric about the spin axis) are the most likely to survive the co-addition process. However, assuming the chemical spots are due to a magnetic field, the rotational period of α And is well known thanks to the Hg variations: P_{rot}=2.38239 ± 0.00011 days (Adelman et al. 2002). Therefore, I can determine at what orbital phase each observation was taken. I assigned the phases using the rotational ephemeris of Adelman et al. (2002)

$$JD = 2449279.689 + 2.38236.n \tag{6.2}$$

where n is an integer.

I then co-added the LSD profiles taken at similar phases. I used a step of 0.1 in phase.

I did not detect signatures in the Stokes V profiles calculated for each phase bin (see Fig. 6.10). The detection probability is between 20 and 90%, which corresponds to non-detections (see Table 6.8). The high detection probability corresponds to the phase bin 0.0-0.1 and 0.9-1.0 and the low probability corresponds to the phase bin 0.3-0.4 and 0.4-0.5. The maximum of the equivalent width of the Hg line at 398.4 nm occurs around the phase ϕ=0.95 and the minimum at the phase ϕ=0.4 (Adelman et al. 2002). Therefore, even though there is no formal detection, the probability seems correlated with the Hg variation. This could be a hint that there is an undetected field, or that the line profile variations influenced the Stokes V measurement. However, the N measurement does not seem correlated with Hg variations.

TABLE 6.8: **Measurement of the longitudinal magnetic field of α And** The columns contain the phase bin, the averaged S/N in the LSD Stokes V pseudo-line profiles (±rms), the longitudinal magnetic field and it error bars and the null polarization and its error bars

Phase	S/N	Detection	$B_l \pm \sigma B_l$	N$\pm\sigma$ N
all	461720	ND	0.8 ± 0.5	-0.2 ± 0.5
0.0-0.1	136819	ND	0.8 ± 1.6	-0.2 ± 1.6
0.1-0.2	155781	ND	2.4 ± 1.3	-1.0 ± 1.3
0.2-0.3	122237	ND	1.7 ± 1.7	-0.6 ± 1.7
0.3-0.4	163117	ND	1.6 ± 1.3	1.5 ± 1.3
0.4-0.5	140252	ND	2.4 ± 1.5	-0.9 ± 1.5
0.5-0.6	150784	ND	0.0 ± 1.4	-2.5 ± 1.4
0.6-0.7	146271	ND	-0.1 ± 1.4	0.6 ± 1.4
0.7-0.8	167229	ND	0.9 ± 1.3	0.4 ± 1.3
0.8-0.9	166801	ND	-0.4 ± 1.2	1.7 ± 1.2
0.9-1.0	157151	ND	1.1 ± 1.4	-1.6 ± 1.4

In spite of the non-detection, using the centre-of-gravity method (see Sect. 2.5.4) with a mean wavelength of 500 nm and a mean Landé factor of ∼1.28 corresponding to the normalization parameters used in the LSD, I calculated the longitudinal field value (B_l) corresponding to these Zeeman measurements over the velocity range [-54:54] km s^{-1}.

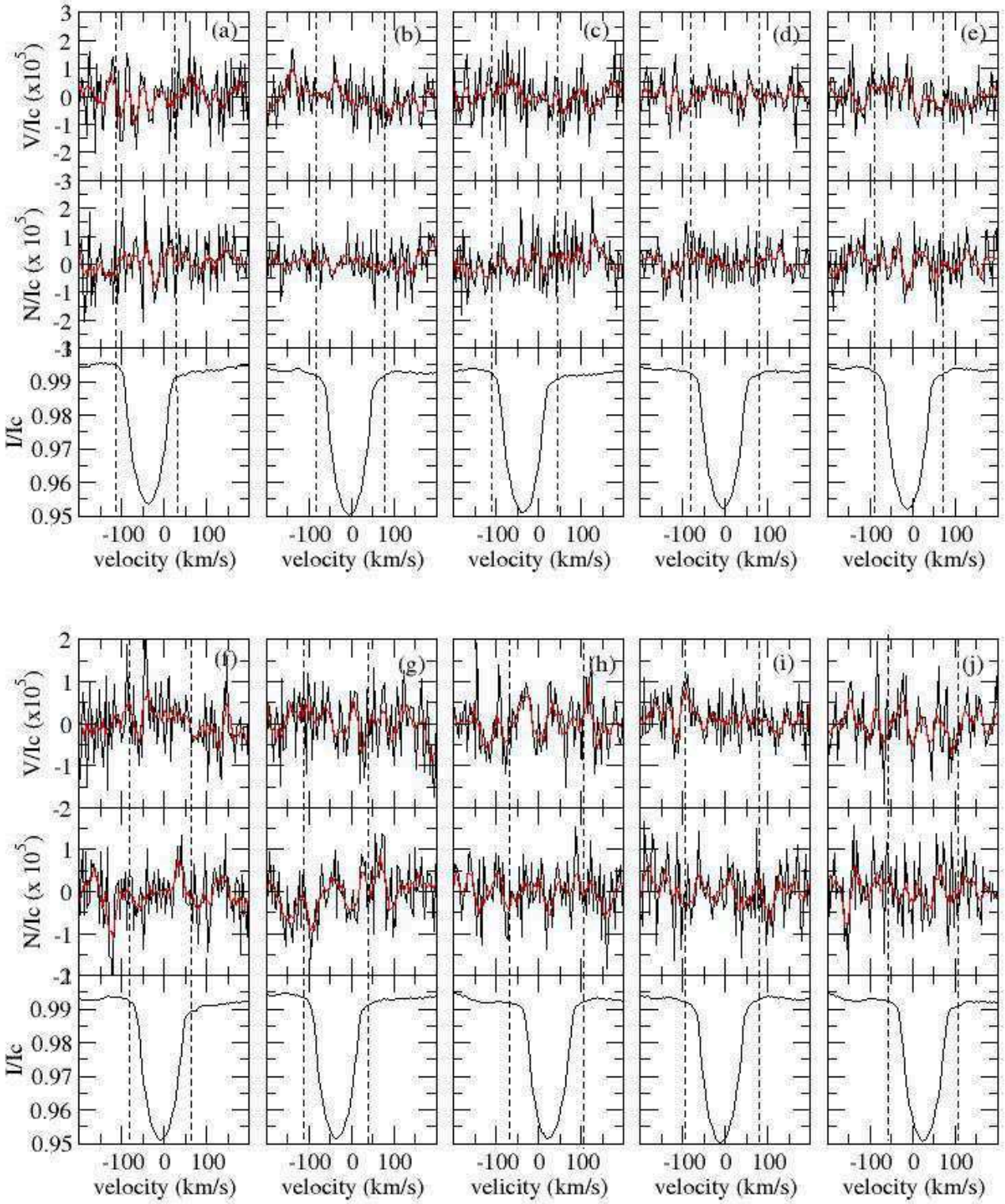

FIGURE 6.10: **Mean LSD profiles of α And A for each phase** for Stokes I (bottom), the null N polarization (center), and Stokes V (top). Panels (a) to (j) correspond to the co-addition of the LSD profiles taken from between 0.0 and 0.1 up to between 0.9 and 1.

The longitudinal magnetic field value for the grand average LSD profiles and the phase-averaged LSD profiles, and the corresponding null values, are shown in Table 6.8.

The longitudinal magnetic field measured in the grand average LSD profile is 0.8 ± 0.5 G. For the phase-averaged LSD profiles, the measured longitudinal magnetic field is between -0.4 and 2.4 G with error bars between 1.2 and 1.7 G. None of the B_l measurements is above 3σ

However, the correlation with the Hg variations suggest that a magnetic field could be hidden in the noise of the Stokes V profiles. I thus used the same method as for ζ Ori Ab (see Sect. 3.6.2) to determine the upper limit of the possible non-detected magnetic field. On the grand-averaged profile, the upper limit of the undetected magnetic field is $\sim$ 90 G.

I also run this method on the phase-averaged Stokes V profiles. The upper limit for the possible undetected dipolar field strength for each phase varies between ∼50 and ∼600 G (see Fig. 6.11).

I extracted a stricter upper limit by combining the 10 phases taking into account that the field has not been detected in any of the 10 phases (see Neiner et al. 2015a). The final upper limit derived from this combined probability for α And A for a 90% detection probability is ∼90 G (see thick line in Fig. 6.11). This is compatible with the value obtained for the grand average profile. If α And hosts a dipolar magnetic field with a strength lower than 90 G, it could have remained hidden in the noise.

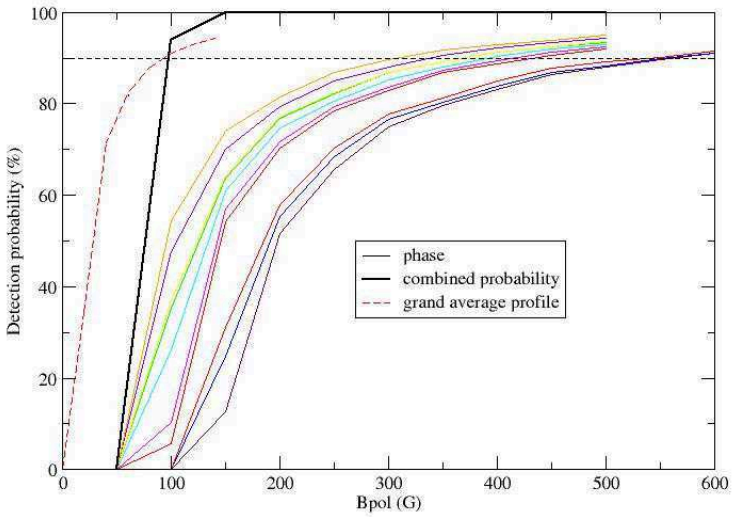

FIGURE 6.11: **Upper limit of the non-detected magnetic field in α And A.** Detection probability of a magnetic field in each phase of α And A (thin color lines) as a function of the magnetic polar field strength. The horizontal dashed line indicates the 90% detection probability, and the thick black curve shows the combined probability. The red dashed line corresponds to the detection probability in the grand average profile.

6.3.4 The secondary: α And B

The secondary component of the α And system is classified as an A3V (Tomkin et al. 1995), with a temperature of 8500 K and a log g = 4. It is also interesting to check for the presence of an ultra-weak magnetic field in the secondary component because it is also an intermediate-mass star. To this aim, I ran again the LSD technique on the α And spectra with a line mask adapted to the temperature and log g of the secondary star, which contains 2576 lines. I did not clean the mask, except for the H lines, because it is difficult to detect the lines of the secondary in the spectra.

I did not detect Zeeman signatures in the individual Stokes V profiles, so I co-added all LSD profiles after correction of the radial velocity of the secondary. Due to the high rotation rate of the secondary ($v \sin i$ =110 km s^{-1}) and the fact that the LSD profiles are polluted by the primary, it is difficult to measure the radial velocity in the intensity profiles. However, the orbital parameters are well known and I calculated the radial velocity of the secondary for each observation thanks to this orbit.

The final S/N is 995229 and I did not detect signatures in the grand average profile of α And B (see Fig. 6.12), with a detection probability of 17% and a FAP of 8.236×10^{-1}.

Despite the high S/N, the error bar on the measured longitudinal magnetic field (B_l=2.8 $\pm$ 3.5 G) over the [-140:150] km s^{-1} domain is too high to detected an ultra-weak magnetic field, due to the high $v \sin i$ (110 km s^{-1}) of α And B.

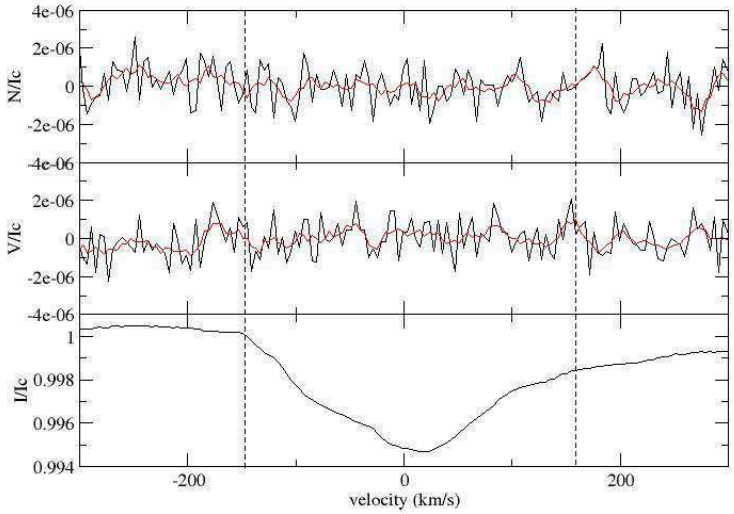

FIGURE 6.12: **Mean LSD profiles of α And B** for Stokes I (bottom), the null N polarization (center), and Stokes V (top).

I calculated the upper limit of a potential magnetic field hidden in the noise of the LSD profiles (see Fig. 6.13). I found an upper limit of ∼240 G. A magnetic field with a strength below 240 G could have remained undetected. This value is lower than the

upper limit of the magnetic desert, thus α And does not host a strong magnetic field but could host a weak magnetic field that cannot be detected with our data.

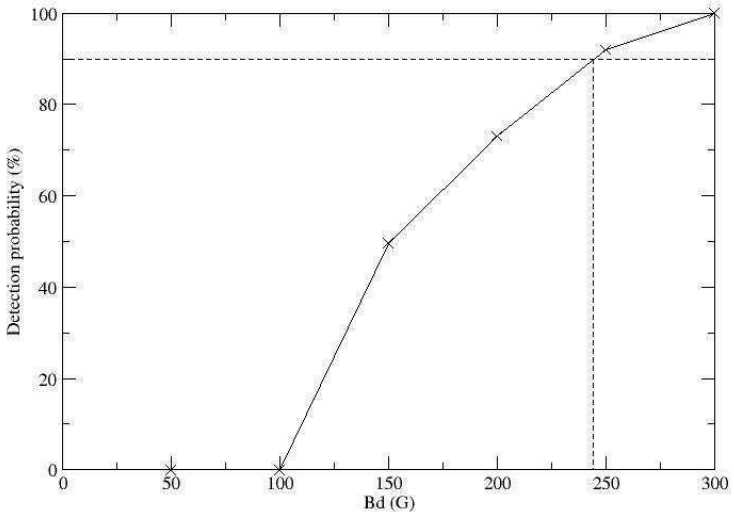

FIGURE 6.13: **Upper limit of the non-detected magnetic field in α And B.** Detection probability of a magnetic field in the grand average LSD profiles of α And B as a function of the magnetic polar field strength. The horizontal dashed line indicates the 90% detection probability.

6.3.5 Conclusion

Based on Narval spectropolarimetric data, I did not detect an ultra-weak field on the HgMn star α And A. The longitudinal field measurements correspond to a non significant detection for the grand average profile and for the phase-averaged profiles. I reached a precision of 0.5 G for the longitudinal magnetic field when I co-added all LSD profiles and a precision between 1.2 and 1.7 G for the phase-averaged LSD profiles. It is the first time that such a precision is reached for an HgMn star. Nevertheless, the upper limit of the non-detected dipolar magnetic field is ∼90 G. A dipolar magnetic field with a strength below 90 G could exist on α And A and have remained undetected in our data. A hint is provided by the correlation between the detection probability and Hg variations, that should be further tested with future additional data.

For the secondary, I did not detect a magnetic field in the grand average profile, due to the high $v \sin i$ of α And B. The accuracy is not enough to detect an weak magnetic field. The upper limit of the possible non detected magnetic field is ∼240G.

6.4 Conclusion

I demonstrated the existence of a new class of magnetic intermediate-mass stars: the magnetic Am stars. These stars host an ultra-weak magnetic field. The detection rate is 100% as soon as deep spectropolarimetric studies of Am stars are performed. However, only 4 Am stars have been studied with the required precision to detect ultra-weak magnetic fields so far. Moreover, all the studied Am stars have similar stellar parameters: they are hot Am stars and they have a weak Am character. Although we have a detection of an ultra-weak magnetic field in all Am stars, the shape of their magnetic signatures are different: some exhibit peculiar signatures with a positive prominent lobe and some exhibit normal signatures. Spectropolarimetric studies of cooler and more peculiar Am stars could bring us constraints on the physical processes that occur in Am stars and help us determine if the amplitude and shape of the signatures depend on specific stellar parameters. One hypothesis to explain the dichotomy between the peculiar and the normal signatures is based on the microturbulence : observing additional Am stars will help us to determine if this hypothesis is correct.

In addition, some HgMn stars show Hg line variations (Adelman et al. 2002), which can be interpreted as a consequence of a non-uniform photospheric abundance distribution. For Ap/Bp stars the magnetic field is indeed one of the most important ingredients to explain the non-uniform photospheric abundance distribution and scenarios to explain the variability in the HgMn stars also require a weak magnetic field (less than 100 Gauss, see e.g. Alecian 2012). The deeply spectropolarimetric study of the HgMn star α And did not reveal the existence of a magnetic field in this star. I reached a precision of 0.5G, however the limit of the non-detected dipolar magnetic field is 90 G. Thus, if a magnetic field exists on α And, its strength is below 90 G, which would be compatible with the required field strength in the scenarios mentioned above.

Chapter 7

Conclusions and perspectives

The observational studies performed during my PhD thesis bring new information about the magnetism of massive and intermediate-mass stars and they will allow us to better understand the properties of the different kinds of magnetic fields that exist in these stars.

At the surface of hot stars, two kinds of magnetic fields exist: the strong and the weak magnetic fields, separated by a magnetic desert between B_d of a few and ∼300 G. The latter was discovered for the first time on Vega (Lignières et al. 2009). This detection raised the issue of the existence of weak fields in all hot stars that do not host a strong magnetic field. A second weak magnetic field was discovered on the Am star Sirius (Petit et al. 2011). However, the peculiarity of the shape of the signature with one prominent positive lobe was not expected in the Zeeman theory and questioned the possible magnetic origin. Some scenarios were developed to explain the dichotomy between the strong and the weak magnetic fields. My works brings constraints to improve these scenarios by searching for weak magnetic fields in hot stars and studying the weakest of the strong magnetic hot stars.

In the first part of my thesis, I studied the strong magnetic fields to constraint the upper limit of the magnetic desert. I confirmed the magnetic field of ζ Ori A and I determined that it is the primary ζ Ori Aa, a supergiant O star, which is magnetic. It is the first detection of a magnetic field in a supergiant O star. The dipolar magnetic field B_d ∼140 G is weaker than the previously known upper limit of the magnetic desert. However, while I find a rotational modulation of ∼6.829 days with the data taken in 2007 and 2008, this rotational modulation disappears in the data taken in 2011-2012. This disappearance is not expected in hot stars, because the magnetic field is fossil and stable over the life of the star. I showed that this apparent change in magnetism is likely not due to the binarity, the distance between the two components is too large to produce tidal interactions. ζ Ori Ab is a B star, and no magnetic field was detected on its surface. However, a magnetic field can remain hidden in the noise of the LSD profiles. The strict upper limit of the non-detected magnetic field of ζ Ori Ab is ∼ 150 G. ζ Ori Aa remain an interesting star and needs to be observed again to understand what happens with the magnetic field on this star. For example, recent photometric

observations of ζ Ori show that the apparent variation in the magnetic field of ζ Ori Aa might be due to mass-loss events (Buysschaert et al. 2016, in prep.)

In addition, the scenario developped by Aurière et al. (2007) predicts that the upper limit of the magnetic desert depends on the rotation of the star based on an analysis of Ap/Bp stars. However, in this study, there is a lack of obervations of fast rotators with a rotational period less than 2 days. To improve the observational constraint for this scenario, I analyzed data of 6 Ap/Bp stars with known rotational periods and for which the magnetic field has not been detected or only marginally detected. I determined the dipolar magnetic field for only three of them. For two of them the dipolar magnetic field is less than the predicted upper limit of the magnetic desert given by the relation of Aurière et al. (2007). For one of the stars, the S/N of the observations was not high enough to detect the signatures of the magnetic field. This means that its magnetic field is weak. Observing it again to improve the S/N, and observing other Ap/Bp stars with non-detected or marginally detected magnetic fields, will bring additional constraints on the observational upper limit of the magnetic desert.

A second part of my thesis was dedicated to the search for weak magnetic fields and to study their properties in hot stars. The scenarios developed to explain the dichotomy (Aurière et al. 2007; Braithwaite & Cantiello 2013) predict that all hot stars that do not host a strong magnetic field have a weak magnetic field like the one of Vega. However, due to the weakness of the expected Zeeman signatures, it is challenging to detect such fields and it takes a lot of observing time per star.

I first searched for variability over the years in the magnetic field of Vega. I found that the magnetic field of Vega is stable over 7 years of observations, which no variation in the Stokes V profiles nor in intensity. This confirms that the magnetic field of Vega is of fossil origin, as predicted by the various scenarios to explain the dichotomy between strong and weak magnetic fields.

I then analyzed the data of another normal star: UZ Lyn. During one night of observations I obtained a marginal detection. However, I did not get a detection in the grand-average LSD profile, with a detection probability of $\sim$67%. The precision, I reached is 1 G, which is not enough to detect a magnetic field like the one of Vega. The inclination of UZ Lyn is unknown, so the grand-average includes data taken at random phases, which can average out the magnetic field over the surface of the star. The co-addition of all observations is a good method to detect the magnetic field of the pole-on star Vega, but it is not the best method to detect an ultra-weak magnetic field on UZ Lyn. To know if UZ Lyn hosts a weak magnetic field or not, we should observe it again by changing the observational strategy: take more observations per night to avoid the phase smearing problem.

To check whether weak magnetic fields also exist in higher-mass stars, I initiated an observational program to search for weak magnetic fields on B stars. I carefully chose the targets for this study. Two stars have been observed so far: ι Her and γ Peg. They are the easiest targets due to their brightness and their very low $v \sin i$. I planned to reach a precision of 0.1 G for these stars. However, due to bad weather conditions, the S/N of the LSD profiles is not high enough to reach the required precision. With the achieved data quality, I did not obtain a detection of a magnetic field on ι Her

and γ Peg. However, the probability of detection inside the stellar line is not null: I obtained 86% for ι Her and 55% for γ Peg. New observations of these stars are planned to reach the precision of 0.1 G. Whatever the result of these studies, they will improve our understanding of weak magnetic fields. If we detect a magnetic field, it will confirm the fossil field scenario and if we do not detect a magnetic field, new scenarios will have to be developed to explain why weak magnetic fields exist in A stars and not in B stars.

In addition, I discovered a new class of magnetic stars: the weakly magnetic Am stars. Only 4 stars were observed with the required precision to detect weak magnetic fields, and all of them host a weak magnetic field. Three of them (Sirius A, β UMa and θ Leo) show peculiar magnetic signatures with a prominent positive lobe and one (Alhena) star a normal Zeeman signature. The measured longitudinal magnetic field for Alhena is around -6 G and gives a minimum dipolar field $B_{d,min} \sim 30$ G. That is weak but it is higher than the one of Vega ($\sim$ 7 G, Petit et al. 2010). The preliminary explanation for the peculiar signatures observed in most Am stars is a combination of a gradient in velocity and in magnetic field. This explanation is sustained by the fact that these Am stars have a high microturbulence and host a superficial layer of convection at their surface. Moreover, some preliminary models reproduce this kind of signatures. The Am star that hosts a normal signature (Alhena) has a lower microturbulence compared to the other Am stars. Therefore, microturbulence could be an explanation for the peculiar versus normal signatures in Am stars. All Am stars observed so far have similar spectral parameters (temperature, mass, radius, metallicity,...), they are hot and weakly Am stars. Observing cooler Am stars and stronger Am stars could help us to understand the physical processes that produce the peculiar signatures and determine if the amplitude and the shape of the magnetic signatures depend on particular stellar parameters.

On the Ap/Bp stars, the non-uniform chemical abundances at the surface of the stars are explained by the presence of a strong magnetic field. Some HgMn stars show similar non-uniform abundances at their surface. Some spectropolarimetric studies concluded that HgMn stars did not host a strong magnetic field. However, some theories to explain the non-uniform abundance on the surface of HgMn stars argue that it is due to a weak magnetic field (Alecian 2012). Moreover, I showed that the Am stars host a weak magnetic field that can be linked to the chemical peculiarity. Therefore, I analyzed the data of α And, a well known HgMn star. When, I co-added all individual LSD profiles data taken at different rotational phases, I reached a precision of 0.5 G, which was not sufficient to detect a weak magnetic field. The period of α And is well known, so I also co-added the data taken at similar phases. The precision is then between 1.3 and 2.4 G. I did not detected a magnetic field in the phase-average LSD profiles neither, however the probability of detection reached 89% for one phase and seems to be correlated with the variations of the Hg lines. It is not enough to claim a detection but it provides an encouraging hint for further observations of this star. The upper limit of a non-detected magnetic field in α And is $\sim$ 90 G. It is the only HgMn star studied with such a high precision, close to the one of Vega.

For the moment, the only known weakly magnetic stars are the normal A star Vega and the Am stars Sirius A, θ Leo, β UMa, and Alhena. The search for weak magnetic fields is very challenging and telescope time consuming. However, it important to continue

to explore it because magnetic fields play a fundamental role in stellar evolution. If we demonstrate that weak magnetic fields are common in hot stars, it would have a strong impact on stellar evolution models. Strong magnetic fields concern only a small fraction of hot stars and have thus been ignored in most stellar evolution codes until recently. One strategy to detect weak magnetic fields will be to observe stars which are known to be viewed pole-on or stars with a well known rotational period.

To conclude my thesis, the magnetic fields seem to be weaker in massive stars than in intermediate-mass stars, both for the strong magnetic fields and the weak magnetic fields. This is probably because the radius of massive stars is larger than the one of the intermediate-mass stars. This trend was confirmed by the discovery of a dipolar magnetic field with a strength of 100-150 G on the massive main sequence star ζ Cas (Briquet et al. 2016). The dipolar magnetic field of ζ Ori Aa is also weaker than the upper limit of the magnetic desert. However, it is a supergiant star, so it is evolved and its radius has increased. By conservation of the magnetic flux, the strength of its field has thus decreased. However, it is interesting to study the magnetism of evolved hot stars to know the influence of the magnetic field on evolution and how fossil fields evolve during the last stages of the life of hot stars.

The upper limit of the magnetic desert predicted by the scenario developped by Aurière et al. (2007) depends on the stellar rotation. This prediction is supported by the results of simulation, Jouve et al. (2015) found that the upper limit of the magnetic desert depends on the rotation rate. Even if no observations contradict this dependence, the studies of the dipolar field of Ap/Bp stars do not allow us to confirm dependence. The new studies of Ap/Bp stars such as the one presented in this thesis, try to fill the lack of observations for fast rotators. However, it is challenging to detect the Zeeman signatures in fast rotators because almost all of them have a high $v \sin i$ and the S/N is sometimes not enough to detect the Zeeman signatures. We should reobserve these stars and other rapidly rotating Ap/Bp stars with a high precision to characterize the dipolar magnetic field and determine the rotational dependence.

Some theoretical works showed that, during the pre-main sequence, fields relax onto a stable mixed configuration of poloïdal and toroïdal field, whatever the rotation of the star (Emeriau & Mathis 2015). These works supported the fossil field origin. However, the relaxation time needed to reach equilibrium increases with rotation (Braithwaite & Cantiello 2013). Therefore, it is probably more difficult for a rapidly rotating star to reach a stable dipolar configuration. However, Am stars are slow rotators and they host weak magnetic fields. The rotation may thus not be the only ingredient of the dichotomy in hot stars. Detecting new ultra-weak fields would improve our knowledge of the properties of these fields and bring constraints for theories.

Finally, the magnetic field is rarely taken into account in stellar evolution models of hot stars due to the fact that, until recently, only 7% of hot stars were known magnetic. However, magnetic fields influence significantly the evolution of stars, even if they are weak. Weak magnetic fields are predicted to exist in all hot stars that do not host strong magnetic fields. Now, we know that weak magnetic fields exist at the surface of Vega (Lignières et al. 2009) and 4 Am stars (Petit et al. 2011 and this thesis). In addition, there are some hints about the existence of a weak magnetic field in two B stars (ι Her

and γ Peg) and on a normal A star UZ Lyn. If we demonstrate that weak fields are common in hot stars, the modeling should integrate it and this may change our picture of the evolution of hot stars.

Appendix A

Paper on the magnetic field of ζ Ori A

A&A 582, A110 (2015)
DOI: 10.1051/0004-6361/201526855

Astronomy & Astrophysics

The magnetic field of ζ Orionis A[⋆,⋆⋆]

A. Blazère[1], C. Neiner[1], A. Tkachenko[2], J.-C. Bouret[3], Th. Rivinius[4], and the MiMeS collaboration

[1] LESIA, Observatoire de Paris, PSL Research University, CNRS, Sorbonne Universités, UPMC Univ. Paris 06, Univ. Paris Diderot, Sorbonne Paris Cité, 5 place Jules Janssen, 92195 Meudon, France
e-mail: aurore.blazere@obspm.fr
[2] Instituut voor Sterrenkunde, KU Leuven, Celestijnenlaan 200D, 3001 Leuven, Belgium
[3] Aix-Marseille University, CNRS, LAM (Laboratoire d'Astrophysique de Marseille), UMR 7326, 13388 Marseille, France
[4] ESO – European Organisation for Astron. Research in the Southern Hemisphere, Casilla 19001, Santiago, Chile

Received 29 June 2015 / Accepted 5 August 2015

ABSTRACT

Context. ζ Ori A is a hot star claimed to host a weak magnetic field, but no clear magnetic detection was obtained so far. In addition, it was recently shown to be a binary system composed of a O9.5I supergiant and a B1IV star.
Aims. We aim at verifying the presence of a magnetic field in ζ Ori A, identifying to which of the two binary components it belongs (or whether both stars are magnetic), and characterizing the field.
Methods. Very high signal-to-noise spectropolarimetric data were obtained with Narval at the *Bernard Lyot* Telescope (TBL) in France. Archival HEROS, FEROS and UVES spectroscopic data were also used. The data were first disentangled to separate the two components. We then analyzed them with the least-squares deconvolution technique to extract the magnetic information.
Results. We confirm that ζ Ori A is magnetic. We find that the supergiant component ζ Ori Aa is the magnetic component: Zeeman signatures are observed and rotational modulation of the longitudinal magnetic field is clearly detected with a period of 6.829 d. This is the only magnetic O supergiant known as of today. With an oblique dipole field model of the Stokes V profiles, we show that the polar field strength is ∼140 G. Because the magnetic field is weak and the stellar wind is strong, ζ Ori Aa does not host a centrifugally supported magnetosphere. It may host a dynamical magnetosphere. Its companion ζ Ori Ab does not show any magnetic signature, with an upper limit on the undetected field of ∼300 G.

Key words. stars: magnetic field – stars: massive – binaries: spectroscopic – supergiants – stars: individual: zeta Ori A

1. Introduction

Magnetic fields play a significant role in the evolution of hot massive stars. However, the basic properties of the magnetic fields of massive stars are poorly known. About 7% of the massive stars are found to be magnetic at a level that is detectable with current instrumentation (Wade et al. 2014). In particular, only 11 magnetic O stars are known. Detecting magnetic field in O stars is particularly challenging because they only have few, often broad, lines from which to measure the field. There is therefore a deficit in the knowledge of the basic magnetic properties of O stars.

We here study the O star ζ Ori A. A magnetic field seems to have been detected in this star by Bouret et al. (2008). Their detailed spectroscopic study of the stellar parameters led to the determination of an effective temperature of $T_{\rm eff}$ = 29 500 ± 1000 K and $\log g$ = 3.25 ± 0.10 with solar abundances. This makes ζ Ori A the only magnetic O supergiant. Moreover, Bouret et al. (2008) found a magnetic field of 61 ± 10 G, which makes it the weakest ever reported field in a hot massive star (typically ten times weaker than those detected in other magnetic massive stars). They found a rotational period of ∼7 days from the temporal variability of spectral lines and the modulation of the Zeeman signatures. To derive the magnetic properties, they used six lines that are not or only weakly affected by the wind. The rotation period they obtained is compatible with their measured $v \sin i$ = 100 km s^{-1}.

In addition, the measurement of the magnetic field provided by Bouret et al. (2008) allows characterizing the magnetosphere of ζ Ori A and locating it in the magnetic confinement-rotation diagram (Petit et al. 2013): ζ Ori A is the only known magnetic massive star with a confinement parameter below 1, that is, without a magnetosphere.

For all these reasons, the study of the magnetic field of ζ Ori A is of the highest importance. Each massive star that is detected to be magnetic moves us closer to understanding the stellar magnetism of hot stars. Studying this unique magnetic massive supergiant is also of particular relevance for our understanding of the evolution of the magnetic field in hot stars.

ζ Ori A has a known B0III companion, ζ Ori B. In addition, Hummel et al. (2013) found that ζ Ori A consists of two companion stars located at 40 mas of each other, orbiting with a period of 2687.3 ± 7.0 days. To determine a dynamical mass of the components, Hummel et al. (2013) analyzed archival spectra to measure the radial velocity variations. The conclusions reached are presented below. The primary ζ Ori Aa is a O9.5I supergiant star, whose radius is estimated to 20.0 ± 3.2 $R_\odot$ and whose mass is estimated to 33 ± 10 $M_\odot$. The secondary ζ Ori Ab is a B1IV with an estimated radius of 7.3 ± 1.0 $R_\odot$ and an estimated mass of 14 ± 3 $R_\odot$. Moreover, ζ Ori A is situated at a distance

⋆ Based on observations obtained at the Télescope *Bernard Lyot* (USR5026) operated by the Observatoire Midi-Pyrénées, Université de Toulouse (Paul Sabatier), Centre National de la Recherche Scientifique of France.
⋆⋆ Appendix A is available in electronic form at http://www.aanda.org

of 387 pc. Initial estimates of the elements of the apparent orbit were obtained by Hummel et al. (2013) using the Thiele-Innes method. The estimation provided a value of the periastron epoch of JD 2 452 734.2 ± 9.0 with a longitude of 24.2 ± 1.2°. The eccentricity is estimated to be 0.338 ± 0.004.

Bouret et al. (2008) considered ζ Ori A as a single star of 40 $M_\odot$ with a radius equal to 25 $R_\odot$, seen from Earth at an inclination angle of 40°. Taking into account that the star is a binary could strongly modify the magnetic field value derived for only one of the binary components. In their analysis, the magnetic signature was normalized by the full intensity of the lines from both components, and if only one of the two stars is magnetic, the field was thus underestimated. Moreover, the position in the magnetic confinement-rotation diagram will be modified as a result of the new magnetic strength value, but also as a consequence of the new stellar parameters.

Based on new spectropolarimetric observations of ζ Ori A and archival spectra presented in Sect. 2, we here seek to confirm that ζ Ori A is a magnetic star (Sect. 3). We determine with several techniques, including by disentangling the composite spectrum (Sect. 4) whether the magnetic field is hosted by the primary or the secondary star of ζ Ori A. We then determine the field strength of the magnetic component (Sect. 5) and quantify the non-detection of a field in the companion (Sect. 6). In addition, we investigate the rotational modulation of the magnetic field, its configuration (Sect. 7), and the possible presence of a magnetosphere (Sect. 8). Finally, we discuss our results and draw conclusions in Sect. 9.

2. Observations

2.1. Narval spectropolarimetric observations

Spectropolarimetric data of ζ Ori A were collected with Narval in the frame of the project Magnetism in Massive Stars (MimeS; see e.g. Neiner et al. 2011). This is the same instrument with which the magnetic field of ζ Ori A was discovered by Bouret et al. (2008). Narval is a spectropolarimeter installed on the two-meter *Bernard Lyot* Telescope (TBL) at the summit of the Pic du Midi in the French Pyrénées. This fibre-fed spectropolarimeter (designed and optimized to detect stellar magnetic fields through the polarization they generate) provides complete coverage of the optical spectrum from 3700 to 10 500 Å on 40 echelle orders with a spectral resolution of ~65 000. Considering the size of the fiber, the light from ζ Ori B was not recorded in the spectra, but light from both components of ζ Ori A was collected.

ζ Ori A was first observed in October 2007 during 7 nights (PI: J.-C. Bouret) and these data were used in Bouret et al. (2008). Then, this star was observed again in October 2008 during 5 nights (PI: J.-C. Bouret) and between October 2011 and February 2012 during 24 nights by the MiMeS collaboration (PI: C. Neiner). This provides a total number of 36 nights of observations. The observations were taken in circular polarimetric mode, that is, measuring Stokes V. Each measurement was divided into four subexposures with a different polarimeter configuration.

Since ζ Ori A is very bright (V = 1.77), only a very short exposure time could be used to avoid saturation. To increase the total signal-to-noise ratio (S/N), we thus obtained a number of successive measurements each night, which were co-added. The exposure time of each subexposure of each measurement varies between 20 and 120 s, and the total integration time for a night varies between 1280 and 7680 s (see Table 1).

Table 1. Journal of Narval observations.

#	Date	mid-HJD	$T_{\rm exp}$ (s)	S/N	$\phi_{\rm orb}$
1	17 Oct. 07	2 454 391.559	48 × 4 × 20	4750	0.617
2	18 Oct. 07	2 454 392.719	8 × 4 × 40	2220	0.617
3	19 Oct. 07	2 454 393.570	44 × 4 × 40	6940	0.617
4	20 Oct. 07	2 454 394.491	48 × 4 × 40	6860	0.618
5	21 Oct. 07	2 454 395.518	48 × 4 × 40	7070	0.618
6	23 Oct. 07	2 454 397.496	48 × 4 × 40	7180	0.619
7	24 Oct. 07	2 454 398.526	48 × 4 × 40	7270	0.619
8	22 Oct. 08	2 454 762.644	40 × 4 × 50	6660	0.755
9	23 Oct. 08	2 454 763.645	38 × 4 × 50	5530	0.755
10	24 Oct. 08	2 454 764.654	36 × 4 × 50	6790	0.756
11	25 Oct. 08	2 454 765.639	37 × 4 × 50	6140	0.756
12	26 Oct. 08	2 454 766.635	38 × 4 × 50	6420	0.756
13	04 Oct. 11	2 455 839.688	12 × 4 × 90	5810	0.156
14	05 Oct. 11	2 455 840.670	12 × 4 × 90	5790	0.156
15	10 Oct. 11	2 455 845.608	12 × 4 × 90	2040	0.158
16	11 Oct. 11	2 455 846.632	12 × 4 × 90	3450	0.158
17	30 Oct. 11	2 455 865.712	12 × 4 × 90	5610	0.165
18	07 Nov. 11	2 455 873.557	5 × 4 × 90	2700	0.168
19	11 Nov. 11	2 455 877.626	12 × 4 × 90	4860	0.170
20	12 Nov. 11	2 455 878.565	12 × 4 × 90	4830	0.170
21	24 Nov. 11	2 455 890.673	12 × 4 × 90	4180	0.175
22	25 Nov. 11	2 455 891.660	12 × 4 × 90	4900	0.175
23	26 Nov. 11	2 455 892.502	12 × 4 × 90	4490	0.175
24	29 Nov. 11	2 455 895.667	12 × 4 × 90	5400	0.176
25	30 Nov. 11	2 455 896.600	6 × 4 × 90	2030	0.177
26	14 Dec. 11	2 455 910.477	12 × 4 × 90	1360	0.182
27	08 Jan. 12	2 455 935.555	12 × 4 × 90	5630	0.191
28	13 Jan. 12	2 455 940.536	12 × 4 × 90	5060	0.193
29	14 Jan. 12	2 455 941.539	12 × 4 × 90	5350	0.193
30	15 Jan. 12	2 455 942.475	12 × 4 × 90	4680	0.194
31	16 Jan. 12	2 455 943.367	12 × 4 × 90	4520	0.194
32	25 Jan. 12	2 455 952.529	12 × 4 × 90	5120	0.198
33	26 Jan. 12	2 455 953.431	8 × 4 × 90	3200	0.198
34	08 Feb. 12	2 455 966.472	12 × 4 × 90	3900	0.203
35	09 Feb. 12	2 455 967.402	11 × 4 × 120	4340	0.203
36	10 Feb. 12	2 455 968.343	12 × 4 × 90	2198	0.203

Notes. The columns list the date and the heliocentric Julian date (HJD) for the middle of observation, the number of sequences, and the exposure time per individual subexposure, the signal-to-noise ratio in the I profiles, and the orbital phase.

Data were reduced at the telescope using the Libre-Esprit reduction package (Donati et al. 1997). We then normalized each of the 40 echelle orders of each of the 756 spectra with the continuum task of IRAF[1]. Finally, we co-added all the spectra obtained within each night to improve the S/N, which varies between 1360 and 7270 in the intensity spectra (see Table 1). We therefore obtained 36 nightly averaged measurements.

2.2. Archival spectroscopic observations

In addition to the spectropolarimetric data, we used archival spectroscopic data of ζ Ori A taken with various echelle spectrographs.

[1] IRAF is distributed by the National Optical Astronomy Observatories, which are operated by the Association of Universities for Research in Astronomy, Inc., under cooperative agreement with the National Science Foundation.

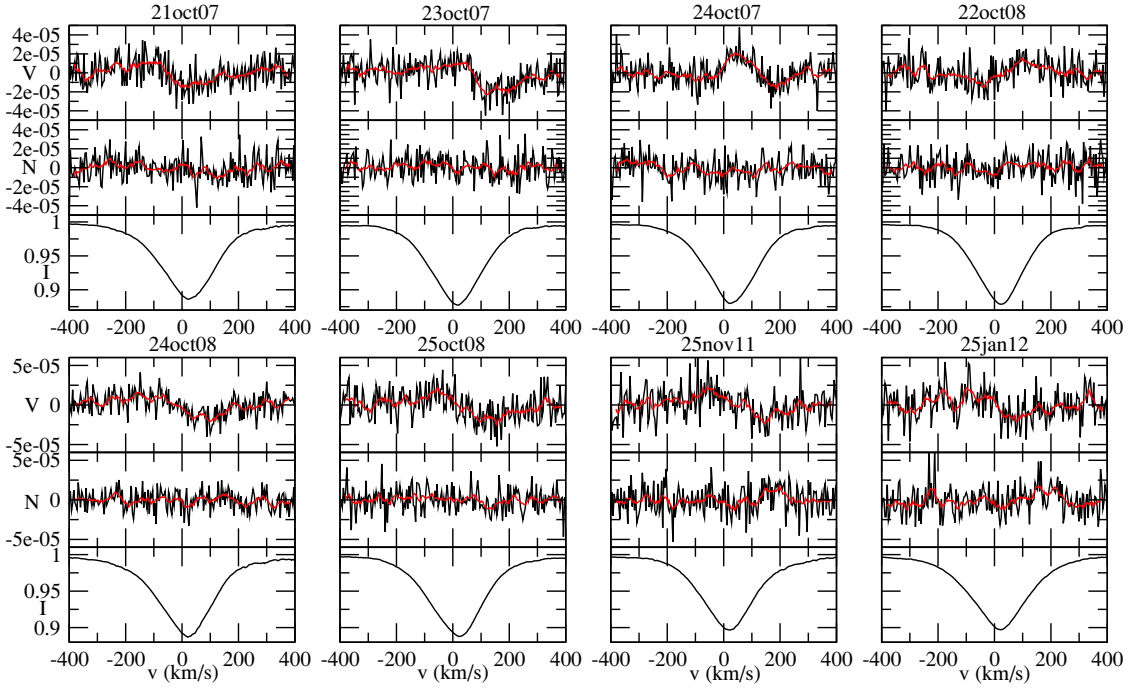

Fig. 1. LSD Stokes I (*bottom*), Stokes V (*top*), and null N (*middle*) profiles, normalized to Ic, for 8 selected nights. The red line is a smoothed profile.

Table 2. Journal of archival spectroscopic observations of ζ Ori A obtained with HEROS, FEROS and UVES.

Date	JD	Instrument	$T_{\rm exp}$	S/N	$\phi_{\rm orb}$
1995	2 449 776.024	HEROS	57 × 1200	1200	0.90
1997	2 450 454.379	HEROS	16 × 1200	1000	0.15
1999	2 451 147.333	HEROS	64 × 1200	1200	0.41
2006	2 453 738.159	FEROS	60	100	0.37
2007	2 454 501.018	FEROS	2 × 20	250	0.66
2009	2 454 953.970	FEROS	5 × 10	200	0.84
2010	2 455 435.373	UVES	36 × 2	2000	0.01

Notes. Columns: date and heliocentric Julian date, instrument used, exposure time, signal-to-noise ratio, and orbital phase.

In 1995, 1997 and 1999, spectra were obtained with the HEROS instrument, installed at the ESO Dutch 0.9 m telescope at the La Silla Observatory. The spectral resolution of HEROS is 20 000, with a spectral domain from about 350 to 870 nm. In addition, in 2006, 2007 and 2009, data were taken with the FEROS spectrograph installed at the ESO 2.2 m at the La Silla observatory. The spectral resolution of FEROS is about 48 000 and the spectral domain ranges from about 370 to 900 nm. Finally, in 2010, spectra were taken with the UVES spectrograph (Dekker et al. 2000) installed at the VLT at the Paranal Observatory. Its spectral domain ranges from about 300 to 1100 nm with a spectral resolution of 80 000 and 110 000 in the blue and red domains respectively.

We co-added spectra collected for each year to improve the final S/N. We therefore have seven spectra for seven different years, with a S/N of between about 100 and 2000 (see Table 2).

3. Checking for the presence of a magnetic field

The magnetic field of ζ Ori A claimed by Bouret et al. (2008) has not been confirmed by independent observations so far and one of the goals of this study is to confirm or disprove its existence using additional observations.

To test whether ζ Ori A is magnetic, we applied the least-squares deconvolution (LSD) technique (Donati et al. 1997). We first created a line mask for ζ Ori A. We started from a list of lines extracted from VALD (Piskunov et al. 1995; Kupka & Ryabchikova 1999) for an O star with $T_{\rm eff}$ = 30 000 K and $\log g$ = 3.25, with their Landé factors and theoretical line depths. We then cleaned this line list by removing the hydrogen lines, the lines that are blended with hydrogen lines, and those that are not visible in the spectra. We also added some lines visible in the spectra that were not in the original O-star mask. Altogether, we obtained a mask of 210 lines. We then adjusted the depth of these 210 lines in the mask to fit the observed line depths.

Using the final line mask, we extracted LSD Stokes I and V profiles for each night. We also extracted null (N) polarization profiles to check for spurious signatures. The LSD I, Stokes V and the null N profiles are shown in Fig. 1 for 8 of 36 nights. A plot of all profiles is available in Fig. A.1. Zeeman signatures are clearly seen for these 8 nights and some others as well, but are not systematically observed for all nights. We calculated the false alarm probability (FAP) by comparing the signal inside the lines with no signal (Donati et al. 1997). If FAP < 0.001%, the magnetic detection is definite; if it is 0.001% < FAP < 0.1% the detection is marginal, otherwise there is no detection. Table 3 indicates whether a definite detection (DD), marginal detection (MD) or no detection (ND) was obtained for each of the night. DD or MD were obtained

Table 3. Longitudinal magnetic field of the magnetic primary star ζ Ori Aa.

#	mid-HJD	B_l	σB_l	Detect.	N	σN
1	2 454 391.559	–5.7	7.7	MD	–3.9	7.7
2	2 454 392.719	–26.9	16.6	ND	37.2	16.6
3	2 454 393.570	–9.3	5.5	ND	3.6	5.5
4	2 454 394.491	–0.3	5.4	ND	6.3	5.4
5	2 454 395.518	18.1	5.2	MD	12.4	5.4
6	2 454 397.496	25.5	5.1	MD	3.9	5.1
7	2 454 398.526	4.7	5.1	MD	–3.7	5.1
8	2 454 762.644	–15.1	5.5	MD	–6.9	5.5
9	2 454 763.645	12.8	6.6	ND	–5.4	6.6
10	2 454 764.654	28.0	5.3	MD	3.6	5.3
11	2 454 765.639	32.8	6.3	DD	11.1	6.3
12	2 454 766.635	10.9	6.4	MD	12.7	6.4
13	2 455 839.688	–3.9	6.5	ND	2.9	6.5
14	2 455 840.670	3.9	6.5	ND	–6.7	6.6
15	2 455 845.608	21.3	9.4	ND	4.8	9.4
16	2 455 846.632	–9.7	11.0	ND	–1.8	11.0
17	2 455 865.712	12.4	6.5	ND	–0.9	6.6
18	2 455 873.557	25.2	13.5	MD	–3.6	13.5
19	2 455 877.626	13.6	7.5	ND	–13.5	7.5
20	2 455 878.565	7.7	7.5	ND	6.8	7.5
21	2 455 890.673	6.1	8.7	ND	11.0	8.7
22	2 455 891.660	24.0	7.4	MD	–6.7	7.4
23	2 455 892.502	6.0	8.1	ND	–11.4	8.1
24	2 455 895.667	1.3	6.9	ND	–8.0	6.9
25	2 455 896.600	–22.6	22.3	ND	22.3	22.5
26	2 455 910.477	4.1	13.8	ND	13.6	13.8
27	2 455 935.555	–7.2	7.0	MD	4.2	7.0
28	2 455 940.536	5.9	7.2	ND	–10.1	7.2
29	2 455 941.539	–3.1	6.8	MD	4.5	6.8
30	2 455 942.475	–5.3	8.0	ND	–4.4	8.0
31	2 455 943.367	4.8	8.4	ND	4.3	8.4
32	2 455 952.529	25.2	7.3	MD	–12.5	7.3
33	2 455 953.431	72.3	59.1	DD	–60.4	59.1
34	2 455 966.472	51.0	9.5	MD	–0.3	9.5
35	2 455 967.402	1.7	8.5	ND	11.3	8.4
36	2 455 968.343	10.7	16.7	ND	–13.7	16.6

Notes. The columns list the heliocentric Julian dates (HJD) for the middle of observation, the longitudinal magnetic field and its error in Gauss, the detection status: definite detection (DD), marginal detection (MD) and no detection (ND), and the "null" polarization and its error in Gauss.

in 15 out of 36 nights. The existence of Zeeman signatures confirms that ζ Ori A hosts a magnetic field, as previously reported by Bouret et al. (2008).

The previous study of the magnetic field of ζ Ori A (Bouret et al. 2008) only used a few lines that were not affected by the wind. However, we need to use as many lines as possible to improve the S/N. We therefore checked whethe our results were changed by using lines that might be affected by the wind. We compared the LSD results obtained with the mask used by Bouret et al. (2008) and our own mask (see Fig. 2). The signatures in Stokes V are similar with both masks and the measurements of the longitudinal magnetic field are consistent (e.g., 44.5 ± 19.6 G with the mask of Bouret et al. (2008) and 35.8 ± 7.2 G with our mask for measurement # 11, see Fig. 2). However, the S/N is better with our mask (the S/N of Stokes V is 57 624) than with the mask of Bouret et al. (2008) (the S/N of Stokes V is 27 296). Therefore, we used all available lines for this study.

However, the line mask used in this first analysis includes lines from both components of ζ Ori A. We thus ignored

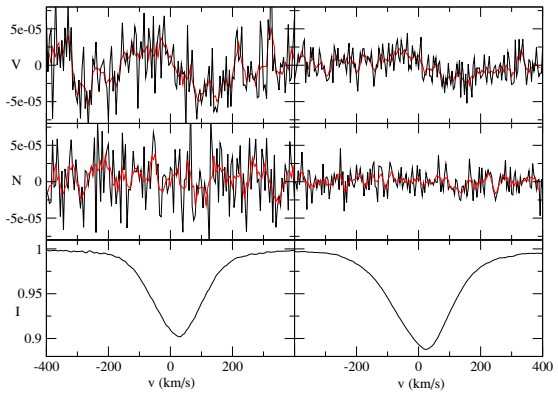

Fig. 2. LSD Stokes I (*bottom*), Stokes V (*top*), and null N (*middle*) profiles, normalized to Ic, for the night of 25 October 2008 for the mask of Bouret et al. (2008) (*left*) and for our own mask (*right*). The red line is a smoothed profile.

which component of the binary is magnetic or whether both components are magnetic. To provide an answer to this question, we must separate the composite spectra.

4. Separating the two components

4.1. Identifying the lines of each component

We first created synthetic spectra of each component. The goal was to identify which lines come from the primary component, the secondary component, or both. To this aim, we used TLUSTY (Hubeny & Lanz 1995). This program calculates plane-parallel, horizontally homogeneous stellar atmosphere models in radiative and hydrostatic equilibrium. One of the most important features of the program is that it allows for a fully consistent, non-LTE metal line blanketing. However, TLUSTY does not take winds into account, which can be important in massive stars, especially in supergiants.

For the primary component ζ Ori Aa, we computed a model with an effective temperature $T_{\rm eff}$ = 29 500 K and $\log g$ = 3.25, corresponding to the spectral type of the primary as given by Hummel et al. (2013). For the secondary, we computed a model with an effective temperature $T_{\rm eff}$ = 29 000 K et $\log g$ = 4.0, again following Hummel et al. (2013). We used solar abundances, for both stars. The emergent spectrum from a given model atmosphere was calculated with SYNSPEC[2]. This program is complemented by the program ROTINS, which calculates the rotational and instrumental convolutions for the net spectrum produced by SYNSPEC.

Comparing these two synthetic spectra to the observed spectra of ζ Ori A, we identified which lines belong only to ζ Ori Aa, only to ζ Ori Ab, and which are a blend of the lines of both components. If one observed line only existed in one synthetic spectrum, we considered that this line is only emitted from one component of the binary. If it existed in both synthetic spectra, we considered this line to be a blend of both components. We then created line lists containing lines from the three categories (only Aa, only Ab, or both).

In addition, we gathered archival spectra of ζ Ori A taken with the spectrographs FEROS, HEROS and UVES (see

[2] Synspec is a general spectrum synthesis program developed by Ivan Hubeny and Thierry Lanz: http://nova.astro.umd.edu/Synspec49/synspec.html

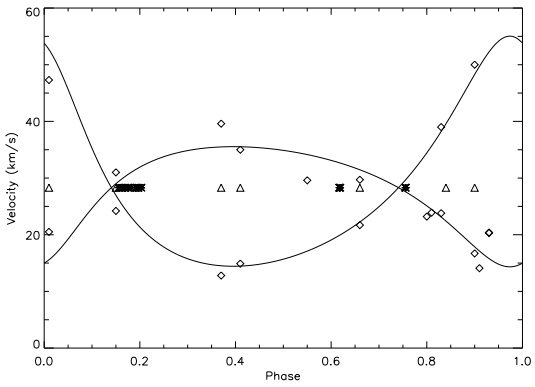

Fig. 3. Orbital phase distribution of the spectra of ζ Ori A. The diamonds indicate the radial velocity measured by Hummel et al. (2013). The lines correspond to the best fit of the radial velocity of each component. The crosses correspond to our Narval observations and the triangles to the archival spectroscopic data. Phase zero corresponds to the time of periastron passage (T_0 = 2 452 734.2 HJD) as reported by Hummel et al. (2013).

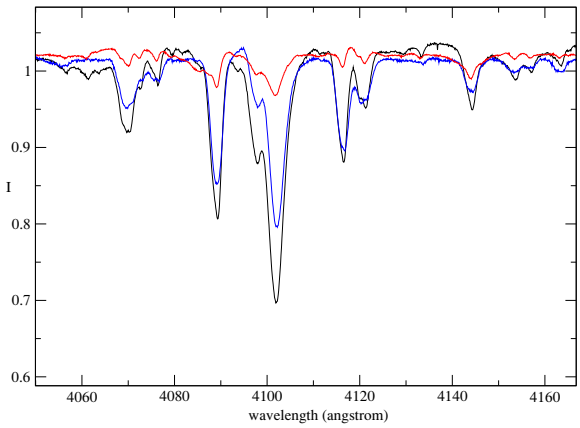

Fig. 4. Small part of the spectrum of ζ Ori A showing the composite observed spectrum (black), the spectrum of ζ Ori Aa (blue) and that of ζ Ori Ab (red).

Sect. 2.2). While these spectra do not include polarimetric information, they cover the orbital period much better than our Narval data (see Table 2 and Fig. 3). In particular, some spectra were obtained close to the maximum or minimum of the radial velocity (RV) curve.

We compared the spectrum taken close to the maximum and minimum RV, because the line shift is maximum between these two spectra. We arbitrarily decided to use the spectra taken close to the maximum as reference. Depending on the shift, we determined the origin of the lines. If the lines of the spectrum taken at minimum RV are shifted to the blue (respectively red) side compared to the spectrum at maximum RV, the line comes from the primary Aa (respectively secondary Ab) component. When lines from the two components are blended, the core of the lines are shifted to the red side and the wings to the blue side.

The identification of lines made this way resulted in similar line lists as those obtained by comparing the observed spectra with synthetic ones.

We then ran LSD again on the observed Narval spectra, once with the mask containing the 157 lines only belonging to ζ Ori Aa and once with the mask only containing the 67 lines from ζ Ori Ab. We observe magnetic signatures in the LSD V profiles of ζ Ori Aa that are similar to those obtained in the original LSD analysis presented in Sect. 3. In the contrast, we do not observe magnetic signatures in the LSD Stokes V profiles of ζ Ori Ab. We conclude that ζ Ori Aa is magnetic and ζ Ori Ab is not.

However, the LSD profiles of ζ Ori Aa obtained this way are very noisy, because of the low number of lines in the mask, and they cannot be used to precisely estimate the longitudinal magnetic field strength. To go further, it is necessary to disentangle the spectra, so that more lines can be used.

4.2. Spectral disentangling of Narval data

We first attempted to use the Fourier-based formulation of the spectral disentangling (hereafter,) method (Hadrava 1995) as implemented in the FDB code (Ilijic et al. 2004) to simultaneously determine the orbital elements and the individual spectra of the two components Aa and Ab of the ζ Ori A binary system. The Fourier-based method is superior to the original formulation presented by Simon & Sturm (1994) that is applied in the wavelength domain in that it is less time-consuming. In particular, this increases the technique's efficiency when it is applied to long time-series of high-resolution spectroscopic data.

One of the pre-conditions for the method to work efficiently is a homogeneous phase coverage of the orbital cycle with the data. In particular, covering the regions of maximum/minimum radial velocity (RV) separation of the two stars is essential, because these phases provide key information about the RV semi-amplitudes of both stellar components.

Figure 3 illustrates the phase distribution of our Narval spectra according to the orbital period of 2687.3 days reported by Hummel et al. (2013). Obviously, the spectra provide very poor phase coverage; no measurements exist at phases ~0.0 and 0.4, corresponding to a maximum RV separation of the components (see Fig. 5 in Hummel et al. 2013). This prevents determining of accurate orbital elements from our Narval spectra.

Our attempt to use the orbital solution obtained by Hummel et al. (2013) to separate the spectra of the individual components also failed: although all regions in which we disentangled the spectra indicate the presence of lines from the secondary in the composite spectra, the separated spectra themselves are unreliable.

4.3. Disentangling using the archival spectroscopic data

Since the method failed in disentangling the Narval spectra because of the poor phase coverage, we again used the spectroscopic archival data obtained with FEROS, HEROS, and UVES. The orbital coverage of these spectra is much better than the one of the Narval data. We have seven spectra taken at different orbital phases, including phases of maximum RV separation of the components (see Table 3). We first normalized the spectra with IRAF. We used the orbital parameters given by Hummel et al. (2013) for the disentangling.

The coverage of these spectra enables the disentangling using FDB . As an illustration of the results, a small part of the disentangled spectra is shown in Fig. 4. The results confirms the origin of the lines that were determined in Sect. 4.1, and also the spectral types of the components given by Hummel et al. (2013).

5. Measuring the longitudinal magnetic field of ζ Ori Aa

Following these results, we assume that ζ Ori Ab is not magnetic and that the Stokes V signal only comes from ζ Ori Aa. Therefore, we ran the LSD technique on the Narval spectra with a mask containing all lines emitted from ζ Ori Aa, even those that are blended with the ones of ζ Ori Ab, to obtain the LSD Stokes V profile of ζ Ori Aa. The contribution of ζ Ori Ab to this Stokes V signal will be null, as the magnetic signal is only provided by ζ Ori Aa.

However, we were unable to disentangle the Narval data (see Sect. 4.2), therefore the LSD Stokes I spectra of ζ Ori Aa could not be computed in the same way as the LSD Stokes V spectra. As a consequence, we attempted to compute the LSD Stokes I profiles in several ways.

5.1. Using the Narval data and correcting for the companion

For the I profiles, we first proceeded in the following way: we computed the LSD Stokes I profiles with different masks that only contained the lines of ζ Ori Aa, only the lines of ζ Ori Ab, and the only blended lines. We subtracted the LSD Stokes I profiles obtained for the lines of ζ Ori Ab alone from the LSD Stokes I profiles obtained for blended lines to remove the contribution from the Ab component. We then averaged the LSD Stokes I profiles obtained this way and the one obtained for the lines of ζ Ori Aa alone. In this way the same list of lines (those of Aa alone and the blended ones) are used in the final LSD Stokes I profiles as in the LSD Stokes V profiles calculated above.

This allowed us to use more lines than in Sect. 4.1 (i.e., to include the blended lines) and to improve the resulting S/N. We obtained magnetic signatures similar to those derived in Sects. 3 and 4.1 (see Fig. 1). However, the S/N remained low, and some contribution from the Ab component is probably still present in the LSD Stokes I profile. Longitudinal field values extracted from these LSD profiles may thus be unreliable.

5.2. Using synthetic intensity profiles

To improve the LSD I profiles, we attempted to use the synthetic TLUSTY/SYNSPEC spectra calculated in Sect. 4.1 for ζ Ori Aa. We ran the LSD tool on the synthetic spectra to produce the synthetic LSD Stokes I profiles of ζ Ori Aa with the same line mask as the one used for the LSD Stokes V profiles above.

We then computed the longitudinal magnetic field values from the observed LSD Stokes V profiles and the synthetic LSD Stokes I profiles. We calculated the longitudinal magnetic field B_l for all observations with the center-of-gravity method (Rees & Semel 1979),

$$B_l = -2.14 \times 10^{-11} \frac{\int vV(v)\mathrm{d}v}{\lambda_0 g_m c \int (1 - I(v))\mathrm{d}v} \text{ G}.$$

We obtained longitudinal magnetic field values between −144 and +112 G with error bars between 20 and 100 G.

5.3. Using disentangled spectroscopic data

Although we were unable to disentangle the Narval data, we obtained disentangled spectra from the purely spectroscopic archival data. To derive the longitudinal magnetic field values more accurately, we therefore used the disentangled spectra obtained from the purely spectroscopic data.

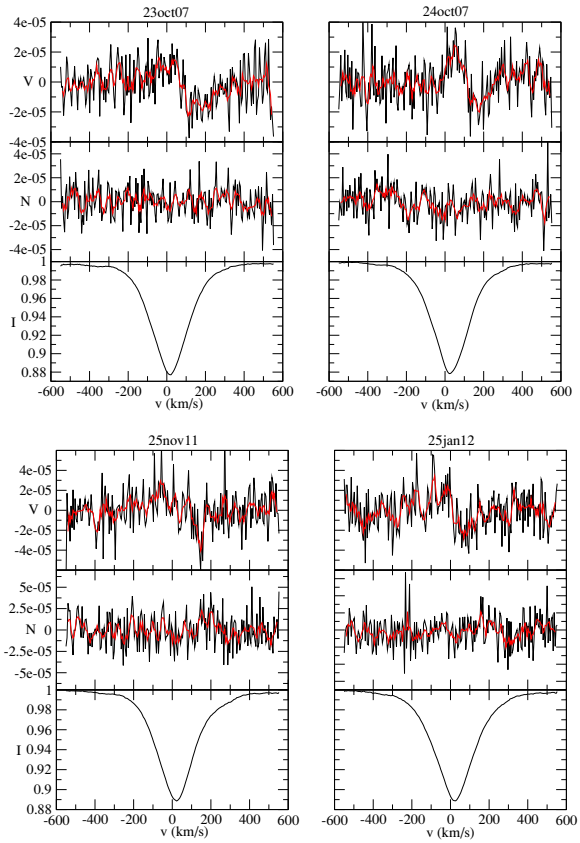

Fig. 5. Examples of LSD Stokes I profiles (*bottom*) computed from the disentangled spectroscopic data, Stokes V (*top*) and null N (*middle*) profiles, normalized to Ic, from the Narval data for the primary component ζ Ori Aa for a few nights of observations. The red line is a smoothed profile.

We ran the LSD technique on the disentangled archival spectra obtained for ζ Ori Aa using the same line list as we used for Stokes V. Thus, we obtained the observed mean intensity profile for ζ Ori Aa alone. We then computed the longitudinal magnetic field values from the observed LSD Stokes V profiles from Narval and the observed LSD Stokes I profiles from the disentangled spectroscopic spectra.

The shape of the magnetic signatures in LSD Stokes V profiles (Fig. 5) is similar to the shapes obtained for the combined spectra (Fig. 1) and the various methods presented above. The LSD Stokes I spectra now better represent the observed ζ Ori Aa spectrum, however. We therefore adopted these LSD profiles in the remainder of this work. Fifteen of the 36 measurements are DD or MD.

As above, we calculated the longitudinal magnetic field B_l for all observations with the center-of-gravity method (Rees & Semel 1979). Results are given in Table 3. The longitudinal field B_l varies between about −30 and +50 G, with typical error bars below 10 G. N values are systematically compatible with 0 within $3\sigma N$, where σN is the error on N, while B_l values are above $3\sigma B_l$ in seven instances, where σB_l is the error on B_l.

Table 4. Longitudinal magnetic field measurements for the secondary ζ Ori Ab.

#	mid-HJD	B_l	σB_l	Detect.	N	σN
1	2 454 391.559	–62.9	74.5	ND	46.5	74.4
2	2 454 392.719	–80.4	132.7	ND	91.9	132.8
3	2 454 393.570	26.0	54.8	ND	–60.6	54.9
4	2 454 394.491	31.0	56.7	ND	24.1	56.6
5	2 454 395.518	86.7	47.6	ND	101.4	47.7
6	2 454 397.496	–49.4	45.5	ND	14.3	45.9
7	2 454 398.526	14.2	46.0	ND	44.6	46.1
8	2 454 762.644	–14.2	50.8	ND	73.0	50.6
9	2 454 763.645	–24.1	65.4	ND	43.3	65.5
10	2 454 764.654	–40.1	49.2	ND	80.0	49.4
11	2 454 765.639	–32.9	73.5	ND	47.2	73.6
12	2 454 766.635	7.9	60.5	ND	–26.5	60.6
13	2 455 839.688	–62.3	53.2	ND	–30.5	53.6
14	2 455 840.670	–8.3	58.3	ND	3.4	58.2
15	2 455 845.608	–19.1	92.2	ND	–21.9	91.1
16	2 455 846.632	–126.4	91.9	ND	–102.1	91.2
17	2 455 865.712	35.7	63.2	ND	173.4	63.9
18	2 455 873.557	141.5	112.7	ND	–224.0	113.0
19	2 455 877.626	55.7	60.0	ND	2.5	60.0
20	2 455 878.565	34.8	68.3	ND	75.0	68.7
21	2 455 890.673	–105.9	106.6	ND	–154.9	107.5
22	2 455 891.660	8.7	82.6	ND	86.6	82.8
23	2 455 892.502	77.1	84.3	ND	–63.7	84.8
24	2 455 895.667	–27.0	75.2	ND	–63.8	75.5
25	2 455 896.600	–33.7	289.4	ND	–113.7	296.7
26	2 455 910.477	171.0	183.7	ND	129.3	183.4
27	2 455 935.555	–82.4	70.1	ND	–58.6	69.9
28	2 455 940.536	–12.3	63.5	ND	–55.8	63.7
29	2 455 941.539	20.3	67.3	ND	116.9	67.8
30	2 455 942.475	31.8	70.6	ND	–97.2	71.1
31	2 455 943.367	–6.2	78.8	ND	–27.7	79.2
32	2 455 952.529	–72.4	71.0	ND	1.1	71.3
33	2 455 953.431	173.6	478.5	ND	–152.6	480.7
34	2 455 966.472	52.9	79.9	ND	–32.1	79.8
35	2 455 967.402	–57.8	74.6	ND	62.8	74.3
36	2 455 968.343	–152.8	186.5	ND	–92.9	187.2

Notes. The columns list the heliocentric Julian dates (HJD) for the middle of observation, the longitudinal magnetic field and its error in Gauss, the detection status: no detection (ND) in all cases, and the "null" polarization and its error in Gauss.

6. No magnetic field in ζ Ori Ab

6.1. Longitudinal magnetic field values for ζ Ori Ab

To confirm the non-detection of a magnetic field in ζ Ori Ab, we ran the LSD technique with a mask that only contained lines emitted from ζ Ori Ab, that is 67 lines. This ensures that the LSD Stokes V profiles are not polluted by the magnetic field of ζ Ori Aa. Signatures in the LSD Stokes V profiles are not detected in any of the profiles (all ND), as shown in Table 4 and in Fig. 6 for selected nights when a signal is detected in ζ Ori Aa.

Using these LSD profiles and the center-of-gravity method, we calculated the longitudinal field value, the null polarization, and their error bars for ζ Ori Ab. We find that both B_l and N are compatible with 0 within 3σ for all nights (see Table 4). However, the error bars on the longitudinal field values of

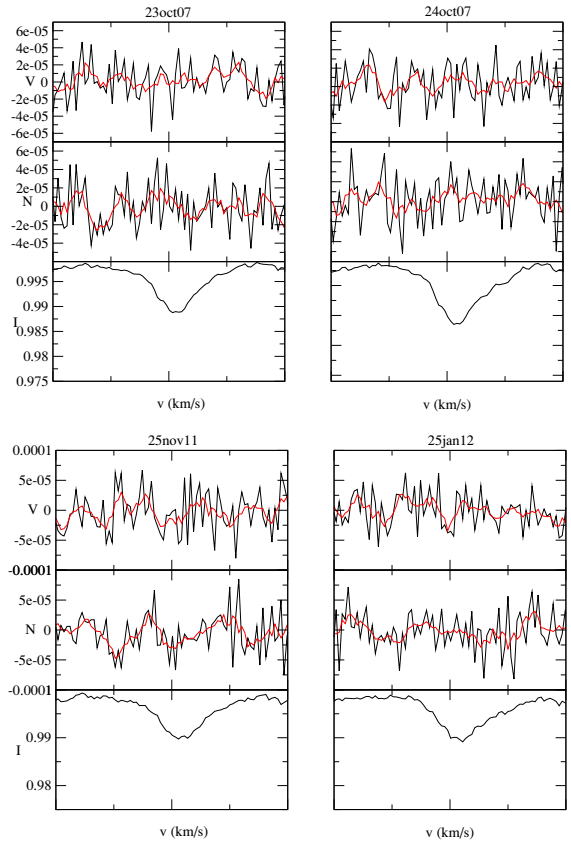

Fig. 6. Examples of LSD Stokes I (*bottom*), Stokes V (*top*), and null N (*middle*) profiles, normalized to Ic, for the secondary component ζ Ori Ab for a few nights of observations, computed from Narval data using only the 82 lines belonging to the secondary component. The red line is a smoothed profile.

ζ Ori Ab are much higher (typically 70 G) than those for ζ Ori Aa (typically 10 G), because far fewer lines could be used to extract the signal for ζ Ori Ab.

6.2. Upper limit on the non-detected field in ζ Ori Ab

The signature of a weak magnetic field might have remained hidden in the noise of the spectra of the ζ Ori Ab. To evaluate its maximum strength, we first fitted the LSD I profiles computed above for ζ Ori Ab with a double Gaussian profile. This fit does not use physical stellar parameters, but it reproduces the I profiles as well as possible. We then calculated 1000 oblique dipole models of each of the LSD Stokes V profiles for various values of the polar magnetic field strength $B_{\rm pol}$. Each of these models uses a random inclination angle i, obliquity angle β, and rotational phase, as well as a white Gaussian noise with a null average and a variance corresponding to the S/N of each observed profile. Using the fitted LSD I profiles, we calculated local Stokes V profiles assuming the weak-field case, and we integrated over the visible hemisphere of the star. We obtained synthetic Stokes V profiles, which we normalized to the intensity of the continuum. These synthetic profiles have the same mean Landé factor and wavelength as the observations.

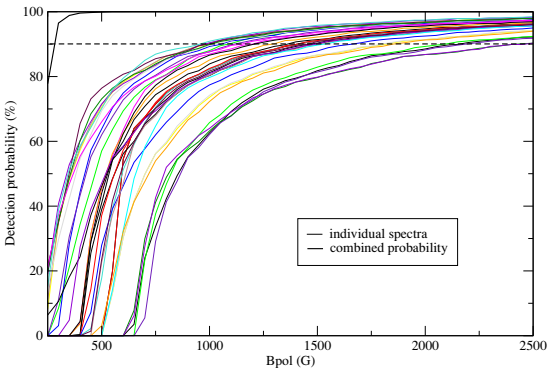

Fig. 7. Detection probability of a magnetic field in each spectrum of the secondary component of ζ Ori Ab (thin color lines) as a function of the magnetic polar field strength. The horizontal dashed line indicates the 90% detection probability, and the thick black curve (top left corner) shows the combined probability.

We then computed the probability of detecting a dipolar oblique magnetic field in this set of models by applying the Neyman-Pearson likelihood ratio test (see e.g. Helstrom 1995; Kay 1998; Levy 2008). This allowed us to decide between two hypotheses: the profile only contains noise, or it contains a noisy Stokes V signal. This rule selects the hypothesis that maximizes the detection probability while ensuring that the FAP is not higher than 10^{-3} for a marginal magnetic detection. We then calculated the rate of detections in the 1000 models for each of the profiles depending on the field strength (see Fig. 7).

We required a 90% detection rate to consider that the field would statistically be detected. This translates into an upper limit for the possible undetected dipolar field strength for each spectrum, which varies between ~900 and ~2350 G (see Fig. 7).

Since 36 spectra are at our disposal, statistics can be combined to extract a stricter upper limit taking into account that the field has not been detected in any of the 36 observations (see Neiner et al. 2015). The final upper limit derived from this combined probability for ζ Ori Ab for a 90% detection probability is ~300 G (see thick line in Fig. 7).

7. Magnetic field configuration

7.1. Rotational modulation

We searched for a period of variation in the 36 longitudinal magnetic field measurements of ζ Ori Aa with the clean-NG algorithm (see Gutiérrez-Soto et al. 2009). We obtained a frequency $f = 0.146421$ c d^{-1}, which corresponds to a period of 6.829621 days. This value is consistent with the period of ~7 days suggested by Bouret et al. (2008). Assuming that the magnetic field is a dipole with its axis inclined to the rotation axis, as is found in the vast majority of massive stars, this period corresponds to the rotation period of the star.

We used this period and plotted the longitudinal magnetic field as a function of phase. For the data taken in 2007 and 2008, the phase-folded field measurements show a clear sinusoidal behavior, as expected from a dipolar field model (see top panel of Fig. 8). A dipolar fit to the data, that is, a sine fit of the form $B(x) = B_0 + B_a \times \sin(2\pi(x + \phi_d))$, resulted in $B_0 = 6.9$ G and $B_a = 19.2$ G. A quadrupolar fit to the phase-folded data only shows an insignificant departure from the dipolar fit.

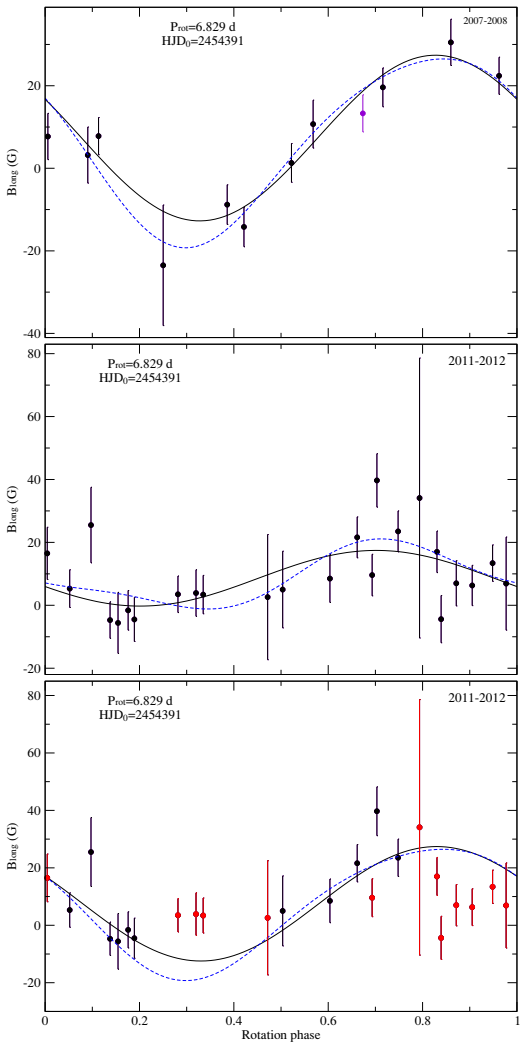

Fig. 8. Rotational modulation of the longitudinal magnetic field of ζ Ori Aa for the observations taken in 2007–2008 (*top*) and 2011–2012 (*center*). The black line corresponds to the best dipolar fit, while the dashed blue line corresponds to the best quadrupolar fit. The *bottom panel* compares the fit of the dipole and the quadrupole obtained from the 2007–2008 data with the observations obtained in 2011–2012 (see Sect. 7.3). The data for which the Stokes V model matches the observed LSD V profiles are shown in black, while the data for which the Stokes V model does not match are in red.

However, the period of ~6.829 days does not to match the measurements collected in 2011 and 2012 very well (see middle panel of Fig. 8). None of the dipolar or quadrupolar fits to these data provide a reasonable match. A further search for a different period in these 2011–2012 data alone provided no significant result.

The magnetic fields of main-sequence massive stars are of fossil origin. These fields are known to be stable over decades and are only modulated by the rotation of the star. A change of period in the field modulation between the 2007–8 and 2011–12 epochs is thus not expected in ζ Ori Aa.

ζ Ori Aa has a companion, therefore we investigated the possibility that the magnetic field has been affected by the companion. Indeed, in 2011 and 2012, ζ Ori Ab was close to periastron, which means that the distance between the two stars was smaller than in 2007 and 2008. We calculated this distance to check whether some binary interactions might have occurred.

To calculate the distance between the two components, we used the photometric distance of ζ Ori A, $d = 387$ pc (Hummel et al. 2013). From Hummel et al. (2013), we know the orbital parameters of the binary. The shortest distance between the two stars is $r_{\rm min} = a - \sqrt{a^2 - b^2} = 23.8$ mas, where a is the semi-major axis and b the semi-minor axis. From the distance of ζ Ori A, we can compute $r_{\rm min} = \sin(\theta)/d$ in pc, where θ is the parallax in radian. We obtained a distance of 81 R_*, where R_* is the radius of ζ Ori Aa.

The distance between the two stars at periastron therefore appears too large for interactions between the two stars to occur. In addition, the binary system is still significantly eccentric (0.338, Hummel et al. 2013) even though ζ Ori Aa has already evolved into a supergiant. Tidal interactions have apparently not been able to circularize the system yet, which would confirm that these interactions are weak (Zahn 2008).

However, in addition to ζ Ori Aa and Ab, a third star ζ Ori B may also interfere with the ζ Ori A system. Correia et al. (2012) showed that when a third component comes into play, tidal effects combined with gravitational interactions may increase the eccentricity of ζ Ori A, which would otherwise have circularized. We thus cannot exclude that tidal interactions are stronger than they seem in the ζ Ori A system.

7.2. Field strength and geometrical configuration

Assuming that the period detected in Sect. 7.1 is the rotation period of the star, we can determine the inclination angle of the star i by measuring $v \sin i$. In massive stars, line broadening does not come from rotational broadening alone, but also from turbulence and stellar wind. This is particularly true for supergiant stars.

Based on the synthetic spectra calculated in Sect. 4.1 and the lines identified to belong to only one of the two components, we determined the broadening needed in the synthetic spectra to fit the observations. For ζ Ori Aa, a broadening of 230 km s^{-1} was necessary to provide a good fit to the observed lines, while for ζ Ori Ab we needed 100 km s^{-1}. These broadening values are upper limits of the $v \sin i$ values because they include all physical processes that broaden the lines. In fact, with a period of 6.829 days and a radius of 20 $R_\odot$ as given by Hummel et al. (2013), the maximum possible $v \sin i$ for ζ Ori Aa is 148 km s^{-1}.

In addition, Bouret et al. (2008) determined $v \sin i$ through a Fourier transform of the average of the 5801 and 5812 Å CIV and 5592 Å OIII line profiles. They found a $v \sin i$ of 110 ± 10 km s^{-1}. From our disentangling of the spectra, we know that the two CIV lines originate from ζ Ori Aa, but the OIII 5590 Å line is partly (∼10%) polluted by ζ Ori Ab. As a consequence, we applied the Fourier transform method to the LSD Stokes I profiles we calculated from the lines that only originate from ζ Ori Aa. We obtained $v \sin i = 140$ km s^{-1}. However, it is known that $v \sin i$ values determined from LSD profiles might be overestimated.

Finally, taking macroturbulence into account but not binarity, foe example, Simón-Díaz & Herrero (2014) found that $v \sin i$ for ζ Ori A is between 102 and 127 km s^{-1}, depending on the method they used.

In the following, we thus consider that $v \sin i$ is between 100 km s^{-1}and 148 km s^{-1}for ζ Ori Aa. In addition, we adopt the radius of 20 $R_\odot$ given by Hummel et al. (2013) and the rotation period of 6.829 d. Using $v \sin i = [100–148]$ km s^{-1}, we obtain $i \sim [42–87]°$.

Using the dipolar fit to the 2007–2008 longitudinal field measurements and the inclination angle i, we can deduce the obliquity angle β of the magnetic field with respect to the rotation axis. To this aim, we used the formula $r = B_{\rm min}/B_{\rm max} = \cos(i-\beta)/\cos(i+\beta)$ (Shore 1987). The dipolar fit of the longitudinal field values gives $r = 0.47$. With $i \sim [42–87]°$, we obtain $\beta \sim [71–8]°$.

In addition, from the dipolar fit to the longitudinal field values and the angles i and β determined above, we can estimate the polar field strength with the formula $B_0 \pm B_{\rm a} = 0.296 \times B_{\rm pol} \cos(\beta \pm i)$, where the limb-darkening coefficient is assumed to be 0.4 (see Borra & Landstreet 1980). We found $B_{\rm pol} = [110 \pm 5 – 524 \pm 65]$ G. The dipolar magnetic field that we find is thus higher than the one found by Bouret et al. (2008).

In 2011–2012, the maximum measured $B_{\rm l}$ is 51 G and the minimum polar field strength is thus $B_{\rm pol} \geq 3.3 B_{\rm l,max} = 168 \pm 33$ G. This value is compatible with the range derived from the 2007–2008 data.

7.3. Stokes V modeling

Since the $B_{\rm l}$ data taken in 2007–2008 point toward the presence of a dipole field, we used an oblique rotator model to fit the LSD Stokes V and I profiles.

We used Gaussian local intensity profiles with a width calculated according to the resolving power of Narval and a macroturbulence value of 100 km s^{-1} determined by Bouret et al. (2008). We fit the observed LSD I profiles by Gaussian profiles to determine the depth, $v \sin i$ and radial velocity of the intensity profile. We used the weighted mean Landé factor and wavelength derived from the LSD mask applied to the Narval observations and the rotation period of 6.829 days. The fit includes five parameters: i, β, $B_{\rm pol}$, a phase shift ϕ, and a possible off-centering distance $d_{\rm d}$ of the dipole with respect to the center of the star ($d_{\rm d} = 0$ for a centered dipole and $d_{\rm d} = 1$ if the center of the dipole is at the surface of the star).

8. Magnetospheres

8.1. Magnetospheric parameters

We calculated a grid of V profiles for each phase of observation by varying the five parameters mentioned above and applied a χ^2 minimization to obtain the best fit of all observations simultaneously. More details of the modeling technique can be found in Alecian et al. (2008). The parameters of the best fit are $i = 79.89°$, $\beta = 21.5°$, $\phi = 0.68$, $B_{\rm pol} = 142.2$ G and $d_{\rm d} = 0.0$. The values for the angles i and β are within the error boxes derived in Sect. 7.2, and the value for the polar field strength $B_{\rm pol}$ fits the $B_{\rm l}$ results well. Moreover, the best fit is obtained for $d_{\rm d} = 0$, which confirms that no quadrupolar component is found.

The 36 Stokes V profiles for this best fit are shown in Fig. 9 overplotted on the observations. As expected, for the nights in 2007–2008, the model fits the observations well. For some nights in 2011–2012, the observations are too noisy to see whether the model fits well. Considering the nights in 2011–2012 for which the S/N is sufficient, the model fits some the observations but not all. For those nights for which the model fitted well the observations, we compared the values

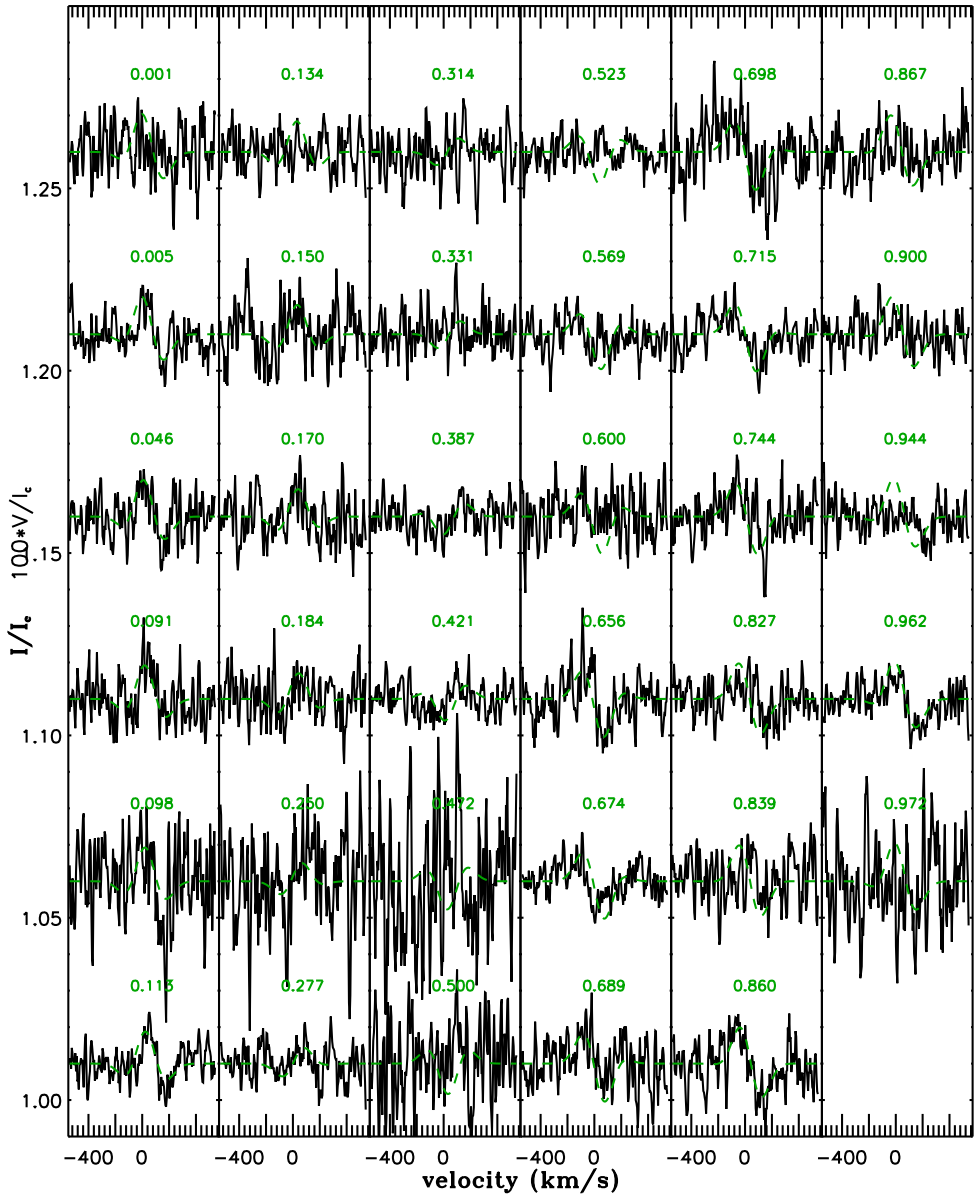

Fig. 9. Best dipolar model fit (green) of the observed Stokes V profiles (black). The green numbers correspond to the rotational phase. The very noisy observation at phase 0.793 is not shown.

of the longitudinal magnetic field B_l to the dipolar fit obtained for the B_l measurements of 2007–2008 (see bottom panel of Fig. 8). The 2011–2012 data that match the Stokes V models also match the B_l dipolar fit curve. Therefore, it seems that at least part of the 2011–2012 data show the same rotational modulation and dipole field as in 2007–2008. Only part of the 2011–2012 dataset does not match the rest of the observations.

With the polar magnetic field strength $B_{\rm pol}$ = 142.2 G determined with to the Stokes V model, we calculated the wind confinement parameter η_* which characterizes the ability of the magnetic field to confine the wind particles into a magnetosphere (ud-Doula & Owocki 2002). If $\eta_* \leq 1$, ζ Ori Aa is located in the weakly magnetized winds region of the magnetic confinement-rotation diagram and it does not have a magnetosphere. However, for $\eta_* > 1$, wind material is channeled along magnetic field lines toward the magnetic equator and ζ Ori Aa hosts a magnetosphere.

To calculate η_*, we first used the fiducial mass-loss rate $\dot{M}_{B=0} = 1.4 \times 10^{-6}\ M_\odot\ {\rm yr}^{-1}$ and the terminal speed V_∞ = 2100 km s^{-1} determined by Bouret et al. (2008). They measured the mass-loss rate from the emission of Hα and used archival International Ultraviolet Explorer (IUE) spectra to measure the

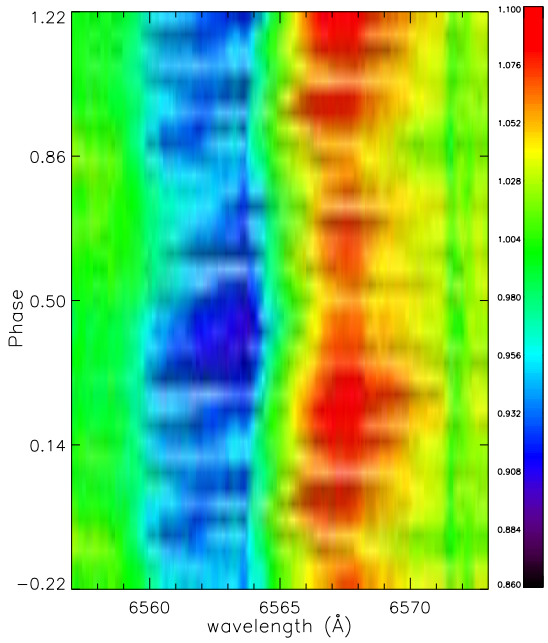

Fig. 10. Dynamic plot of each individual archival H_α spectrum in phase with the rotation period.

wind terminal velocity from the blueward extension of the strong UV P Cygni profile. We obtain $\eta_* = 0.9$.

We then recalculated η_* but this time using the mass-loss rate of $\dot{M} = 3.4 \times 10^{-7}\ M_\odot\ \mathrm{yr}^{-1}$ and $V_\infty = 1850\ \mathrm{km\,s}^{-1}$ determined by Cohen et al. (2014). This gives $\eta_* = 4.2$.

A magnetosphere can only exist below the Alfvén radius R_A, which is proportional to η_*, with $R_\mathrm{A} = \eta_*^{1/4} R_*$. For ζ Ori Aa, using the two above determinations of η_*, $R_\mathrm{A} = [0.98 - 1.43]R_*$. Moreover, the magnetosphere can be centrifugally supported above the corotation Kepler radius R_K. $R_\mathrm{K} = (2\pi R_*/P_\mathrm{rot}\sqrt{(GM/R_*)})^{2/3}$, thus for ζ Ori Aa $R_\mathrm{K} = 2.8R_*$. Since $R_\mathrm{K} > R_\mathrm{A}$, no centrifugally supported magnetosphere can exist.

Therefore, ζ Ori Aa is either in the weakly magnetized winds region of the magnetic confinement-rotation diagram, meaning that ζ Ori Aa does not have a magnetosphere ($\eta_* < 1$), or it hosts a dynamical magnetosphere ($1 < \eta_* < 4.2$).

8.2. H_α variations

The H_α line shows significant variability in emission and absorption. For stars that have a magnetosphere, we expect magnetospheric emission at H_α, which varies with the rotation period (see e.g. Grunhut 2015).

To check whether there is a signature of the presence of a magnetosphere around ζ Ori Aa, we studied the variation of its H_α line in the archival spectra (see Sect. 2.2). We confirm that the emission in H_α does indeed vary. While most of the variations are problably related to variations in the stellar wind of the supergiant, the signature of a weak rotationally modulated dynamical magnetosphere is observed in H_α (see Fig. 10).

The ratio $\log R_\mathrm{A}/R_\mathrm{K}$ gives a measure of the volume of the magnetosphere. For ζ Ori Aa, $\log R_\mathrm{A}/R_\mathrm{K}$ is very small (<0.06), and it is thus not surprising that H_α only weakly reflects magnetic confinement.

9. Discussion and conclusions

Based on archival spectrocopic data and Narval spectropolarimetric data, we confirm the presence of a magnetic field in the massive star ζ Ori A, as initally suggested by Bouret et al. (2008). However, Bouret et al. (2008) ignored that ζ Ori A is a binary star, which was subsequently shown by Hummel et al. (2013) with interferometry.

We disentangle the spectra and could thus show that the primary O supergiant component ζ Ori Aa is the magnetic star, while the secondary ζ Ori Ab is not magnetic at the achieved detection level. ζ Ori Aa is the only magnetic O supergiant known as of today.

The magnetic field of ζ Ori Aa is a typical oblique dipole field, similar to those observed in main-sequence massive stars. From Stokes modeling, the polar magnetic field strength B_pol of ζ Ori Aa is found to be about 140 G. If we assume field conservation during the evolution of ζ Ori Aa because the stellar radius increased from ~10 to ~20 $R_\odot$, the surface magnetic polar field strength decreased by a factor ~4. This implies that the polar field strength of ζ Ori Aa when it was on the main sequence was about 600 G. This is similar to what is observed in other main-sequence magnetic O stars.

The current field strength and rotation rate of ζ Ori Aa are weak, with respect to the wind energy, for the star to be able to host a centrifugally supported magnetosphere. However, it seems to host a dynamical magnetosphere. All other ten known magnetic O stars host dynamical magnetospheres, except for the complicated system of Plaskett's star, which has a very strong magnetic field and hosts a centrifugally supported magnetosphere (see Grunhut et al. 2013). However, these other magnetic O stars are not supergiants.

Although ζ Ori A is one of the brightest O star in the X-ray domain, Cohen et al. (2014) found that it resembles a non-magnetic star, with no evidence for magnetic activity in the X-ray domain and a spherical wind. This probably results from the weakness of the magnetosphere around ζ Ori Aa.

The rotation period of ζ Ori Aa, $P_\mathrm{rot} = 6.829$ d, was determined from the variations of the longitudinal magnetic field. This period is clearly seen in the data obtained in 2007–2008, but only part of the spectropolarimetric measurements obtained in 2011 and 2012 seem to follow that rotational modulation. The reason for the lack of periodicity for part of the magnetic measurements of 2011–2012 was not identified. Although passage at the binary periastron occured between 2008 and 2011, the distance between the two companions seems too large for the companion to have perturbed the magnetic field of the primary star, unless it is ζ Ori B which has maintained the two components of ζ Ori A at a distance (see Sect. 7.1).

ζ Ori A therefore remains an interesting star that needs to be studied further. More spectropolarimetric observations should be collected at appropriate orbital phases to allow for a more accurate spectral disentangling. this would allow obtaining stronger constraints on the magnetic field strength and configuration, studying the field as a function of orbital phase, and understanding the magnetic field perturbations that seem to have occurred during the observations in 2011–2012.

Acknowledgements. A.B. thanks Patricia Lampens and Yves Frémat for useful discussions on the disentangling technique. A.B. and C.N. also thank Stéphane Mathis for valuable discussions on tidal effects and Fabrice Martins for helpful discussion about the spectral classification. A.B. and C.N. acknowledge support from the Agence Nationale de la Recherche (ANR) project Imagine. This research has made use of the SIMBAD database operated at CDS, Strasbourg (France), and of NASA's Astrophysics Data System (ADS).

References

Alecian, E., Catala, C., Wade, G. A., et al. 2008, MNRAS, 385, 391
Borra, E. F., & Landstreet, J. D. 1980, ApJS, 42, 421
Bouret, J.-C., Donati, J.-F., Martins, F., et al. 2008, MNRAS, 389, 75
Cohen, D. H., Li, Z., Gayley, K. G., et al. 2014, MNRAS, 444, 3729
Correia, A. C. M., Boué, G., & Laskar, J. 2012, ApJ, 744, L23
Dekker, H., D'Odorico, S., Kaufer, A., Delabre, B., & Kotzlowski, H. 2000, in Optical and IR Telescope Instrumentation and Detectors, eds. M. Iye, & A. F. Moorwood, SPIE Conf. Ser., 4008, 534
Donati, J.-F., Semel, M., Carter, B. D., Rees, D. E., & Collier Cameron, A. 1997, MNRAS, 291, 658
Grunhut, J. H. 2015, in New window on massive stars: asteroseismology, interferometry and spectropolarimetry, IAU Symp., 307, 301
Grunhut, J. H., Wade, G. A., Leutenegger, M., et al. 2013, MNRAS, 428, 1686
Gutiérrez-Soto, J., Floquet, M., Samadi, R., et al. 2009, A&A, 506, 133
Hadrava, P. 1995, A&AS, 114, 393
Helstrom, C. W. 1995, Elements of Signal Detection and Estimation (Prentice Hall)
Hubeny, I., & Lanz, T. 1995, ApJ, 439, 875
Hummel, C. A., Rivinius, T., Nieva, M.-F., et al. 2013, A&A, 554, A52
Ilijic, S., Hensberge, H., Pavlovski, K., & Freyhammer, L. M. 2004, ASP Conf. Ser., 318, 111
Kay, S. M. 1998, Fundamentals of Statistical Signal Processing, Vol. 2: Detection Theory (Prentice Hall)
Kupka, F., & Ryabchikova, T. A. 1999, Publications de l'Observatoire Astronomique de Beograd, 65, 223
Levy, B. C. 2008, Principles of signal detection and parameters estimation (Springer)
Neiner, C., Alecian, E., & Mathis, S. 2011, in SF2A-2011: Proc. Annual meeting of the French Society of Astronomy and Astrophysics, eds. G. Alecian, K. Belkacem, R. Samadi, & D. Valls-Gabaud, 509
Neiner, C., Grunhut, J., Leroy, B., De Becker, M., & Rauw, G. 2015, A&A, 575, A66
Petit, V., Owocki, S. P., Wade, G. A., et al. 2013, MNRAS, 429, 398
Piskunov, N. E., Kupka, F., Ryabchikova, T. A., Weiss, W. W., & Jeffery, C. S. 1995, A&AS, 112, 525
Rees, D. E., & Semel, M. D. 1979, A&A, 74, 1
Shore, S. N. 1987, AJ, 94, 731
Simon, K. P., & Sturm, E. 1994, A&A, 281, 286
Simón-Díaz, S., & Herrero, A. 2014, A&A, 562, A135
ud-Doula, A., & Owocki, S. P. 2002, ApJ, 576, 413
Wade, G. A., Grunhut, J., Alecian, E., et al. 2014, in Magnetic fields throughout stellar evolution, IAU Symp., 302, 265
Zahn, J.-P. 2008, in EAS Pub. Ser. 29, eds. M.-J. Goupil, & J.-P. Zahn, 67

Appendix A: Additional figure

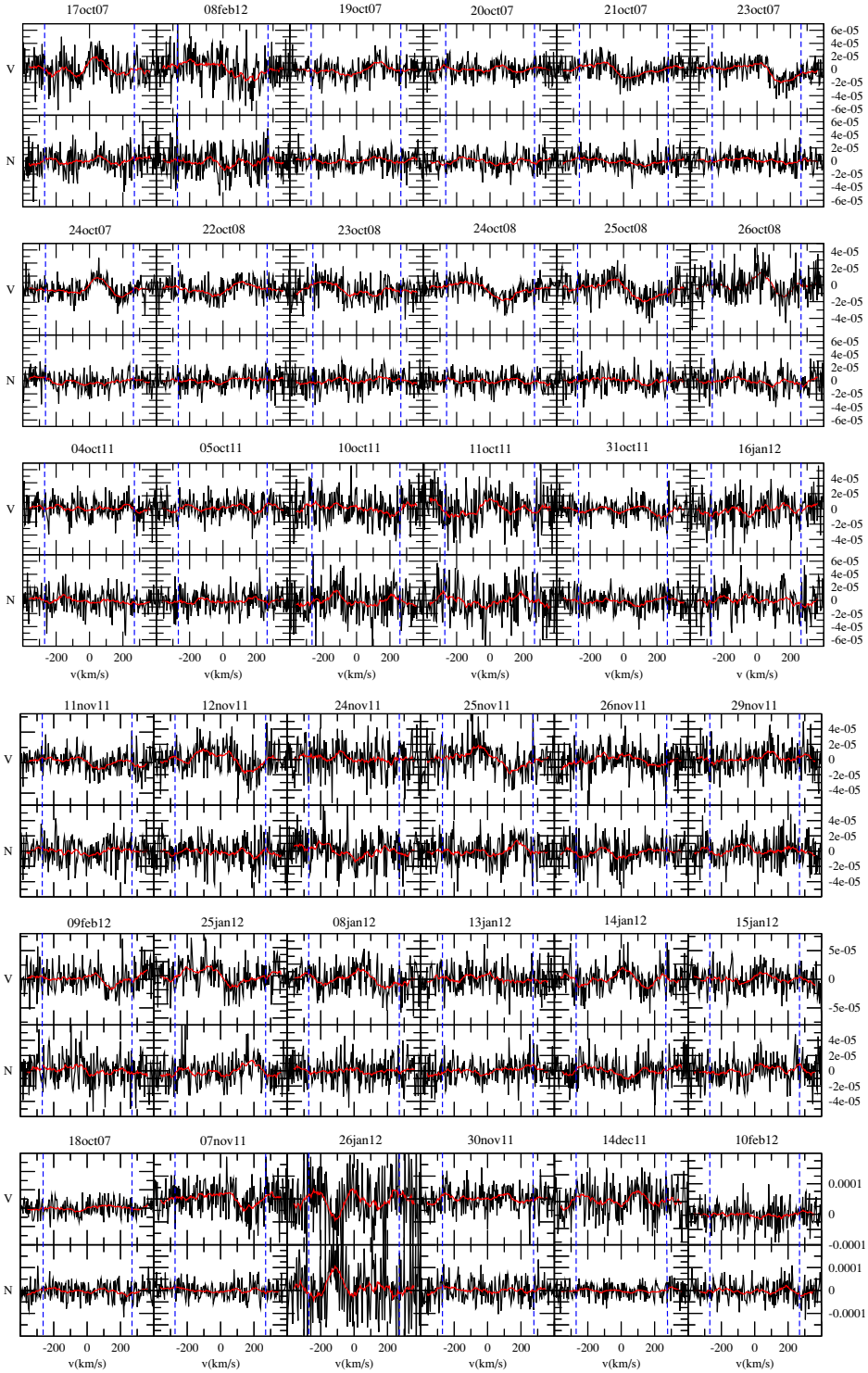

Fig. A.1. LSD Stokes *I* profiles (*bottom*) computed from the disentangled spectroscopic data, Stokes *V* (*top*) and null *N* (*middle*) profiles, normalized to Ic, from the Narval data, for ζ Ori A. The red line is a smoothed profile.

Appendix B

Paper on magnetic field on β Uma and θ Leo

A&A 586, A97 (2016)
DOI: 10.1051/0004-6361/201527556

Astronomy & Astrophysics

Detection of ultra-weak magnetic fields in Am stars: β Ursae Majoris and θ Leonis

A. Blazère[1,2,3], P. Petit[2,3], F. Lignières[2,3], M. Aurière[2,3], J. Ballot[2,3], T. Böhm[2,3], C. P. Folsom[2,3,4], M. Gaurat[2,3], L. Jouve[2,3], A. Lopez Ariste[2,3], C. Neiner[1], and G. A .Wade[5]

[1] LESIA, Observatoire de Paris, PSL Research University, CNRS, Sorbonne Universités, UPMC Univ. Paris 06, Univ. Paris Diderot, Sorbonne Paris Cité, 5 place Jules Janssen, 92195 Meudon, France
e-mail: aurore.blazere@obspm.fr
[2] Université de Toulouse, UPS-OMP, Institut de Recherche en Astrophysique et Planétologie, 31062 Toulouse, France
[3] CNRS, Institut de Recherche en Astrophysique et Planétologie, 14 avenue Édouard Belin, 31400 Toulouse, France
[4] IPAG, UJF-Grenoble 1/CNRS-INSU, UMR 5274, 38041 Grenoble, France
[5] Department of Physics, Royal Military College of Canada, PO Box 17000 Station Forces, Kingston, ON K7K 0C6, Canada

Received 14 October 2015 / Accepted 2 December 2015

ABSTRACT

Context. An extremely weak circularly polarized signature was recently discovered in spectral lines of the chemically peculiar Am star Sirius A. A weak surface magnetic field was proposed to account for the observed polarized signal, but the shape of the phase-averaged signature, dominated by a prominent positive lobe, is not expected in the standard theory of the Zeeman effect.
Aims. We aim at verifying the presence of weak circularly polarized signatures in two other bright Am stars, β UMa and θ Leo, and investigating the physical origin of Sirius-like polarized signals further.
Methods. We present here a set of deep spectropolarimetric observations of β UMa and θ Leo, observed with the NARVAL spectropolarimeter. We analyzed all spectra with the least squares deconvolution multiline procedure. To improve the signal-to-noise ratio and detect extremely weak signatures in Stokes V profiles, we co-added all available spectra of each star (around 150 observations each time). Finally, we ran several tests to evaluate whether the detected signatures are consistent with the behavior expected from the Zeeman effect.
Results. The line profiles of the two stars display circularly polarized signatures similar in shape and amplitude to the observations previously gathered for Sirius A. Our series of tests brings further evidence of a magnetic origin of the recorded signal.
Conclusions. These new detections suggest that very weak magnetic fields may well be present in the photospheres of a significant fraction of intermediate-mass stars. The strongly asymmetric Zeeman signatures measured so far in Am stars (featuring a dominant single-sign lobe) are not expected in the standard theory of the Zeeman effect and may be linked to sharp vertical gradients in photospheric velocities and magnetic field strengths.

Key words. stars: magnetic field – stars: chemically peculiar – stars: individual: β UMa – stars: individual: θ Leo

1. Introduction

About 5% to 10% of hot stars (stars with O, B, and A spectral types) are found to be strongly magnetic with a longitudinal magnetic field strength in excess of 100 G (e.g., Wade et al. 2013; Aurière et al. 2007), which is generally associated with a simple and stable field geometry (e.g., Lüftinger et al. 2010; Silvester et al. 2014). However, the physical origin and even some basic properties of these magnetic fields are still poorly understood. The current paradigm, the fossil field hypothesis, describes this magnetism as the remnant of magnetic field accumulated or produced during an early phase of stellar life. In this conceptual framework, magnetic fields observed in these stars today are proposed to result from a seed field in the molecular cloud from which the star was formed, rather than being currently produced by an active dynamo as in the Sun. This initial field may also have been amplified during the early phases of the evolution of the star, when it was temporarily surrounded by an extended convective envelope hosting a global dynamo. In practice, the fossil field theory leaves many basic questions unanswered, such as the precise origin of this magnetism and its low incidence among intermediate-mass and massive stars. However, it is strongly supported by many of their observational properties (e.g., Braithwaite & Spruit 2015).

Recently, a longitudinal magnetic field much weaker than any previous detection in intermediate-mass stars has been discovered in the early A star Vega (Lignières et al. 2009). The spectropolarimetric time series was interpreted in terms of a surface magnetic field distribution using the Zeeman-Doppler Imaging technique (ZDI, Petit et al. 2010), unveiling a peak local field strength of about 7 G (Petit et al. 2014a). The results of that study support the view that Vega is a rapidly rotating star seen nearly pole-on, and the reconstruction of the magnetic topology at two epochs revealed a magnetic region of radial field orientation, closely concentrated around the rotation pole. Vega may well be the first confirmed member of a much larger, as yet unexplored, class of weakly magnetic hot stars. Weak magnetic fields of the same kind were also searched for in two normal B stars, γ Peg (Neiner et al. 2014a) and ι Her (Wade et al. 2014), although no magnetic fields were detected in both stars with a precision of 0.3−0.4 G. However, Wade et al. (2014) demonstrate that, if a large-scale magnetic field identical to the ZDI magnetic geometry of Vega existed in γ Peg and ι Her, no detection would

be expected at this level of accuracy given the spectral line properties of both B-type targets.

The only other example of a weak Stokes V detection in spectral lines of an intermediate-mass star has been reported for the bright Am star Sirius A (Petit et al. 2011). For this object, however, the polarized signature observed in circular polarization is not a null integral over the width of the line profile, as expected in the usual descriptions of the Zeeman effect. Instead, the Stokes V line profile exhibits a positive lobe dominating the negative one (in amplitude and integrated flux). The interpretation of a Zeeman origin was favored by Petit et al., in particular after excluding the possibility of an instrumental crosstalk from linear to circular polarization. However, the abnormal shape of the polarized profile remained a puzzle and required further investigation.

The motivation to progress on this topic is strong because the discovery of a new, potentially widespread class of weakly magnetic A stars offers important new information about the dichotomy between strong and weak magnetic fields in tepid stars. In an attempt to interpret this division, Aurière et al. (2007) proposed a scenario based on the stability of a large scale magnetic configuration in a differentially rotating star, leading to estimating a critical field strength above which magnetic fields can remain stable on long time scales, while magnetic fields below this limit would likely be destroyed by the internal shear. More detailed models including 2D and 3D numerical simulations (Jouve et al. 2015; Gaurat et al. 2015) tend to confirm the existence of a critical field in such configurations, where the pre-main sequence contraction is a possible way to force differential rotation. On the other hand, the magnetic dichotomy might simply be the result of two different magnetic field generation processes. Braithwaite & Cantiello (2013) propose that Vega-like magnetic stars are the result of the slow evolution of magnetic configurations characterized by weak initial magnetic helicity and argue that it should be widespread among most intermediate-mass and massive stars. Meanwhile, Ferrario et al. (2009) propose that the small fraction of strong magnetic fields could be produced in early stellar merging events.

In the rest of this paper, we first present the two bright Am stars selected for this study. We then present the observations and the analysis methods used. A series of tests was performed to constrain the physical origin of the recorded polarimetric signatures further, and finally we discuss our results in the broader context of weakly magnetic star of intermediate mass.

2. Selected targets

Here, we present the results of deep spectropolarimetric campaigns carried out for two bright Am stars in which magnetic fields were previously undetected (Aurière et al. 2010). Am stars are chemically peculiar stars exhibiting overabundances of iron-group elements such as zinc, strontium, zirconium, and barium and deficiencies of a few elements, particularly calcium and scandium. Most Am stars also feature low projected rotational velocities, as compared to normal A stars (Abt 2009). The targets of this study are β Ursa Majoris (HD 95418) and θ Leonis (HD 97633). Abundances measured for β UMa place this star among targets featuring weak Am characterictics with noticeable overabundance in V , Mn , Ni , Ni , Zn , Sr , Y , Zr , and Ba and underabundances in He , C , C , and Sc (for more details see Adelman et al. 2011). The source θ Leo is also on the weak side of Am abnormality, with large reported overabundance in S , V , Cr , Sr , Y , and Zr and Ba and underabundance in A , Ca , Sc , Mn , and Ni , (Adelman et al. 2015).

Table 1. Fundamental parameters of β UMa and θ Leo.

	β UMa	θ Leo
Spectral type	A1V	A2V
$T_{\rm eff}$	9480 K ± 10 K[a]	9280 ± 10 K[a]
$\log g$	3.82[b]	3.65[c]
Mass	2.64 ± 0.01 $M_\odot$[a]	2.94 ± 0.2 $M_\odot$[a]
Radius	3.021 ± 0.038 $R_\odot$[d]	4.03 ± 0.10 $R_\odot$[e]
$v \sin i$	46 ± 3 km s^{-1}[f]	23 ± 3 km s^{-1}[f]
$L_\odot$	72 ± 11[a]	127 ± 13[a]
Frac. age	0.778[a]	0.943[a]
Metallicity	−0.03[g]	−0.13[g]

References. [(a)] Zorec & Royer (2012); [(b)] Allende Prieto et al. (1999); [(c)] Adelman et al. (2015); [(d)] Boyajian et al. (2012); [(e)] Maestro et al. (2013); [(f)] Royer et al. (2002); [(g)] Anderson & Francis (2012).

The fundamental parameters of both targets are presented in Table 1. The two objects are early A-type targets. Both of them benefit from an interferometric estimate of their radius, which is distinctly larger than the radius of main sequence stars of similar spectral types. Accordingly, their surface gravities are found to be below main sequence values. High luminosity values complete this picture, confirming that both targets are already on their way off the main sequence. Using evolutionary models matching the position of both stars in the H-R diagram, Zorec & Royer (2012) find that the fractional age on the main sequence of β UMa and θ Leo are equal to 0.778 and 0.943, respectively, giving further support to the idea that both stars have completed most of their path on the main sequence. That β UMa is reported to belong to the Ursa Majoris association gives another constraint on the age, which is estimated to be around 500 Myr for this group of stars (Monier 2005). Based on *Spitzer* measurements of IR excess, Ballering et al. (2013) attribute ages of 310 Myr and 500 Myr to β UMa and θ Leo, respectively, which is too young to be reconciled with other stellar parameters, but may provide an additional hint that θ Leo is more evolved than β UMa.

The projected rotational velocities estimated for both stars are fairly typical of values reported for Am stars (Abt 2009). In the absence of any direct estimate of the rotation period of our targets, it cannot be determined whether the higher $v \sin i$ value reported for β UMa is linked to a faster rotation or higher inclination angle.

3. Data analysis

Data were taken with the NARVAL spectropolarimeter (Aurière 2003, Silvester et al. 2012) in operation at the two-meter *Bernard Lyot* Telescope (TBL) at the summit of Pic du Midi Observatory in the French Pyrénées. This high resolution spectropolarimeter is specially designed and optimized to detect stellar magnetic fields through the polarization they generate in photospheric spectral lines. The polarimetric unit is mounted at the Cassegrain focus of the telescope and allows two orthogonal states of a given polarization (circular or linear) to be recorded throughout the entire optical domain, thanks to the high achromaticity of its polarimetric optics. The upper part of the polarimeter contains the guiding camera, an atmospheric dispersion corrector, and a calibration wheel. Following that, the main polarimetric device constitutes three Fresnel rhomb retarders (two half-wave rhombs that can rotate about the optical axis and one fixed quarter-wave rhomb), which are used to perform the polarimetric analysis. The

light emerging from the retarders is sent to a Wollaston prism, consisting of two orthogonal calcite prisms that are cemented together, acting as a polarizing beamsplitter.

The two beams of light emerging from the beamsplitter are transmitted by some 30 m of optical fiber to the bench-mounted spectrograph, where an image slicer converts the circular image of the fiber head into a pseudo-slit shape. The spectrograph provides complete coverage of the optical spectrum from 3700 to 10 500 Å on 40 echelle orders with a spectral resolution of about 65 000 in polarimetric mode. The spectrograph unit contains a double set of high-reflectance collimators cut from a single 680 mm parabolic mirror with a focal length of 1500 mm. The grating is a 79 gr/mm monolithic grating with dimensions of 200 by 400 mm, and the cross-dispersion is achieved by a high dispersion prism. The camera lens is a fully dioptric f/2 388 mm focal length lens with a 210 mm free diameter. The spectrograph thermal stability is kept to within 0.1 K, thanks to the use of a double-layer thermal enclosure.

All data used in the present paper are collected in the polarimetric mode measuring Stokes V (circular polarization).To minimize systematic errors, one complete Stokes V sequence consists of four successive subexposures taken with the half-wave rhombs oriented at different azimuths. This follows the method of Semel et al. (1993) to reduce the amplitude of possible spurious signatures of instrumental origin. This strategy also provides a strong test to discard the possibility of a spurious signal by computing a "null" spectrum. This is calculated from a different combination of the four subexposures constituting the polarimetric sequence (Donati et al. 1997), and it should not display any signal. This "null" check parameter is automatically produced for each Stokes V sequence.The data are reduced by Libre-Esprit, a dedicated and fully automated software (Donati et al. 1997) specifically developed for reducing echelle spectropolarimetric data and optimized for NARVAL. Libre-Esprit proceeds in three steps: the first stage consists of performing a geometrical analysis from a sequence of calibration exposures; the position and shape of orders is derived from a mean flat field image, while the details of the wavelength to pixel relation along and across each spectral order is obtained from comparison frames obtained from a ThAr lamp and a Fabry-Perot setup. The second step performs spectrum optimal extraction (Horne 1986; Marsh 1989), using the geometrical information derived in step 1. A last step consists of refining the wavelength calibration using telluric lines recorded in the reduced spectrum, therefore reaching a radial velocity accuracy close to 30 m s^{-1} (Moutou et al. 2007). Spectra processed with Libre-Esprit include the flux and polarization information, as well as the "null" spectrum computed from two different combinations (dubbed "Null1" and "Null2" in our plots) and error bars at each wavelength point in the spectrum.

The source β UMa was observed in March/April 2010 and March/April 2011 for a total of 149 spectra. For its part, θ Leo was observed in January/March/April 2012, March/April 2013, and May/June 2014 for a total of 171 spectra (see Table A.1 for the detailed distribution of observations among individual nights). For each star, the exposure time was adjusted to reach a peak signal-to-noise ratio (S/N) throughout the Stokes V spectrum between 1000 and 2000 per 1.8 km s^{-1} bin, depending on weather conditions. These relatively high values are safely away from the saturation level of the EEV detector used in fast readout mode.

In the absence of any detectable polarized signatures in individual spectral lines of β UMa and θ Leo, we apply the well-known and commonly used least squares deconvolution (LSD) procedure (Donati et al. 1997; Kochukhov et al. 2010) to each spectrum of both stars. This method is a cross-correlation technique for computing average pseudo-line profiles from a list of spectral lines in order to get a multiplex increase in the S/N. This powerful technique, based upon several rough approximations (additive line profiles, wavelength-independent limb-darkening, self-similar local profile shape, weak magnetic fields), makes use of the possibility of describing stellar spectra as a line pattern convolved with an average pseudo-line profile. Here, we choose to compute the LSD Stokes I and V pseudo-profiles for all available photospheric lines. Our line lists are taken from the VALD atomic data base (Piskunov et al. 1995; Kupka & Ryabchikova 1999) using the respective effective temperature and $\log g$ of both stars (Table 1). Our line lists are extracted using $T_{\rm eff}$ = 9500 K and $\log g$ = 4.0 for β UMa and $T_{\rm eff}$ = 9250 K and $\log g$ = 3.5 for θ Leo. We reject the lines whose depth is less than 1% of the continuum. By doing so we obtain a mask of 1173 lines and 1133 lines for β UMa and θ Leo, respectively. Then, we adjust the depth of the lines in the mask to fit the observed line depths. To reduce the noise per spectral bin further and then reduce the spectral resolution of LSD line profiles. Instead of the default spectral bin spanning 1.8 km s^{-1} at a spectral resolution of 65 000, we used 9 km s^{-1} for β UMa and 5.4 km s^{-1} for θ Leo, which leaves us with about ten velocity bins in the pseudo line profile. With this modification of the spectral resolution, the additional gain in the S/N is a factor of 2.1 for β UMa and 1.7 for θ Leo. The nightly averaged S/Ns of the resulting Stokes V LSD profiles (i.e., the average of the S/Ns of individual profiles) are between 45 000 and 77 000 for β UMa and between 25 000 and 48 000 for θ Leo (Table A.1). The dispersion of the S/N between individual Stokes V sequence of a given night is often the lowest during nights featuring the highest average S/N, because of the excellent (and stable) sky transparency.

Polarized signals remain undetected in individual LSD Stokes V pseudo-profiles of our two targets. However, their typical S/N remains far too low to detect polarized signatures as weak as the one previously reported for Sirius A (Petit et al. 2011). To further improve the S/N, we coadd all available LSD profiles for each star, resulting in one "grand average" pseudo-line profile. This method was successfully used for Vega (Lignières et al. 2009; Petit et al. 2010) and Sirius (Petit et al. 2011) to detect signatures with amplitudes as low as about 10^{-5} of the continuum level. To coadd the LSD profiles, we weight each individual LSD profile proportionally to its squared S/N:

$$w_i = SNR_i^2 / \sum_{i=0}^{n} SNR_i^2 \quad (1)$$

where w_i and SNR_i are the weight and S/N of the ith pseudo profile.

We choose here to keep all profiles in this process, even those with the lowest S/N (LSD profiles with S/N lower than 10 000 represent 16 observations for β UMa and 2 for θ Leo), because this systematic rejection was found to provide us with nothing more than a marginal modification of the result (and no noticeable improvement). The grand average LSD profiles are presented in Fig. 1. With the large number of spectra collected here, the coaddition of all profiles increases the S/N by a factor ≈10, compared to individual profiles. The resulting S/N of the grand average V profiles is 653 640 for β UMa and 512 370 for θ Leo (using the normalization parameters listed in Table B.1).

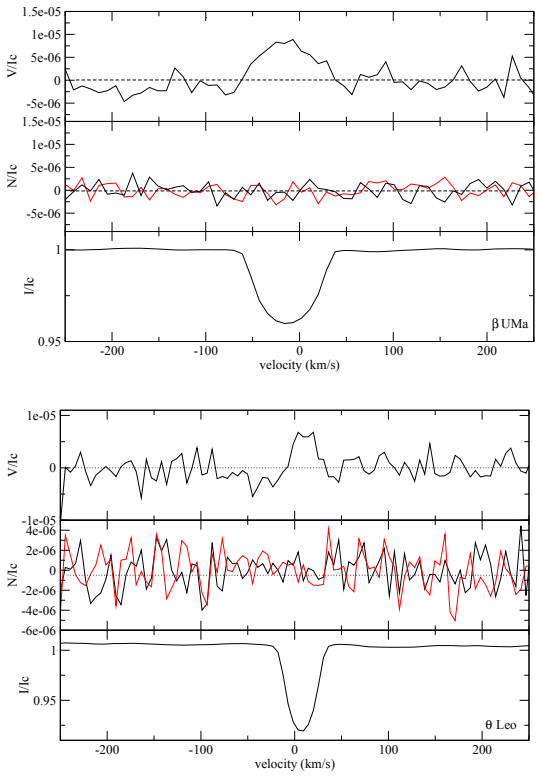

Fig. 1. Coadded LSD profiles in Stokes I (*bottom*) and V (*top*). The two available "null" control parameters Null1 and Null2 are shown in the middle panel. *Top*: β UMa observations. *Bottom*: same figure for θ Leo. All profiles are normalized to the continuum level.

One limitation of this rough co-addition method is that we average together observations taken at different rotational phases. In the absence of any known rotation period, we assume our data are distributed over all rotation phases with the same probability. We therefore lose any phase-resolved information, and the axisymmetric surface structures (i.e., structures symmetric about the spin axis) are the most likely to survive the coaddition process and actually contribute to the grand average. This strategy is, however, successful at reducing the noise level enough to permit the detection of circularly polarized signatures in both stars, while the null profiles remain free of any feature above noise level.

Reduced spectra are provided by Libre-Esprit with a normalized continuum, although the actual resulting continuum typically deviates by up to 15% from unity, especially in the bluest orders of the spectra. To test the impact of this imperfect automated processing on the result of our LSD analysis, we normalized each of the 40 echelle orders for each spectrum (see Neiner et al. 2014b) with the continuum task of IRAF[1]. The new normalization improves the S/N of the individual LSD profiles by about 5%. We notice that the upgraded normalization changes the resulting LSD profiles slightly, however the improvement is very marginal, even at the extremely high S/N of our grand average profiles. In spite of the limited quality of the default continuum normalization, the robustness of LSD is mainly due to the large number of lines taken into account in the LSD process, compared to hotter stars for which the improved normalization is more useful. As a consequence, we simply consider here the spectra normalized with Libre-Esprit for consistency with the previous studies on Vega (Lignières et al. 2009; Petit et al. 2010) and Sirius (Petit et al. 2011) in which the default renormalization was used.

[1] Image Reduction and Analysis Facility, http://iraf.noao.edu/

4. Results

4.1. LSD profiles with complete line mask

The Stokes I, V, Null1 and Null2 co-added LSD profiles of β UMa and θ Leo are shown in Fig. 1. They display clear Stokes V signatures at the radial velocity of the Stokes I line profiles. The circularly polarized signal observed for both stars covers most of the width of the line and is mostly symmetric about the line centroid. In both cases, a positive lobe dominates the signal. No detectable signal is seen in the Null1 and Null2 control profiles. We computed the detection probability of the Stokes V signal by using the χ^2 test proposed by Donati et al. (1992), getting a detection probability of ~100 % for both stars with a false alarm probability below 10^{-11} for β UMa and equal to 6.5×10^{-6} for θ Leo. Outside of the stellar lines, we obtained a marginal signal detection for β UMa, due to the negative bump in the Stokes V continuum showing up at a radial velocity of around -200 km s^{-1}. This continuum feature, not observed for θ Leo, may be due to residuals of line blends (Kochukhov et al. 2010).

We note that the Stokes V signatures detected in the co-added LSD profiles probably stem from a significant fraction of the individual LSD profiles, as various subsets from our complete data set (e.g., observations taken during a given year, see Fig. 5) display the same signal when co-added separately, although with a higher noise level. The single-epoch subsets are obtained over a timespan that is much longer than the longest possible rotation period of the two targets, so that the co-addition process of many individual rotational phases should result, in all cases, in a filtering of any signatures resulting from nonaxisymmetric magnetic structures.

4.2. Possible instrumental artifacts at high S/N

The very high S/N achieved to detect weak polarimetric signatures in intermediate-mass stars raises the question of possible instrumental effects that could contribute to generate spurious signatures in NARVAL Stokes V sequences. All spectra obtained for our study display a peak S/N below 2000, and the majority of them are kept below 1500. At such S/N values, we safely stay away from the saturation regime of the detector (S/N above 2000 for standard early-type stars). We note that subsets extracted from our complete time-series display consistent signatures, regardless of the S/N of the subset, as highlighted by, e.g., Fig. 5. In any case, most spurious signatures generated by nonlinear behavior of the detector are expected to show up in the Null1 and Null2 check profiles (especially if the S/N is fluctuating from one subexposure to the next), which is not seen here.

From an empirical point of view, we stress that the signatures recorded so far for Sirius A (Petit et al. 2011; Kochukhov 2014) display a similar shape using three different instrumental setups (ESPaDOnS, NARVAL, HARPSpol) and three different models of CCD detector and two different reduction pipelines, giving strong confidence in a stellar origin of the polarized signature. We finally emphasize that a number of stars belonging to several classes were previously observed at a comparable S/N,

which resulted in no Stokes V detection in two normal B stars (Wade et al. 2014; Neiner et al. 2014b), in a definite Stokes V detection (with a standard Zeeman shape) for the λ Boo star Vega (Lignières et al. 2009), and in a definite Zeeman detection (again with a standard shape) for the cool giant Pollux (Aurière et al. 2009).

Another potential source of instrumental artifacts, especially for very weak Stokes V signatures, is possible crosstalk from linear to circular polarization. This effect is documented for NARVAL and ESPaDOnS (e.g., Silvester et al. 2012). Stokes Q and U spectra were obtained for Sirius A by Petit et al. (2011), featuring no polarimetric signal at a level that could significantly contribute to the Stokes V signal. The same profile shape obtained for Sirius A using three instruments affected by different crosstalk levels is, in itself, an independent evidence that linear polarization did not contaminate the Stokes V signature.

Considering this context as a whole, we conclude that a convincing body of evidence now exists to safely conclude that the Stokes V signal observed for β UMa and θ Leo most likely has a stellar origin.

4.3. Establishing the Zeeman origin of Stokes V signatures

4.3.1. Method outline

The shapes of the signatures in the Stokes V profiles (mainly constituted of a positive lobe) are not expected in the standard theory of the Zeeman effect, which predicts that lobes of positive and negative signs should be observed, resulting in a zero-integral Stokes V profile. This surprising observation, and the extremely low amplitude of the recorded signatures, raise natural concerns about possible artifacts that may contribute to the observed polarized signal. Considered all together, the standard series of tests detailed in Sect. 4.1 provides us with strong evidence that the recorded signatures are stellar in origin. Other convincing evidence includes the possibility that crosstalk from linear to circular polarization is not involved (Petit et al. 2011) and that no similar signatures were observed in other hot or tepid stars studied at a similar level of accuracy (Lignières et al. 2009; Wade et al. 2014; Neiner et al. 2014b), in spite of a strictly identical instrumental setup. HARPSpol observations reported by Kochukhov (2014) also confirm that the peculiar signature reported for Sirius A is still obtained when using a completely different instrument and different reduction software.

Even if instrumental effects can be safely excluded, the physical origin of the signal still requires further investigation. We propose here a series of tests to ascertain the Zeeman origin of the recorded signal. The basic idea is that the amplitude of Zeeman signatures is expected to depend on various line parameters (Landé factor, wavelength, line depth), so that a careful selection of spectral lines for the LSD procedure should confirm or refute this dependence in our data. We therefore run again the LSD process using a number of new line lists, extracted from our original list but featuring a selection of lines where one line parameter has been restricted to a given range. In the weak field approximation, Stokes V signals are related to line parameters according to the following equation:

$$V \propto g.\lambda_0^2.B_{\parallel}.\partial I/\partial\lambda \quad (2)$$

where λ_0 represents the wavelength of the line profile, $B_{\parallel}$ the line-of-sight projection of the magnetic field vector, and g the effective Landé factor. At a given value of $B_{\parallel}$, the amplitude of Stokes V is therefore expected to follow simple variations with λ_0, g, and with the line depth.

As a reference, we use here the standard Ap star α^2 CVn and a NARVAL observation downloaded from PolarBase (Petit et al. 2014b) and already used by Silvester et al. (2014). The star α^2 CVn is bright and variable A0p with $v \sin i$ = 18 ± 0.5 km s^{-1}, an effective temperature of 11 600 ± 500 K, and a logarithmic surface gravity equal to 3.9 ± 0.1 (Silvester et al. 2014). Its spectral properties are therefore reasonably similar to β UMa and θ Leo, except its slightly higher surface temperature. The interesting characteristic of α^2 CVn is its strong and organized surface magnetic field (locally up to 2 kG), resulting in very large circularly polarized signatures. We applied our series of tests to this reference star to better highlight the expected results in the presence of a strong magnetic field, with negligible noise in the polarized profile.

The average line parameters for all submasks used to compute the new LSD profiles are listed in Table B.1. They vary slightly from one star to the next mostly because of the different VALD models employed. The largest star-to-star differences are observed when we define the line sublists according to a wavelength threshold. We also list in Table B.1 the normalization parameters used for the LSD procedure, forcing a normalized wavelength of 500 nm everywhere, except when we set a wavelength threshold, in which case we force a normalized Landé factor equal to 1.2. Finally, we correct for any difference in the depth of Stokes I profiles, except when the submasks are defined with a line depth threshold.

4.3.2. Outcome for β UMa and θ Leo

As a first test, we ran LSD for two submasks containing lines with an average Landé factor g lower (resp. greater) than the mean Landé factor of the original line list (see Table B.1). Hereafter, we consider the normalizing Landé factors used as part of the LSD procedure, since it is the relevant quantity for direct comparison of different LSD profiles. (The normalizing g values follow the same trend as the average Landé factors of the submasks.) The resulting Stokes V profiles are plotted in Fig. 2 for the two Am stars and the control Ap star. The Stokes V profiles are corrected for a ∼10% difference in equivalent width observed in their associated Stokes I profile. Because of a higher noise level than obtained with the complete line mask, the high-g and low-g profiles of β UMa and θ Leo do not display any statistically conclusive differences. The overplotted running average helps to improve the situation, showing that the high-g signals possess higher amplitudes than their low-g counterparts. We note that their amplitude ratio is roughly consistent with the g ratio, although this point is difficult to establish with high accuracy (even with the running average) because of the level of noise.

As second test, two sublists were defined from our original list by containing lines with a wavelength lower (resp. greater) than the mean wavelength of the original list (Table B.1). For a given star, the Stokes V profiles were corrected for the ∼30% difference in equivalent width observed in their associated Stokes I profiles. The outcome of this test is illustrated in Fig. 3, which illustrates a marginally larger amplitude of the Stokes V signal when the wavelength increases. As for the previous test, we computed a moving average of the signal to confirm the trend that is otherwise completely hidden in the noise and to check that the trend observed in both Am stars is consistent with the outcome obtained for α 2 CVn.

As a last test, we define two sublists using spectral lines with an average depth lower (resp. greater) than the mean depth of the original list (Table B.1). The Stokes V LSD profiles obtained from the sublists are displayed in Fig. 4 and, for our two Am stars

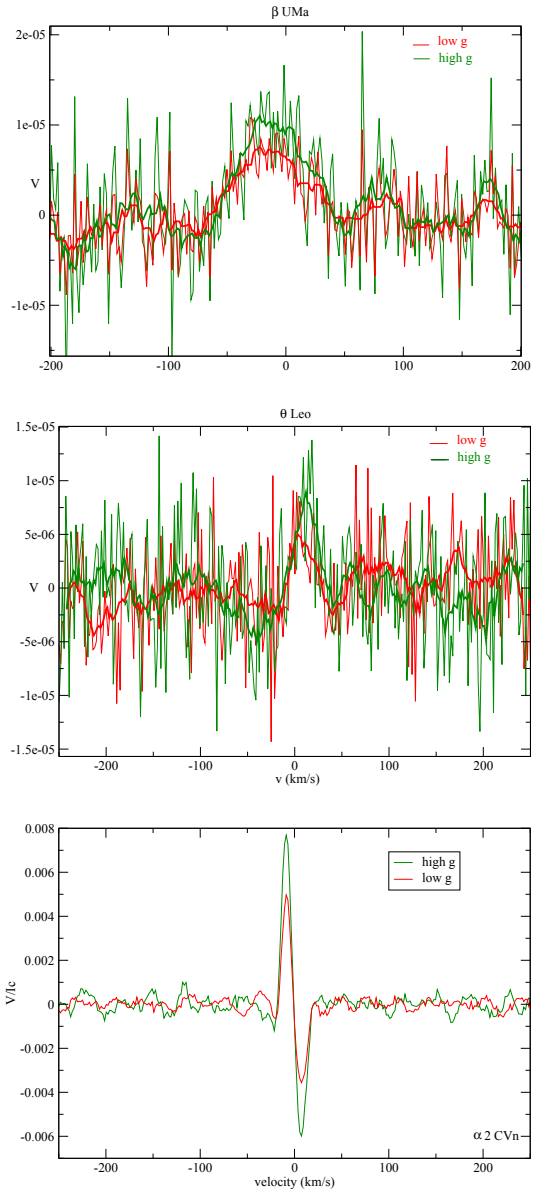

Fig. 2. *Top*: comparison of the Stokes V profiles obtained by selecting photospheric lines of low (red thin line) and high (green thin line) magnetic sensitivity for β UMa. The thick red and green lines represent a moving average over three spectral bins of the thin lines. *Center*: same figure for θ Leo. *Bottom*: same for α^2 CVn. All profiles are normalized to the continuum level.

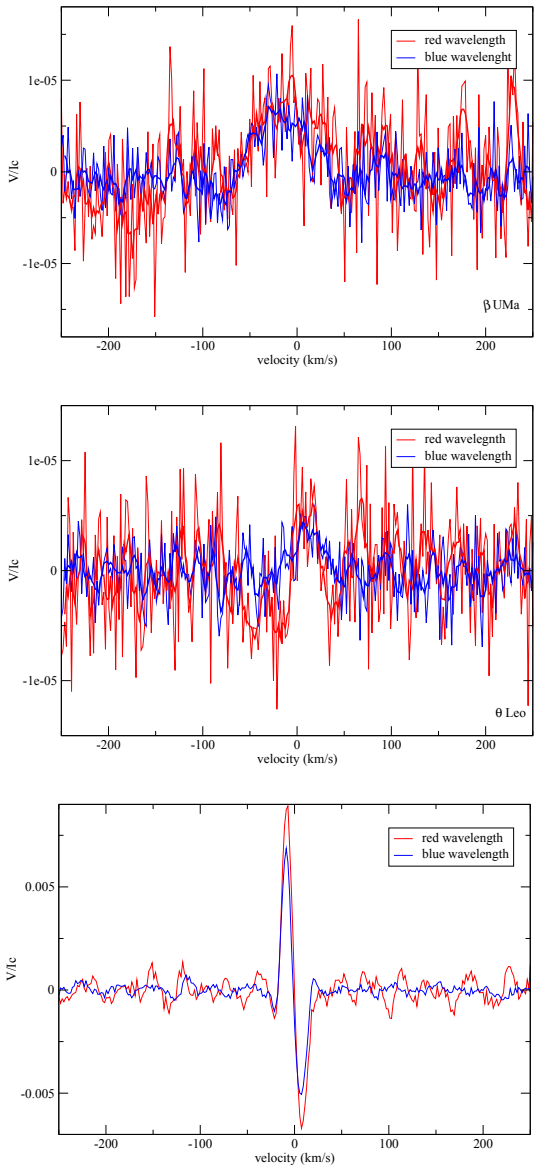

Fig. 3. Same as Fig. 2 for photospheric lines of low (thin blue line) and high (thin red line) wavelength.

and our reference star, clearly show a lower amplitude whenever the average line depth is smaller. This outcome is expected in the case of a signature of magnetic origin, but also for most instrumental artifacts.

From the series of tests presented here, only the one with low versus high Landé factors was performed by Petit et al. (2011) for Sirius A. For consistency, we used their observing material to reproduce with Sirius A the three tests applied to β UMa and θ Leo. The result, not shown here, is fully consistent with the conclusions reached in the present study. Considered together, this series of tests strongly suggests that the circularly polarized signatures obtained for the three bright Am stars observed so far have a Zeeman origin.

Based on this conclusion, it is tempting to estimate the surface field strength from our set of measurements, using the classical center of gravity (or first moment) method (Rees & Semel 1979). We must stress, however, that this widely used technique is based on the standard assumption that the Stokes V signature is antisymmetric about the line center, which is very far from the actual shape of our Stokes V signatures. A purely symmetric signature (closer to what is obtained for β UMa and θ Leo)

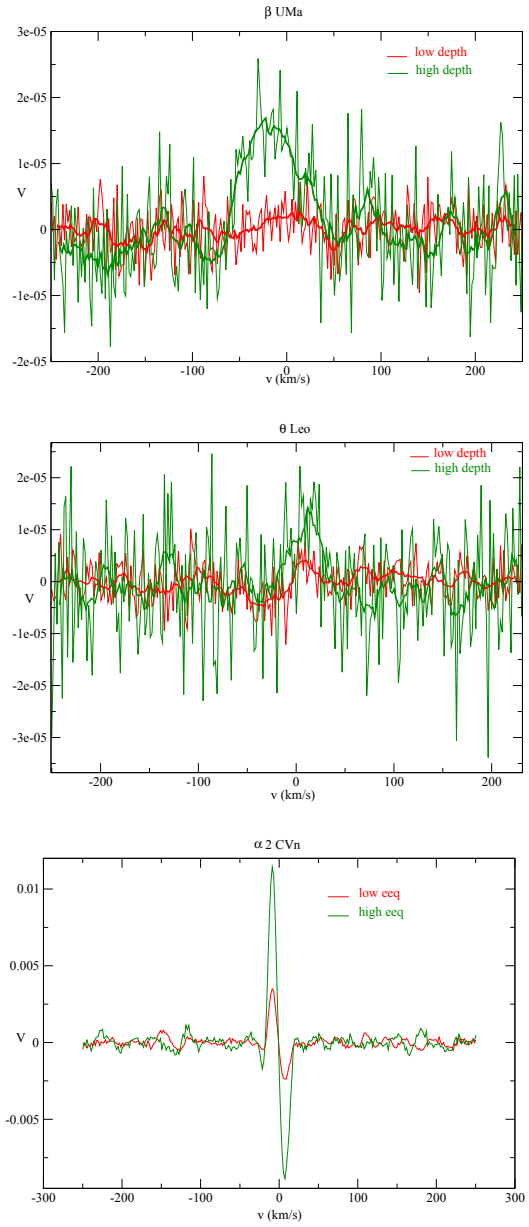

Fig. 4. Same as Fig. 2 for photospheric lines of low (thin red line) and high (thin green line) central depth.

will be interpreted as a zero longitudinal field strength, regardless of the amplitude of the Stokes V signal, similarly to dipolar fields observed at the rotational phase of a crossover configuration (e.g., Aurière et al. 2007). The situation here is obviously different, because the large time span of data collection is very unlikely to be restricted to a crossover phase. Nevertheless, such a measurement (and in particular its error bar) provides us with a quality measure of the sensitivity of the magnetic diagnosis that can be compared to similar studies. The first moment estimate of the magnetic field provides us with a field strength of -1 ± 0.8 G for β UMa and -0.4 ± 0.3 G for θ Leo that is unsurprisingly consistent with zero (as previously reported with Sirius A). As an attempt to propose a more relevant proxy of the field strength, we calculate the equivalent width (EW) of the Stokes V signature and normalize this EW by the one of the Stokes I profile. By doing so, we obtain a normalized EW equal to 1.96×10^{-4} for β UMa, and 5.44×10^{-5} for θ Leo. For Sirius A, the normalized EW is equal to 6.68×10^{-5}.

5. Discussion

5.1. Peculiar Stokes V signatures in Am stars

The observations presented here provide new clues to the weak polarized signatures produced in the photospheres of intermediate-mass stars. We report the detection of weak Stokes V signatures in two of the brightest Am stars, which complements the previous detection of a similar polarized signal for Sirius A (Petit et al. 2011)[2]. Considered together, the three polarimetric detections constitute a 100 percent detection rate so far in our sample of bright Am stars, suggesting widespread similar signatures in this stellar class.

All signals observed to now possess roughly the same shape, with one positive lobe roughly symmetric about the line center and occupying most of the width of the line profile. Negative lobes surrounding the positive one, if they exist, do not exceed the noise level in the data sets available to us. These profile shapes displaying net circular polarization are atypical of Zeeman signatures observed in other classes of magnetic stars, where the integral of the Stokes V profile is generally close to null. This peculiar shape naturally prompts questions about the origin of these polarized spectral features. The tests conducted in our study show that these unexpected signatures depend on spectral line parameters (wavelength, Landé factor, line depth), as expected from a Zeeman signal.

Stokes V profiles that are nearly symmetric about the line center are common. These patterns are temporarily observed when two magnetic poles of an inclined dipole are seen on the visible hemisphere of a star, close to the limb, and therefore with different radial velocities (at the so-called crossover rotational phases). This simple interpretation is, however, very unlikely here since our co-added LSD profiles mix data collected over timespans much longer than the typical rotation periods of Am stars, merging a large number of random rotation phases. A dominant toroidal magnetic field component is also able to generate symmetric Stokes V profiles (Donati et al. 2005), although this specific type of magnetic geometry should not produce any net circular polarization, as observed here. In any case, a purely geometric explanation is not able to account for the absence of negative lobes in the Stokes V profiles.

A number of cool active stars were reported to display weak net circular polarization after integration over LSD line profiles (Petit et al. 2005; Aurière et al. 2008, 2011; Morgenthaler et al. 2012; Tsvetkova et al. 2013; Lèbre et al. 2014). However, no similar findings have been reported so far in strongly magnetic massive stars or intermediate-mass stars, and the very subtle effect reported for cool stars is nowhere near the extreme situation reported here. For cool stars, the proposed interpretation was adapted from solar physics, where abnormal Stokes V are routinely described (e.g., Solanki 1993) and attributed to simultaneous vertical gradients in velocities and magnetic field strengths (López Ariste 2002 and references therein). Single-lobed signatures resembling those recorded for Am stars can

[2] An observation confirmed by independent HARPSpol observations carried out by Kochukhov (2014).

be locally observed in solar magnetic elements (Viticchié & Sánchez Almeida 2011; Sainz Dalda et al. 2012), but they are more difficult to justify in the case of disk-integrated measurements (as obtained for unresolved stars) because of the organized flows and magnetic fields invoked to justify their shape. Relatively strong magnetic fields are also involved in asymmetric solar Stokes V profiles, although the very weak disk-integrated signatures reported here do not tell much about local magnetic strengths, which could potentially be rather large in the case of a very tangled field geometry.

The absence of any similar phenomenon in Ap stars (in spite of masses roughly identical to those of Am stars) may simply be related to the lack of any significant surface turbulence due to the strong magnetic fields permeating their photosphere (Folsom et al. 2013) and, in the case of Bp stars, to a photospheric temperature too high to allow for a thin convective shell, even in the absence of their magnetic field. The situation is different for Am stars, for which high-resolution spectra have revealed stronger microturbulence than for normal A stars (Landstreet et al. 2009), as long as their effective temperature remains below about 10 000 K, a condition fulfilled by our two targets and by Sirius A. The very shallow convective shell producing this turbulent velocity field may host supersonic convection flows (Kupka et al. 2009). This could provide the source of sharp velocity and magnetic gradients needed to produce strongly asymmetric profiles. Shocks traveling in this superficial turbulent zone may also contribute to amplify any existing magnetic field, as previously proposed in the context of the Mira star χ Cygni (Lèbre et al. 2014).

In any case, a physical model able to produce a convincing reproduction of the peculiar polarized signatures reported for Am stars still needs to be developed. Preliminary simulations of Stokes V profiles with velocity and field gradients show that signatures such as those observed in beta UMa, theta Leo, and Sirius A can be reproduced (C. Folsom, priv. comm.). Without such a tool at our disposal, any quantitative description of the associated surface magnetic fields is out of reach, since techniques commonly used to estimate stellar magnetic field strengths (like the center-of-gravity method) are not suited to model Stokes V profiles following such unexpected shape. In practice, magnetic strengths derived for β UMa and θ Leo by applying the usual methods can only provide us with a lower limit of a few tenths of a gauss on the surface axisymmetric field component, which is consistent with the estimate available for on Sirius A.

5.2. Origin of the magnetism of Am stars

With only small number of objects observed so far and polarimetric signatures close to the detection limit, our observations only offer a few hints to the physical ingredients involved in the generation of the weak surface magnetic fields observed in Am stars.

An important clue to distinguishing between a dynamo-generated field and most other scenarios is the long-term evolution of the observed magnetic field, because a dynamo-generated field is likely to experience some temporal variability on a secular timescale. By splitting our data sets into subsets limited to a given year of observation, we are able to get a first glimpse at the stability of the polarimetric signal (Fig. 5). We find that signatures recovered one year apart are consistent with each other, showing that any variability over this timespan remains below the noise level. This outcome is consistent with similar attempts for Sirius A and Vega.

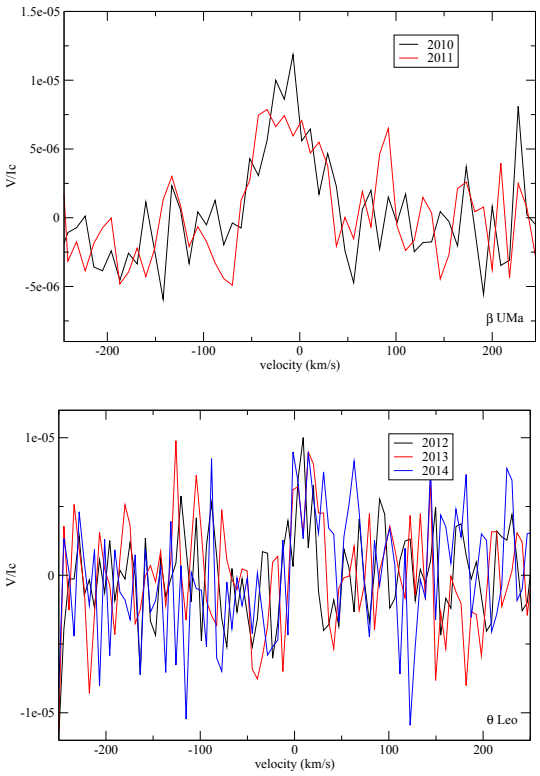

Fig. 5. *Top*: mean Stokes V profiles for the different years of observation of β UMa. *Bottom*: same figure for θ Leo.

Surface brightness inhomogeneities are usually associated with the structured magnetic field produced by a global dynamo. The lack of any rotation period estimate available in the literature for β UMa and θ Leo suggests that any such brightness patches must take place on relatively small spatial scales or be limited to a very low contrast. We note that the recent discovery of rotational modulation in Am stars of the *Kepler* field by Balona et al. (2015) was limited to targets that are significantly cooler than the objects of our study. A possibility is that the deeper convective envelope of stars in the *Kepler* sample may be more favorable to the onset of a large-scale dynamo. A very sensitive method, such as the one employed by Böhm et al. (2015) to detect very faint starspots on Vega, may be the key to unveiling surface features on weakly magnetic Am stars like those studied here. We also note the lack of documented flaring events for these bright and well-studied stars, again in contrast to claims for cooler intermediate-mass stars observed with *Kepler* (Balona 2013; Balona et al. 2015).

5.3. Toward a systematic exploration of weak magnetic fields in Am stars

The ultra-deep polarimetric campaign carried out for three bright Am stars is far from exhausting the exploration of this stellar class. The most noticeable difference between these stars is that β UMa and θ Leo seem to be located near the end of the main sequence, while Sirius A is a more standard main sequence object. One conclusion of our study is that these differences in the

evolutionary status do not affect the recorded polarimetric signatures in any obvious way.

While Sirius A and θ Leo share a low projected rotational velocity, β UMa displays a higher $v \sin i$ value, although it is not possible to distinguish between the contribution of rotational and inclination effects in this parameter. The larger normalized EW of the polarimetric signal reported for β UMa may be a first hint of a rotational dependence of the weak magnetism of Am stars, although a much larger sample is required to seriously test this hypothesis.

Finally, all three objects observed so far were confined to a quite narrow band in effective temperature. The active behavior of cooler Am stars (Balona 2013; Balona et al. 2015) is a strong motivation to expand the available sample to Am stars of late-A spectral types. Since the peculiar polarized signatures observed up to now are proposed to be indirect tracers of surface convective motions, gathering observations in cooler stars is an obvious way to test this hypothesis by considering the effects of varying the surface turbulent flows on the polarized signature.

Acknowledgements. We acknowledge support from the ANR (Agence Nationale de la Recherche) project Imagine. This research has made use of the SIMBAD database operated at the CDS, Strasbourg (France) and of NASA's Astrophysics Data System (ADS). C.P.F. is supported by the ANR grant "Toupies: Towards understanding the spin evolution of stars". G.A.W. acknowledges Discovery Grant support from the Natural Science and Engineering Research Council (NSERC) of Canada. We are grateful to the referee, Iosif Romanyuk, for constructive comments.

References

Abt, H. A. 2009, AJ, 138, 28
Adelman, S. J., Yu, K., & Gulliver, A. F. 2011, Astron. Nachr., 332, 153
Adelman, S. J., Gulliver, A. F., & Heaton, R. J. 2015, PASP, 127, 58
Allende Prieto, C., García López, R. J., Lambert, D. L., & Gustafsson, B. 1999, ApJ, 527, 879
Anderson, E., & Francis, C. 2012, Astron. Lett., 38, 331
Aurière, M. 2003, in EAS Pub. Ser. 9, eds. J. Arnaud, & N. Meunier, 105
Aurière, M., Wade, G. A., Silvester, J., et al. 2007, A&A, 475, 1053
Aurière, M., Wade, G. A., Lignières, F., et al. 2008, Contributions of the Astronomical Observatory Skalnate Pleso, 38, 211
Aurière, M., Wade, G. A., Konstantinova-Antova, R., et al. 2009, A&A, 504, 231
Aurière, M., Wade, G. A., Lignières, F., et al. 2010, A&A, 523, A40
Aurière, M., Konstantinova-Antova, R., Petit, P., et al. 2011, A&A, 534, A139
Ballering, N. P., Rieke, G. H., Su, K. Y. L., & Montiel, E. 2013, ApJ, 775, 55
Balona, L. A. 2013, MNRAS, 431, 2240
Balona, L. A., Catanzaro, G., Abedigamba, O. P., Ripepi, V., & Smalley, B. 2015, MNRAS, 448, 1378
Böhm, T., Holschneider, M., Lignières, F., et al. 2015, A&A, 577, A64
Boyajian, T. S., McAlister, H. A., van Belle, G., et al. 2012, ApJ, 746, 101
Braithwaite, J., & Cantiello, M. 2013, MNRAS, 428, 2789
Braithwaite, J., & Spruit, H. C. 2015, ArXiv e-prints [arXiv:1510.03198]
Donati, J.-F., Semel, M., & Rees, D. E. 1992, A&A, 265, 669
Donati, J.-F., Semel, M., Carter, B. D., Rees, D. E., & Collier Cameron, A. 1997, MNRAS, 291, 658
Donati, J.-F., Paletou, F., Bouvier, J., & Ferreira, J. 2005, Nature, 438, 466
Ferrario, L., Pringle, J. E., Tout, C. A., & Wickramasinghe, D. T. 2009, MNRAS, 400, L71
Folsom, C. P., Likuski, K., Wade, G. A., et al. 2013, MNRAS, 431, 1513
Gaurat, M., Jouve, L., Lignières, F., & Gastine, T. 2015, A&A, 580, A103
Horne, K. 1986, PASP, 98, 609
Jouve, L., Gastine, T., & Lignières, F. 2015, A&A, 575, A106
Kochukhov, O. 2014, in Putting A Stars into Context: Evolution, Environment, and Related Stars, eds. G. Mathys, E. R. Griffin, O. Kochukhov, R. Monier, & G. M. Wahlgren, 389
Kochukhov, O., Makaganiuk, V., & Piskunov, N. 2010, A&A, 524, A5
Kupka, F., & Ryabchikova, T. A. 1999, Publications de l'Observatoire Astronomique de Beograd, 65, 223
Kupka, F., Ballot, J., & Muthsam, H. J. 2009, Comm. Asteroseismol., 160, 30
Landstreet, J. D., Kupka, F., Ford, H. A., et al. 2009, A&A, 503, 973
Lèbre, A., Aurière, M., Fabas, N., et al. 2014, A&A, 561, A85
Lignières, F., Petit, P., Böhm, T., & Aurière, M. 2009, A&A, 500, L41
López Ariste, A. 2002, ApJ, 564, 379
Lüftinger, T., Fröhlich, H.-E., Weiss, W. W., et al. 2010, A&A, 509, A43
Maestro, V., Che, X., Huber, D., et al. 2013, MNRAS, 434, 1321
Marsh, T. R. 1989, PASP, 101, 1032
Monier, R. 2005, A&A, 442, 563
Morgenthaler, A., Petit, P., Saar, S., et al. 2012, A&A, 540, A138
Moutou, C., Donati, J.-F., Savalle, R., et al. 2007, A&A, 473, 651
Neiner, C., Monin, D., Leroy, B., Mathis, S., & Bohlender, D. 2014a, A&A, 562, A59
Neiner, C., Tkachenko, A., & MiMeS Collaboration. 2014b, A&A, 563, L7
Petit, P., Donati, J.-F., Aurière, M., et al. 2005, MNRAS, 361, 837
Petit, P., Lignières, F., Aurière, M., et al. 2011, A&A, 532, L13
Petit, P., Lignières, F., Wade, G. A., et al. 2010, A&A, 523, A41
Petit, P., Lignières, F., Wade, G. A., et al. 2014a, A&A, 568, C1
Petit, P., Louge, T., Théado, S., et al. 2014b, PASP, 126, 469
Piskunov, N. E., Kupka, F., Ryabchikova, T. A., Weiss, W. W., & Jeffery, C. S. 1995, A&AS, 112, 525
Rees, D. E., & Semel, M. D. 1979, A&A, 74, 1
Royer, F., Gerbaldi, M., Faraggiana, R., & Gómez, A. E. 2002, A&A, 381, 105
Sainz Dalda, A., Martínez-Sykora, J., Bellot Rubio, L., & Title, A. 2012, ApJ, 748, 38
Semel, M., Donati, J.-F., & Rees, D. E. 1993, A&A, 278, 231
Silvester, J., Wade, G. A., Kochukhov, O., et al. 2012, MNRAS, 426, 1003
Silvester, J., Kochukhov, O., & Wade, G. A. 2014, MNRAS, 444, 1442
Solanki, S. K. 1993, Space Sci. Rev., 63, 1
Tsvetkova, S., Petit, P., Aurière, M., et al. 2013, A&A, 556, A43
Viticchié, B., & Sánchez Almeida, J. 2011, A&A, 530, A14
Wade, G. A., Grunhut, J., Alecian, E., et al. 2013, Proc. International Astronomical Union, IAU Symp., 302, 265
Wade, G. A., Folsom, C. P., Petit, P., et al. 2014, MNRAS, 444, 1993
Zorec, J., & Royer, F. 2012, A&A, 537, A120

Appendix A: Journal of observations

Table A.1. Journal of observations.

Date	Mid-HJD	Star	T_{exp} (s)	S/N
17 Mar. 2010	2 455 273.520	β UMa	$16 \times 4 \times 107$	52 707 ± 6090
06 Apr. 2010	2 455 293.412	β UMa	$17 \times 4 \times 107$	49 436 ± 22 333
10 Apr. 2010	2 455 297.444	β UMa	$19 \times 4 \times 107$	76 493 ± 1960
11 Apr. 2010	2 455 298.397	β UMa	$19 \times 4 \times 107$	32 500 ± 7752
25 Mar. 2011	2 455 646.426	β UMa	$25 \times 4 \times 107$	56 378 ± 24 444
31 Mar. 2011	2 455 652.504	β UMa	$25 \times 4 \times 107$	45 963 ± 4907
02 Apr. 2011	2 455 654.379	β UMa	$03 \times 4 \times 107$	53 964 ± 8998
04 Apr. 2011	2 455 656.462	β UMa	$24 \times 4 \times 107$	69 029 ± 6099
22 Jan. 2012	2 455 949.644	θ Leo	$05 \times 4 \times 180$	44 503 ± 1018
23 Jan. 2012	2 455 950.628	θ Leo	$05 \times 4 \times 180$	39 774 ± 5090
24 Jan. 2012	2 455 951.624	θ Leo	$05 \times 4 \times 180$	41 547 ± 3889
25 Jan. 2012	2 455 952.640	θ Leo	$05 \times 4 \times 180$	41 737 ± 3134
14 Mar. 2012	2 456 001.579	θ Leo	$05 \times 4 \times 180$	43 929 ± 1810
15 Mar. 2012	2 456 002.524	θ Leo	$10 \times 4 \times 180$	47 360 ± 698
24 Mar. 2012	2 456 011.526	θ Leo	$05 \times 4 \times 180$	44 880 ± 1487
25 Mar. 2012	2 456 012.502	θ Leo	$05 \times 4 \times 180$	47 392 ± 506
27 Mar. 2012	2 456 013.400	θ Leo	$10 \times 4 \times 180$	40 883 ± 1229
21 Mar. 2013	2 456 373.488	θ Leo	$09 \times 4 \times 180$	25 542 ± 4619
23 Mar. 2013	2 456 375.465	θ Leo	$09 \times 4 \times 180$	29 220 ± 2557
16 Apr. 2013	2 456 399.444	θ Leo	$09 \times 4 \times 180$	23 751 ± 3600
17 Apr. 2013	2 456 400.492	θ Leo	$09 \times 4 \times 180$	45 010 ± 1529
22 Apr. 2013	2 456 405.512	θ Leo	$09 \times 4 \times 180$	42 777 ± 1707
23 Apr 2013	2 456 406.454	θ Leo	$09 \times 4 \times 180$	42 064 ± 2815
24 Apr. 2013	2 456 407.502	θ Leo	$09 \times 4 \times 180$	39 578 ± 2497
14 Apr. 2014	2 456 762.445	θ Leo	$05 \times 4 \times 180$	25 433 ± 8566
07 May 2014	2 456 785.408	θ Leo	$05 \times 4 \times 180$	42 839 ± 3748
08 May 2014	2 456 786.411	θ Leo	$05 \times 4 \times 180$	39 435 ± 2842
09 May 2014	2 456 787.416	θ Leo	$05 \times 4 \times 180$	44 236 ± 617
14 May 2014	2 456 792.471	θ Leo	$05 \times 4 \times 180$	42 041 ± 543
15 May 2014	2 456 793.413	θ Leo	$05 \times 4 \times 180$	44 653 ± 1052
07 Jun. 2014	2 456 816.408	θ Leo	$05 \times 4 \times 180$	29 599 ± 1530
10 Jun. 2014	2 456 819.415	θ Leo	$05 \times 4 \times 180$	29 931 ± 3928

Notes. The columns contain the date for each Stokes V sequence, the heliocentric Julian date corresponding to the middle of the observation time, the object name, the number of sequences, the exposure time per individual subexposure and the averaged S/N in the individual LSD Stokes V pseudo-line profiles (±rms).

Appendix B: Parameters of LSD profiles

Table B.1. Mean and normalization parameters of the original mean LSD line profiles for β UMa, θ Leo, and α^2 CVn.

	β UMa	θ Leo	α^2 CVn
Original Mask			
Mean Landé factor g	1.207	1.206	1.218
Mean wavelength (nm)	475.72	489.05	493.34
Mean line depth	0.322	0.311	0.297
Normalized Landé factor	1.216	1.227	1.241
Normalized wavelength (nm)	500.00	500.00	500.00
Normalized depth	0.450	0.433	0.410
Low$g$LSD			
Mean Landé factor g	0.941	0.956	0.971
Mean wavelength (nm)	472.22	488.71	494.91
Mean line depth	0.311	0.317	0.308
Normalized Landé factor	0.939	0.957	0.992
Normalized wavelength (nm)	500.00	500.00	500.00
Normalized depth	0.464	0.441	0.421
High$g$LSD			
Mean Landé factor g	1.529	1.516	1.533
Mean wavelength (nm)	479.95	489.48	491.27
Mean line depth	0.310	0.305	0.283
Normalized Landé factor	1.469	1.463	1.489
Normalized wavelength (nm)	500.00	500.00	500.00
Normalized depth	0.436	0.4253	0.397
Low wavelength LSD			
Mean Landé factor g	1.219	1.217	1.229
Mean wavelength (nm)	419.88	420.29	400.88
Mean	0.381	0.361	0.049
Normalized Landé factor	1.2	1.2	1.2
Normalized wavelength (nm)	450.03	457.57	464.26
Normalized depth	0.522	0.495	0.465
High wavelength LSD			
Mean Landé factor g	1.197	1.195	1.206
Mean wavelength (nm)	573.3	604.7	713.43
Mean line depth	0.275	0.267	0.256
Normalized Landé factor	1.2	1.2	1.2
Normalized wavelength	593.28	606.06	623.95
Normalized depth	0.375	0.358	0.333
Low depth LSD			
Mean Landé factor g	1.219	1.209	1.226
Mean wavelength (nm)	505.58	507.28	512.475
Mean line depth	0.214	0.212	0.203
Normalized Landé factor	1.328	1.358	1.405
Normalized wavelength (nm)	500.00	500.00	500.00
Normalized depth	0.253	0.252	0.238
High depth LSD			
Mean Landé factor g	1.170	1.192	1.193
Mean wavelength (nm)	480.14	481.97	480.45
Mean line depth	0.628	0.643	0.588
Normalized Landé factor	1.205	1.141	1.208
Normalized wavelength (nm)	500.00	500.00	500.00
Normalized depth	0.646	0.649	0.599

Appendix C

Letter on the discovery of the magnetic field of Alhena

Monthly Notices
of the
ROYAL ASTRONOMICAL SOCIETY

MNRAS **459,** L81–L84 (2016)
Advance Access publication 2016 May 23

doi:10.1093/mnrasl/slw050

Discovery of a very weak magnetic field on the Am star Alhena

A. Blazère,[1,2]★ C. Neiner[1] and P. Petit[2,3]

[1]*LESIA, Observatoire de Paris, PSL Research University, CNRS, Sorbonne Universités, UPMC Univ. Paris 06, Univ. Paris Diderot, Sorbonne Paris Cité, 5 place Jules Janssen, F-92195 Meudon, France*
[2]*Université de Toulouse, UPS-OMP, Institut de Recherche en Astrophysique et Planétologie, F-31400, Toulouse, France*
[3]*CNRS, Institut de Recherche en Astrophysique et Planétologie, 14 Avenue Edouard Belin, F-31400 Toulouse, France*

Accepted 2016 March 21. Received 2016 March 21; in original form 2016 February 8

ABSTRACT

Alhena (γ Gem) was observed in the frame of the BRIght Target Explorer spectropolarimetric survey, which gathers high resolution, high signal-to-noise, high sensitivity, spectropolarimetric observations of all stars brighter than $V = 4$ to combine seismic and spectropolarimetric studies of bright stars. We present here the discovery of a very weak magnetic field on the Am star Alhena, thanks to very high signal-to-noise spectropolarimetric data obtained with Narval at Télescope Bernard Lyot. All previously studied Am stars show the presence of ultraweak (sub-Gauss) fields with Zeeman signatures with an unexpected prominent positive lobe. However, Alhena presents a slightly stronger (but still very weak, only a few Gauss) field with normal Zeeman signatures with a positive and negative lobe, as found in stronger field (hundreds or thousands of Gauss) stars. It is the first detection of a normal magnetic signature in an Am star. Alhena is thus a very interesting object, which might provide the clue to understanding the peculiar shapes of the magnetic signatures of the other Am stars.

Key words: stars: chemically peculiar – stars: individual: γ Gem – stars: magnetic field.

1 INTRODUCTION

1.1 Magnetism in hot stars

Over the last decades, magnetic fields have been discovered in a significant number of hot (A, B, and O) stars, and these fields probably play a significant role in their evolution. However, the detailed properties of hot star magnetism are not well understood yet. About 7 per cent of hot stars are found to be magnetic (Grunhut & Neiner 2015) with dipolar magnetic fields above 300 G. The detection rate for the A-type stars is similar (∼10 per cent; Wolff 1968; Power et al. 2007). In addition, sub-Gauss longitudinal magnetic fields have recently been discovered in a few A and Am stars.

The normal A star Vega was the first ultraweak field star discovered (Lignières et al. 2009). Its spectropolarimetric time series was interpreted in terms of an ultraweak surface magnetic field using Zeeman–Doppler Imaging. The results of this study support the fact that Vega is a rapidly rotating star seen nearly pole-on. The reconstructed magnetic topology revealed a magnetic region close to the pole with radial field orientation.

In addition, ultraweak magnetic field signatures have been detected in three Am stars: Sirius A (Petit et al. 2011), β UMa, and θ Leo (Blazère et al. 2016), thanks to very precise spectropolarimetric observations. For these objects, the signature in circular polarization is not of null integral over the line profile but exhibits a positive lobe dominating over the negative one. This peculiar signal, although not expected in the standard Zeeman effect theory, was demonstrated to follow the same dependence on spectral line parameters as a signal of magnetic origin and has been confirmed to be magnetic (Blazère et al. 2016). Preliminary explanations are being proposed to explain the peculiar shape of the signatures. In Am stars, high-resolution spectra have revealed stronger microturbulence compared to normal A stars (Landstreet et al. 2009). The very shallow convective shell producing this turbulent velocity field may host supersonic convection flows (Kupka, Ballot & Muthsam 2009). This could provide the source of sharp velocity and magnetic gradients needed to produce strongly asymmetric profiles. Shocks travelling in this superficial turbulent zone may also contribute to amplify any existing magnetic field.

Vega, Sirius A, β UMa, and θ Leo may well be the first confirmed members of a new class of magnetic hot stars: the ultraweakly magnetic hot stars. Such ultraweak magnetic fields are difficult to detect due to the weak amplitude of their Zeeman signatures and may exist in other hot stars. However, ultraweakly magnetic stars are considered a separate class of magnetic stars compared to the ∼7 per cent of stronger field stars, because no magnetic stars exist with a polar field strength between ∼300 G and the Gauss-level fields observed in ultraweak magnetic stars.

To explain this dichotomy between strong and weak magnetic fields in hot stars, Aurière et al. (2007) proposed a new scenario based on the stability of a large-scale magnetic configuration in

★E-mail: aurore.blazere@obspm.fr

Table 1. Fundamental parameters of the Am stars Alhena and θ Leo.

	Alhena A	θ Leo
Spectral type	A0IVm	A2Vm
$T_{\rm eff}$ (K)	9260 ± 10^a	9280 ± 10^b
log g	3.6^a	3.65^c
Mass ($M_\odot$)	2.84 ± 0.01^b	2.94 ± 0.2^b
Radius ($R_\odot$)	3.9 ± 0.1^d	4.03 ± 0.10^e
$v \sin i$ (km s^{-1})	15 ± 3^f	23 ± 3^f
Luminosity ($L_\odot$)	123 ± 11^b	127 ± 13^b
Age (Myr)	484^g	436^g
Microturb. (km s^{-1})	2^a	1^b

Notes. [a]Adelman et al. (2015b).
[b]Zorec & Royer (2012).
[c]Adelman et al. (2015a).
[d]Pasinetti Fracassini et al. (2001).
[e]Royer, Zorec & Gómez (2007).
[f]Royer et al. (2002).
[h]David & Hillenbrand (2015).

a differentially rotating star: strong magnetic fields correspond to stable configurations and weak magnetic fields to unstable configurations. Another theory to explain the dichotomy is the failed fossil theory (Braithwaite & Cantiello 2013): strong magnetic fields rapidly reach an equilibrium whereas weak magnetic fields are still dynamically evolving towards the equilibrium and decreased due to the instability.

1.2 The Am star Alhena

Alhena was observed in the frame of the BRITE (BRIght Target Explorer) spectropolarimetric survey. The BRITE constellation of nano-satellites performs asteroseismology of stars with $V \leq 4$ (Weiss et al. 2014). In this context, we are performing a high resolution, high signal-to-noise (S/N), high sensitivity, spectropolarimetric survey of all stars brighter than $V = 4$, with the ultimate aim to combine seismic and spectropolarimetric studies of bright stars.

Alhena is a bright ($V = 1.90$) spectroscopic binary, in which the primary is a sub-giant A0IVm star (Gray 2014) and the secondary is a cool G star (Thalmann et al. 2014). The orbital elements of the binary have been measured thanks to interferometry (Drummond 2014). The orbital period is 12.63 yr and the orbit is very eccentric with $e = 0.89$. The mass of the primary is estimated to 2.84 $M_\odot$ and the one of the secondary to 1.07 $M_\odot$. The primary, Alhena A, is a weakly Am star (Adelman, Gulliver & Kaewkornmaung 2015b), similar to the three known magnetic Am stars. The stellar parameters of Alhena A are actually very close to the ones of θ Leo, which exhibits peculiar magnetic signatures in its Stokes V profiles (see Table 1).

2 OBSERVATIONS

Data were collected with the NARVAL spectropolarimeter (Aurière 2003; Silvester et al. 2012), installed at the 2-m Bernard Lyot Telescope (TBL) at the summit of Pic du Midi Observatory in the French Pyrénées. Narval is a high-resolution spectropolarimeter, very efficient to detect stellar magnetic fields thanks the polarization they generate in photospheric spectral lines. It covers a wavelength domain from about 375–1050 nm, with a resolving power of ∼68 000.

We used the polarimetry mode to measure the circular polarization (Stokes V). The four sub-exposures are constructively combined to obtain the Stokes V spectrum in addition to the intensity (Stokes I) spectrum. The sub-exposures are also destructively combined to produce a null polarization (N) spectrum to check for spurious detection due to e.g. instrumental effects, variable observing conditions, or non-magnetic physical effects such as pulsations. Alhena was observed on 2014 October 27 and 2015 September 18 and 19. The journal of observations is provided in Table 2.

Table 2. Journal of observations indicating the Heliocentric Julian Date at the middle of the observations (mid-HJD – 2450000), the exposure time in seconds, and the mean signal-to-noise ratio, S/N, of the intensity spectrum at ∼500 nm.

	2014 October 27	2015 September 18	2015 September 19
Mid-HJD	6958.650	7284.695	7285.694
$T_{\rm exp}$ (s)	4 × 25	4 × 35	4 × 35
S/N	986	1016	1093

We used the LIBRE–ESPRIT reduction package (Donati et al. 1997) to reduce the data. We then normalized each of the 40 echelle orders of each of the three Stokes I spectra with the continuum task of IRAF.[1] We applied the same normalization to the Stokes V and N spectra.

3 MAGNETIC ANALYSIS

To test whether Alhena is magnetic, we use the Least Square Deconvolution (LSD) technique. It is a cross-correlation technique for computing average pseudo-line profiles from a list of spectral lines in order to increase the S/N ratio. Under several rough approximations (additive line profiles, wavelength-independent limb-darkening, self-similar local profile shape, weak magnetic fields), stellar spectra can indeed be seen as a line pattern convolved with an average line profile.

We first created a line mask corresponding to the primary component of Alhena. We started from a list of lines extracted from VALD (Piskunov et al. 1995; Kupka & Ryabchikova 1999) for an A star with $T_{\rm eff} = 9250$ K and log g = 3.5, with their Landé factors and theoretical line depths. We then cleaned this line list by removing the hydrogen lines, the lines that are blended with hydrogen lines, as well as those that are not visible in the spectra. We also added some lines visible in the spectra that were not in the original A-star mask. Altogether, we obtained a mask of 1052 lines. We then adjusted the depth of these 1052 lines in the mask to fit the observed line depths.

The results of the LSD analysis are show in Fig. 1. The Stokes V profiles show clear Zeeman signatures for all three nights. We computed the detection probability of the Stokes V signal by using the χ^2 test proposed by Donati, Semel & Rees (1992), getting a detection probability of ≈100 per cent for all observations, with a false alarm probability always smaller than 1.117×10^{-7} inside the stellar line. Therefore, we have a definite detection of a magnetic field in all three nights. We note that the magnetic signatures are strong enough to be detected in individual LSD Stokes V profiles, while for other magnetic Am stars co-addition of many Stokes V profiles were necessary to extract a magnetic signature (Blazère et al. 2016). Outside the stellar line, we obtained a detection probability between 20 per cent and 40 per cent and a false alarm probability between 7.356×10^{-1} and 5.351×10^{1}, that corresponds to a non detection outside the stellar lines.

[1] IRAF is distributed by the National Optical Astronomy Observatories, which are operated by the Association of Universities for Research in Astronomy, Inc., under cooperative agreement with the National Science Foundation.

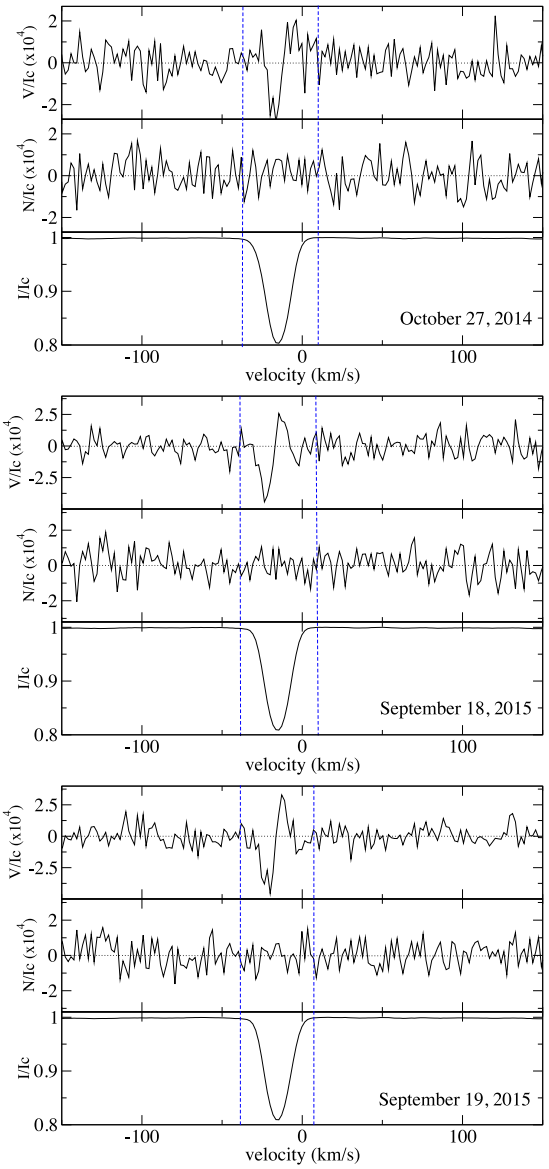

Figure 1. LSD profiles of Alhena A for Stokes I, the null *N* polarization, and Stokes V for the 2014 October 27 (top), 2015 September 18 (centre) and 2015 September 19 (bottom). The vertical blue dashed lines indicate the domain of integration used to determine the longitudinal field values.

Since the diameter of the fibre of Narval is 2.8 arcsec, the two components of the binary have been recorded in the observations. However, the secondary is 5–6 magnitudes fainter than the primary, so only ∼2 per cent of the received light comes from the secondary component. Moreover, the secondary is not visible in the spectra. Thus, the contribution of the lines of the secondary are considered negligible unless its radial velocity is very close to the one of the primary. In addition, we ran the LSD analysis with a mask corresponding to a main-sequence G star and the signatures in the Stokes

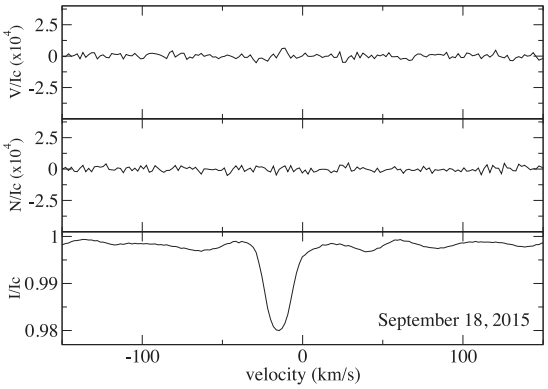

Figure 2. LSD profiles of the companion Alhena B for Stokes I, the null *N* polarization, and Stokes V for 2015 September 18.

Table 3. Longitudinal magnetic field (B_l) and null (N) measurements with their respective error bars and magnetic detection status.

	2014 October 27	2015 September 18	2015 September 19
B_l (G)	-5.1 ± 2.7	-5.6 ± 2.7	-5.5 ± 2.5
N (G)	-1.5 ± 2.7	1.6 ± 2.7	-2.6 ± 2.5
Detection	Definite	Definite	Definite

V profiles disappeared (see Fig. 2). We thus confirm that the signatures in the Stokes V profiles come from the primary star, i.e. that the Am star is magnetic.

Using the centre-of-gravity method (Rees & Semel 1979) with a mean wavelength of 500 nm and a mean Landé factor of ∼1.46 corresponding to the normalization parameters used in the LSD, we calculated the longitudinal field value (B_l) corresponding to these Zeeman signatures over the velocity range [−40:8] km s^{-1}.

$$B_l \propto -\frac{\int v V(v) \mathrm{d}v}{\lambda_0 g_m c \int (1 - I(v)) \mathrm{d}v}, \quad (1)$$

where v (km s^{-1}) is the radial velocity, λ_0 (nm) the normalized wavelength of the line-list used to compute the LSD profiles, g the normalized Landé factor and c (km s^{-1}) the light velocity. The longitudinal magnetic field value for the three observations, and the corresponding null values, are shown in Table 3. The values of the longitudinal magnetic field is around −5 G, with an error bar smaller than 3 G. The values extracted from the *N* profiles are compatible with 0 G.

The shape of the Zeeman signatures in the Stokes V profiles slightly changed between the observation obtained in 2014 and the ones from 2015. This could be due to a rotational modulation of the longitudinal magnetic field, if the field is oblique compared to the rotation axis, as observed in most hot stars (Grunhut & Neiner 2015). In 2014, the signature would look like a cross-over signature, while in 2015, the negative pole may be observed.

On the contrary, the signatures obtained over two consecutive nights in 2015 did not change. This suggests that either Alhena is an intrinsically slow rotator, or the rotational modulation is small because the star is seen under a specific geometrical configuration with an inclination or obliquity angle close to 0.

4 DISCUSSION AND CONCLUSION

The observations presented in this Letter correspond to the first detection of a magnetic field in an Am star with a normal Zeeman signature, i.e. with a positive and negative lobe as seen in the ultra-weakly magnetic A star Vega and in all strongly magnetic hot stars. On the contrary, all the other Am stars studied in spectropolarimetry with a high accuracy exhibit peculiar magnetic signatures with only a prominent positive lobe.

The difference between the field of Alhena and the other Am stars is thus puzzling. In particular, Alhena has very similar stellar parameters as the ones of the magnetic Am star θ Leo. However, the signatures in the Stokes V profiles are very different. θ Leo shows peculiar signatures, while Alhena shows normal signatures. Considering the oblique rotator model, the dipolar magnetic field $B_{\rm d}$ is at least 3.3 times the maximum observed $B_{\rm l}$ value (Preston 1976; Aurière et al. 2007). Therefore, the longitudinal field values measured for Alhena point towards a polar magnetic field strength of the order of 15 G, i.e. weak but much stronger than what is observed in θ Leo and the other magnetic Am stars.

An explanation to the difference between the characteristics of the magnetic field observed in Alhena and in other Am stars may be found in their microturbulence value. The microturbulence of Alhena A is $\sim$1 km s^{-1}(Adelman et al. 2015b), while the one of θ Leo, β UMa, and Sirius A is $\sim$2 km s^{-1} (Landstreet et al. 2009; Adelman, Yu & Gulliver 2011; Adelman, Gulliver & Heaton 2015a). Indeed, the peculiar shape of the magnetic signatures of the latter three Am stars is thought to be related to their stronger microturbulence, compared to normal A stars (Blazère et al. 2016). The very shallow convective shell producing this turbulent velocity field may host supersonic convection flows (Kupka et al. 2009), which could be the source of sharp velocity and magnetic gradients producing strongly asymmetric Zeeman profiles. Alhena A may have a too weak microturbulence to undergo this effect.

Another difference between Alhena and θ Leo is that Alhena is a binary star with a G-type companion, while θ Leo is a single star. However, Sirius is also a binary star and Sirius A does present peculiar magnetic signatures like θ Leo. The distance between the two components of Sirius is larger ($P_{\rm orb}$ = 50.1 yr) than the one of Alhena, nevertheless Alhena is a wide binary as well ($P_{\rm orb}$ = 12.63 yr). However, the orbit of Alhena B is more eccentric (e = 0.89) than the orbit of Sirius B (e = 0.59), and there could thus be more tidal interactions between the two components of Alhena than between the components of Sirius.

Alhena is thus a very interesting star to understand the magnetism of Am stars and ultraweak magnetic fields in general. We will continue to observe Alhena in the frame of the BRITE spectropolarimetric survey to obtain more information about its magnetic field. In particular, the comparison between the observations obtained in 2014 and 2015 indicate that the Stokes V profile could be rotationally modulated, although either the rotation period is long or the geometrical configuration leads to only weak modulation. This could be tested, and the geometrical configuration constrained, thanks to more spectropolarimetric observations spread over the rotation period of Alhena A.

ACKNOWLEDGEMENTS

We thank Oleg Kochukhov and Colin Folsom for useful discussions. We acknowledge support from the ANR (Agence Nationale de la Recherche) project Imagine. This research has made use of the SIMBAD data base operated at CDS, Strasbourg (France), and of NASA's Astrophysics Data System (ADS).

REFERENCES

Adelman S. J., Yu K., Gulliver A. F., 2011, Astron. Nachr.n, 332, 153
Adelman S. J., Gulliver A. F., Heaton R. J., 2015a, PASP, 127, 58
Adelman S. J., Gulliver A. F., Kaewkornmaung P., 2015b, PASP, 127, 340
Aurière M., 2003, in Arnaud J., Meunier N., eds, EAS Publ. Ser. Vol. 9, Stellar Polarimetry with Narval. Cambridge Univ. Press, Cambridge, p. 105
Aurière M. et al., 2007, A&A, 475, 1053
Blazère A. et al., 2016, A&A, 586, A97
Braithwaite J., Cantiello M., 2013, MNRAS, 428, 2789
David T. J., Hillenbrand L. A., 2015, ApJ, 804, 146
Donati J.-F., Semel M., Rees D. E., 1992, A&A, 265, 669
Donati J.-F., Semel M., Carter B. D., Rees D. E., Collier Cameron A., 1997, MNRAS, 291, 658
Drummond J. D., 2014, AJ, 147, 65
Gray D. F., 2014, AJ, 147, 81
Grunhut J. H., Neiner C., 2015, in Nagendra K. N., Bagnulo S., Centeno R., Jesús Martínez González M., eds, Proc. IAU Symp. 305, Polarimetry: From the Sun to Stars and Stellar Environments. Kluwer, Dordrecht, p. 53
Kupka F., Ryabchikova T. A., 1999, Serb. Astron. J., 65, 223
Kupka F., Ballot J., Muthsam H. J., 2009, Commun. Asteroseismology, 160, 30
Landstreet J. D., Kupka F., Ford H. A., Officer T., Sigut T. A. A., Silaj J., Strasser S., Townshend A., 2009, A&A, 503, 973
Lignières F., Petit P., Böhm T., Aurière M., 2009, A&A, 500, L41
Pasinetti Fracassini L. E., Pastori L., Covino S., Pozzi A., 2001, A&A, 367, 521
Petit P. et al., 2011, A&A, 532, L13
Piskunov N. E., Kupka F., Ryabchikova T. A., Weiss W. W., Jeffery C. S., 1995, A&AS, 112, 525
Power J., Wade G. A., Hanes D. A., Aurier M., Silvester J., 2007, in Romanyuk I. I., Kudryavtsev D. O., Neizvestnaya O. M., Shapoval V. M., eds, Properties of a Volume-limited Sample of Magnetic Ap/Bp Stars: Physics of Magnetic Stars. p. 89
Preston G. W., 1976, ApJ, 150, 547
Rees D. E., Semel M. D., 1979, A&A, 74, 1
Royer F., Gerbaldi M., Faraggiana R., Gómez A. E., 2002, A&A, 381, 105
Royer F., Zorec J., Gómez A. E., 2007, A&A, 463, 671
Silvester J., Wade G. A., Kochukhov O., Bagnulo S., Folsom C. P., Hanes D., 2012, MNRAS, 426, 1003
Thalmann C. et al., 2014, A&A, 572, A91
Weiss W. W. et al., 2014, in Guzik J. A., Chaplin W. J., Handler G., Pigulski A., eds, Proc. IAU Symp. 301, Precision Asteroseismology. Kluwer, Dordrecht, p. 67
Wolff S. C., 1968, PASP, 80, 281
Zorec J., Royer F., 2012, A&A, 537, A120

This paper has been typeset from a TEX/LATEX file prepared by the author.

Appendix D

Other refereed publications

1. Böhm T., Holschneider M., Lignières F., Petit P., Rainer M., Paletou F., Wade G., Alecian E., Carfantan H., Blazère A., Mirouh G. M, *Discovery of starspots on Vega. First spectroscopic detection of surface structures on a normal A-type star*, 2015, A&A,577, 64

2. Neiner Coralie, Buysschaert Bram, Oksala Mary E., Blazère Aurore, *Discovery of two new bright magnetic B stars: ι Car and Atlas*, MNRAS, 454,56

3. Wade G. A., Neiner C., Alecian E., Grunhut J. H., Petit V., Batz B. de, Bohlender D. A., Cohen D. H., Henrichs H. F., Kochukhov O., Landstreet J. D., Manset N., Martins F., Mathis S., Oksala M. E., Owocki S. P., Rivinius Th., Shultz M. E., Sundqvist J. O., Townsend R. H. D., ud-Doula A., Bouret J.-C., Braithwaite J., Briquet M., Carciofi A. C., David-Uraz A., Folsom C. P., Fullerton A. W., Leroy B., Marcolino W. L. F., Moffat A. F. J., Nazé Y., Louis N. St, Aurière M., Bagnulo S., Bailey J. D., Barbá R. H., Blazère A., Böhm T., Catala C., Donati J.-F., Ferrario L., Harrington D., Howarth I. D., Ignace R., Kaper L., Lüftinger T., Prinja R., Vink J. S., Weiss W. W., Yakunin I., *The MiMeS survey of magnetism in massive stars: introduction and overview*,2016, A&A, 456,2

4. Schneider N. , Bontemps S. , Motte F. , Blazere A. , André Ph. , Anderson L. D. , Arzoumanian D. , Comerón F. , Didelon P. , Di Francesco J. , Duarte-Cabral A. , Guarcello M. G. , Hennemann M. , Hill T. , Könyves V. , Marston A. , Minier V. , Rygl K. L. J. , Röllig M. , Roy A. , Spinoglio L. , Tremblin P. , White G. J. , Wright N. J., *Globules and pillars in Cygnus X. I. Herschel far-infrared imaging of the Cygnus OB2 environment*, 2016, A&A, 591,40

Bibliography

Abt, H. A. 2009, AJ, 138, 28

Adelman, S. J. 1997, PASP, 109, 9

Adelman, S. J., Gulliver, A. F., & Heaton, R. J. 2015a, PASP, 127, 58

Adelman, S. J., Gulliver, A. F., & Kaewkornmaung, P. 2015b, PASP, 127, 340

Adelman, S. J., Gulliver, A. F., Kochukhov, O. P., & Ryabchikova, T. A. 2002, ApJ, 575, 449

Adelman, S. J., Yu, K., & Gulliver, A. F. 2011, Astronomische Nachrichten, 332, 153

Alecian, E., Catala, C., Wade, G. A., et al. 2008, MNRAS, 385, 391

Alecian, G. 2012, in Astronomical Society of the Pacific Conference Series, Vol. 462, Progress in Solar/Stellar Physics with Helio- and Asteroseismology, ed. H. Shibahashi, M. Takata, & A. E. Lynas-Gray, 80

Allende Prieto, C., García López, R. J., Lambert, D. L., & Gustafsson, B. 1999, ApJ, 527, 879

Anderson, E. & Francis, C. 2012, Astronomy Letters, 38, 331

Aurière, M. 2003, in EAS Publications Series, Vol. 9, EAS Publications Series, ed. J. Arnaud & N. Meunier, 105

Aurière, M., Konstantinova-Antova, R., Petit, P., et al. 2011, A & A, 534, A139

Aurière, M., Silvester, J., Wade, G. A., et al. 2004, in IAU Symposium, Vol. 224, The A-Star Puzzle, ed. J. Zverko, J. Ziznovsky, S. J. Adelman, & W. W. Weiss, 633–636

Aurière, M., Wade, G. A., Konstantinova-Antova, R., et al. 2009, A & A, 504, 231

Aurière, M., Wade, G. A., Lignières, F., et al. 2010, A & A, 523, A40

Aurière, M., Wade, G. A., Lignières, F., et al. 2008, Contributions of the Astronomical Observatory Skalnate Pleso, 38, 211

Aurière, M., Wade, G. A., Silvester, J., et al. 2007, A & A, 475, 1053

Babcock, H. W. 1947, PASP, 59, 260

Babu, G. S. D. & Shylaja, B. S. 1981, apss, 79, 243

Ballering, N. P., Rieke, G. H., Su, K. Y. L., & Montiel, E. 2013, ApJ, 775, 55

Balona, L. A. 2011, MNRAS, 415, 1691

Balona, L. A. 2013, MNRAS, 431, 2240

Balona, L. A., Catanzaro, G., Abedigamba, O. P., Ripepi, V., & Smalley, B. 2015, MNRAS, 448, 1378

Böhm, T., Holschneider, M., Lignières, F., et al. 2015, A & A, 577, A64

Borra, E. F. & Landstreet, J. D. 1980, ApJs, 42, 421

Borra, E. F., Landstreet, J. D., & Thompson, I. 1983, ApJs, 53, 151

Bouret, J.-C., Donati, J.-F., Martins, F., et al. 2008, MNRAS, 389, 75

Boyajian, T. S., McAlister, H. A., van Belle, G., et al. 2012, ApJ, 746, 101

Braithwaite, J. & Cantiello, M. 2013, MNRAS, 428, 2789

Braithwaite, J. & Spruit, H. C. 2004, nature, 431, 819

Briquet, M., Neiner, C., Petit, P., Leroy, B., & de Batz, B. 2016, A & A, 587, A126

Butkovskaya, V., Plachinda, S., Valyavin, G., Baklanova, D., & Lee, B.-C. 2011, Astronomische Nachrichten, 332, 956

Bychkov, V. D., Bychkova, L. V., & Madej, J. 2005, A & A, 430, 1143

Caliskan, H. & Adelman, S. J. 1997, MNRAS, 288, 501

Cantiello, M. & Braithwaite, J. 2011, A & A, 534, A140

Chapellier, E., Mathias, P., Le Contel, J.-M., et al. 2000, A & A, 362, 189

Charbonneau, P. & MacGregor, K. B. 2001, ApJ, 559, 1094

Chountonov, G. 2001, in Astronomical Society of the Pacific Conference Series, Vol. 248, Magnetic Fields Across the Hertzsprung-Russell Diagram, ed. G. Mathys, S. K. Solanki, & D. T. Wickramasinghe, 385

Cohen, D. H., Li, Z., Gayley, K. G., et al. 2014, MNRAS, 444, 3729

Correia, A. C. M., Boué, G., & Laskar, J. 2012, ApJl, 744, L23

David, T. J. & Hillenbrand, L. A. 2015, ApJ, 804, 146

Dekker, H., D'Odorico, S., Kaufer, A., Delabre, B., & Kotzlowski, H. 2000, in Society of Photo-Optical Instrumentation Engineers (SPIE) Conference Series, Vol. 4008, Optical and IR Telescope Instrumentation and Detectors, ed. M. Iye & A. F. Moorwood, 534–545

Donati, J.-F., Babel, J., Harries, T. J., et al. 2002, MNRAS, 333, 55

Donati, J.-F., Paletou, F., Bouvier, J., & Ferreira, J. 2005, nature, 438, 466

Donati, J.-F., Semel, M., Carter, B. D., Rees, D. E., & Collier Cameron, A. 1997, MNRAS, 291, 658

Donati, J.-F., Semel, M., & Rees, D. E. 1992, A & A, 265, 669

Drummond, J. D. 2014, AJ, 147, 65

Duez, V. & Mathis, S. 2010, A & A, 517, A58

Emeriau, C. & Mathis, S. 2015, in IAU Symposium, Vol. 307, New Windows on Massive Stars, ed. G. Meynet, C. Georgy, J. Groh, & P. Stee, 373–374

Featherstone, N. A., Browning, M. K., Brun, A. S., & Toomre, J. 2009, ApJ, 705, 1000

Ferrario, L., Pringle, J. E., Tout, C. A., & Wickramasinghe, D. T. 2009, MNRAS, 400, L71

Ferreira, J., Pelletier, G., & Appl, S. 2000, MNRAS, 312, 387

Folsom, C. P., Likuski, K., Wade, G. A., et al. 2013, MNRAS, 431, 1513

Gaurat, M., Jouve, L., Lignières, F., & Gastine, T. 2015, A & A, 580, A103

Glagolevskii, Y. V., Romanyuk, I. I., Bychkov, V. D., & Naidenov, I. D. 1985, Soviet Astronomy Letters, 11, 45

Glebbeek, E., Gaburov, E., Portegies Zwart, S., & Pols, O. R. 2013, MNRAS, 434, 3497

Gray, D. F. 2014, AJ, 147, 81

Grunhut, J. H. 2015, in IAU Symposium, Vol. 307, IAU Symposium, 301–310

Grunhut, J. H. & Neiner, C. 2015, in IAU Symposium, Vol. 305, , 53

Grunhut, J. H., Wade, G. A., Leutenegger, M., et al. 2013, MNRAS, 428, 1686

Gutiérrez-Soto, J., Floquet, M., Samadi, R., et al. 2009, A & A, 506, 133

Hadrava, P. 1995, A & As, 114, 393

Hale, G. E. 1908, PASP, 20, 287

Handler, G., Matthews, J. M., Eaton, J. A., et al. 2009, ApJl, 698, L56

Helstrom, C. W. 1995, Elements of Signal Detection and Estimation (Prentice Hall)

Hennebelle, P. & Fromang, S. 2008, A & A, 477, 9

Horne, K. 1986, PASP, 98, 609

Hubeny, I. & Lanz, T. 1995, ApJ, 439, 875

Hummel, C. A., Rivinius, T., Nieva, M.-F., et al. 2013, A & A, 554, A52

Ilijic, S., Hensberge, H., Pavlovski, K., & Freyhammer, L. M. 2004, in , 111

Jouve, L., Gastine, T., & Lignières, F. 2015, A & A, 575, A106

Kay, S. M. 1998, Fundamentals of Statistical Signal Processing, Volume 2: Detection Theory (Prentice Hall)

Kochukhov, O. 2014, in Putting A Stars into Context: Evolution, Environment, and Related Stars, ed. G. Mathys, E. R. Griffin, O. Kochukhov, R. Monier, & G. M. Wahlgren, 389–397

Kochukhov, O., Makaganiuk, V., & Piskunov, N. 2010, A & A, 524, A5

Kochukhov, O. & Wade, G. A. 2016, A & A, 586, A30

Kupka, F., Ballot, J., & Muthsam, H. J. 2009, Communications in Asteroseismology, 160, 30

Kupka, F. & Ryabchikova, T. A. 1999, Publications de l'Observatoire Astronomique de Beograd, 65, 223

Landi Degl'Innocenti, E. & Landolfi, M., eds. 2004, Astrophysics and Space Science Library, Vol. 307, Polarization in Spectral Lines

Landstreet, J. D., Kupka, F., Ford, H. A., et al. 2009, A & A, 503, 973

Lèbre, A., Aurière, M., Fabas, N., et al. 2014, A & A, 561, A85

Lefever, K., Puls, J., Morel, T., et al. 2010, A & A, 515, A74

Lehmann, H., Egorova, I., Scholz, G., Hildebrandt, G., & Andrievsky, S. M. 2003, A & A, 402, 229

Levy, B. C. 2008, Principles of signal detection and parameters estimation (Springer)

Lignières, F., Petit, P., Böhm, T., & Aurière, M. 2009, A & A, 500, L41

López Ariste, A. 2002, ApJ, 564, 379

Lüftinger, T., Fröhlich, H.-E., Weiss, W. W., et al. 2010, A & A, 509, A43

MacGregor, K. B. & Cassinelli, J. P. 2003, ApJ, 586, 480

Maestro, V., Che, X., Huber, D., et al. 2013, MNRAS, 434, 1321

Marsh, T. R. 1989, PASP, 101, 1032

Mestel, L. 1999, Stellar magnetism

Michaud, G. 1970, ApJ, 160, 641

Monier, R. 2005, A & A, 442, 563

Morgenthaler, A., Petit, P., Saar, S., et al. 2012, A & A, 540, A138

Moutou, C., Donati, J.-F., Savalle, R., et al. 2007, A & A, 473, 651

Neiner, C., Alecian, E., & Mathis, S. 2011, in SF2A-2011: Proceedings of the Annual meeting of the French Society of Astronomy and Astrophysics, ed. G. Alecian, K. Belkacem, R. Samadi, & D. Valls-Gabaud, 509–513

Neiner, C., Folsom, C. P., & Blazere, A. 2014a, in SF2A-2014, 163–166

Neiner, C., Grunhut, J., Leroy, B., De Becker, M., & Rauw, G. 2015a, A & A, 575, A66

Neiner, C. & Lèbre, A. 2014, in SF2A-2014: Proceedings of the Annual meeting of the French Society of Astronomy and Astrophysics, ed. J. Ballet, F. Martins, F. Bournaud, R. Monier, & C. Reylé, 505–508

Neiner, C., Mathis, S., Alecian, E., et al. 2015b, in IAU Symposium, Vol. 305, Polarimetry, ed. K. N. Nagendra, S. Bagnulo, R. Centeno, & M. Jesús Martínez González, 61–66

Neiner, C., Monin, D., Leroy, B., Mathis, S., & Bohlender, D. 2014b, A & A, 562, A59

Neiner, C., Tkachenko, A., & MiMeS Collaboration. 2014c, A & A, 563, L7

Nieva, M.-F. 2013, A & A, 550, A26

Pasinetti Fracassini, L. E., Pastori, L., Covino, S., & Pozzi, A. 2001, A & A, 367, 521

Petit, P., Donati, J.-F., Aurière, M., et al. 2005, MNRAS, 361, 837

Petit, P., Lignières, F., Aurière, M., et al. 2011, A & A, 532, L13

Petit, P., Lignières, F., Wade, G. A., et al. 2010, A & A, 523, A41

Petit, P., Lignières, F., Wade, G. A., et al. 2014a, A & A, 568, C2

Petit, P., Louge, T., Théado, S., et al. 2014b, PASP, 126, 469

Petit, V. 2011, PhD thesis, Faculté des sciences et de génie ,Université Laval,Québec

Petit, V., Owocki, S. P., Wade, G. A., et al. 2013, MNRAS, 429, 398

Piskunov, N. E., Kupka, F., Ryabchikova, T. A., Weiss, W. W., & Jeffery, C. S. 1995, A & As, 112, 525

Power, J., Wade, G. A., Hanes, D. A., Aurier, M., & Silvester, J. 2007, in Physics of Magnetic Stars, ed. I. I. Romanyuk, D. O. Kudryavtsev, O. M. Neizvestnaya, & V. M. Shapoval, 89–97

Preston, G. W. 1967, ApJ, 150, 547

Prugniel, P., Vauglin, I., & Koleva, M. 2011, A & A, 531, A165

Rees, D. E. & Semel, M. D. 1979, A & A, 74, 1

Royer, F., Gerbaldi, M., Faraggiana, R., & Gómez, A. E. 2002, A & A, 381, 105

Royer, F., Zorec, J., & Gómez, A. E. 2007, A & A, 463, 671

Ryabchikova, T., Malanushenko, V., & Adelman, S. J. 1998, Contributions of the Astronomical Observatory Skalnate Pleso, 27, 356

Ryabchikova, T. A., Malanushenko, V. P., & Adelman, S. J. 1999, A & A, 351, 963

Sainz Dalda, A., Martínez-Sykora, J., Bellot Rubio, L., & Title, A. 2012, ApJ, 748, 38

Schneider, F. R. N., Podsiadlowski, P., Langer, N., Castro, N., & Fossati, L. 2016, MNRAS, 457, 2355

Semel, M., Donati, J.-F., & Rees, D. E. 1993, A & A, 278, 231

Shore, S. N. 1987, AJ, 94, 731

Shorlin, S. L. S., Wade, G. A., Donati, J.-F., et al. 2002, A & A, 392, 637

Shultz, M., Wade, G. A., Alecian, E., & BinaMIcS Collaboration. 2015, MNRAS, 454, L1

Silvester, J., Kochukhov, O., & Wade, G. A. 2014, MNRAS, 444, 1442

Silvester, J., Wade, G. A., Kochukhov, O., et al. 2012, MNRAS, 426, 1003

Simon, K. P. & Sturm, E. 1994, A & A, 281, 286

Simón-Díaz, S. & Herrero, A. 2014, A & A, 562, A135

Solanki, S. K. 1993, ssr, 63, 1

Stepien, K. & Czechowski, W. 1993, A & A, 268, 187

Stibbs, D. W. N. 1950, MNRAS, 110, 395

Takeda, Y., Kawanomoto, S., & Ohishi, N. 2008, ApJ, 678, 446

Telting, J. H., Schrijvers, C., Ilyin, I. V., et al. 2006, A & A, 452, 945

Thalmann, C., Desidera, S., Bonavita, M., et al. 2014, A & A, 572, A91

Tomkin, J., Pan, X., & McCarthy, J. K. 1995, AJ, 109, 780

Tsvetkova, S., Petit, P., Aurière, M., et al. 2013, A & A, 556, A43

ud-Doula, A. & Owocki, S. P. 2002, ApJ, 576, 413

Viticchié, B. & Sánchez Almeida, J. 2011, A & A, 530, A14

Wade, G. A., Aurière, M., Bagnulo, S., et al. 2006, A & A, 451, 293

Wade, G. A., Donati, J.-F., Landstreet, J. D., & Shorlin, S. L. S. 2000, MNRAS, 313, 823

Wade, G. A., Folsom, C. P., Petit, P., et al. 2014a, MNRAS, 444, 1993

Wade, G. A., Grunhut, J., Alecian, E., et al. 2014b, in IAU Symposium, Vol. 302, 265–269

Wade, G. A., Neiner, C., Alecian, E., et al. 2016, MNRAS, 456, 2

Weiss, W. W., Moffat, A. F. J., Schwarzenberg-Czerny, A., et al. 2014, in IAU Symposium, Vol. 301, IAU Symposium, ed. J. A. Guzik, W. J. Chaplin, G. Handler, & A. Pigulski, 67

Zahn, J.-P. 2008, in EAS Publications Series, Vol. 29, EAS Publications Series, ed. M.-J. Goupil & J.-P. Zahn, 67–90

Zeeman, P. 1897, nature, 55, 347

Zorec, J. & Royer, F. 2012, A & A, 537, A120

Résumé

Les champs magnétiques jouent un rôle important dans l'évolution stellaire, mais les propriétés magnétiques des étoiles massives et de masse intermédiaire sont mal connues. Seule une petite fraction (7%) des étoiles massives et de masse intermédiaire possèdent un champ magnétique et la force de leur champ dipolaire est supérieure à ~300 Gauss. La théorie pour expliquer l'origine de ces champs, la théorie des champs fossiles, n'explique pas pourquoi seulement une petite partie des étoiles chaudes ont un champ magnétique. Récemment, un champ magnétique ultra-faible (moins de 1 Gauss) à été découvert sur deux étoiles de masse intermédiaire (Vega et Sirius). Ce sont peut être les premières detections d'un nouveau type de champ magnétique faible. Deux familles d'étoiles magnétiques chaudes pourraient donc exister, avec des champs forts ou ultra-faibles, séparées par ce qu'on apelle le désert magnétique.

Ma thèse consiste à analyser des données spectropolarimétriques prises avec des spectropolarimètres haute résolution, principalement avec Narval installé au télescope de 2 mètres à l'Observatoire du Pic du Midi. Une partie de ma thèse été dediée à l'étude des champs magnétiques les plus faibles, parmi les champs forts. J'ai analysé les observations de l'étoiles O massive ζ Ori A. Peu d'étoiles O sont connues pour être magnétiques et ζ Ori A possède le plus faible champ magnétique. J'ai aussi participé à un programme observationel pour déterminer la limite supérieure du désert magnétique grâce aux étoiles Ap/Bp. Le but de ces études est de tester la dépendance de la limite supérieure du désert magnétique par rapport à la rotation et à la masse. Une deuxième partie de ma thèse est consacrée à la recherche des champs ultra-faibles pour fournir des contraintes aux divers scenarios qui expliquent la dichotomie entre les champs forts et faibles et améliorer notre connaissance des propriétés de ce type de champ magnétique. Je présente les résultats d'études d'étoiles normales, UZ Lyn et Vega, ainsi que celles de plusieurs d'étoiles chimiquement particulières (Am et HgMn). Les études présentées dans ma thèse apportent une lumière nouvelle sur le magnétisme des étoiles chaudes et des contraintes pour la physique stellaire en général, en particulier pour l'évolution stellaire.

Mot Clés

Champs magnétiques, spectropolarimétrie, étoiles chaudes

Abstract

Magnetic fields are known to play a fundamental role in stellar evolution but the magnetic properties of massive and intermediate-mass stars are not well understood. Only a small (7%) fraction of massive and intermediate-mass stars are found to be magnetic and their dipolar magnetic field strength is above ~300 Gauss. The current paradigm, the fossil field theory, describes this magnetism as remnant of an early phase of the star-life, but leaves many basic questions unanswered, such as the small fraction of magnetic stars, and in practice provides no constraint to stellar evolution theory. Recently, an ultra weak magnetic field (less than 1 Gauss) has been discovered in two intermediate mass stars (Vega and Sirius). They may be the first detections of a new type of weak magnetic fields. Two families of magnetic stars may thus exist: with strong or ultra-weak fields, separated by the so-called magnetic desert.

My PhD thesis consists in analyzing observational data taken with high-resolution spectropolarimeters, mainly with Narval installed on the 2-meter telescope at the Pic du Midi Observatory, to detect magnetic fields. One part of my thesis is dedicated to the study of the weakest end of strong magnetic fields. I analyzed the observations of a massive O star, ζ Ori A. Only a few O stars are known to be magnetic and z Ori A has the weakest field. I was also involved in a project to determine the upper limit of the magnetic desert thanks to observations of Ap/Bp stars. The goal of these studies is to test the dependence of the upper limit with rotation and mass. The other part of my thesis is dedicated to the search for ultra-weak fields in hot stars to provide constraints to the various scenarios that explain the strong vs weak field dichotomy and improve our understanding of the properties of this kind of weak field. I present the result of the studies of normal stars, UZ Lyn and Vega, and of several chemically peculiar (Am and HgMn) stars. The studies presented in my PhD thesis provide new clues about magnetism in hot stars and constraint for stellar physics in general, in particular for stellar evolution.

Keywords

Magnetic fields, spectropolarimetry, hot stars